

Poznan University of Technology
Faculty of Civil and Environmental Engineering



Doctoral Thesis

APPLICATION OF PASSIVE DAMPING SYSTEMS IN BLAST RESISTANT GATES

by

Hasan Ali Sultan AL-RIFAIE

Supervisor

Dr. Hab. Eng. Wojciech Sumelka

Co-Supervisor

Dr. Eng. Piotr W. Sielicki

“Submitted in partial fulfilment of the requirements for the degree, Doctor of Philosophy (Ph.D.), in Structural Engineering, in the Faculty of Civil and Environmental Engineering, Poznan University of Technology, Poznan, Poland”

Poznan, 2018

Acknowledgements

First and foremost, I would like to thank God for giving me the strength, knowledge and opportunity to undertake this research.

In my journey towards this degree, I have found a teacher, a friend and a supervisor, who is Dr. Hab. Eng. Wojciech Sumelka. I wish to express my special thanks to him for numerous hours of discussions during the preparation of the thesis. He has been there providing his scientific support and guidance with giving me all the freedom to pursue my research. His encouragement and ideas were main contributors in the completion of this thesis.

I have great pleasure in acknowledging my co-supervisor, Dr. Eng. Piotr W. Sielicki, for his technical support during the work. We spent many afternoons discussing academic problems and sharing experiences that enriched me beyond expectations.

I am very grateful to Prof. Tomasz Lodygowski, for all his kind support and assistance. His advice and wise guidance during my "final steps" are non-forgettable. Moreover, special thanks to Prof. Adam Glema for giving me the opportunity to join the Faculty of Civil and Environmental Engineering at early stages as a researcher, and then encouraging me to start my PhD.

I would like to thank all my colleagues from the Institute of Structural Engineering, for a friendly atmosphere, suggestions, discussions and continuous interest in the progress of this research.

My acknowledgement would be incomplete without thanking the biggest source of my strength, my family; starting from parents, whose support and encouragement mean the most to me; my wife, for her patience, constant support and love; and finally, my kids, for adding joy and meaning to my life.

Abstract

Blast resistant gates are essential for sensitive infrastructure, such as embassies, ministries or parliaments. Lightweight gates equipped with ‘energy absorbing systems’ have better operational performance than the traditional costly and bulky design. Graded auxetic structures have not yet been used as potential passive damping systems in the supporting frame of blast resistant gates. Consequently, this thesis tried to design a new graded auxetic damping system and investigate if it could maintain a 3000x4500mm steel gate operable after high blast pressure of 6.6 MPa, from 100kg TNT at 5m stand-off distance. Blast-induced response of the gate was assessed, with and without the proposed Uniaxial Graded Auxetic Damper (UGAD), using Abaqus/Explicit solver.

Results showed that the attachment of the proposed UGAD to the gate, led to a dramatic decrease in permanent deformations (a critical factor for gate operability after a blast event). Hence, a lighter, more economical gate (with 50% reduction in mass) was required to satisfy the operability condition. In addition, 49% of peak reaction forces were diminished, that had a direct impact on the concrete supporting frame. Results also showed that internal energy in the whole model composed mainly of plastic dissipation energy, with 56% achieved from the UGADs, and 44% from the gate. The additional plastic dissipation energy gained from those sacrificial light-weight auxetics justifies the significant reduction in permanent deformations, mass of the gate and reaction forces. Finally, a proper reinforced concrete supporting system was modelled and showed to stay in the elastic range. The UGAD may also be used in different scales for other structural applications, such as; blast-resistant façade and crash energy absorbers in automotive industry. The outcomes of this research may have a positive impact on other sectors beyond academia, such as industry, economy and public safety.

Streszczenie (Abstract in Polish Language)

Bramy odporne na wybuch stanowią kluczowy element infrastruktury krytycznej, w tym budynków ambasad, ministerstw czy też parlamentów. Szczególne znaczenie zajmują w ww. kategorii bram, lekkie bramy wyposażone w systemy absorpcji energii, które to systemy w znaczący sposób poprawiają parametry eksploatacji bramy oraz zmniejszają oddziaływanie na konstrukcję wsporczą. Jednym z możliwych pasywnych systemów absorpcji energii wybuchu, stanowi oryginalna koncepcja gradientowych struktur auksetycznych i to właśnie ona stanowi główny problem badawczy niniejszej rozprawy. W ramach badań rozważano w szczególności układ stalowa brama (o wymiarach 3000x4500mm) z oraz bez systemu absorpcji energii oraz żelbetowa konstrukcja wsporcza, poddany ciśnieniu 6.6MPa (oddziaływanie uzyskane od 100kg TNT z odległości 5m). Finalnym osiągnięciem rozprawy jest konstrukcja Jednoosiowego Gradientowego Tłumika Auksetycznego (JGTA), uzyskana w ramach wirtualnego prototypowania z wykorzystaniem oprogramowania Abaqus/Explicit.

Wyniki uzyskane w ramach zaawansowanego studium numerycznego wykazały, iż zastosowanie systemu JGTA prowadzi do dramatycznego obniżenia deformacji trwałych bramy (krytycznego parametru związanego z oceną użyteczności bramy po wybuchu). Wykorzystanie systemu JGTA umożliwiło redukcję masy bramy o ponad 50% oraz zmniejszenie o 49% sił reakcji na konstrukcję wsporczą, w porównaniu do układu brama-konstrukcja wsporcza bez systemu absorpcji. Wykazano, iż energia wewnętrzna w modelu składa się głównie z plastycznej dyssypacji, w skład której wchodzi dyssypacja z JGTA (56%) oraz plastyczna dyssypacja bramy (44%) – stąd tak znacząca możliwość redukcji masy samej bramy oraz znacząco mniejsze oddziaływania na konstrukcję wsporczą. Jest istotne, iż studium obejmuje również dodatkowo swym zakresem analizę żelbetowej konstrukcji wsporczej. Ważnym osiągnięciem, jest również fakt, iż JGTA może być również wykorzystywany w innych zastosowaniach inżynierii, takich jak fasady odporne na wybuch czy też absorbery energii w przemyśle motoryzacyjnym. W konkluzji, przedstawione wyniki badań, mogą mieć zatem znacznie szerszy wpływ niż środowisko akademickie t.j. wpływ na przemysł, tym samym na ekonomię oraz bezpieczeństwo publiczne.

Publications arising from this thesis

Journal Articles:

1. H. Al-Rifaie, W. Sumelka, Numerical analysis of reaction forces in blast resistant gates, **Structural Engineering & Mechanics** 63(3):347-359, May 2017, DOI: 10.12989/sem.2017.63.3.347
2. P.W.Sielicki, T.Lodygowski, H.Al-Rifaie, W.Sumelka, Designing of blast resistant lightweight elevation system - numerical study, **Procedia Engineering**, Vol. 172, 2017, pp. 991-998.

Conferences:

1. H. Al-Rifaie, W. Sumelka and P.W. Sielicki. Parametric design of re-entrant auxetics for efficient blast energy absorption, **5th International Conference on Protective Structures**, will be held in Poznan, Poland, 20 – 24 August 2018.
2. H. Al-Rifaie, W. Sumelka, Numerical assessment of a blast-protective steel gate with a new damping system, **The 22nd International Conference on Computer Methods in Mechanics**, pp. MS11 (15-16), Lublin 13-16 September 2017.
3. H. Al-Rifaie, W. Sumelka and P.W. Sielicki. Numerical analysis of reaction forces in blast resistant gates, book of Abstracts, T. Lodygowski and W. Sumelka (Eds.), **The 10th International workshop on Dynamic behavior of Materials and its applications in Industrial processes**, pp. 21-23, Poznan, 24-26 August 2016.
4. P.W.Sielicki, T.Lodygowski, H.Al-Rifaie, W.Sumelka, Designing of blast resistant lightweight elevation system - numerical study, **12th International Conference: Modern Building Materials, Structures and Techniques (MBMST)**, May 26-27, 2016, Vilnius, Lithuania.
5. H. Al-Rifaie, A. Glema, M. Malendowski, "Vertical Seismic Load Effects on the Response of Structures with Toggle Brace Dampers", in J. Kruis, Y. Tsompanakis, B.H.V. Topping, (Editors), "Proceedings of **the Fifteenth International Conference on Civil, Structural and Environmental Engineering Computing**", Civil-Comp Press, Stirlingshire, UK, Paper 120, 2015. doi:10.4203

Contents

Acknowledgments.....	i
Abstract.....	ii
Streszczenie (Abstract in Polish Language).....	iii
Publications arising from this thesis.....	iv
Contents.....	v
List of Figures.....	viii
List of Tables.....	xiv
List of Symbols and Abbreviations.....	xvi
1 INTRODUCTION.....	1
1.1 Motivation.....	1
1.2 Aim and objectives.....	3
1.3 Structure of the thesis.....	4
2 FUNDAMENTALS OF BLAST RESISTANT DESIGN.....	6
2.1 Blast phenomenon.....	6
2.2 Blast loading.....	7
2.3 Structural response of SDOF system.....	10
2.4 Engineering manuals and standards.....	13
2.5 Blast simulation techniques.....	15
2.6 Numerical codes.....	17
2.6.1 Simulia Abaqus Software.....	17
2.6.2 Implicit/explicit time discretization.....	18
2.6.3 ConWep/CEL tools.....	18
3 LITERATURE REVIEW.....	20
3.1 Reaction forces and loading nature.....	20
3.2 Blast Resistant Gates.....	22

3.3	Damping Systems.....	24
3.4	Auxetic Structures.....	28
3.5	Conclusions.....	32
4	THEORITICAL FRAMEWORK.....	33
4.1	Continuum Mechanics.....	33
4.1.1	Kinematics.....	33
4.1.2	Balance Laws.....	39
4.1.3	Constitutive Laws.....	42
4.2	Finite Element Method.....	44
4.2.1	Finite elements formulation of quasi-static problems.....	45
4.2.2	Finite elements formulation of dynamic problems.....	47
5	BLAST- INDUCED REACTION FORCES.....	49
5.1	Preface.....	49
5.2	Case study.....	50
5.2.1	Geometry.....	51
5.2.2	Boundary conditions.....	52
5.2.3	Material and J-C model.....	53
5.2.4	Loading.....	56
5.3	Methodology.....	57
5.3.1	Static analysis.....	57
5.3.2	Dynamic analysis.....	61
5.4	Results and discussion.....	62
5.4.1	Static analysis.....	62
5.4.2	Dynamic analysis.....	64
5.4.3	Effects of variation in explosive mass and position.....	72
5.5	Conclusions.....	74
6	VIRTUAL DESIGN OF THE GATE.....	76
6.1	Site plan and Assumptions.....	76
6.2	Geometrical and material properties of the gate.....	77

6.3	Threat Assessment and Blast Loading.....	79
6.4	Numerical Modelling.....	81
6.5	Peak nodal reaction forces.....	83
6.5.1	Effect of explosive location.....	84
6.5.2	Effect of blast pressure level.....	86
6.5.3	Effect of gate mass.....	87
6.6	Gate Performance.....	88
6.7	Conclusions.....	91
7	PARAMETRIC DESIGN AND APPLICATION OF UNIAXIAL GRADED AUXETIC DAMPER.....	92
7.1	Auxetic damper properties.....	92
7.1.1	Geometry and location.....	92
7.1.2	Material of the auxetic core.....	95
7.1.3	Numerical Model.....	98
7.2	Parametric study of the auxetic core.....	100
7.2.1	Loading direction.....	100
7.2.2	Cell dimension.....	103
7.2.3	Aluminium grade.....	105
7.2.4	Cell angle.....	106
7.2.5	Re-entrant auxetics vs. non-auxetic Honeycombs.....	108
7.2.6	Number of layers.....	110
7.3	Cell wall thickness t	112
7.3.1	Optimum value of t for 3.3 MPa blast level (50kg TNT, R=5m).....	114
7.3.2	Optimum value of t for 4.95 MPa blast level (75kg TNT, R=5m).....	115
7.3.3	Optimum value of t for 6.6 MPa blast level (100kg TNT, R=5m).....	116
7.4	Final properties of the UGAD.....	117
7.5	Gate behaviour with the proposed auxetic damper.....	121
7.6	Designing a reinforced concrete supporting structure.....	127
8	CONCLUSIONS.....	137
	BIBLIOGRAPHY.....	140

List of Figures

Fig. 1.1	Blast resistant gates	2
Fig. 2.1	Vehicle threat and blast scene parameters	7
Fig. 2.2	Typical time-history of blast wave pressure	8
Fig. 2.3	Structural-load idealization	11
Fig. 2.4	UCSD blast simulator and testing scene	16
Fig. 3.1	Blast Sandwich panel with RFHDS damping system	25
Fig. 3.2	UPD components	26
Fig. 3.3	VE solid damper configuration and applied blast pressure	26
Fig. 3.4	Schematics of normal and auxetic deformation behaviour of 2D elements under tension or compression	28
Fig. 3.5	Some cellular geometries that give auxetic behaviour	29
Fig. 3.6	Geometrical parameters of the Aux (left) and Hex (right) unit cell	31
Fig. 4.1	Mapping of infinitesimal geometrical elements from reference configuration to current configuration	34
Fig. 4.2	Traction vectors T and t in \mathcal{B}_0 and \mathcal{B}_t , respectively	38
Fig. 4.3	Finite element mesh of a steel plate with a hole	44
Fig. 5.1	Blast scene under consideration	51
Fig. 5.2	Selected boundary conditions	52
Fig. 5.3	The 12 cases under consideration (four BCs and three ARs)	52
Fig. 5.4	Variation of the explosive centroid position in x, y and z directions	56
Fig. 5.5	Plate configuration	57
Fig. 5.6	Loading of the SSSS case, AR=1, and the corresponding HMH stresses	60
Fig. 5.7	The amount and distribution of pressure (in MPa) generated from ConWep ($M = 100\text{kg}$ TNT, $R = 30\text{m}$) on the surface of steel plate, AR=1	61
Fig. 5.8	Distribution of reaction forces (in N/mm) along the edges at two different time steps, SSSS case, AR=1, surface blast of TNT ($M = 100\text{kg}$, $R = 30\text{m}$)	64

Fig. 5.9	Reaction force-time history at vertical edge mid-point and a corner point (SSSS, AR=1, surface blast of TNT M=100kg, R=30m)	64
Fig. 5.10	Values of $(D/S)_{avg.}$ for the horizontal and vertical edges of all cases	70
Fig. 5.11	Comparison between the distribution pattern of peak reaction forces in SSSS and SFSF cases, subjected to surface blast of TNT, M = 100kg, R = 30m	71
Fig. 5.12	Percentage of increase in max. reaction force at vertical edge mid-point of the SFSF, AR=1 steel plate, due to the change in TNT mass, at fixed R = 30m	73
Fig. 5.13	Percentage of reduction in max. reaction force at vertical edge mid-point of the SFSF, AR=1 steel plate, due to the change in stand-off distance, for TNT mass M = 100 kg	73
Fig. 6.1	Top (a), front (b) and isometric (c) views of the blast scene	76
Fig.6.2	Top (a), front (b), side (c) and 3D (d) views of the Steel gate. A 3D view without frontal plate (d) shows the stiffening frame	78
Fig. 6.3	Pressure and Impulse history of the 4 blast levels (25kg, 50kg, 75kg and 100kg, R=5m)	80
Fig. 6.4	Schematic of explosive centroid effective locations, denoted as A to G, situated on the a gate projection, with M=100kg TNT, R= 5m	80
Fig. 6.5	Applied boundary conditions (a) 3D view, (b) top view, (c) side view and (d) detail	82
Fig. 6.6	Variation of plastic dissipation energy with mesh size, for Gate G5, M=100kg, R= 5m	83
Fig. 6.7	Reaction force variation with mesh size, for Gate G5, support S5, M=100kg, R= 5m	83
Fig. 6.8	Comparison between R _{Fx} , R _{Fy} and R _{Fz} at Support S5, for 100kg of TNT, R=5m, explosive location (A)	84
Fig. 6.9	The effect of the position of explosive centroid; denoted as A to G in Fig. 6.4; on reaction forces at supports S1-S5, Gate G5, M=100kg TNT, R=5m.	85
Fig. 6.10	Effect of blast pressure level (mass of TNT) on peak RFs	86
Fig. 6.11	Reaction forces for the 4 gates G2.5, G5, G7.5 and G10, under a blast of 100kg of TNT, R=5m, explosive location A	87
Fig. 6.12	Deformation limit	88
Fig. 6.13	Displacement of G2.5 after 6.6 MPa blast pressure	88
Fig. 6.14	Spatial displacement of front and back plates of gate G5 after 6.6 MPa blast pressure	89

Fig. 6.15	Energy components for 4 gates G2.5, G5, G7.5 and G10, under a blast of 6.6 MPa (from 100kg of TNT, R=5m, explosive location A)	90
Fig. 7.1	Geometry and components of the Uniaxial Graded Auxetic Damper (UGAD) proposed in this thesis	93
Fig. 7.2	3D view of UGAD body, auxetic core with its dimensions	93
Fig. 7.3	Front, rear and side views the gate system, showing the gate, the placement of 20 UGADs, shear walls and movable cover plate.	95
Fig. 7.4	Stress-Strain relationship for the 3 aluminium grades, at different strain rates	96
Fig. 7.5	BCs and constraints of the bearing plate, piston and damper body	98
Fig. 7.6	Finding the most accurate-less expensive auxetic core model (different SM/L ratios), based on comparing plastic dissipation energy (PDE) and reaction force (RFd), for an auxetic core of L=10mm, t=1mm, S4R elements, AL3 aluminium, pulse load of 0.5×10^6 N in 0.002s	99
Fig. 7.7	Numerical model of quarter of the system showing the symmetry about x and y	99
Fig. 7.8	Ratio of compressed length to total length per time, for an auxetic core loaded in two different directions D1 and D2 ($t=0.75$ mm, L=5mm, $t/L=0.15$, $\theta=60^\circ$, AL2 grade)	102
Fig. 7.9	Plastic dissipation energy PDE with respect to time, for an auxetic core loaded in two different directions D1 and D2 ($t=0.75$ mm, L=5mm, $t/L=0.15$, $\theta=60^\circ$, AL2 grade)	102
Fig. 7.10	Ratio of RFd/P with respect to time, for an auxetic core loaded in two different directions D1 and D2, ($t=0.75$ mm, L=5mm, $t/L=0.15$, $\theta=60^\circ$, AL2 grade)	103
Fig. 7.11	Ratio of PDE/Mass with respect to time, for 3 different cell dimensions A, B and C with $\theta =60^\circ$, $t/L=0.2$, subjected to same loading conditions.	104
Fig. 7.12	RFd/P–time history, for 3 different cell dimensions A, B and C with $\theta =60^\circ$, $t/L=0.2$, subjected to same loading conditions	104
Fig. 7.13	Peak value of RFd/P, for the 3 cell dimensions A, B and C	104
Fig. 7.14	Ratio of PDE/Mass with respect to time, for 3 different Aluminium grades AL1, AL2 and AL3, of an auxetic core with L=10mm, t= 2mm, $t/L=0.2$	105
Fig. 7.15	RFd/P time history, for 3 different Aluminium grades AL1, AL2 and AL3, of an auxetic core with L=10mm, t= 2mm, $t/L=0.2$	105
Fig. 7.16	PDE/Mass with respect to time, for 3 different cell angles, of an auxetic core with L=10mm, t= 2.6mm, $t/L=0.26$	107

Fig. 7.17	Mass of auxetic cores with 3 different cell angles, and $L=10\text{mm}$, $t=2.6\text{mm}$, $t/L=0.26$	107
Fig. 7.18	RFd/P with respect to time, for 3 different cell angles, of an auxetic core with $L=10\text{mm}$, $t=2.6\text{mm}$, $t/L=0.26$	107
Fig. 7.19	Max. value of RFd/P for 3 different cell angles	107
Fig.7.20	PDE/Mass with respect to time, for auxetic and honeycomb cores of the same geometrical properties and loading conditions, loading direction D1, Grade AL3, Cell dimension B ($L=10\text{mm}$), $t=2.6\text{mm}$, $t/L=0.26$, $\theta_{Aux}=60^\circ$, $\theta_{Hex}=120^\circ$.	108
Fig.7.21	RFd/P with respect to time, for auxetic and honeycomb cores of the same geometrical properties and loading conditions, loading direction D1, Grade AL3, Cell dimension B ($L=10\text{mm}$), $t=2.6\text{mm}$, $t/L=0.26$, $\theta_{Aux}=60^\circ$, $\theta_{Hex}=120^\circ$.	108
Fig. 7.22	Deformation patterns of 3 auxetic cores with different number of layers of the same geometrical properties and loading conditions, having the same loading direction D1, Grade AL3, Cell dimension B ($L=10\text{mm}$), $t=2.6\text{mm}$, $t/L=0.26$, $\theta_{Aux}=60^\circ$	110
Fig. 7.23	PDE with respect to time, for auxetic cores of different no. of layers, having the same geometrical properties and loading conditions, $L=10\text{mm}$, $t=2.6\text{mm}$, $t/L=0.26$, cell angle= 60° , AL3	111
Fig. 7.24	PDE/Mass with respect to time, for auxetic cores of different no. of layers, having the same geometrical properties and loading conditions, $L=10\text{mm}$, $t=2.6\text{mm}$, $t/L=0.26$, cell angle= 60° , AL3	111
Fig.7.25	RFd/P with respect to time, of 3 auxetic cores with different number of layers of the same geometrical properties and loading conditions, having the same loading direction D1, Grade AL3, Cell dimension B ($L=10\text{mm}$), $t=2.6\text{mm}$, $t/L=0.26$, $\theta_{Aux}=60^\circ$	111
Fig.7.26	Peak value of RFd/P of 3 auxetic cores with different number of layers; having the same geometrical properties and loading conditions	111
Fig. 7.27	Uniaxial Graded Auxetic Damper (UGAD) cross-section with 3 auxetic cores for 3 different blast levels	112
Fig. 7.28:	Parametric design of cell wall thickness t for a single auxetic core subjected to certain blast level, loading direction D1, $L=10\text{mm}$, aluminium grade AL3, cell angle $\theta=60^\circ$.	113
Fig. 7.29	Parametric design of the first auxetic core (Aux.1) to absorb gate reaction forces resulting from 3.3 MPa blast pressure from 50kg TNT at $R=5\text{m}$. Curves present the values of RFd at supports S1-S5, for $t=1, 1.4$ and 1.8mm .	114

Fig. 7.30	Parametric design of the first auxetic core (Aux.1) to absorb gate energy resulting from 3.3 MPa blast pressure from 50kg TNT at R=5m. Curves present PDE, for $t = 1, 1.4$ and 1.8mm .	114
Fig. 7.31	Parametric design of the second auxetic core (Aux.2) to absorb gate reaction forces resulting from 4.95 MPa blast pressure from 75kg TNT at R=5m. Curves present the values of RFd at supports S1-S5, for $t = 1.4, 1.8$ and 2.2mm .	115
Fig. 7.32	Parametric design of the second auxetic core (Aux.2) to absorb gate energy resulting from 4.95 MPa blast pressure from 75kg TNT at R=5m. Curves present PDE, for $t = 1.4, 1.8$ and 2.2mm .	115
Fig. 7.33	Parametric design of the third auxetic core (Aux.3) to absorb gate reaction forces resulting from 6.6 MPa blast pressure from 100kg TNT at R=5m. Curves present the values of RFd at supports S1-S5, for $t = 1.8, 2.2$ and 2.6mm .	116
Fig. 7.34	Parametric design of the third auxetic core (Aux.3) to absorb gate energy resulting from 6.6 MPa blast pressure from 100kg TNT at R=5m. Curves present PDE, for $t = 1.8, 2.2$ and 2.6mm .	116
Fig. 7.35	Stress-strain curve of Aux.1 under 20m/s impact velocity, showing the 4 stages of crushing a re-entrant auxetic structure.	118
Fig. 7.36	Numerical stress-strain curve of Aux.1 under different impact velocities, compared to analytical “dynamic crushing strength”	120
Fig. 7.37	Stress-strain curve of the 3 auxetic cores together in the UGAD under different impact velocities, 1m/s, 20m/s and 40m/s.	120
Fig. 7.38	Displacement of Gate G5 and the Auxetic damper after a blast pressure of 1.65 MPa from 25kg TNT at R=5m	122
Fig. 7.39	Displacement of Gate G5 and the Auxetic damper after a blast pressure of 3.3 MPa from 50kg TNT at R=5m	122
Fig. 7.40	Displacement of Gate G5 and the Auxetic damper after a blast pressure of 4.95 MPa from 75kg TNT at R=5m	123
Fig. 7.41	Displacement of Gate G5 and the Auxetic damper after a blast pressure of 6.6 MPa from 100kg TNT at R=5m	123
Fig. 7.42	Displacements of Pistons’ heads (i.e. compressed length of auxetic cores) at supports S1-S5, after a blast pressure of 6.6 MPa from 100kg TNT at R=5m, Gate G5.	124
Fig. 7.43	Velocity of Pistons’ heads (i.e. velocity of compressing auxetic cores) at supports S1-S5, after a blast pressure of 6.6 MPa from 100kg TNT at R=5m, Gate G5.	124
Fig. 7.44	Reaction forces RF at supports S1-S5 without external dampers, after a blast pressure of 6.6 MPa from 100kg TNT at R=5m, Gate G5.	124

Fig.7.45	Reaction forces RFd at supports S1-S5 with the auxetic dampers, after a blast pressure of 6.6 MPa from 100kg TNT at R=5m, Gate G5.	124
Fig.7.46	Energy components of the model (shown in Fig.7.7), after a blast pressure of 6.6 MPa from 100kg TNT at R=5m, Gate G5.	125
Fig.7.47	PDE by the dampers, gate and the total PDE in the model (shown in Fig.7.7), after a blast pressure of 6.6 MPa from 100kg TNT at R=5m, Gate G5.	125
Fig. 7.48	Displacement of Gate G5 and the Auxetic damper after a blast pressure of 9.9 MPa from 150kg TNT at R=5m	126
Fig. 7.49	Front, side, top and 3D view of the proposed concrete frame with its dimensions	128
Fig. 7.50	Reinforcement and boundary conditions of the concrete frame	129
Fig. 7.51	The typical uniaxial compression and tensile stress-strain constitutive relations in the CDP model	130
Fig. 7.52	The uniaxial load cycle of CDP model with default stiffness recovery factors	131
Fig. 7.53	Relationship between strain rate and DIF for concrete peak strength under compression and tension	132
Fig. 7.54	Damage parameters, adopted in the CDP material model of the UHP-FRC, with respect to the inelastic and cracking strains of uniaxial compression (a) and tension (b), respectively	133
Fig. 7.55	Plastic strain with respect to compressive (a) and tensile (b) stresses, for different strain rates, adopted in the CDP material model of the UHP-FRC, presented in this study.	133
Fig. 7.56	Distribution of peak HMH stresses in the steel reinforcement, for M=100kg TNT, R=10m.	134
Fig. 7.57	Tension and compression damage in the concrete material, for M=100kg TNT, R=10m.	135
Fig. 7.58	Peak deflections in the concrete fame and reinforcement, for M=100kg TNT, R=10m.	135
Fig. 7.59	Energy components in the whole numerical model (Gate, UGADs and the reinforced concrete support), subjected to a blast pressure from 100kg of TNT, R=10m	136

List of Tables

Table 2.1	Peak reflected overpressures P_r (in MPa) with different W-R combinations	9
Table 2.2	Buildings level of protection	12
Table 2.3	Blast performance of a door assembly	15
Table 3.1	SH Door Tech Co. products specifications	23
Table 3.2	Review of recent studies related to parametric design of re-entrant auxetics (Aux) and comparisons with Hexagonal Honeycombs (Hex)	30
Table 5.1	Material parameters for Weldox 460E Steel	55
Table 5.2	Shear and moment factors at horizontal and vertical edge mid-points for both analytical and numerical solutions (under static loading)	62
Table 5.3	Analytical and numerical solutions for reaction factors at vertical edge midpoint under static loading	63
Table 5.4	Time required to reach peak reaction forces for all BCs (ordered from the shortest to the longest), subjected to surface blast of TNT, $M = 100\text{kg}$, $R = 30\text{m}$	65
Table 5.5	Comparison between reaction forces along the edges of steel plates, with $AR=1$ and different BCs, using dynamic (Abaqus/Explicit) and the Static (Abaqus/Standard) analyses, under surface blast as a dynamic loading (TNT, $M = 100\text{kg}$, $R = 30\text{m}$) and its equivalent static uniform pressure (0.06 MPa)	67
Table 5.6	Comparison between reaction forces along the edges of steel plates, with $AR=1.5$ and different BCs, using dynamic (Abaqus/Explicit) and the Static (Abaqus/Standard) analyses, under surface blast as a dynamic loading (TNT, $M = 100\text{kg}$, $R = 30\text{m}$) and its equivalent static uniform pressure (0.06 MPa)	68
Table 5.7	Comparison between reaction forces along the edges of steel plates, with $AR=2$ and different BCs, using dynamic (Abaqus/Explicit) and the Static (Abaqus/Standard) analyses, under surface blast as a dynamic loading (TNT, $M = 100\text{kg}$, $R = 30\text{m}$) and its equivalent static uniform pressure (0.06 MPa)	69
Table 5.8	TNT mass and stand-off distance combinations considered in this study and their scaled distances	73

Table 6.1	Mass of the 4 gates G2.5, G5, G7.5 and G10	87
Table 6.2	Plastic strain, permanent deformation and operability for the 4 gates under consideration, subjected to 6.6 MPa blast pressure from 100kg TNT at R=5m	89
Table 7.1	Fixed and variable geometrical parameters of the UGAD auxetic core	94
Table 7.2	The three aluminium grades used for the auxetic core and their applications	96
Table 7.3	Material parameters of the 3 aluminium grades used in UGAD auxetic core	97
Table 7.4	Loading directions D1 and D2 and their effect on the collapse mode and deformation of an auxetic core ($t=0.75\text{mm}$, $L=5\text{mm}$, $t/L=0.15$, $\theta=60^\circ$, AL2 grade)	101
Table 7.5	Auxetic cores with 3 different cell dimensions and their properties	103
Table 7.6	Auxetic cores with 3 different cell angles and their properties	106
Table 7.7	Deformation patterns of auxetic and honeycomb cores of the same geometrical properties and loading conditions, loading direction D1, Grade AL3, Cell dimension B ($L=10\text{mm}$), $t=2.6\text{mm}$, $t/L=0.26$, $\theta_{\text{Aux}}=60^\circ$, $\theta_{\text{Hex}}=120^\circ$	109
Table 7.8	The three auxetic cores with their geometric and mechanical properties	117
Table 7.9	Plastic strain, permanent deformation and operability of the gates with the proposed auxetic damper, subjected to 6.6 MPa blast pressure from 100kgTNT at R=5m	121
Table 7.10	Dynamic Increase Factors (DIF) implemented in the concrete material model	132
Table 7.11	UHP-FRC material parameters	132

List of Symbols and Abbreviations

M	Mass of the explosive material
R	Standoff distance
t_A	Blast wave arrival time to the target
p_0	Ambient pressure in a blast scene
p_{s0}	Blast incident peak overpressure
Z	Scaled distance
q_s	Maximum value of dynamic pressure of a blast
P_r	Peak reflected overpressure
F_m	Maximum magnitude of the simplified triangular shape of a blast pulse
t_d	Positive duration of the simplified triangular shape of a blast pulse
I	Blast impulse
SDOF	Single degree of freedom system
ω	natural circular frequency
T	natural period of vibration
y_m	maximum dynamic deflection
Aux	re-entrant auxetic structure
Hex	non-auxetic hexagonal honeycomb structure
\mathcal{B}	abstract body which is a set of material particles P
\mathbb{R}^3	three-dimensional <i>Euclidean space</i>
$\partial\mathcal{B}$	Surface of the physical body \mathcal{B}
\mathcal{B}_0	The reference configuration of the physical body \mathcal{B} , also called material or Lagrangian configuration
\mathcal{B}_t	The current configuration of the physical body \mathcal{B} , also called spatial or Eulerian configuration
\mathbf{X}	Position vector of a material point at \mathcal{B}_0
\mathbf{x}	Position vector of a material point at \mathcal{B}_t
φ	Vector field mapping the reference configuration to current configuration in \mathbb{R}^3
\mathbf{F}	Deformation gradient

J	Jacobian J , the volume ratio between infinitesimal material volume element and a spatial one
\mathbf{R}	Rotation tensor
\mathbf{U}	Right stretch tensor
\mathbf{V}	Left stretch tensor
\mathbf{C}	Right <i>Cauchy-Green tensors</i>
\mathbf{b}	Left <i>Cauchy-Green tensors</i>
\mathbf{E}	The <i>Green-Lagrange strain tensor</i>
\mathbf{e}	The <i>Euler-Almansi strain tensor</i>
\mathbf{V}	Material velocity
\mathbf{A}	Material acceleration
\mathbf{v}	the <i>Eulerian</i> description of velocity
\mathbf{a}	the <i>Eulerian</i> description of acceleration
\mathbf{t}	Traction vector
$\boldsymbol{\sigma}$	The <i>Cauchy stress tensor</i>
σ_V	von Misses stress (HMH)
\mathbf{P}	The <i>first Piola-Kirchhoff stress tensor</i>
$\boldsymbol{\tau}$	The <i>Kirchhoff stress tensor</i>
\mathbf{S}	The <i>second Piola-Kirchhoff stress tensor</i>
\mathcal{P}_{int}	The internal stress power
M	The total mass of a body \mathcal{B}
$f^{ext.}$	External force
\mathbf{b}_f	Body forces
\mathbf{h}	The angular momentum
$M^{ext.}$	External moment
\mathbf{K}	Global stiffness matrix
\mathbf{R}	Global residual vector
\mathbf{D}	Global nodal displacement field
\mathbf{M}	Mass matrix
\mathbf{K}	Stiffness Matrix
\mathbf{F}	Vector of applied loads
$\mathbf{u}, \dot{\mathbf{u}}, \ddot{\mathbf{u}}$	Displacement, velocity and acceleration, respectively
$\Delta \mathbf{u}^{(i)}$	Increment of displacement, the superscript $^{(i)}$ is the increment number

Δt	Time increment
ω_{max}	The element maximum eigenvalue
L_e	The characteristic element dimension
C_d	The current effective dilatational wave speed of the material
AR	Aspect ratio
SSSS	Four edges simply supported
SFSF	Two opposite edges simply supported and two free
CFCF	Two opposite edges clamped and two free
CCCC	Four edges clamped
J-C	Johnson-Cook material model
E	Modulus of Elasticity
ν	Poisson's ratio
ρ	Mass density
A	Yield Strength
B	Ultimate Strength
n	work-hardening exponent
$\dot{\epsilon}_0$	Reference Strain rate
C	strain rate factor
D_c	Critical Damage
p_d	Damage threshold
C_p	Specific heat
χ	Taylor Quinney empirical constant/inelastic heat fraction
α	Coefficient of thermal expansion
T_m	Melting Temperature
T_0	Room Temperature
m	Thermal-softening exponent
$d_1 - d_5$	Failure parameters
Δ	A two-dimensional laplace operator
D	The bending stiffness of a plate
β and γ	Moment and shear factors
M_y	Moment at the centre of plate supporting edges
Q	Shear at the centre of plate supporting edges
HMH	Huber-Mises-Hencky stress

$(D/S)_{avg}$	average dynamic/static ratio- the average increase or decrease in the reaction for a single edge of a plate
BC	Boundary condition
PDE	Plastic dissipation Energy
UGADs	Uniaxial Graded Auxetic Damper
RF	Nodal reaction forces at gate supports, without UGADs
RFd	Nodal reaction forces at gate supports, with UGADs
d_{frame}	Maximum value of permanent deformation in the frame of the gate
D_{limit}	UFC permanent deformation limit for gate operability after a blast event
SM	Size of mesh
CDP	Concrete Damage Plasticity model
σ_{c0}	Initial compression yield in concrete
σ_{cu}	Ultimate stress in concrete
σ_{t0}	Failure tension strength
ε_c and ε_t	Engineering total strains, where, the subscripts c and t refer to the compression and tension, respectively
ε_c^{in} and ε_t^{in}	Inelastic strains, where, the subscripts c and t refer to the compression and tension, respectively
d_c	Compressive damage parameter
d_t	Tensile damage parameter
ε_c^{pl} and ε_t^{pl}	Plastic strains, where, the subscripts c and t refer to the compression and tension, respectively
ω_c	Compression stiffness recovery factor
ω_t	Tension stiffness recovery factor
DIF	Dynamic Increase Factor
UHP-FRC	Ultra High Performance Fiber Reinforced Concrete

Chapter 1

Introduction

1.1 Motivation

Accidental or intentional explosions have become a major security problem that is wide spread around the world. Protection of civilians is a priority that includes prediction and mitigation of losses due to such events. Many countries are vulnerable to this type of man-made disasters and they are taking serious precautions. An explosion nearby a building can cause catastrophic damage to buildings' structural and non-structural elements. Loss of life or injury is a consequence of blast shock, structural collapse, debris impact, fire or smoke [1]. The first defence line for sensitive infrastructure; such as embassies, ministries or parliaments; is reinforced concrete perimeter wall. This system requires secured and safe gates that can withstand multiple high intensity explosions.

The key to a successful design of a protective system is the detection of weakest points in the structure. A research at the United States Air Force Research Laboratory [2], emphasizes that doors or gates have always been one of the weakest points in many structures. In addition, the traditional heavy and solid design of gates led to higher manufacturing cost and poor operational performance [3], as shown in Fig. 1.1. These massive doors are not suitable for general-purpose usage such as armoured cars, airplanes and residential premises. Accordingly, gates are required to be lightweight and able to mitigate extreme loading effect. This may be achieved through "*innovative design of a gate*" and its "*supporting frame*". The first is well covered in literature while the latter is often overlooked [2].

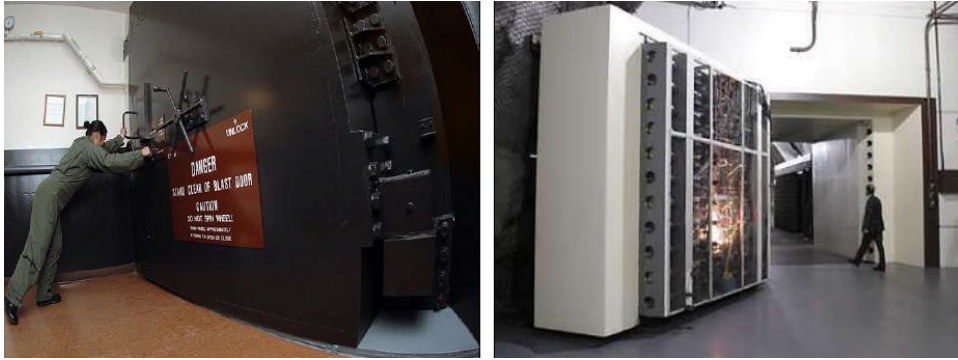


Fig. 1.1 Blast resistant gates [4]

In terms of the gate itself, several energy absorbing techniques were investigated by researchers. One of the studies of the US Air force Research Laboratory recommends the use of Accordion-Flex Door [2]. The proposed door is an accordion panel that is allowed to deform significantly when exposed to blast pressure. Chen and Hao [5], introduce a new configuration for blast doors which consists of a double-layered panel with a structural form of multi-arched-surface. Blast resistance and energy absorption capacities were numerically investigated using FE code. The research proved that multi-arch panel can sustain higher blast loads. The use of innovative materials instead of changing structural form was of interest to Yun, et al. [6]. The study suggests the use of aluminium alloy foam to improve blast pressure mitigation. Significant reduction in permanent deformation was recorded when using high density foam [6]. These techniques focus on absorbing the blast energy by the gate structure and reduce the amount of forces transferred to the supporting frame.

Supporting frames of blast resistant gates play an important role in blast events. In literature, and according to the author survey, the frames of blast resistant gates are usually assumed to be rigid or stiff enough to hold the gate, and that the failure would appear either in the gate itself or in the hinges connecting the gate to the supporting frame. This may be correct when the gate itself is able to absorb the dynamic energy. However, for better performance, the supporting frame may also be designed to absorb the dynamic impact through incorporation of passive damping systems. One of the very few studies that implement a damping system is the one done by Fang, et al. [7]. The study mentions that *“the resistance of the blast doors can be increased obviously by the springs and the dampers, and the shorter the duration of the loads, the more effective the increasing of the resistance”*.

Cellular materials; such as metal foams, honeycomb and auxetics; are among the preferred options to absorb blast energy through plastic deformation. Recently, auxetic panels attracted more attention due to their energy absorption potential [8]. A research by Hou, et al. [9] reveals that re-entrant topology, where the auxetic effect of negative Poisson's ratio appears, sustained larger impact strength than hexagon honeycomb of the same size and material. Auxetic panels have not yet been used as potential damping systems in the supporting frame of blast resistant gates. Consequently, this doctoral thesis tries to investigate if auxetic panels could probably maintain the gate operable after a relatively high blast pressure. To conclude, this thesis tries to fill the scientific gaps mentioned earlier through:

The design of passive damping systems of graded auxetic nature for the supporting frame of a relatively light weight-economic-operable blast resistant steel gate that can resist multiple high intensity blast pressure of up to 6.6 MPa (from 100kg of TNT at 5m stand-off distance).

The target mentioned above is new and considered as a novel idea presented in this thesis.

1.2 Aim and Objectives

The aim of this study is to design a gate, equipped with passive dampers, to resist high intensity blast threats. This is to protect civilians and infrastructure from the increasing danger of terrorism attacks.

The main *objectives* of this research are:

1. Reviewing state-of-the-art research in the field of blast resistant gates and damping systems;
2. Conducting static and dynamic analyses of reaction forces in blast resistant gates (for different boundary condition, aspect ratios, and loading);
3. Defining a case study and assessing the behaviour of a blast resistant gate (without passive dampers);
4. Designing a uniaxial graded auxetic damper through detailed parametric study;
5. Analysing the gate performance with the proposed auxetic damper.

1.3 Structure of the thesis

The thesis consists of 8 chapters followed by the bibliography list, as described below:

Chapter 1; gives an introduction through describing the motivation and the detailed aim of the work conducted in this thesis.

Chapter 2; explains the fundamentals of blast resistant design, starting from defining blast phenomenon, loading and corresponding structural response. Then, it provides a description of blast-related engineering manuals and standards. Finally, the chapter states the recent experimental and numerical blast simulation techniques, with thorough overview of Simulia ABAQUS, the computational tool that has been used in this thesis.

Chapter 3; reviews the state-of-the-art studies in the field of blast resistant gates/doors. It is divided into four sections; reaction forces and loading nature, blast resistant gates, damping systems and auxetic structures.

Chapter 4; focuses on summarizing the fundamentals of continuum mechanics (kinematics, balance laws and constitutive laws). Then, it deals with fundamentals of finite element method (strong form, weak form and FEM formulation) for static and dynamic processes.

Chapter 5; is devoted for the analysis of reaction forces in supporting structure of rectangular steel gates. The analyses include both static and dynamic cases using analytical and numerical methods to emphasize the difference between both approaches, and provide some practical hints for engineers. It covers four different boundary conditions and three length-to-width ratios. Moreover, the effect of explosive charge and stand-off distance on reaction forces is also studied.

In Chapter 6; the structural response of a steel gate is numerically assessed for a defined site and threat possibilities. The gate performance is based on the gate itself, without any supplementary damping systems. The results are then compared with the performance of the gate equipped with the new proposed passive damper in Chapter 7.

The aim of Chapter 7, is the design and assessment of a new uniaxial graded auxetic damper (UGAD). A thorough parametric study is conducted to design the graded

auxetic damper. Then, the damper is tested and its static and dynamic constitutive relations are derived and validated analytically. Finally, the performance of the blast resistant gate with the proposed graded auxetic damper is covered and comparisons with Chapter 6 are drawn.

The last chapter provides a detailed conclusion of the work conducted, generalization, and propositions for future work.

Chapter 2

Fundamentals of Blast Resistant Design

Blast resistant design relied previously on judgment in addition to trial-and-error testing. In the past two decades, structural engineers have been empowered by recent technologies and computational tools, which have enhanced the efficiency and precision of their designs. This chapter tries to explain the fundamentals of blast resistant design, starting from defining blast phenomenon, loading and corresponding structural response. Then, it provides a description of blast-related engineering manuals and standards. Finally, the chapter states the recent experimental and numerical blast simulation techniques, with thorough overview of Simulia ABAQUS, the computational tool that has been used in this thesis.

2.1 Blast Phenomenon

An explosion can be defined as a sudden and rapid release of energy to its surroundings in the form of moving blast wave [10]. Explosions can be used for destructive purposes, such as military weapons and terrorist bombs. They might also be used for construction, such as mining and road building or for entertainment, such as fireworks and film making.

There are different sources of blast: nuclear, physical and chemical events [1]. In nuclear explosions, energy released from sudden nuclear reaction has a large-scale destructive energy and was used once in the modern history; in Hiroshima and Nagasaki, 1945. Physical explosions are catastrophic failure of vessels containing compressed gas or liquid. The burst of the container allows the compressed fluid to spread rapidly causing shock wave. This type of explosion is usually accidental, rare and small in size. A highly overinflated automobile tire might burst causing this type of blast shock. Chemical explosions may result from either decomposition or combination reactions. Decomposition reactions occur in materials such as trinitrotoluene (TNT) and nitro-glycerine. They usually classified as “Secondary” according to their ignition

sensitivity [1]. Combination reactions require that two or more components react together. Common used examples are ammonium nitrate and fuel oil (ANFO), gunpowder or fireworks components. This type of explosives is listed in “Primary” ignition sensitivity category.

2.2 Blast Loading

Two main factors change the influence of a conventional bomb, the Mass (M) of the explosive material and the standoff distance (R) between the blast source and the target [1]. Fig. 2.1 shows vehicle threat and blast scene parameters [11].

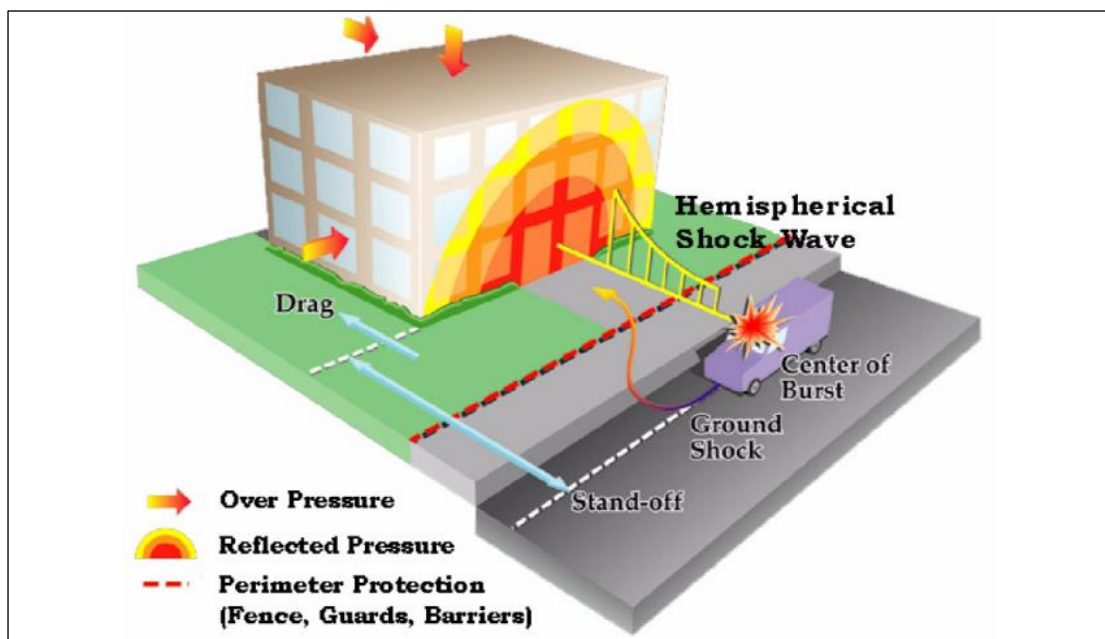


Fig. 2.1 Vehicle threat and blast scene parameters [11]

The pressure of a blast wave depends on the physical properties of the explosion scene and varies with time. Fig. 2.2 shows a typical time-history of blast wave pressure. At the arrival time t_A , the pressure suddenly rise to its maximum value p_{s0} . The pressure then decays to the ambient pressure and this duration is called “positive phase”. Afterward, the pressure reduces to a level under the ambient pressure (causing partial vacuum) and then return back to its natural state. This duration is called “negative phase” [1]. This vacuum usually carries debris and cause further damage.

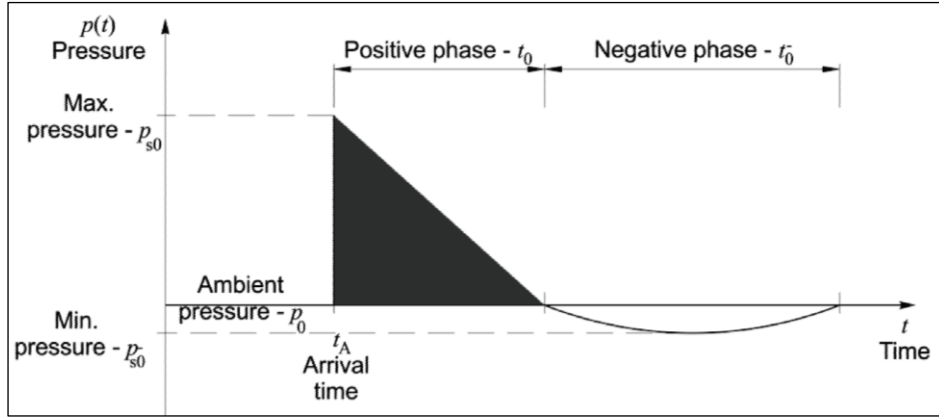


Fig. 2.2 Typical time-history of blast wave pressure [12]

As the standoff distance increases, the positive phase would have longer duration, lower intensity and uniformly-distributed shock wave. Charges situated close to a target usually leads to concentrated high-impulsive shock waves over a relatively short period of time [1].

To estimate the incident peak overpressure p_{s0} , a scaled distance Z should be used that links charge mass M to the standoff distance R as follow:

$$Z = \frac{R}{\sqrt[3]{M}} . \quad (2.1)$$

The scaled distance in Eq. (2.1) has units of $m/kg^{\frac{1}{3}}$. The incident peak overpressure p_{s0} in kPa can be expressed as [1]:

$$p_{s0} = \frac{1772}{Z^3} - \frac{114}{Z^2} + \frac{108}{Z} . \quad (2.2)$$

As the blast wave propagates in the air, the velocity of the air particles (and hence, the wind pressure) is related to the peak overpressure of the blast wave and is usually called dynamic pressure $q(t)$ with maximum value of q_s :

$$q_s = \frac{5p_{s0}^2}{2(p_{s0}+7p_0)} . \quad (2.3)$$

When the blast wave encounters an obstacle, the wave will be reflected and the pressure increases depending on the angle of the facing surface of the obstacle. If the face is perpendicular to the direction of propagation, then the reflected overpressure P_r is [12]:

$$P_r = 2p_{s0} + (\gamma + 1)q_s , \quad (2.4)$$

where γ is the ratio of the specific heats of the medium, i.e., air. If γ is taken as 1.4, which is the value at moderate temperatures, and by substituting Eq. (2.3) into Eq. (2.4), the reflected overpressure P_r is [12]:

$$P_r = 2p_{s0} \left\{ \frac{7p_0 + 4p_{s0}}{7p_0 + p_{s0}} \right\}. \quad (2.5)$$

Some representative peak reflected overpressure values P_r with different M-R combinations are listed in Table 2.1 [1]. The shaded cells represent the critical cases that should be avoided because of their destructive nature. These values are within 0 – 15 m standoff distance. Therefore, it is highly recommended to keep the blast threat as far as possible from the target. For instance, 100 kg of TNT has a peak reflected overpressures P_r of 165.8 MPa at standoff distance R of 1m. However it reduces to 0.85 MPa at R of 10m. That means a reduction of 99.5%.

Table 2.1 Peak reflected overpressures P_r (in MPa) with different M-R combinations [1]

R	M=100 kg TNT	M=500 kg TNT	M=1000 kg TNT	M=2000 kg TNT
1 m	165.8	354.5	464.5	602.9
2.5 m	34.2	89.4	130.8	188.4
5 m	6.65	24.8	39.5	60.19
10 m	0.85	4.25	8.15	14.7
15 m	0.27	1.25	2.53	5.01
20 m	0.14	0.54	1.06	2.13
25 m	0.09	0.29	0.55	1.08
30 m	0.06	0.19	0.33	0.63

2.3 Structural Response of SDOF system

Blast shock, from an explosion, cause a sudden impact on a target. To protect the target, the associated kinetic energy on the facing component should be absorbed or dissipated. This can be achieved from changing the kinetic energy into strain energy. The strain or deformation of the component represent the dynamic structural response [13]. The velocity of change in the strain is called strain rate. Blast loads typically produce very high strain rates between $10^2 - 10^4 S^{-1}$ [1]. Under high strain rates, material resistance or strength usually increases more than that at static loading. Brara and Klepaczko [14], mention that the static compressive strength of concrete can be doubled at high strain rates while the tensile strength may increase even 10 times more.

Blast design of structures involves many uncertainties including: non-linear material behaviour, boundary conditions, blast loading description. Therefore, to simplify the design procedure, the structure is often idealized as a single degree of freedom SDOF system [1, 12, 13] as shown in Fig. 2.3 (a). The external force $F(t)$ has an effect on the structural mass M , and the system resistance is expressed in terms of linear displacement $y(t)$ and spring stiffness K .

The blast load can also be simplified by a triangular pulse that represents the positive overpressure period, Fig. 2.3 (b). It has a maximum magnitude F_m and positive phase duration t_d . The force value at any time is given as :

$$F(t) = F_m \left(1 - \frac{t}{t_d}\right). \quad (2.6)$$

The area of the triangle represents the blast impulse:

$$I = \frac{1}{2} F_m t_d . \quad (2.7)$$

The equation of motion of un-damped SDOF is [15]:

$$M\ddot{y} + Ky = F_m \left(1 - \frac{t}{t_d}\right), \quad (2.8)$$

and hence, the solution for the displacement can be expressed as :

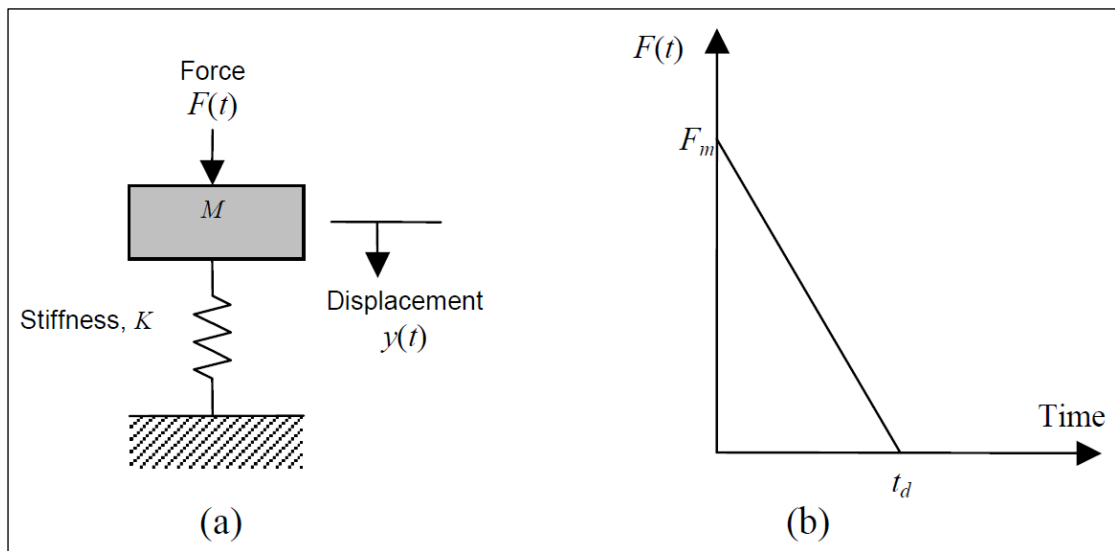
$$y(t) = \frac{F_m}{K} (1 - \cos \omega t) + \frac{F_m}{K t_d} \left(\frac{\sin \omega t}{\omega} - t \right), \quad (2.9)$$

where ω is the natural circular frequency, which is:

$$\omega = \frac{2\pi}{T} = \sqrt{\frac{K}{M}}, \quad (2.10)$$

where T is the natural period of vibration.

The maximum dynamic deflection y_m , which occurs at time t_m , represents the maximum structural response under blast incident.



(a) SDOF system (b) Blast loading
Fig. 2.3 Structural-load idealization [1]

The structural design of building components depends primarily on the importance of the facility. Dusenberry [13] classifies building levels of protection based on performance goals and estimated building damage as shown in Table 2.2. Building importance is the key factor in blast design of structures. Embassies, ministries, hospitals and safety shelters need high level of protection IV. On the other hand, construction of agricultural facilities and rural warehouses requires very low level of protection I.

Table 2.2 Buildings level of protection [13]

Level of Protection	Performance Goals	Overall Damage
I (Very low)	<u><i>Collapse prevention:</i></u> Surviving occupants will likely be able to evacuate, but the building is not reusable; contents may not remain intact.	Damage is expected, up to the onset of total collapse, but progressive collapse is unlikely.
II (Low)	<u><i>Life safety:</i></u> Surviving occupants will likely be able to evacuate and then return only temporarily; contents will likely remain intact for retrieval.	Damage is expected, such that the building is not likely to be economically repairable, but progressive collapse is unlikely.
III (Medium)	<u><i>Property preservation:</i></u> Surviving occupants may have to evacuate temporarily, but will likely be able to return after clean-up and repairs to resume operations; contents will likely remain at least partially functional, but may be impaired for a time.	Damage is expected, but building is expected to be economically repairable, and progressive collapse is unlikely.
IV (High)	<u><i>Continuous occupancy:</i></u> Occupants will likely be able to stay and maintain operations without interruption; contents will likely remain fully functional.	Only superficial damage is expected.

2.4 Engineering manuals and standards

Manuals, dealing with blast load calculations and responses of structural systems, are used in military applications and civil design practice. Before 1980, codes were used particularly for military and defence sectors. However, after the emerge of terrorism attacks and the increased number of internal accidental explosions in industrial premises, the usage of these codes in civil structures gained more importance. This section summarizes the available official codes of practice which are related to blast resistant design of structures in general, and blast resistant gates, in particular.

Eurocode 1 (2006) [16] “*General actions - Accidental actions*”, is the only section in Eurocode which is devoted to accidental and explosive loading applied to structures. It focuses on assessing the structural response for accidental loading, including:

- impact forces from vehicles, rail traffic, ships and helicopters,
- internal explosions,
- consequences of local failure.

It focuses on the internal explosions (dust, gas and vapour explosions), their effect on structural members and ways of mitigating the risk of such incidents. However, Eurocode 1 (2006) , Section 1.1 (6), states that the mentioned code “*does not specifically deal with accidental actions caused by external explosions, warfare and terrorist activities*” [16]. That limits the use of this code to protect buildings from terrorism explosions, which is the main path of this study.

An alternative comprehensive manual (available for public release) is the *Unified Facilities Criteria UFC 3-340-02 (2008); Structures to resist the effects of accidental Explosions*; have been prepared by the “U.S Army Corp of Engineers” [17]. This is a living manual that is being updated frequently based on the state-of-the-art knowledge. The last update was on the 1st of September 2014. This manual supersedes the widely used and well-known code in blast design of structures TM 5-1300, dated November 1990.

The aims of UFC 3-340-02 code is “*to establish design procedures and construction techniques whereby propagation of explosion (from one structure or part of a structure to another) or mass detonation can be prevented and to provide protection for*

personnel and valuable equipment' [17]. It consists of 6 chapters starting from an introduction, then defining blast, fragment and shock loads, moving to the principles of dynamic analysis, reinforced concrete design, structural steel design, and finally, special considerations in explosive facility design. The last chapter deals with special structures such as masonry walls, precast elements, connections, blast resistant windows, underground structures and shock isolation systems.

The description and engineering design procedure of blast doors appears in Chapter 5 of the UFC 3-340-02 code, in Section 5-36 namely "Blast Door Design". The section starts with categorizing blast doors to its functions and method of opening. Then, it describes the design considerations such as deflections, rebound mechanism, fragment protection, leakage protection and type of construction. The section also provides 4 calculation examples to illustrate the relationship between the function of a blast door and its design considerations.

Three other supplementary codes in this field are the UFC 4-010-01, UFC 4-022-02 and the UFC 4-022-03. The first is related to minimum antiterrorism standards for buildings. The second deals with the "*selection and application of vehicle barriers*" and provides a "*unified approach for the design, selection, and installation of active and passive vehicle barriers*". In other words, the standard deals mainly with the resistance of bullroads, fences and gates to car crash impact. The third code, UFC 4-022-03, titled as "Security fences and gates" is devoted explicitly for the criteria and structural detailing in fences and gates of sensitive infrastructures.

Example of older technical standards are:

- Structures to Resist the Effects of Accidental Explosions, TM 5-1300 (U.S. Departments of the Army, Navy and Air Force, 1990).
- A Manual for the Prediction of Blast and Fragment Loadings on Structures, DOE/TIC-11268 (U.S. Department of Energy, 1992).
- Protective Construction Design Manual, ESLTR-87-57 (Air Force Engineering and Services Centre, 1989).
- The Design and Analysis of Hardened Structures to Conventional Weapons Effects (DAHS CWE, 1998)

American manufacturers follow the ASTM F2247-03 technical standard for blast doors and assure that their products provide a minimum Category II response, Table 2.3. The standard specifies four performance levels for a blast door ranging from category I (best performance) to category IV (worst performance).

Table 2.3: Blast performance of a door assembly (ASTM F2247-03)

Category I	The specimen is unchanged (no permanent deformation) after the loading incident and the door is fully operable. The specimen remains intact and responds elastically
Category II	The door is operable but measurable permanent deformation to the door panel exceeding 2 mm (5/64") has been experienced. The specimen remains as an integral system.
Category III	Non-catastrophic failure. No structural failure occurs to the specimen that prevents the specimen from providing a barrier to blast wave propagation. However, the specimen is permanently deformed and the door panel is inoperable.
Category IV	The door panel is severely deformed. For a seating load test, the deformation of the door panel must be limited to a level that does not cause the door panel to force through the door frame opening. For an unseating load test, the latching mechanism is permitted to fail, allowing the door to swing open; however, the door panel shall remain supported by the hinges and it is evident that the door panel will not become a flying debris hazard.

2.5 Blast simulation techniques

Development of simplified and accurate models, for estimating the structural response due to blast waves, is a subject of extensive studies in the last decades [18]. As defined earlier, explosion are sudden and rapid release of energy to its surroundings in the form of moving blast wave [10]. It is obvious that properly planned field testing with live explosives reflects the most reliable outcomes. However, legal permissions, consecutive cost and time limits are all obstacles that make this choice harder to select [19]. Therefore, mathematical/virtual methods including analytical analysis, numerical simulations or laboratory techniques are most important alternatives at the initial stage of product development. Numerical simulations provide an alternative for more complex structures, where analytical option is time consuming or even impossible to

accomplish. Computer programs are used for prediction of blast loading action on the structure, calculation of structural response or both. It can be noticed that the use of FE codes has been extensively covered by researchers such as Lee, et al. [20], Gong, et al. [21], Sielicki [22], Amadio and Bedon [23], Sielicki, et al. [24]. More details about numerical codes including Simulia Abaqus will be presented in the next section.

In terms of Lab-based experiments, to estimate the correct structural response due to a blast load, it is important to ensure that the experimental loading is nearly the same as the actual impact from a possible terrorist threat. Therefore, literature suggests also laboratory techniques that work as alternatives. Good examples are “Shock tube” and the “UCSD blast simulator”. Recent studies are focusing on evaluating and improving the performance of these lab-based tests. Andreotti, et al. [25], examine the pressure losses at the shock tube and their effect on the incident and reflected peak pressures. Another study, by Courtney, et al. [26], was successful in increasing the shock tube peak pressure from 1 MPa to 2.64 MPa to simulate high-intensity blast waves. A non-explosive method to simulate a blast loading is the use of UCSD Blast simulator. The advantage of using this tool is that the high-speed camera photos are not obscured by a fireball. Recent studies, [27-29], show the ability of UCSD blast simulator to produce impulsive impact that is similar to the real blast load as shown in Fig. 2.4 below.

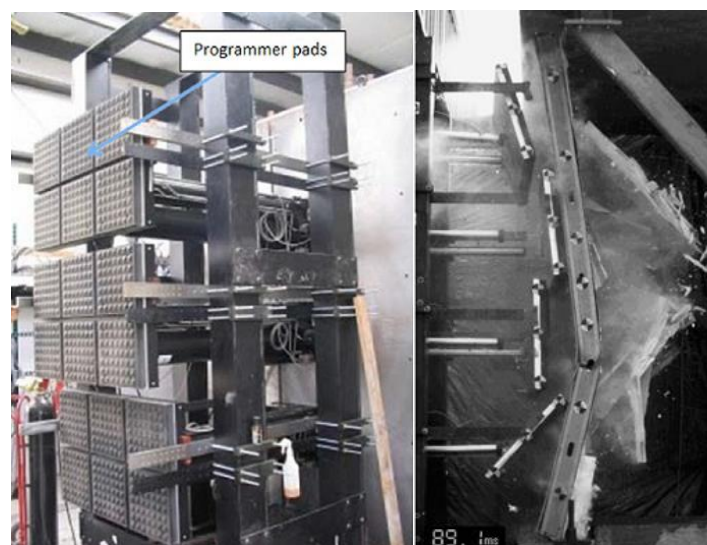


Fig. 2.4: UCSD blast simulator and testing scene [27]

2.6 Numerical Codes

Computer programs are used for prediction of blast loading on the structure, calculation of structural response or both. Blast loading modelling uses CFD (Computational Fluid Mechanics) while structural response modelling is achieved through CSM (computational Solid Mechanics). Examples of computer codes are BLASTX, CTH, FEFLO, FOIL, AUTODYN, DYNA3D, LSDYNA and ABAQUS [1]. The latter, *SIMULIA ABAQUS* software, has been used in this study. Detailed information about Abaqus is provided in the following section.

2.6.1 Simulia Abaqus Software

Simulia Abaqus is a powerful tool for a vast spectrum of engineering problems ranging from routine to most sophisticated applications [30]. Abaqus product suite consists of:

- Abaqus/Standard: Solves traditional implicit FE problems including static, dynamic and thermal analyses.
- Abaqus/Explicit: Solves short transient dynamic events such as impact, crash or blast situations.
- Abaqus/CFD: Provides advanced computational fluid dynamic capabilities
- Abaqus/CAE: CAE is an abbreviation for “Complete Abaqus Environment”. It provides a comprehensive visualization and modelling environment for Abaqus users. CAE used as a pre-processing and post-processing viewer starting from modelling, meshing and ending with the Finite elements results. CAE depend on the Standard, Explicit and CFD analysis tools to view the outcomes [31].

Finite Elements simulations are being widely used to find the optimum design of blast resistant doors, their supporting frames and hinges [32, 33]. For example, a study conducted by Salomoni, et al. [34], presents the non-linear modelling, design and testing of a series of blast resistant doors. Using FE code, the response of plate, internal frame and hinges of a blast door was evaluated. The best numerically designed door then manufactured to be physically tested. The use of FE codes in literature was not limited to steel doors. In Chen, et al. [35], the dynamic responses of a reinforced concrete arched blast door was analysed by the finite element program Simulia Abaqus.

2.6.2 Implicit/explicit time discretization

Implicit analysis is devoted for slow to medium paced dynamic applications. Explicit analysis is more efficient for fast-paced events such as ballistic impact. Implicit method has no limit on the time step in contrast to the explicit that should be relatively small [36, 37]. Implicit analysis is unconditionally stable regardless of the size of time step. However, in explicit cases, to remain stable, the time step must be less than the time taken for a stress wave to cross the smallest element in the mesh. So, explicit time steps are 100 to 1000 times smaller than those used with implicit codes and it is extremely important to avoid very small elements in the mesh [38].

Another difference can be highlighted is that the implicit analysis requires a series of iterations to reach equilibrium while the explicit analysis needs no iterations as nodal accelerations are solved directly. According to Dassault Systèmes [39], the small time increment size of explicit method depends on highest natural frequencies of a model, regardless to the type and duration of loading. On the other hand, implicit methods do not put a limitation on the time increment size; but the cost per increment is greater than that of explicit method. More details on the finite element formulation of the implicit and explicit methods are provided in Chapter 4, Section 4.2.2.

2.7.3 ConWep/CEL tools

Blast simulation can be performed in Abaqus using either ConWep or CEL tools. ConWep (Conventional Weapons) was developed by the US army and then was incorporated in the Abaqus solver [40]. It is a blast loading predictive tool that is based on real-field experimental data with different TNT mass and stand-off distances from Kingery and Bulmash [41]. The benefit of using this tool is that the blast loading is applied directly on the target without the need to model the surrounding air. This makes the computations less expensive. However, in that case, blast pressure estimation would not be linked to scene configuration such as reflection (of multiple blast waves), shadowing (object is blocking a surface of the structure from direct blast wave) or confinement (due to geometry of the structure) [42]. In ConWep model, there are two types of waves, spherical waves for explosions in mid-air and hemispherical waves for explosions at ground level in which ground effects are included [31].

The second tool is CEL that employs coupled Eulerian-Lagrangian blast load analysis by modelling the structure and the surrounding ambient medium. This technique deals with the blast wave propagation in the air, the blast wave interaction with the structure and the related structural behaviour [43]. CEL uses the CFD (Computational fluid dynamic) model for blast load prediction and the CSM (computational solid mechanics) that would predict the structural response. CEL tool automate the whole process with less user inclusion in defining “angles of incidents” or reflection surfaces. The CFD model examines how the blast wave interacts with the structure assuming that the structure cannot deform. Then the CSM uses the output of CFD (the blast pressure) and apply it on the structure. It is important to notice that this coupling between the two codes gives very accurate results providing that the deformation of the structure has little impact on how the blast waves interacts with the structure. In addition, CEL model computations are more expensive and time-consuming [43].

It is totally the analyst decision whether to choose ConWep or CEL based on the complexity of the blast scene and the number of possible blast scenarios that should be analysed.

Chapter 3

Literature Review

This Chapter reviews the state-of-the-art studies and technologies in the field of blast engineering, and in particular, blast resistant gates/doors. It is divided into four sections. The first section highlights the important role of reaction forces and blast loading estimation in the failure mechanism of structures. The second section summarizes proposed scientific solutions to improve the performance of blast resistant doors; and then, tries to list industry manufactured blast-resistant doors and their capacity potential. The third section reviews recent papers related to the use of dampers in blast resistant structures. The fourth section provides in-depth overview of auxetic structures and their energy dissipative characteristics. At the end, a conclusion of the presented themes is drawn. It highlights important points and author remarks from the reviewed material.

3.1 Reaction forces and loading nature

Boundary conditions and related reaction forces are crucial as they play an important role in the failure mechanism of gates, understood as a plate structure. Bonorchis and Nurick [44], mention that “*few papers have been published on the effect of boundary conditions on the high strain rate response of plates subjected to blast (impulsive) loading*”. An experimental study, by Nurick and Shave [45], address the rupture scenarios in a fully clamped square and circular plates subjected to uniform impulsive load. Three failure modes were highlighted which are mode I (large ductile deformation), mode II (tensile-tearing and deformation) and mode III (transverse shear). The study concludes that the failure mode was directly attributed to the boundary condition. A recent comprehensive review in 2016 by Yuen, et al. [46], summarizes experimental studies conducted in the last 25 years in the field of thin plates subjected to air-blast loading. The review paper groups the studies according to four classifications; which are loading type (uniform, localized), Plate geometry (Circular,

quadrangular, stiffened, flat), failure modes and boundary conditions. The paper confirms that the severity and location of failure modes, mentioned earlier, is primarily determined by spatial distribution of the blast loading across the plate surface, and the plate boundary conditions. Rudrapatna, et al. [47] show the numerical results for clamped, thin square steel plates subjected to blast loading. Their study covers the effect of material and geometrical non-linearities in addition to strain rate sensitivity. The outcomes clearly demonstrate the influence of shear near boundaries on the failure mechanism. In addition to the mentioned role of boundary conditions, reaction forces are affected directly by the loading type (uniform or localized).

Far-field blast pressure apply uniform loading on the face of the target. Borenstein and Benaroya [48], mention that the use of Hopkinson-Cranz scaled distance Z to find blast load parameters is accurate when the target is relatively far from the source of explosion. Their research deals with the elastic deformation of steel plate due to near field explosion. Results from the analytical and FE models show response sensitivity to plate thickness and stand-off distance [48]. A non-linear SDOF model has been examined by Feldgun, et al. [49] to simulate the blast response of elastic thin rectangular plates that undergo large deflections. A comparison of static and dynamic nonlinear solutions is performed. Both simply support and fully clamped boundary conditions were taken into account with the assumption of uniform blast pressure loading [49]. The distribution of blast pressure on fully clamped circular steel plates has been studied by Jacob, et al. [50]. Based on theoretical and experimental analyses, the study confirms that “at stand-off distances less than the plate radius, the blast load is considered to be focused (localized). For stand-off distances greater than the plate radius, the loading is considered uniformly distributed over the entire plate area”[50]. Therefore, loading type (uniform, localized) is changing based on the explosive mass or its centroid stand-off distance.

The effect of changing the explosive mass or its centroid stand-off distance on the response of plates is studied by some researchers, such as [48, 50, 51]. Curry and Langdon [51], use high speed imaging and digital image correlation techniques to investigate the transient deformation and strain evolution of a deformable plate for different charge and stand-off distances. The work concludes that permanent deformation dropped with increasing stand-off distance and rose linearly with

increasing the explosive mass. The results of another study, by Aune, et al. [52], provides blast-structure response spectrum based on numerical and experimental investigations. The spectrum provide the change of permanent mid-point deflection with respect to the steel plate thickness ($x - axis$) and stand-off distance ($y - axis$). The study confirms the decrease in the mid-point deflection with respect to the increase in the stand-off distance. The reviewed literature in this field bases their calculations on analytical, numerical or physical models.

To conclude, steel gate failure mechanism depends mainly on boundary conditions, loading pattern and corresponding reaction forces, which are the aims of Chapter 5 of this thesis, namely, blast-induced reaction forces.

3.2 Blast Resistant Gates

Traditionally, blast-resistant doors rely on strength and mass to provide protection from explosions. The dynamic response of steel or steel-concrete blast doors have been covered in research [53] and in engineering standards [17]. For instance, the UFC standard [17] provides the engineering design steps for blast resistant doors with 2 illustrative examples. The first example is a double-leaf built-up A36 steel door with dimensions 6x8 ft. (1830 x 2438mm). The door has to sustain low blast pressure of 14.8 psi (0.1 MPa) and leakage is permitted. A $\frac{3}{4}$ inch plate (19mm thick) with L4x3x $\frac{1}{2}$ satisfied the requirements. The second example is a single-leaf steel door with dimensions 4x7 ft. (1219 x 2133mm). The door has to sustain high blast pressure of 1100 psi (7.5 MPa) and leakage is not permitted. A 2 inch plate thickness (50.8 mm) was required to satisfy the design. However, from operation or economic point of view, these massive doors are not suitable for general-purpose usage. Current needs require a blast door to be lightweight and blast protective.

The blast performance of arched panels, in general, was of interest of several researchers [54, 55]. Hence, the blast resistance properties of arched blast doors, in particular, were investigated [35, 56], using one arch that transfers the blast load to the arch supports. However, this technique may, in return, require very strong supports. Chen and Hao [5], introduce a new configuration that consists of a double-layered panel with a structural form of multi-arched-surface. Blast resistance and energy absorption capacities were numerically investigated using FE code. Using parametric studies to

find the optimum design, the research proved that multi-arch panel performs better than other forms of panels, i.e., can sustain higher blast loads [5].

One of the studies recommends the use of Accordion-Flex Door [2]. The proposed door is an accordion panel that is allowed to deform significantly when exposed to blast pressure. The lightweight door showed to withstand 50 psi (0.34 MPa) peak reflected overpressure.

Addition of stiffeners to blast doors has been investigated by several researchers such as Hsieh, et al. [57], Mohammed, et al. [58], Goel, et al. [59] and Veeredhi and Rao [60]. For example, Hsieh, et al. [57], analysed the performance of a blast door with different dimensions of an I-shaped inter stiffener. The door consists of a rectangular steel plate of 5140x2560x20 mm. The I-shaped stiffener width is 120 mm which has been kept constant, while the depth and web thickness were optimized through the study. The ratio of stiffener's stress to plate stress was the key factor to evaluate the influence of the stiffener. As a result, the door was capable of sustaining a localized pressure of 2.5 MPa which is more than the recommended value by TM5-1300 [61].

Patented technical solutions are also available such as the “Lightweight armoured panels and doors [62]” and the “Ablative blast resistant security door panel [63]”. Manufacturers usually make use of the patented ideas and standards to construct those blast resistant doors. SH Door Tech Co., is a leading Korean company in the field. They are offering a wide range of products such as the “High Level Protection” door, “Laboratory Door” and the “Sliding Blast Proof Door”. The size, type, resisting pressure and field of application of those steel doors are listed in Table 3.1. The 11.3m long giant gate, *High Level Protection*, claimed to resist 50 bars (5 MPa) of blast pressure.

Table 3.1: SH Door Tech Co. products specifications

Name	Size (mm)	Type	Pressure (bar)	Field
High Level Protection	11266 x 3375	Swing, double	50 (5 MPa)	Missile storage
Laboratory Door	1000 x 1800	Swing, single	40 (4 MPa)	Laboratory
Sliding Blast Proof Door	4000 x 5000	Sliding, double	4.6 (0.46 MPa)	Military

A Finnish company, TEMET, is a leading European group that manufactures a wide range of blast resistant doors. One of their products is the SO-6 double wing blast door. The door is fabricated from a steel plate stiffened by I-beams. Different sizes are available with a maximum possible width of 4900mm and height of 4000mm leading to 20 tons of weight (1 ton/m²). The manufacturer confirms that the door has resistance against multiple blast loads ranging from 9-18 bars (0.9-1.8 MPa) peak reflected overpressure, and that the steel material behaves within the elastic range.

It is evident from the reviewed blast resistant gates in this section, that the design of a relatively light-weight, 3000x4500mm gate that could sustain 6.6 MPa of pressure is a challenging target in this thesis. Moreover, the implementation of damping systems is essential to decrease the weight of those heavy gates that may exceed 1000 kg/m². Hence, the following section provides in-depth overview of the current damping systems used in blast resistant applications.

3.3 Damping Systems

Damping can be defined as the phenomenon by which mechanical energy is dissipated in dynamic systems [64]. When a structure does not have enough damping to absorb a dynamic force, additional external dampers are required to protect the structure from severe plastic deformation. Dampers are devices that dissipate energy through some sort of motion. They are used in mechanical, civil and aerospace applications [65]. In multi-storey buildings, as an example, damping systems are extensively used as seismic vibration controllers [66-68]. Dampers are either passive (works without external power need) or active (have actuators and sensors that require external power). The “passive” type of dampers is more favoured in blast resistant design as external power cut is most probable.

There are three sources of energy dissipation mechanisms in damping systems; internal damping, structural damping or fluid damping. The first originates within the material from different microscopic and macroscopic processes. For instance, rubber absorbs impact energy elastically, whereas metals dissipate more energy in plastic deformation. The second mechanism, structural damping, is a result of friction between components or intermittent contact at joints in a structure (such as friction and impact dampers). It is extremely difficult to estimate structural damping through analytical models and “measurement” is the common alternative. The third mechanism, the fluid damping,

arises from drag forces and interactions of a moving part in a fluid, such as fluid dampers [64, 69]. The latter mechanism is less implemented in blast protective design as their response is relatively slow compared to the fast pace of blast shock propagation.

Dampers (or energy absorbers) can be used effectively in dissipating blast wave energy, which would in return, protects human lives and properties [70]. After 9/11, the US department of Defence and Homeland Security urged the need for high capacity blast absorbers [70]. In addition, Monir [71] states that the “*Application of passive yielding dampers in structures for attenuation of blast effects is a complicated topic and needs more research works*” [71].

Improvements were made to existing friction dampers. Chen and Hao [72], introduce a new sandwich panel equipped with friction dampers to resist blast loading. The sandwich panel is $300 \times 300 \text{ mm}$ with outer and inner steel plates (5 mm thick each). Fully clamped boundary condition is applies to the perimeter of the inner plate. The damper is a rotational friction hinge device with spring (RFHDS) distributed as 6 rows by 6 columns (36 in total) between the outer and inner plates of the sandwich panel, as shown in Fig. 3.1. The friction hinges absorb the blast energy while the spring restores the system to its initial form after the incident. Analytical solutions and numerical simulations (using Ls-Dyna) were performed. The results were compared with a monolithic plate of 10 mm thickness (the 2 plates of the sandwich plates together). Compared values were peak and permanent displacements, internal energy dissipation and reaction forces. Results show that the use of RFHDS partially recovers the plate’s original configuration after the action of blast loading and reduces 75.6% of peak reaction forces. In addition, the parametric study of the RFHDS highlight the application potential of this system [72].

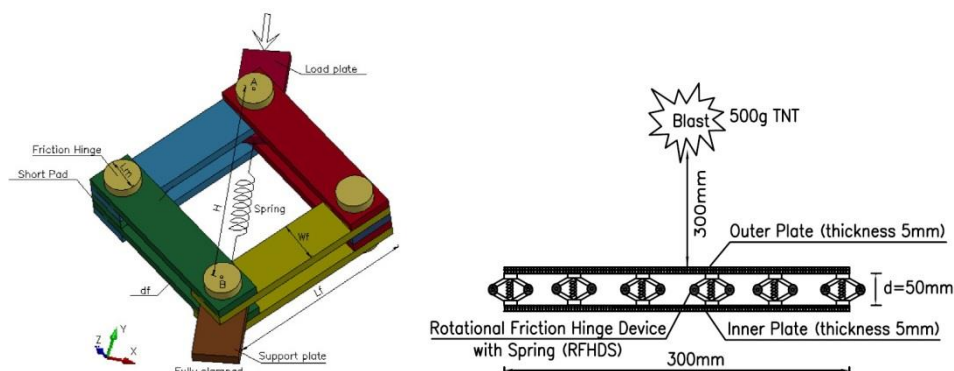


Fig. 3.1: Blast Sandwich panel with RFHDS damping system [72]

Monir [71], draws attention on re-centering problem after a blast event and tests a proposed self-centering solution called Unidirectional Passive Damper (UPD). The system works as blast absorber in the positive phase and has no influence in the restoring phase. This allows the structure to return back freely without any locking. Fig. 3.2 present the UPD components [71]. Results revealed that the proposed passive damper UPD was able to restore top floor displacement to initial form with energy dissipation of 17 000 J for the dampers when the frame was laterally impacted with 500kN in 10 ms.

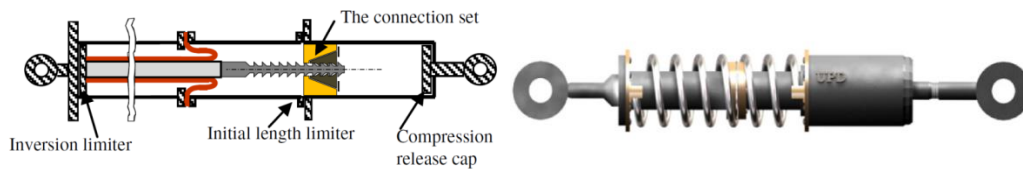


Fig. 3.2: UPD components [71]

Bedon and Amadio [73] suggest a viscoelastic (VE) solid damper for conventional glazing curtain wall subjected to air blast loads of 150kg, 75kg and 25kg at a stand-off distance of 30m (Fig. 3.3). The VE device is made of a rubber placed between two steel plates. It showed satisfactory levels of dynamic performances as it dissipate part of the incoming blast energy, preventing brittle behaviour of the glass, and hence possible injures [73].

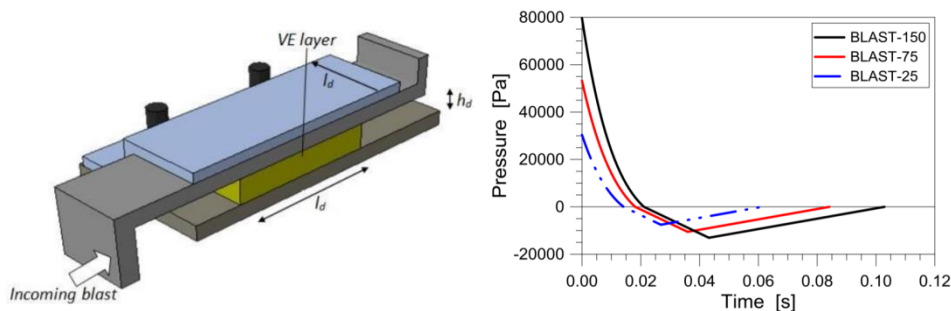


Fig. 3.3: VE solid damper configuration and applied blast pressure [73]

Cellular materials; such as metal foams, honeycomb and auxetics; are developing alternatives with light weight, high specific strength, high specific toughness and good energy dissipating properties [74, 75]. They are generally in the form of sacrificial sandwich panels that absorbs blast energy through plastic deformation, thus protecting the structure. Their energy absorption capacity can be defined as the energy required to deform a specimen to its densification strain.

Metal foams are frequently made from aluminium, namely (aluminium foams). They are either open cell or closed cell foam. Properties and test data are provided in Pecherski, et al. [76], Nowak, et al. [77], Andrews, et al. [78], Ashby, et al. [79], Koza, et al. [80], Papadopoulos, et al. [81] and Peroni, et al. [82]. A recent study by Yun, et al. [6] evaluates the mechanical properties of new aluminium alloy foams manufactured by batch casting method. The efficiency of the proposed foam panels were tested in sacrificial cladding, barrier panels and blast doors. The blast door in-filled by the foam, had a plastic deflection of 23 mm after a blast incident of 4.5 MPa reflected pressure. In addition, inside pressure was less than 0.03 MPa (5 psi), the eardrum rupture pressure.

One of the results of Wadley, et al. [83], highlights the effect of aluminium foam strength (implicitly controlled by relative density) upon the minimum foam thickness required to arrest a buffer of 2.5mm steel plate. The study considers 10kg of TNT explosion at standoff distances ranging from 1 – 10m. For example; 10 kg of TNT at 3m standoff distance (2 MPa reflected pressure) requires 110 mm of foam panel thickness. In addition, stronger foams would be thinner but transmit larger stresses [83].

Despite the potential use of aluminium foams in blast and impact applications, the irregularity in its microstructure makes it difficult to optimize foam properties to the applied load. Peroni, et al. [82] state that primary issues in the analysis of aluminium foams are large density scatter and material anisotropy. In return, problems could arise in the evaluation of mechanical properties for real applications. To tackle this barrier, honeycomb and auxetic structures are promising solutions.

Honeycomb structures are used in a wide range of shock absorption applications due to their impact resistant and energy absorption characteristics [84-87]. Analytical [88, 89], numerical [90, 91] and experimental [92, 93] studies have been conducted to describe their mechanical properties and response. However, as mentioned earlier in Chapter 1 of this thesis, recent studies confirms that the unique behaviour of negative poisson's ratio in auxetic structures provides better energy absorption than the traditional honeycomb (hexagonal) topology [9, 94]. Hence, auxetic structures were selected for the design of passive damping system in this thesis. Recent advances in auxetic structures and comparisons with honeycomb performance are provided in the following section in detail.

3.4 Auxetic structures

Auxetics are defined as solids that possess negative Poisson's ratio [95]. Negative Poisson's ratio (or auxetic behaviour) means that when an auxetic sample is stretched in one direction, it expands in the other direction. Reversely, when it is compressed, it contracts in transverse direction [94, 96]. The difference between normal and auxetic behaviour under compression or tension is shown in Fig. 3.4. A number of review studies concerning auxetic materials/structures and their application were conducted. These include, but not limited to, the research of Lakes [97], Alderson [98], Yang, et al. [99], Alderson and Alderson [100], Liu and Hu [101], Greaves [102] and Prawoto [103].

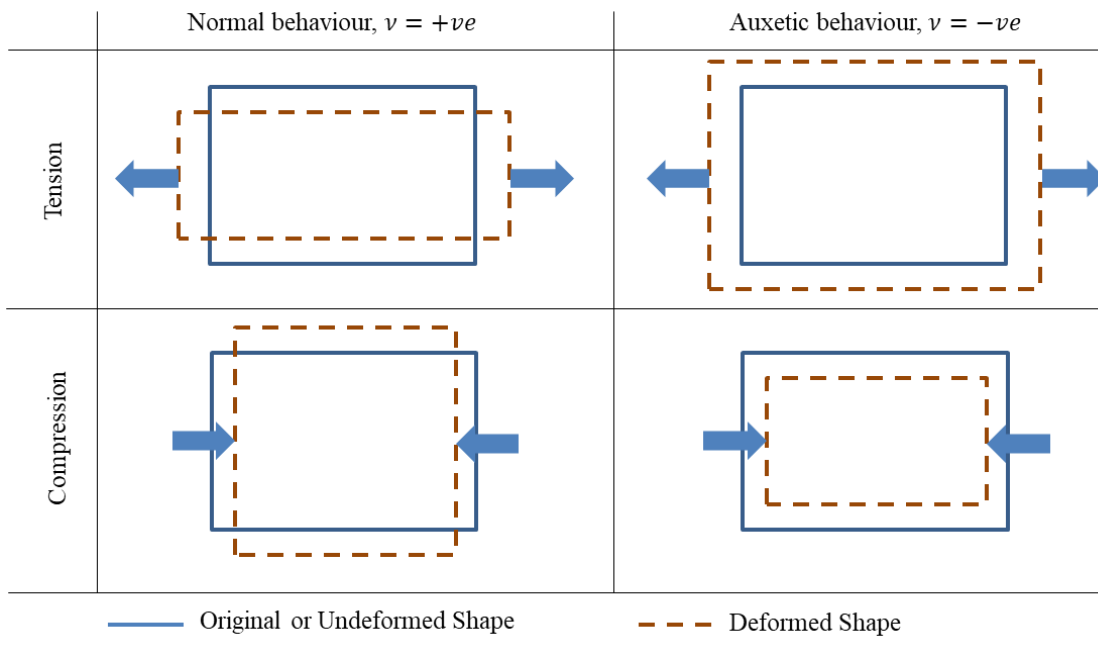


Fig. 3.4: Schematics of normal and auxetic deformation behaviour of 2D elements under tension or compression

The auxetic nature in a body originates either naturally (from the material itself) or man-made (changing the geometry on the micro-structure level). A naturally occurring materials that exhibit negative Poisson's ratio, such as α -cristobalite silicon dioxide [104], are rarely used in engineering applications. The more common is the geometry-related auxetic nature. Fig. 3.5 provides examples of cellular geometries that give auxetic behaviour, such as double arrow-head, re-entrant, chiral and rotating rigid units. They are used to produce foams or auxetic cellular metals, for wide range of applications, such as aerospace, biomedical and military engineering [105].

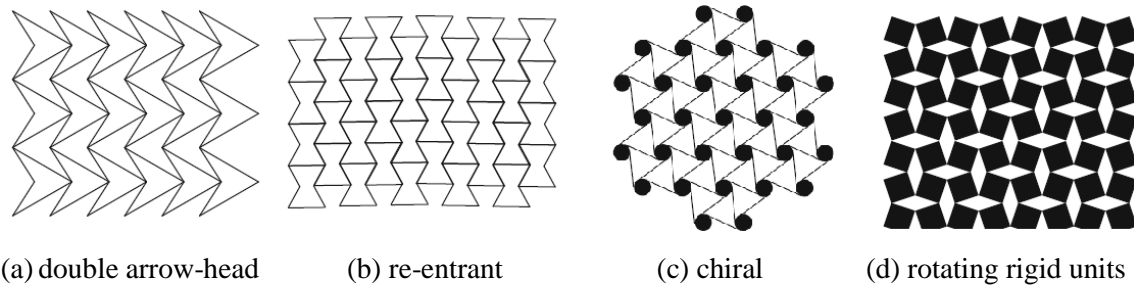


Fig. 3.5: Some cellular geometries that give auxetic behaviour, adopted from [95]

Researchers have demonstrated that auxetic foams show higher strength to weight ratio, lower stiffness and better energy absorption than conventional ones [97, 106-110]. In addition, sandwich panels with auxetic cores; have been investigated under static and blast-induced dynamic shockwaves. Enhanced damage localization [111, 112], flexural response [113], indentation resistance [114-116], and energy absorption [117-119], were obtained.

It is worth mentioning that three-dimensional auxetic structures have also been developed [8]. They have a form of multi-pod lattice [120], an auxetic frame [121] or bow-tie elements [122]. However, in order to manufacture a 3D auxetic structure, sophisticated processes are required accompanied by different challenges due to technological limitations [8, 123]. On the other hand, 2D auxetics can be manufactured through profile-rolling of sheet-metal blanks [119], slotting metal sheets [124] or by 3D printing [125-127]. Based on the remarks above, the 2D re-entrant topology was implemented in this thesis, due to its relatively-simple geometry, and less expensive fabrication, compared to other auxetic topologies. In addition, research in this field show that the abilities of the re-entrant auxetic topology are still waiting to be uncovered, tested and verified [117].

The analysis of dynamic crushing of cellular materials are efficiently performed through numerical FEA tools [128, 129], as experimental approaches need enormous resources [117]. In literature, better performance of re-entrant auxetics (Aux) is assessed based on comparisons with the non-auxetic hexagonal honeycomb (Hex) of the same properties. The simple geometries of the Aux and Hex allow direct optimization process to their blast absorption capabilities through modifying their geometrical parameters (Fig. 3.6). Table 3.2 provides a brief literature review of recent comparisons.

Table 3.2: Review of recent studies related to parametric design of re-entrant auxetics (Aux) and comparisons with Hexagonal Honeycombs (Hex)

Ref. and Year	Fixed parameters in the study ¹	Variable parameters ¹	Main study aims	Related conclusions
Imbalzano, et al. [94], 2017	<p>Square Panel 500x500 mm, height=100mm</p> <p>Armour grade Aluminium 5083-H116 is used with $\sigma_y = 215 \text{ MPa}$ for the cores and AISI 4340 steel alloy for the facets.</p> <p>Tangential contact, friction coefficient =0.3</p> <p>Mesh size= 5mm</p>	<p>Shell element thickness t and hence relative density</p> <p>For Aux: $\theta_{Aux}=30-70^\circ$ $L_2/L_1=0.3-0.7$</p> <p>For Hex: $\theta_{Hex}=120-170^\circ$ $L_2/L_1=1.5-3.5$</p> <p>Impact speed at 5, 20, 40, 70 and 100 m/s</p>	<p>Comparison of the amount of dissipated energy and back face stress for Aux and Hex panels</p> <p>Developing an empirical model for describing the relationship between the geometrical parameters and the crushing strength</p> <p>Effect of number of layers</p> <p>Effect of the angle θ</p>	<p>Aux cores with larger equivalent Poisson's ratio performed better against impulsive loadings in terms of higher energy dissipation and lower back face stress</p> <p>With increasing the number of layers, maximum localized stress on the back face was noticeably lower for Aux panels, while Hex slightly reduced the stress.</p> <p>Energy dissipation is higher for bigger θ Reaction forces are lower for smaller θ</p>
Liu, et al. [117], 2016	<p>Sample: 310mm (width) 320mm (height) 2mm (out-of-plane depth)</p> <p>41 cells in X and 37 cells in Y (loading direction)</p> <p>Aluminium $\sigma_y = 130 \text{ MPa}$</p> <p>$L_3=10\text{mm}$, $\theta_{Aux}=60^\circ$, $\theta_{Hex}=120^\circ$</p> <p>Frictionless general contact</p> <p>Mesh size = $L_3/4=2.5\text{mm}$</p>	<p>Shell element thickness t and hence relative density</p> <p>Impact speed , from 5-200 m/s, or strain rates 15-625 s^{-1}</p>	<p>Comparison of dynamic crushing behaviours</p> <p>Effect of relative density gradient on energy absorption</p>	<p>The crushing pattern of Aux shows densification in the shape of boundary necking and diamond-like core.</p> <p>Aux absorbs more energy than Hex for the same strain rate</p> <p>Under the same impact load, Aux needs smaller crushing strain and time to stop the impact plate</p> <p>Aux and Hex have the same sensitivity to relative density gradient</p>

Ref. and Year	Fixed parameters in the study ¹	Variable parameters ¹	Main study aims	Related Conclusions
Hou, et al. [9], 2016	<p>15 cells in X direction and 11 cells in Y direction for both Aux and Hex</p> <p>$L_3=5\text{mm}$</p> <p>1mm (out-of-plane depth)</p> <p>Aux: $L_1=2L_3$, $\theta_{Aux}=60^\circ$, $\nu = -1$</p> <p>Hex: $L_1=L_3$, $\theta_{Hex}=120^\circ$, $\nu=1$</p> <p>Aluminium, $\sigma_y = 760\text{MPa}$</p> <p>Mesh size = $L_3/10=0.5\text{mm}$</p> <p>General contact definition</p>	<p>Cell wall thickness $t=0.15\text{-}0.926\text{mm}$</p> <p>Aspect ratio $t/L_3=0.03\text{-}0.185$</p> <p>Impact speed, from 7-280 m/s</p> <p>Direction of impact X or Y</p>	<p>The dynamic crushing behaviour</p> <p>Effect of cell wall aspect ratio and impact velocity</p> <p>The auxetic effect on the dynamic crushing resistance and energy absorption</p>	<p>The dynamic crushing strength of Aux along X-direction is higher than that along Y-direction. Energy absorption is vice-versa. So, Aux has anisotropic dynamic properties.</p> <p>The increase in cell wall aspect ratio provides similar effects on deformation mode like decreasing impact velocity.</p> <p>Due to the auxetic effect, Aux revealed higher plateau stress and energy absorption than Hex.</p>
Zhang, et al. [105], 2015	<p>Aux: $L_3=2.7\text{mm}$, $L_1=2L_3=5.4\text{mm}$.</p> <p>15 cells in X direction and 14 cells in Y direction for Aux</p> <p>Mesh size = $L_3/6=0.45\text{mm}$</p> <p>friction coefficient =0.02</p>	<p>Cell wall thickness $t=0.08\text{-}0.4\text{mm}$</p> <p>$\theta_{Aux}=30^\circ, 40^\circ, 60^\circ, 70^\circ, 80^\circ, 85^\circ$.</p> <p>The constant velocity of the crushing rigid steel plate is from 7-200 m/s</p>	<p>Investigate the influence of θ, on plateau stress and energy absorption of Aux in X-direction.</p> <p>Effect of impact velocity</p> <p>Deformation mode and auxetic nature in X-direction</p>	<p>For a specific impact velocity, the plateau stress and energy absorption improves with decreasing θ</p> <p>With the increase in the impact velocity, the effect of changing θ on the absorbed energy is relatively weakened.</p> <p>The Aux sample is showing auxetic effect (transverse shrink) even when loaded in X-direction</p>

¹ As the references are defining the angle θ , the X and Y directions and other parameters in different ways, the values in this table have been unified based on its definition in Fig. 3.x. Therefore they are consistent with the references but may vary numerically.

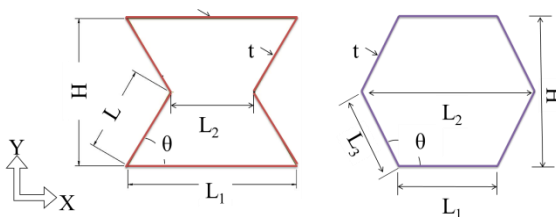


Fig. 3.6 Geometrical parameters of the Aux (left) and Hex (right) unit cell

The reviewed papers in Table 3.2 clearly show the superior performance of re-entrant auxetics (Aux) compared to the conventional hexagonal honeycomb (Hex). The parametric design of the auxetic damper in chapter 7 of this thesis is inspired by studies in Table 3.2., in addition to thorough comparison and validation with other literature. In short, to the author's knowledge, the use of auxetic and non-auxetic dampers in blast resistant structures had been relatively perceived by researchers. Nonetheless, implementation of those energy dissipaters, explicitly in blast resistant doors/gates is restrained to limited studies which highlight the potential need for further explorations, especially graded re-entrant auxetic structures.

3.5 Conclusions

The following points can be concluded from the research reviewed in this chapter:

- Steel gate failure mechanism depends mainly on boundary conditions, loading pattern and corresponding reaction forces
- Scientific studies, patented ideas and market products are proposing different techniques to improve the response of blast resistant doors; however, current needs require a blast door to be lightweight and blast protective. The implementation of damping systems is essential to decrease the weight of those heavy gates that may exceed 1000 kg/m^2 . The design of a relatively light-weight, $3000 \times 4500 \text{ mm}$ gate that could sustain 6.6 MPa of pressure is a challenging target in this thesis.
- Cellular materials; such as metal foams, honeycomb and auxetics; are excellent alternatives to traditional mechanical dampers. In addition, studies confirm that the unique behaviour of negative poisson's ratio in auxetics provides superior energy absorption.
- The use of passive dampers in general and auxetics in particular, in the supporting frame of blast resistant gates has been unnoticed. Therefore, this thesis, "*Application of passive damping systems in blast resistant gates*", tries to fill this original scientific gap.

Theoretical Framework

4.1 Continuum Mechanics

This section reviews the fundamentals of continuum mechanics that are within the scope of this thesis. First, a description of the motion and deformation of a physical body is made. Then, it highlights balance laws of that continuum body. Finally, the section concludes with the governing equations and constitutive relations.

Thorough understanding of a continuum body is crucial to get the physical expression of the material behaviour under different types of loads. Since this part deals with the fundamentals of continuum mechanics, few textbooks were used as bibliographical references, which are Liu [130], Bonet and Wood [131], Holzapfel [132], Richards Jr [133], Mase, et al. [134] and Abeyaratne [135].

4.1.1 Kinematics

Any object occurs in nature can be denoted by an abstract body \mathcal{B} , which is a set of material particles P , where $P \in \mathcal{B}$ in a three-dimensional *Euclidean space* \mathbb{R}^3 . The physical body \mathcal{B} has a surface $\partial\mathcal{B}$. In order to represent the motion or deformation of the continuum body, two configuration would be discussed here; the reference configuration \mathcal{B}_0 and the current configuration \mathcal{B}_t .

The reference configuration $\mathcal{B}_0 \in \mathbb{R}^3$ - also called material or Lagrangian configuration- is a set of material points P at time $t = t_0$, where the position of each point is defined by the position vector \mathbf{X} . The current configuration $\mathcal{B}_t \in \mathbb{R}^3$ - also called spatial or Eulerian configuration- is a set of material points P at time t , where the position of each point is defined by the position vector \mathbf{x} . The one-to-one mapping between the two configurations is denoted by the vector field φ , where:

$$\varphi: \mathcal{B}_0 \mapsto \mathcal{B}_t . \quad (4.1)$$

At any fixed time $t \in \mathbb{R}_+$, the points $\mathbf{X} \in \mathcal{B}_0$ of the reference configuration are mapped by the transformation φ onto points $\mathbf{x} \in \mathcal{B}_t$ of the current configuration, in other words:

$$\mathbf{X} \xrightarrow{\varphi(\mathbf{X},t)} \mathbf{x} . \quad (4.2)$$

The operation can be reversed and the body motion is assumed to be reversible, i.e.:

$$\mathbf{x} \xrightarrow{\varphi^{-1}(\mathbf{x},t)} \mathbf{X} . \quad (4.3)$$

The mapping of infinitesimal geometrical elements from reference configuration to current configuration is shown in Fig. 4.1 below.

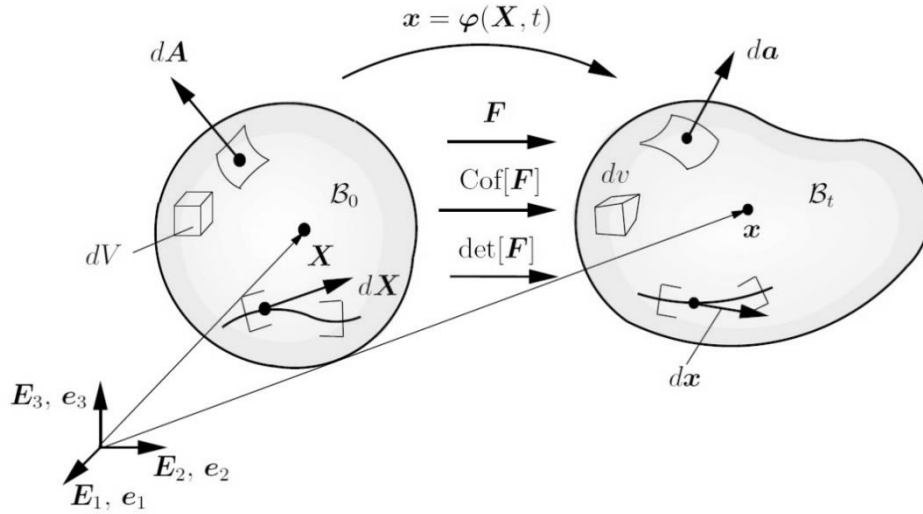


Fig. 4.1: Mapping of infinitesimal geometrical elements from reference configuration to current configuration [136]

A key measure in continuum mechanics is the *deformation gradient* \mathbf{F} . This tensor appears in all equations relating quantities before the deformation to those after or during the deformation process. It is the partial derivative of the deformation mapping $\mathbf{x} = \varphi(\mathbf{X}, t)$ with respect to the reference point coordinates \mathbf{X} :

$$\mathbf{F} = \mathbf{F}(\mathbf{X}, t) = \text{Grad } \mathbf{x} = \frac{\partial \mathbf{x}}{\partial \mathbf{X}} . \quad (4.4)$$

To get the reverse transformation, the inverse of the deformation gradient is taken:

$$\mathbf{F}^{-1} = \mathbf{F}^{-1}(\mathbf{X}, t) = \text{Grad } \mathbf{X} = \frac{\partial \mathbf{X}}{\partial \mathbf{x}} . \quad (4.5)$$

The determinant of \mathbf{F} , also called Jacobian J , should be greater than zero to maintain the non-singularity of \mathbf{F} , in other words:

$$J = \det \mathbf{F}(\mathbf{X}, t) > 0 . \quad (4.6)$$

Three fundamental geometric mappings of the transport theorems are also shown in Fig. 4.1. Those theorems are based on the deformation gradient that links line, area and volume elements from $\mathcal{B}_0 \mapsto \mathcal{B}_t$.

An infinitesimal material line element $d\mathbf{X}$ can be related to an infinitesimal spatial line element $d\mathbf{x}$ by:

$$d\mathbf{x} = \mathbf{F} d\mathbf{X} . \quad (4.7)$$

An infinitesimal material area element $d\mathbf{A}$, with unit normal vector \mathbf{N} in the reference configuration, can be related to an infinitesimal spatial area element $d\mathbf{a}$, with unit normal vector \mathbf{n} in the current configuration, by:

$$d\mathbf{a} = J \mathbf{F}^{-T} d\mathbf{A} = \text{Cof}[\mathbf{F}] d\mathbf{A} , \quad (4.8)$$

using *Nanson's Formula* for the mapping of normal vectors.

In the same way, an infinitesimal material volume element dV can be related to an infinitesimal spatial volume element dv by:

$$dv = J dV = \det[\mathbf{F}] dV . \quad (4.9)$$

Hence, the Jacobian J can be considered as the volume ratio between infinitesimal material volume element and a spatial one. This justifies the condition given in Eq. (4.6) that $J > 0$ because volume elements can not be negative.

In addition to the deformation gradient, the motion of body elements can be expressed in the form of strain tensors related to either \mathcal{B}_0 or \mathcal{B}_t . Using Polar decomposition theorem, the deformation gradient \mathbf{F} can be separated into a pure stretch tensor and a pure rotation tensor:

$$\mathbf{F} = \mathbf{R}\mathbf{U} = \mathbf{V}\mathbf{R}, \quad (4.10)$$

where the rotation tensor \mathbf{R} is orthogonal tensor ($\mathbf{R}^{-1} = \mathbf{R}^T$), the right stretch tensor \mathbf{U} and the left stretch tensor \mathbf{V} are symmetric and are related to the reference and current configurations, respectively. The square value of \mathbf{U} and \mathbf{V} gives the right and left *Cauchy-Green tensors*, \mathbf{C} and \mathbf{b} , respectively:

$$\mathbf{C} = \mathbf{U}^2, \quad \mathbf{b} = \mathbf{V}^2. \quad (4.11)$$

Based upon that, the *Green-Lagrange strain tensor* \mathbf{E} and *Euler-Almansi strain tensor* \mathbf{e} can be found:

$$\mathbf{E} = \frac{1}{2}(\mathbf{C} - \mathbf{1}), \quad \mathbf{e} = \frac{1}{2}(\mathbf{1} - \mathbf{b}^{-1}), \quad (4.12)$$

\mathbf{E} is called material strain tensor because it appear in the reference configuration, while \mathbf{e} is denoted as spacial strain tensor because it operates in the current configuration.

It is important to mention that there is two descriptions of motion; the *Lagrangian* and the *Eulerian* description of motion. The first one follows an individual material particle in the body to understand motion. It is more desired for solid mechanics. In the *Lagrangian* description of motion, the first and second material time derivatives of the motion $\varphi(\mathbf{X}, t)$ give the material velocity and acceleration, respectively:

$$\mathbf{V} = \dot{\varphi}(\mathbf{X}, t) = \frac{\partial \varphi}{\partial t}, \quad (4.13)$$

$$\mathbf{A} = \ddot{\varphi}(\mathbf{X}, t) = \frac{\partial^2 \varphi}{\partial t^2}. \quad (4.14)$$

On the other hand, the *Eulerian* description of motion describes the motion of a body by following a fixed point in space and seeing how the body pass through it. It is more desired for fluid mechanics. By analogy to Eq. (4.13) and (4.14), one defines

$$\mathbf{v} = \mathbf{v}(\mathbf{x}, t) = \frac{\partial \varphi^{-1}}{\partial t}, \quad (4.15)$$

$$\mathbf{a} = \mathbf{a}(\mathbf{x}, t) = \frac{\partial^2 \varphi^{-1}}{\partial t^2}, \quad (4.16)$$

where \mathbf{v} and \mathbf{a} are the *Eulerian* description of velocity and acceleration, respectively.

The *Eulerian* description of motion is more complicated than the *Lagrangian* description of motion because it works in the current/deformed body.

Before moving to balance laws in continuum mechanics, it's worth giving a brief description of the stress concept and power. This leads to full understanding of the different parameters that live in the reference configuration \mathcal{B}_0 than those who works in the current configuration \mathcal{B}_t .

In continuum mechanics, internal stress can be presented through taking a virtual cut by a plane surface at point $\mathbf{x} \in \mathcal{B}_t$ of the deformable continuum body \mathcal{B} (see Fig. 4.2). The traction vector \mathbf{t} , located at point \mathbf{x} , is defined by a force $d\bar{f}$ acting on area element da .

$$\mathbf{t}(\mathbf{x}, t) = \frac{d\bar{f}}{da} \quad (4.17)$$

Following the *Cauchy theorem*, a second-order tensor $\boldsymbol{\sigma}$ transforms the unit normal vector \mathbf{n} of the area element da into the traction vector :

$$\mathbf{t}(\mathbf{x}, t, \mathbf{n}) = \boldsymbol{\sigma}(\mathbf{x}, t)\mathbf{n}. \quad (4.18)$$

This second-order tensor $\boldsymbol{\sigma}$ is called the *Cauchy stress tensor* that is symmetric and represents the *true stress* in the current configuration \mathcal{B}_t . For mechanical analysis of complex boundary value problems, an important stress quantity called von Misses stress (HMH) is used, where:

$$\sigma_V = \sqrt{\frac{3}{2}} \|\text{dev}\boldsymbol{\sigma}\| \quad \text{with} \quad \text{dev}\boldsymbol{\sigma} = \boldsymbol{\sigma} - \frac{1}{3}\text{tr}[\boldsymbol{\sigma}]\mathbf{1} \quad (4.19)$$

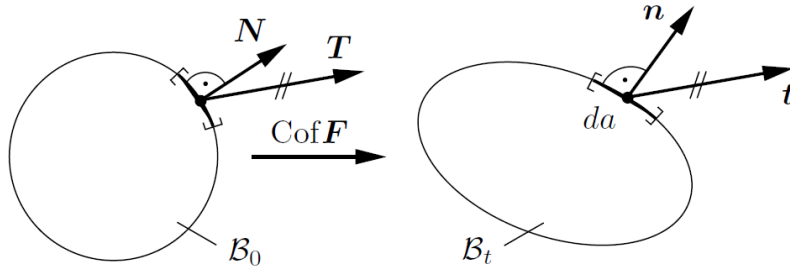


Fig. 4.2: Traction vectors T and t in \mathcal{B}_0 and \mathcal{B}_t , respectively [136]

Working in the current configuration \mathcal{B}_t might be difficult because it represents the deformed body. For that reason, it is always preferred to calculate stresses in \mathcal{B}_t using a description in \mathcal{B}_0 . In \mathcal{B}_0 , the actual traction force can be related to the reference area element using, what is called, the *first Piola-Kirchhoff stress tensor* \mathbf{P} ,

$$\mathbf{T}(\mathbf{X}, t, \mathbf{N}) = \mathbf{P}(\mathbf{X}, t)\mathbf{N}. \quad (4.20)$$

Unlike the *Cauchy stress tensor*, the *first Piola-Kirchhoff stress tensor* \mathbf{P} is non-symmetric and involve two points at distinct configurations. This leads to the need of a stress measure in \mathcal{B}_0 that is symmetric.

Multiplying the *Cauchy stress* by the volume ratio J gives an additional stress measure called the *Kirchhoff stress tensor* :

$$\boldsymbol{\tau} = J\boldsymbol{\sigma}. \quad (4.21)$$

A pull-back operation of the *Kirchhoff stress tensor* $\boldsymbol{\tau}$ leads to the *second Piola-Kirchhoff stress tensor* . The later tensor is symmetric and can be linked to $\boldsymbol{\tau}$, $\boldsymbol{\sigma}$ and \mathbf{P} as follow:

$$\mathbf{S} = \mathbf{F}^{-1}\boldsymbol{\tau}\mathbf{F}^{-T} = \mathbf{F}^{-1}\mathbf{P} = J\mathbf{F}^{-1}\boldsymbol{\sigma}\mathbf{F}^{-T}. \quad (4.22)$$

The first and second *Piola-Kirchhoff stress tensors* are linked through the deformation gradient :

$$\mathbf{P} = \mathbf{F}\mathbf{S} . \quad (4.23)$$

The work conjugated pairs; $(\boldsymbol{\tau}, \mathbf{d})$, $(\mathbf{P}, \dot{\mathbf{F}})$, $(\mathbf{S}, \dot{\mathbf{E}})$; can define the internal stress power \mathcal{P}_{int} in both \mathcal{B}_0 and \mathcal{B}_t as follows:

$$\begin{aligned} \mathcal{P}_{int} &= \int_{\mathcal{B}_t} \boldsymbol{\sigma} : \mathbf{d} \, dv \quad \text{at } \mathcal{B}_t \\ &= \int_{\mathcal{B}_0} \boldsymbol{\tau} : \mathbf{d} \, dV = \int_{\mathcal{B}_0} \mathbf{P} : \dot{\mathbf{F}} \, dV = \int_{\mathcal{B}_0} \mathbf{S} : \dot{\mathbf{E}} \, dV \quad \text{at } \mathcal{B}_0 . \end{aligned} \quad (4.24)$$

4.1.2 Balance Laws

In continuum mechanics, it is important to understand the fundamental conservation laws and balance principles, which are:

- conservation of mass,
- balance of linear momentum,
- balance of angular momentum,
- balance of energy.

In continuum physics, mass is a primitive concept and is not derived from something else. The second assumption is that the total mass of a body is constant during the deformation process (conserved quantity). The mass is expressed in terms of a continuous function of mass density ρ_0 of \mathcal{B}_0 or ρ of \mathcal{B}_t . A continuous function of mass density means that the material does not produce cavities or gaps. Cracks in solids and bubbles in fluids are out of the scope of this thesis, therefore:

$$M = \int_{\mathcal{B}_0} \rho_0(\mathbf{X}) \, dV = \int_{\mathcal{B}_t} \rho(\mathbf{x}, t) \, dv = \text{constant} , \quad (4.25)$$

where M is the total mass of a body \mathcal{B} .

Balance of mass is a question of the rate of change of mass density. In \mathcal{B}_0 , the rate of change of mass density is zero and denotes the conservation of mass in \mathcal{B}_0 :

$$\frac{\partial \rho_0(x)}{\partial t} = 0, \text{ conservation of mass in } \mathcal{B}_0. \quad (4.26)$$

In \mathcal{B}_t , the rate of change of mass density is:

$$\frac{\partial \rho(x)}{\partial t} + \rho \operatorname{div} \mathbf{v} = 0, \text{ conservation of mass in } \mathcal{B}_t. \quad (4.27)$$

The relation between the mass density in both configurations is:

$$\rho_0 = J \rho. \quad (4.28)$$

The linear momentum of a particle in a body is the mass of that particle multiplied by its velocity integrated over the whole body:

$$L = \int_{\mathcal{B}_t} \rho \mathbf{v} dv. \quad (4.29)$$

According to Newton's second law, the rate of change of linear momentum is equal to the external resultant force:

$$\dot{L} = \int_{\mathcal{B}_t} \rho \dot{\mathbf{v}} dv = f^{ext.}. \quad (4.30)$$

In addition, external force is the sum of body forces \mathbf{b}_f and surface traction forces \mathbf{t} :

$$f^{ext.} = \int_{\mathcal{B}_t} \mathbf{b}_f dv + \int_{\partial \mathcal{B}_t} \mathbf{t} da. \quad (4.31)$$

After several steps and using the conservation of mass, the balance of linear momentum in the local form reads as follow:

$$\rho \dot{\mathbf{v}} - \operatorname{div} \boldsymbol{\sigma} - \mathbf{b}_f = 0. \quad (4.32)$$

The angular momentum \mathbf{h} of a particle in a body is the linear momentum of that particle multiplied by its distance to origin integrated over the whole body:

$$\mathbf{h} = \int_{B_t} \mathbf{r} \times \rho \mathbf{v} dv, \quad (4.29)$$

where \mathbf{r} is the particle distance to origin.

According to Euler's law, the rate of change of angular momentum $\dot{\mathbf{h}}$ is equal to the external moment $M^{ext.}$:

$$\dot{\mathbf{h}} = \int_{B_t} \mathbf{r} \times \rho \dot{\mathbf{v}} dv = M^{ext.}. \quad (4.30)$$

In addition, the external moment is:

$$M^{ext.} = \int_{B_t} \mathbf{r} \times \mathbf{b}_f dv + \int_{\partial B_t} \mathbf{r} \times \mathbf{t} da. \quad (4.31)$$

Using the balance of linear momentum principle, the balance of angular momentum in the local form reads as follow:

$$\mathbf{r} \times (\rho \dot{\mathbf{v}} - \text{div } \boldsymbol{\sigma} - \mathbf{b}_f) = 0, \quad (4.32)$$

provided that $\boldsymbol{\sigma}$ is symmetric.

The last part of this section is the balance of energy. In continuum mechanics, the *first principle of thermodynamics* postulates that the total internal power expended by a body should be equal to the total external power. The total internal power $\mathcal{P}_{int.}$ is the sum of internal energy ε and kinetic energy κ , while the total external power $\mathcal{P}_{ext.}$ is the sum of mechanical energy \mathcal{P} and heat fluxes energy \mathcal{Q} .

$$\mathcal{P}_{int.} = \mathcal{P}_{ext.} \quad (4.33)$$

$$\frac{d}{dt}(\varepsilon + \kappa) = \mathcal{P} + \mathcal{Q} \quad (4.34)$$

$$\varepsilon = \int_{B_t} \rho e dv \quad (4.35)$$

$$\kappa = \int_{B_t} \frac{1}{2} \rho \mathbf{v} : \mathbf{v} dv \quad (4.36)$$

$$\mathcal{P} = \int_{B_t} \mathbf{b}_f : \mathbf{v} \, dv + \int_{\partial B_t} \mathbf{t} : \mathbf{v} \, da \quad (4.37)$$

$$\mathcal{Q} = \int_{B_t} \rho r \, dv - \int_{\partial B_t} \mathbf{q} \cdot \mathbf{n} \, da, \quad (4.38)$$

where e is the specific energy density defined per unit mass; r is the heat supply per unit mass and time; and \mathbf{q} is the cauchy heat flux vector that works in the direction of the normal vector \mathbf{n} which is associated with the area element da . Then, the local form of the balance of energy can be written as:

$$\rho \dot{e} = \rho r - \text{div } \mathbf{q} + \boldsymbol{\sigma} : \mathbf{d} \quad , \forall x \in \mathcal{B}_t, \quad (4.39)$$

where \mathbf{d} is the stretching tensor.

The *first principle of thermodynamics* mentioned above only states the conservation of energy during a thermodynamic process while the second one specifies the direction of the process.

Using the *Second principle of thermodynamics* and assuming that the process is isothermal, $\Theta = \text{constant} \Rightarrow \dot{\Theta} = 0$, and choosing the *Helmholtz free energy* $\psi_c = \rho(e - \Theta\eta)$, then the local form of the balance of energy reads:

$$-\dot{\psi}_c + \boldsymbol{\sigma} : \mathbf{d} \geq 0 \quad , \forall x \in \mathcal{B}_t \quad (4.40)$$

The material form of the later equation is:

$$\mathbf{S} : \dot{\mathbf{E}} - \dot{\psi}_c \geq 0 \quad , \forall \mathbf{X} \in \mathcal{B}_t, \quad (4.41)$$

The later equation leads to the constitutive equation for the stresses:

$$\mathbf{S} = \frac{\partial \psi}{\partial \mathbf{E}} \text{ or } = \frac{\partial \psi}{\partial \mathbf{F}}. \quad (4.42)$$

4.1.3 Constitutive Laws

Constitutive equations are the relationships between stresses and strains that make the number of equations equal to the number of unknowns to close a system. Constitutive equations needs certain assumptions; based on the case under investigation; to describe

a fluid, a solid or a gas. As an example, if the body is an ideal fluid, it means that it is “isotropic”, i.e. it has the same pressure in all directions. This assumption reduces the 6 unknown components of the Cauchy stress $\boldsymbol{\sigma}$ to one, which is the pressure p :

$$\boldsymbol{\sigma} = p \mathbf{1} . \quad (4.43)$$

The value of p is determined based on the assumption if the fluid is Incompressible (i.e. $\rho = \rho_0 = \text{constant}$) or Compressible (i.e. the pressure is a function of the density $p = p(\rho)$).

Another example is isotropic elastic solids. In such a continuum body, the properties are the same at every material point. If the body is also homogeneous, the constitutive equations do not rely on the material points. Hence, the constitutive equations in the reference configuration turn to:

$$\mathbf{P} = \mathbf{P}(\mathbf{X}, \mathbf{F}) = P(\mathbf{F}), \quad \psi = \psi(\mathbf{X}, \mathbf{F}) = \psi(\mathbf{F}) \quad (4.44)$$

The last point to mention in this section is that the constitutive equations should fulfil two main principles:

- The principle of material frame indifference (Objectivity): This principle requires that the constitutive equations have to be indifferent against a change of reference system, i.e. observer independent.
- Principle of material symmetry: This principle requires that the constitutive equations have to be invariant with respect to all transformations Q of the material coordinates, which belong to the symmetry group \mathcal{G} of the underlying material.

The material presented in this section, is a brief summary of the main features required to understand the behaviour of a general continuum body. They are considered as the “Strong form of the boundary value problem” and as the bases for the next section, Finite Element Method. This is clear that for thesis purposes, more advanced constitutive models were applied, namely the ones covering plasticity and damage, together with strain rate hardening and thermal softening effect.

4.2 Finite Element Method

The finite element method (FEM) or the finite element analysis (FEA) is based on the concept of dividing a complicated body into subsets, on which appropriate approximated solution is assumed [137]. Physical phenomena can be formulated using differential equations. However, solving these equations by classical analytical tools for complicated conditions is impossible [138]. Therefore, FEM is an effective numerical tool for finding an approximate solution of these differential equations. These equations, in most cases, describe boundary value problems that are either of linear or non-linear character [136]. Nowadays, FEM is widely used in different engineering fields such as mechanical, aerospace, civil, structural, thermal and geomechanics. There are many commercial FEA software packages like Nastran, Ansys, Abaqus, Algor, Cosmos and Dyna-3D.

FEM works in the following pattern:

- Dividing the body into element subdomains connected by nodes (Fig. 4.3).
- Writing equations that describe approximately the local physical behaviour of each element
- Connecting the elements to make an approximate system of equations for the whole structure
- Solving the global set of equations using predefined boundary and initial conditions
- Calculating unknown quantities of interest, such as displacements, stresses or strains, at selected nodes.

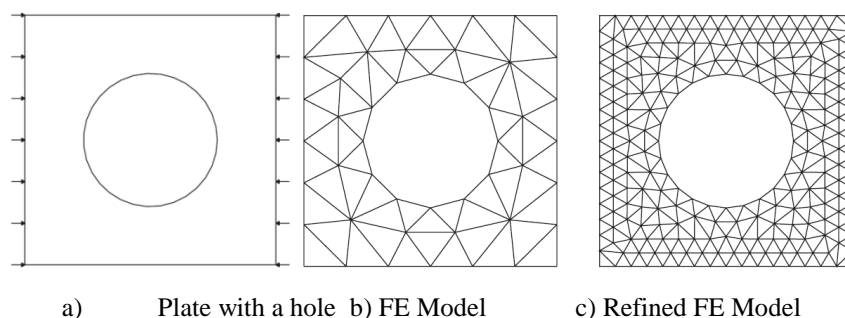


Fig. 4.3: Finite element mesh of a steel plate with a hole [138]

4.2.1 Finite elements formulation of quasi-static problems

For a non-linear boundary value problem, which is hyper elastic, quasi-static and isothermal, the solution can be reached by the following set of differential equations:

$$\text{Kinematic} \quad \mathbf{F} = \text{Grad } \mathbf{x}, \quad (4.45)$$

$$\text{Local form of the balance of linear momentum} \quad \text{Div } \mathbf{P} + \rho_0 \mathbf{f} = 0, \quad (4.46)$$

$$\text{Material law} \quad \mathbf{P} = \partial \mathbf{F} \psi \quad (4.47)$$

The previous mentioned equations are the strong form of the boundary value problem and can be written in other forms using work-conjugated pairs (as discussed in Section 4.1 before). The local form of the balance of linear momentum (Eq. (4.46)) is also known as the *strong form of equilibrium*.

To achieve a full description of the boundary value problem, both stress and displacement conditions on the boundary of the body \mathcal{B}_0 should be defined. For that reason, the reference surface $\partial \mathcal{B}_0$, is divided to two non-overlapping parts $\partial \mathcal{B}_{0t}$ and $\partial \mathcal{B}_{0u}$, so that;

$$\partial \mathcal{B}_0 = \partial \mathcal{B}_{0t} \cup \partial \mathcal{B}_{0u} \quad \text{and} \quad \partial \mathcal{B}_{0t} \cap \partial \mathcal{B}_{0u} = \emptyset \quad (4.48)$$

The stress affecting $\partial \mathcal{B}_{0t}$ part is known as *Neumann boundary conditions*, while the displacement related to $\partial \mathcal{B}_{0u}$ part is known as *Dirichlet boundary conditions* [136], as follow:

$$\text{Neumann boundary conditions} \quad \mathbf{T} = \mathbf{P}\mathbf{N} = \bar{\mathbf{t}} \quad \text{on } \partial \mathcal{B}_{0t} \quad (4.49)$$

$$\text{Dirichlet boundary conditions} \quad \mathbf{u} = \mathbf{u}_0 \quad \text{on } \partial \mathcal{B}_{0u} \quad (4.50)$$

Those equations are associated with the equations of the strong form of the boundary value problem, Eq. (4.45) to (4.47). In most cases, with complex boundary problems, the analytical solution of the strong form differential equations is impossible. Therefore, a discretization method is used to obtain the *weak form of equilibrium*. The *weak form of equilibrium* works as the basis for the FEM formulation.

By multiplying the *strong form of equilibrium* (Eq. (4.46)) by the virtual displacement, and using boundary conditions in Eq. (4.49) and Eq. (4.50), one can get the *weak form of equilibrium*;

$$G(\mathbf{u}, \delta\mathbf{u}) = \underbrace{\int_{\mathcal{B}_0} \mathbf{P} : \delta\mathbf{F} \, dV}_{G_{int}} - \underbrace{\left[\int_{\mathcal{B}_0} \rho_0 \mathbf{f} \cdot \delta\mathbf{u} \, dV + \int_{\mathcal{B}_0 t} \bar{\mathbf{t}} \cdot \delta\mathbf{u} \, dA \right]}_{G_{ext}} = 0, \quad (4.51)$$

where G_{int} and G_{ext} are the work of the internal and external forces acting on the body \mathcal{B}_0 , respectively [136].

The solution of the weak form of equilibrium is difficult and needs an iterative method, such as the *Newton-Raphson iteration scheme*. The later requires linearization of the weak form of equilibrium. However, the analytical solution of the linearization is not possible in most cases. Therefore, the FEM is necessary to gain a numerical solution. It depends on several approximations such as “*the discretization of the considered body by finite elements, the approximation of the primary variable inside the elements by ansatz functions and the calculation of integrals by a numerical integration procedure*” [136]. The discretization of the body assumes that the body is made of n elements. the global system matrices are achieved from the standard assembling procedure of all elements’ matrices such as the global stiffness matrix \mathbf{K} and the global residual vector \mathbf{R} , i.e. ;

$$\mathbf{K} = \prod_{e=1}^n K^e \quad \text{and} \quad \mathbf{R} = \prod_{e=1}^n r^e \quad (4.52)$$

The final system of equation for \mathcal{B}_0 in the discrete form:

$$\delta\mathbf{D}^T (\mathbf{K}\Delta\mathbf{D} + \mathbf{R}) = 0 \Rightarrow \Delta\mathbf{D} = -\mathbf{K}^{-1}\mathbf{R}, \quad (4.53)$$

where the global nodal displacement field \mathbf{D} is updated $\mathbf{D} \leftarrow \mathbf{D} + \Delta\mathbf{D}$ during the *Newton-Raphson iteration scheme*. The iteration stops when the residual vector \mathbf{R} is smaller than a pre-defined tolerance [136]. Further details on static FEM formulation can be found in classical FEM textbooks as it is out of the scope of this thesis.

4.2.2 Finite elements formulation of dynamic problems

It is important to mention here that there are two types of dynamic problems, namely the *structural dynamics* and *wave propagation* problems [139]. In the first type, the whole structure participates in the response, which usually lasts for several seconds. Earthquakes excitations and structural vibrations are good examples of this type. In the *structural dynamics* problem, material and structural damping should be assessed in addition to modes of vibration. The unconditionally stable implicit method is implemented in FEM codes to solve this type of dynamic problems. The implicit method uses an automatic increment strategy that depends on full Newton iterative solution, as follows [140]:

$$\Delta \mathbf{u}^{(i+1)} = \Delta \mathbf{u}^{(i)} + \mathbf{K}_t^{-1} \cdot (\mathbf{F}^{(i)} - \mathbf{I}^{(i)}) , \quad (4.54)$$

where $\Delta \mathbf{u}$ is the increment of displacement, the superscript $^{(i)}$ is the increment number, \mathbf{F} is the applied load vector, \mathbf{K}_t is the current tangent stiffness matrix, and \mathbf{I} is the internal force vector. The algorithm of implicit procedure is defined by Hilber and Hughes [141] as:

$$\mathbf{M}\ddot{\mathbf{u}}^{(i+1)} + (\mathbf{1} + \alpha)\mathbf{K}\mathbf{u}^{(i+1)} - \alpha\mathbf{K}\mathbf{u}^{(i)} = \mathbf{F}^{(i+1)} , \quad (4.55)$$

where \mathbf{M} is the mass matrix, \mathbf{K} is the stiffness matrix, \mathbf{F} is the vector of applied loads and \mathbf{u} , $\dot{\mathbf{u}}$, $\ddot{\mathbf{u}}$ are the displacement, velocity and acceleration, as follows:

$$\mathbf{u}^{(i+1)} = \mathbf{u}^{(i)} + \Delta t \dot{\mathbf{u}}^{(i)} + \Delta t^2 \left(\left(\frac{1}{2} - \beta \right) \ddot{\mathbf{u}}^{(i)} + \beta \ddot{\mathbf{u}}^{(i+1)} \right) , \quad (4.56)$$

$$\dot{\mathbf{u}}^{(i+1)} = \dot{\mathbf{u}}^{(i)} + \Delta t \left((1 - \gamma) \ddot{\mathbf{u}}^{(i)} + \gamma \ddot{\mathbf{u}}^{(i+1)} \right) , \quad (4.57)$$

with

$$\beta = \frac{1}{4}(1 - \alpha^2), \quad \gamma = \frac{1}{2} - \alpha, \quad \frac{1}{3} \leq \alpha \leq 0 , \quad (4.58)$$

where α is a damping term, chosen by default as -0.05 in Abaqus, to remove high frequency noise without affecting lower frequency response.

The second type of dynamic problem is the *wave propagation* (also called transient dynamic). Here the excitation lasts for a fraction of a second such as impact or blast force. Seshu [139], state that in wave propagation problems, “*the entire structure does not instantaneously know that it has been hit*”. Here, the use of implicit procedure may not be efficient as the reduced time increment leads to dramatic increase in the computational cost of the tangent stiffness matrix. Moreover, local instabilities may cause force equilibrium to be difficult to achieve [140]. Therefore, the explicit technique is used to overcome those drawbacks. The explicit method is the implemented technique in this thesis. It follows an explicit integration rule with the use of diagonal or “lumped” element mass matrices. The equation of motion for the body is integrated using an explicit central difference integration rule:

$$\mathbf{u}^{(i+1)} = \mathbf{u}^{(i)} + \Delta t^{(i+1)} \dot{\mathbf{u}}^{(i+1)}, \quad (4.59)$$

$$\dot{\mathbf{u}}^{(i+1/2)} = \dot{\mathbf{u}}^{(i-1/2)} + \frac{1}{2}(\Delta t^{(i+1)} + \Delta t^{(i)})\ddot{\mathbf{u}}^{(i)}, \quad (4.60)$$

where the superscripts $(i - \frac{1}{2})$ and $(i + \frac{1}{2})$ refer to mid-increment values. In addition:

$$\ddot{\mathbf{u}}^{(i)} = \mathbf{M}^{-1}(\mathbf{F}^{(i)} - \mathbf{I}^{(i)}), \quad (4.61)$$

where \mathbf{M} is the lumped mass matrix, \mathbf{F} is the applied load vector and \mathbf{I} is the internal force vector. The computational efficiency associated with the explicit procedure is linked to the use of explicit integration rule and diagonal element mass matrices. Hence, no iterations or tangent stiffness matrix is required. However, the explicit integration is conditionally stable, so that time increments must satisfy:

$$\Delta t \leq \frac{2}{\omega_{max}}, \quad (4.62)$$

where ω_{max} is the element maximum eigenvalue. Stable time increment can be estimated by selecting as the minimum value of all elements, so that:

$$\Delta t = \min\left(\frac{L_e}{C_d}\right), \quad (4.63)$$

where L_e is the characteristic element dimension and C_d is the current effective dilatational wave speed of the material [36].

Blast-Induced Reaction Forces

5.1 Preface

As mentioned earlier, blast resistant gates are required to be lightweight and able to mitigate extreme loading effects. This energy absorption may be achieved through a proper design of the gate and/or its supporting frame. The first is well covered in literature while the latter is often overlooked. The design of supporting frame depends mainly on the boundary conditions and corresponding reaction forces. The later states the novelty and the aim of this chapter, namely, the analysis of reaction forces in supporting structure of rectangular steel gates subjected to “far-field explosions”. Flat steel plate was used as simplified gate structure, since the focus in this chapter was on reaction forces rather than behaviour of gate itself. The analyses include both static and dynamic cases using analytical and numerical methods to emphasize the difference between both approaches, and provide some practical hints for engineers. The comprehensive study of reaction forces presented here, cover four different boundary conditions and three length to width ratios. Moreover, the effect of explosive charge and stand-off distance on reaction forces was also covered. This Chapter was published as an article titled “Numerical analysis of reaction forces in blast resistant gates” in the “*Structural Engineering and Mechanics*”, [142].

The objectives of the Chapter were:

- Finding the reaction forces of plates subjected to static uniform pressure (as an equivalent static approximation of a far-field explosion) using numerical simulation (Abaqus/Standard), and then validating the results with analytical solution at specific points.

- Finding the reaction forces of plates subjected to dynamic loading using numerical method (Abaqus/explicit) and comparing the results with the static outcomes. Then, selecting the optimum BC case for possible future implementation of passive damping systems.
- Examining the influence of changing explosive mass or its position on reaction forces.

Conclusions from these analyses were used in Chapters 6 and 7 for the design of “blast absorbing supporting frame”. This in return, increased the absorbing properties of the gate and led to lighter and more operational blast resistant gates.

5.2 Case Study

Size of blast resistant gates ranges from small doors to large gates with unlimited possibilities of length to width ratio (aspect ratio). Therefore, in this study, the discussion would be based on the most common aspect ratios as an alternative, as the focus here is on the distribution and change of reaction forces rather than solution for a specific case. In terms of boundary conditions, four symmetric boundary conditions were selected as they are the most common combinations used in blast resistant gates.

The pressure due to blast incident varies according to the mass of the explosive (M) and its stand-off distance (R). In urban areas, where sensitive infrastructure exists, such as embassies or parliaments, traffic should be limited to passenger vehicles (i.e., no trailers or load-carrying vehicles). In terms of stand-off distance, barriers should be provided to prevent near field explosion scenarios. In return, protection from direct shock, heat or debris impact can be achieved. The stand-off distances were assumed to be ranging from 5-30m based on the street width. The blast scene is shown in Fig. 5.1. In the following sub-sections, more details are provided for geometry, boundary conditions, material and loading.

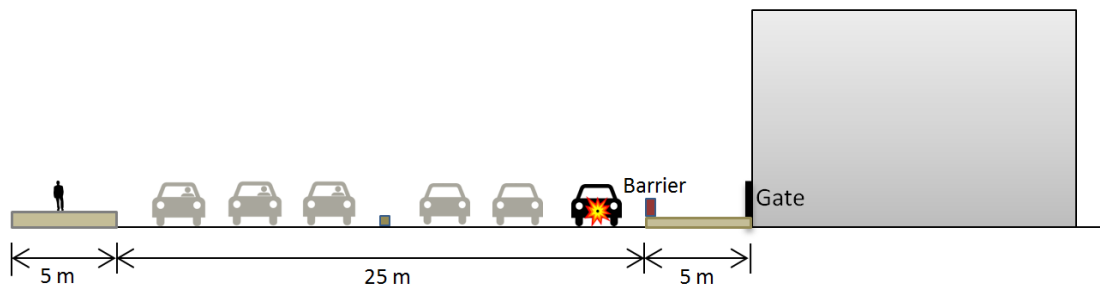


Fig. 5.1 Blast scene under consideration

5.2.1 Geometry

The height to width ratio of a plate, i.e. aspect ratio (AR), can be of any magnitude ranging from 1 (square plate) to ∞ . However, deflection and reaction factors do not change significantly when $AR > 2$, since the plate starts to behave as one way strip. Therefore, three ARs are studied here, which are 1, 1.5 and 2.

For static analysis, the dimensions of a plate and magnitude of the load were treated as model parameters in a non-dimensional manner. However, for a dynamic problem, the pressure from an explosion does not have single value and changing over time. So, the problem cannot be solved in non-dimensional manner. For that reason, and to allow physical understanding, the following values were assumed for dynamic analysis:

- for $AR=1$, the plate dimensions are $1000 \times 1000 \text{ mm}$
- for $AR=1.5$, the plate dimensions are $1000 \times 1500 \text{ mm}$
- for $AR=2$, the plate dimensions are $1000 \times 2000 \text{ mm}$
- Plate thickness= 10 mm

5.2.2 Boundary Conditions

Generally, each edge of the plate can either be free (F), simply supported (S), or Clamped (C) [143]. Therefore, there are 21 possible boundary conditions [144]. Here, four common symmetric boundary conditions were taken into account in the analysis of the steel plate. Those boundary cases are; four edges simply supported (SSSS), two opposite edges simply supported and two free (SFSF), two opposite edges clamped and two free (CFCF) and the last case is four edges clamped (CCCC), see Fig. 5.2.

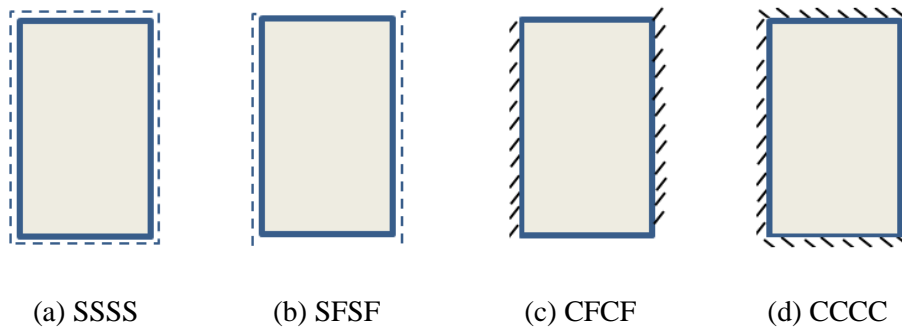


Fig. 5.2 Selected boundary conditions

The four BCs and the three ARs lead to 12 cases in total as shown in the tree diagram (Fig. 5.3).

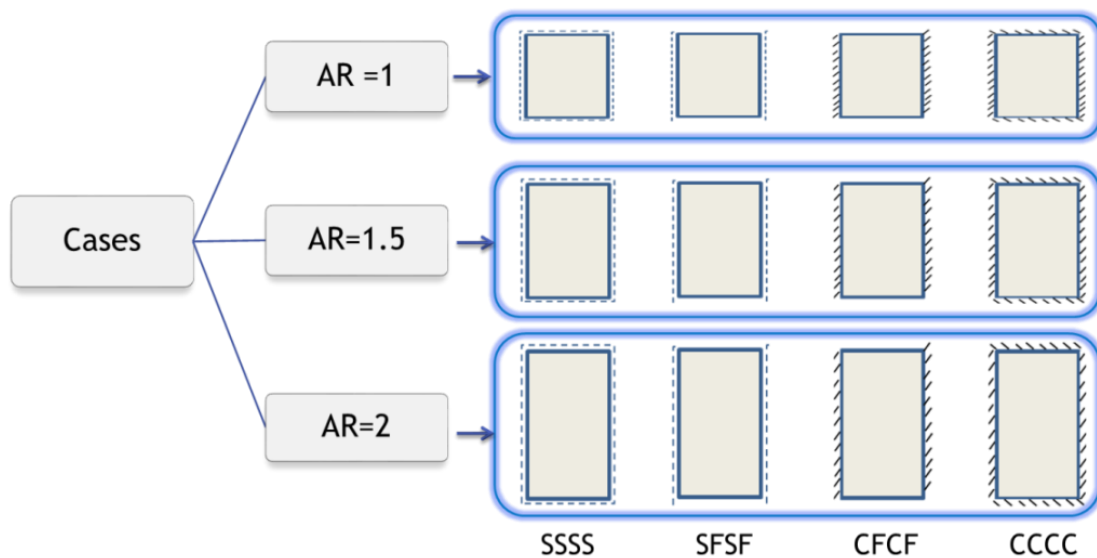


Fig. 5.3 The 12 cases under consideration (four BCs and three ARs)

5.2.3 Material and J-C model

An elastic material model would be sufficient for the static analysis part of this study, since no material hardening or damage was expected. However, when changing the mass of the TNT or its position in dynamic simulations (Section 5.4.3), elastic model may no longer represent the real behaviour. For that reason and for the unity of the analysis, an elasto-plastic model with damage initiation was used for both static and dynamic simulations. Plasticity and damage were defined using Johnson-Cook model.

Johnson-Cook material model is one of the semi-empirical constitutive models that can describe the plastic material behaviour at high strains, high strain rates and high temperatures. The model (in Eq. (5.1)) describes the yield stress σ_y and takes into account the strain rate hardening and thermal softening effects [145-148]. The dimensionless temperature parameter \hat{T} is defined in Eq. (5.2).

$$\sigma_y = (A + B \varepsilon^n) \left[1 + C \ln\left(\frac{\dot{\varepsilon}}{\dot{\varepsilon}_0}\right) \right] [1 - (\hat{T})^m], \quad (5.1)$$

$$\hat{T} = \begin{cases} \hat{T} = 0 & \text{for } T < T_0 \\ \hat{T} = \frac{T - T_0}{T_m - T_0} & \text{for } T_0 < T < T_m \\ \hat{T} = 1 & \text{for } T > T_m \end{cases} \quad (5.2)$$

where, ε is the plastic strain, $\dot{\varepsilon}$ is the plastic strain rate, $\dot{\varepsilon}_0$ is the reference plastic strain rate, T is the current material temperature, T_m is the melting point of the material, and T_0 is the transition/room temperature at or below which there is no temperature dependence of the yield stress. A , B , C , n and m are material parameters measured at or below T_0 . A is the yield stress, B is the pre-exponential factor, C is the strain rate factor, n is the work-hardening exponent and m is the thermal-softening exponent.

In addition, Johnson-Cook dynamic failure model is supplied by Abaqus/Explicit [39]. The failure is assumed to happen when the damage parameter ω exceeds 1. The damage parameter is defined as:

$$\omega = \sum \left(\frac{\Delta \varepsilon}{\varepsilon_f} \right), \quad (5.3)$$

where, $\Delta\varepsilon$ is an increment of the plastic strain, ε_f is the plastic strain at failure, and the summation is performed over all increments in the analysis. The plastic strain at failure ε_f is dependent on the nondimensional plastic strain rate $\frac{\dot{\varepsilon}}{\dot{\varepsilon}_0}$, pressure to HMM stress ratio $\frac{p}{q}$, and the dimensionless temperature parameter \hat{T} . The strain at failure ε_f can be expressed as: d_1

$$\varepsilon_f = \left[d_1 + d_2 \exp\left(d_3 \frac{p}{q}\right) \right] \left[1 + d_4 \ln\left(\frac{\dot{\varepsilon}}{\dot{\varepsilon}_0}\right) \right] (1 + d_5 \hat{T}), \quad (5.4)$$

where $d_1 - d_5$ are failure parameters.

The used material is “Weldox 460E Steel”. Weldox is a class of thermo mechanically rolled ferritic structural steels that offers both ductility and high strength [149]. Børvik, et al. [149] give material parameters for the Weldox 460E Steel as shown in Table 5.1. Such a choice is argued based on previous results by Sumelka and Łodygowski [150], Łodygowski, et al. [151] and Szymczyk, et al. [152].

Table 5.1: Material parameters for Weldox 460E Steel (adopted from [149])

Category	Constant	Description	Unit	Value
Elastic Constants	E	Modulus of Elasticity	<i>MPa</i>	$200 \cdot 10^3$
	ν	Poisson's ratio	-	0.33
Density	ρ	Mass density	<i>t/mm³</i>	$7.85 \cdot 10^{-9}$
Yield stress and strain hardening	A	Yield Strength	<i>MPa</i>	490
	B	Ultimate Strength	<i>MPa</i>	807
	n	work-hardening exponent	-	0.73
Strain-rate hardening	$\dot{\epsilon}_0$	Reference Strain rate	<i>S⁻¹</i>	$5 \cdot 10^{-4}$
	C	strain rate factor	-	0.0114
Damage evolution	D_c	Critical Damage	-	0.3
	p_d	Damage threshold	-	0
Adiabatic heating and temperature softening	C_p	Specific heat	<i>mm².K/S²</i>	$452 \cdot 10^6$
	χ	Taylor Quinney empirical constant/inelastic heat fraction	-	0.9
	α	Coefficient of thermal expansion	<i>K⁻¹</i>	$1.1 \cdot 10^{-5}$
	T_m	Melting Temperature	<i>K</i>	1800
	T_0	Room Temperature	<i>K</i>	293
	m	thermal-softening exponent	-	0.94
	K	-	-	0.74
Fracture Strain Constants	d_1	-	-	0.0705
	d_2	-	-	1.732
	d_3	-	-	-0.54
	d_4	-	-	-0.015
	d_5	-	-	0

5.2.4 Loading

The far-field type of explosions was of interest as it generates flat and uniform pressure. Hence, more valid comparison could be made between the dynamic pressure and its static approximation. As there are four factors affecting the results, namely, BCs, ARs, M and R, one factor was modified at a time to see its influence on reaction forces.

First, the value of M and R were fixed to 100 kg and 30m, respectively. This was to investigate the effect of BCs and ARs on reaction forces and it allowed clearer comparisons between static and dynamic solutions. According to TM-5 1300 (TM5-1300 1990), this combination of mass and stand-off distance generates 0.06 MPa peak reflected over-pressure. This uniform pressure value was used for static analyses (analytical and numerical). For dynamic simulations, ConWep tool was utilised with surface blast incident wave.

Second, the mass of the explosive material and its position was modified in Section 5.4.3 to examine the effect of such a variation on the reaction forces. The value of M was increased gradually with keeping R fixed at 30m. Five steps were taken at 200 kg, 400 kg, 600 kg, 800 kg and 1000 kg. The position of the centroid of the explosive material depends on the stand-off distance (z-direction) and the position in a plane parallel to the plate under consideration, x and y directions (Fig. 5.4). The stand-off distance (R) was increased from 5-30m (5m step) to see its effect on the reaction forces (with keeping the mass at 100 kg and its centroid coincident with the centre of the plate). Then, the position of the centroid was modified to 9 different positions on a plane parallel to the plate under consideration (with keeping the mass at 100 kg and its centroid at R=30m), as shown in Fig. 5.4. Results for the effects of variation in explosive mass and position are shown in Section 4.3.

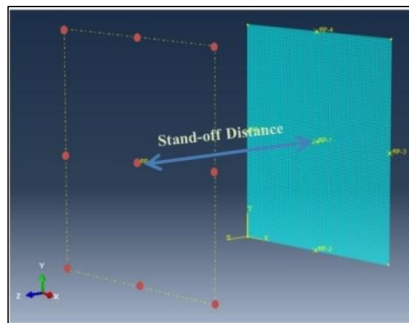


Fig. 5.4: Variation of the explosive centroid position in x, y and z directions

5.3 Methodology

The analyses conducted in this Chapter include both static and dynamic cases using analytical and numerical methods. This section provides a detailed description of the methodology.

5.3.1 Static Analysis

Classical plate theories provide analytical solutions for reaction forces along the edges of thin elastic plates. The boundary conditions, dimensions and loading scenario are the key elements in the solution. Early papers in this field; such as Love [153], Timoshenko and Woinowsky-Krieger [154] and Meleshko [155]; mention that fully simply supported plate (SSSS) was first solved by Navier (1823) through implementing a double trigonometric series. Then, plate with two opposite edges simply supported and the other two free (SFSF) was solved by Levy (1899). After that, clamped plate conditions were considered by Koialovich (1902), Hencky (1913) and Boobnoff (1914). The solutions of the previous mentioned scientists are well quoted in books of plate theory, theory of elasticity or research articles. A brief description is discussed here.

Consider a homogeneous isotropic elastic thin plate, of sides $a' = 2a$, $b' = 2b$. The plate is subjected to a uniformly distributed load of q , with the center of the plate lying on the origin of the cartesian coordinates Oxy . The plate occupies the region $-a \leq x < a$ and $-b \leq y < b$ (Fig. 5.5).

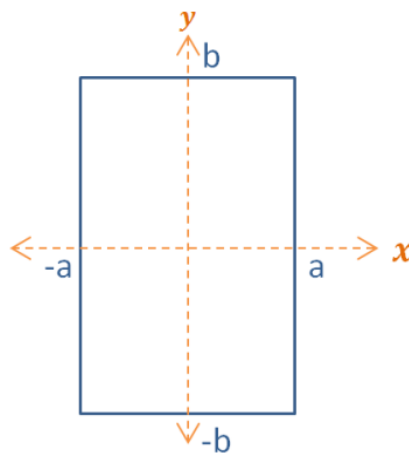


Fig. 5.5 Plate configuration

Then, the plate governing equation is

$$\Delta^2 w = \frac{q}{D}, \quad (5.1)$$

where,

Δ is a two-dimensional laplace operator,

$$\Delta \equiv \frac{\partial^2}{\partial x^2} + \frac{\partial^2}{\partial y^2}, \quad (5.2)$$

D is the bending stiffness,

$$D \equiv \frac{h^3 E}{12(1-\nu^2)}, \quad (5.3)$$

E is the modulus of elasticity, h is the plate thickness, ν is the Poisson's ratio and w is the transverse deflection of the middle plane of the plate. Equation 5.1 can be solved through satisfying the boundary conditions at the edges. The deflection w is

$$w = w_0 + \frac{q}{D} \sum_{n=0}^{\infty} (-1)^n \left(A_n \frac{\cosh \alpha_n y}{\cosh \alpha_n b} + B_n \frac{y \sinh \alpha_n y}{b \cosh \alpha_n b} \right) \cos \alpha_n x + \frac{q}{D} \sum_{n=0}^{\infty} (-1)^n \left(C_n \frac{\cosh \beta_n x}{\cosh \beta_n a} + D_n \frac{x \sinh \beta_n x}{a \cosh \beta_n a} \right) \cos \beta_n y, \quad (5.4)$$

where w_0 is a particular solution satisfying $\Delta^2 w_0 = \frac{q}{D}$ and where

$$\alpha_n \equiv \frac{(2n+1)\pi}{2a} \quad \beta_n \equiv \frac{(2n+1)\pi}{2b} \quad (n = 0, 1, 2, \dots). \quad (5.5)$$

The particular solution w_0 is taken in the form of a symmetrical polynomial of the fourth order in x and

$$w_0 = c_0 + c_1 x^2 + c_2 y^2 + c_3 x^4 + c_4 x^2 y^2 + c_5 y^4. \quad (5.6)$$

This solution should satisfy the plate equation so that

$$3c_3 + c_4 + 3c_5 = \frac{q}{8D}. \quad (5.7)$$

Once w is known, bending moments M_x , M_y and twisting moment M_{xy} can be calculated as follow:

$$\begin{aligned}
M_x &= -D \left(\frac{\partial^2 w}{\partial x^2} + \nu \frac{\partial^2 w}{\partial y^2} \right), \\
M_y &= -D \left(\frac{\partial^2 w}{\partial y^2} + \nu \frac{\partial^2 w}{\partial x^2} \right), \\
M_{xy} &= -(1 - \nu) D \frac{\partial^2 w}{\partial x \partial y}.
\end{aligned} \tag{5.8}$$

Shear forces Q_x, Q_y and effective shear forces V_x, V_y can be found from:

$$Q_x = -D \frac{\partial \Delta w}{\partial x}, \quad Q_y = -D \frac{\partial \Delta w}{\partial y}, \tag{5.9}$$

$$\begin{aligned}
V_x &= -D \left[\frac{\partial^3 w}{\partial x^3} + (2 - \nu) \frac{\partial^3 w}{\partial x \partial y^2} \right], \\
V_y &= -D \left[\frac{\partial^3 w}{\partial y^3} + (2 - \nu) \frac{\partial^3 w}{\partial x^2 \partial y} \right].
\end{aligned} \tag{5.10}$$

The detailed derivation of the deflection, moment and shear coefficients, α, β and γ , respectively, are available in [154] for different boundary conditions and are out of the scope of this study. The magnitudes of β and γ are given in Table 5.2 (under analytical columns) for each of the four cases under consideration; SSSS, SFSS, CFCF and CCCC. Therefore, if the dimensions of the plate (L, W and t) are given, and based on the moment and shear factors, β and γ , one can find the moment and shear at the centre of supporting edges using:

$$M_y = \beta q a'^2, \quad Q = \gamma q a'. \tag{5.11}$$

The achieved moment and shear represent the reaction forces at the centre of supporting edges. These values solved at certain points were used for verification of the reaction forces along the plate edges acquired from static numerical analysis.

The same 12 cases (in Fig. 5.3), were solved numerically using Abaqus/Standard. This was to get the reaction forces at every point on the supporting edges. The achieved results were then compared with the analytical solution solved for specific points. The modelling in Abaqus/CAE had the following properties:

- Deformable shell of planar type,
- FE type = S4 (a 4 node doubly curved general purpose shell element),
- Homogenous continuous plate section of thickness $t = 10$ mm,
- Mesh size= 10 mm,
- Linear analysis.

Although the aim of the research was the analyses of reaction forces rather than the plate behaviour, it was crucial to check the plate situation under blast loading (i.e. elastic, plastic or in the damage range). Therefore, HMH stresses were checked for all cases. It was found that the Maximum HMH stress (across the thickness of the plate) over the whole plate in all cases was below the yield point of the steel material used (i.e. in elastic range). Fig. 5.6 shows the loading pattern of the SSSS case with AR=1 and the corresponding Max. HMH stress (in MPa).

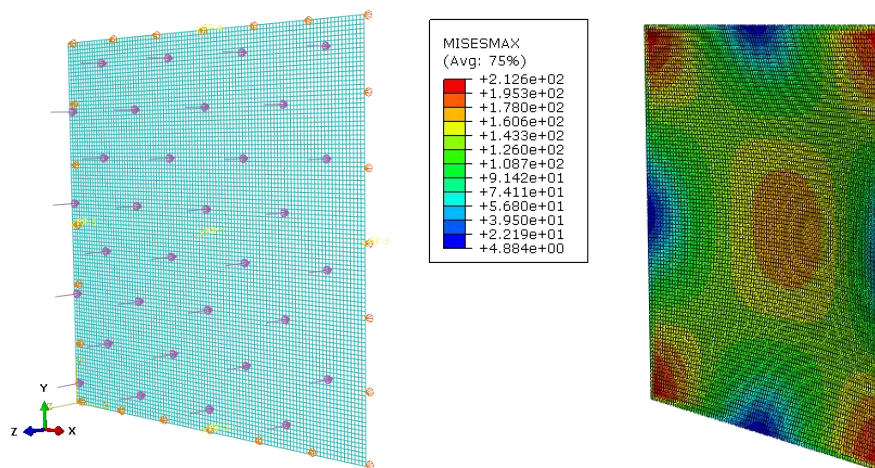


Fig. 5.6 Loading of the SSSS case, AR=1, and the corresponding HMH stresses

5.3.2 Dynamic Analysis

In Section 5.3.1, the 12 cases were analysed for static uniform pressure as far-field explosion. Here, in this section, the response of steel plates (12 cases) is examined under ConWep loading using Abaqus/Explicit numerical solver. The finite element type used is an explicit, linear, quadrilateral four-node, doubly-curved general purpose shell S4 element (size=10x10mm). The blast incident was set at time $t_{\text{incident}} = 0$, and the shock wave travelled 30 m and first hit the plate at arrival time $t_a = 56$ ms. In addition, the pressure evolved from the blast was checked using IWCONWEP option. The amount and distribution of the pressure are shown in Fig. 5.7. The peak value is 0.062 MPa which is quite similar to the estimated value of 0.06 MPa in TM-5 US code [61]. Results of these numerical simulations, for the 12 cases under consideration, subjected to this dynamic loading which is equivalent to the static pressure, are all presented in Section 5.4.2. Then, the effects of variation in explosive mass or position on reaction forces are presented in Section 5.4.3 based on loading conditions discussed earlier in Section 5.2.4.

The selection of the mesh size (10mm) was based on a parametric study of the element size to examine the accuracy of the computed results. Reducing the element size smaller than 10mm showed no significant change in the reaction forces and led to longer computation time (cf. Sielicki and Stachowski [156]). Therefore, the 10 mm element size found to be adequate. The ‘automatic’ option for time step size was selected in Abaqus/Explicit solver, to allow quick and accurate convergence of the analysis.

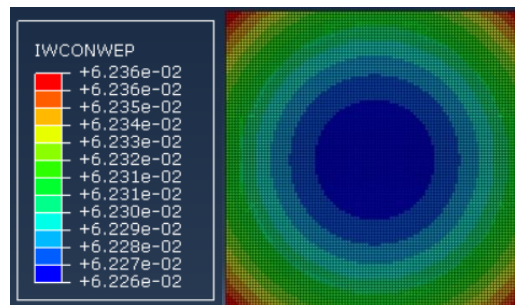


Fig. 5.7 The amount and distribution of pressure (in MPa) generated from ConWep (M = 100kg TNT, R = 30m) on the surface of steel plate, AR=1

5.4 Results and discussion

5.4.1 Static Analysis

When the solution is based on static loading, with one uniform pressure and bending stiffness, the reaction forces and moments can be converted to shear and moment factors using Eq. (5.11). This would allow comparison with the analytical factors to check the numerical simulation against analytical solution at specific points. As mentioned earlier, in this study, the analytical solution was conducted for two specific points which were the mid-points of both horizontal and vertical supporting edges. Table 5.2 shows the shear and moment factors at horizontal edge and vertical edge mid-points. The table provide both analytical and numerical solutions (under static loading).

Table 5.3 was generated based on Table 5.2 for verification and remarks. It shows 6 bar charts of 3 rows and 2 columns. The rows correspond to the three ARs while the columns are for the shear and moment factors, respectively. Based on the bar charts in Table 5.3, the following points can be concluded:

- The analytical results were of high similarity to the numerical outcomes.
- Results were compatible with factors achieved by other researchers, [154] and [157].
- The shear and moment factors for the SFSF and CFCF were less affected by ARs as the other edges were already not supported.
- The moment factor of CCCC case had increased significantly with increase of AR.
- The SSSS case had slight increase in shear factors due to AR change.

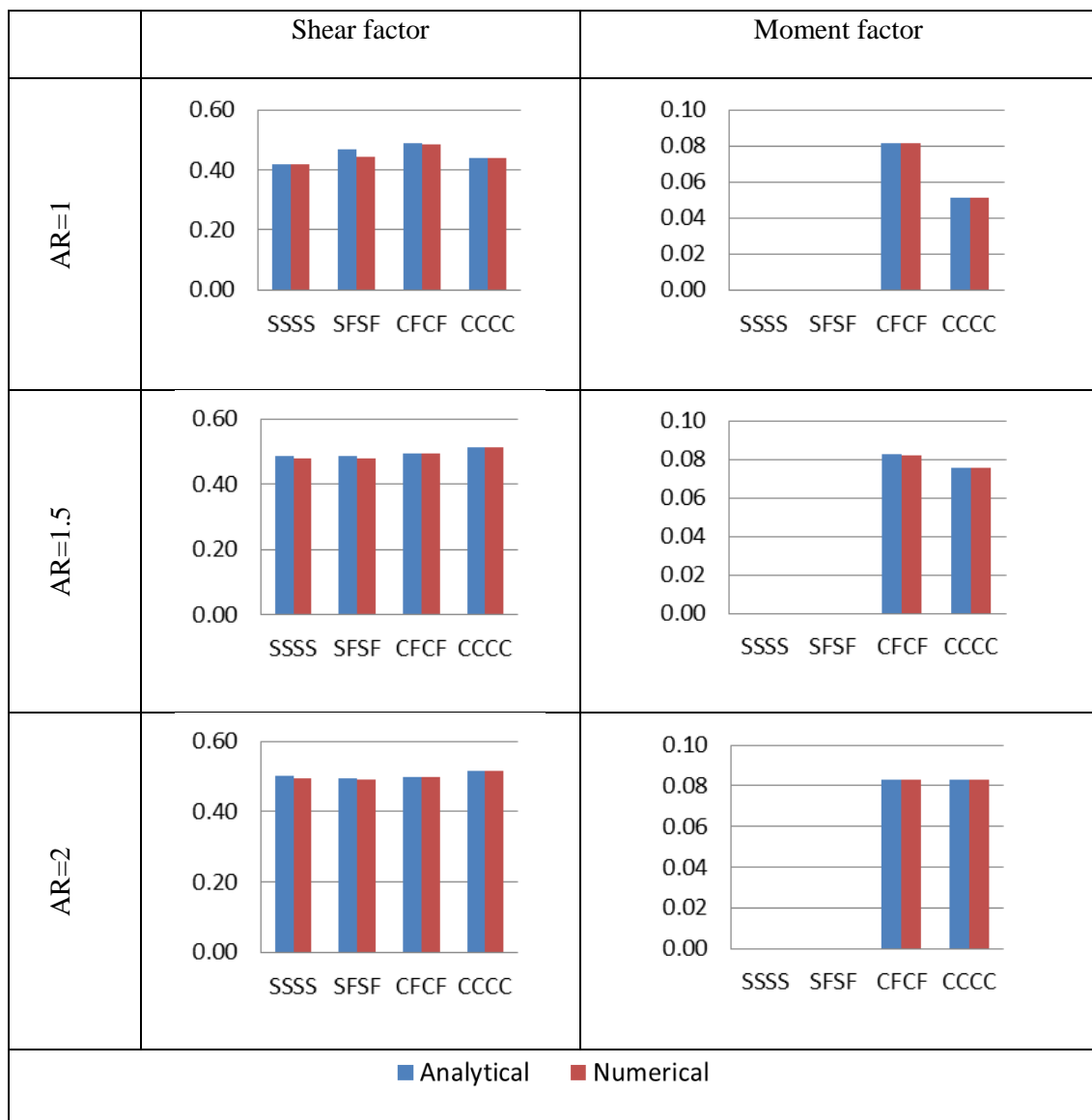
Table 5.2: Shear and moment factors at horizontal and vertical edge mid-points for both analytical and numerical solutions (under static loading)

BC	b/a	At centre of Vertical Edges				At centre of Horizontal Edges			
		Moment factor β		Shear factor γ		Moment factor β		Shear factor γ	
		Analyt.	Num.	Analyt.	Num.	Analyt.	Num.	Analyt.	Num.
SSSS	1	0	0	0.4200	0.4200	0	0	0.4200	0.4200
	1.5	0	0	0.4850	0.4800	0	0	0.4850	0.4800
	2	0	0	0.5030	0.4950	0	0	0.5030	0.4950
SFSF	1	0	0	0.4687	0.4445	0	0	0	0
	1.5	0	0	0.4860	0.4780	0	0	0	0
	2	0	0	0.4940	0.4920	0	0	0	0
CFCF	1	0.0816	0.0815	0.4880	0.4840	0	0	0	0

	1.5	0.0824	0.0823	0.4953	0.4952	0	0	0	0
	2	0.0830	0.0830	0.4992	0.4992	0	0	0	0
CCCC	1	0.0513	0.0513	0.4413	0.4390	0.0513	0.0513	0.4413	0.4390
	1.5	0.0756	0.0756	0.5140	0.5130	0.0570	0.0569	0.4654	0.4625
	2	0.0829	0.0829	0.5160	0.5160	0.0570	0.0569	0.4639	0.4610

Detailed reaction forces due to static loading (Abaqus/Standard), at every point along the vertical and horizontal edges, are presented in the first columns of Table 5.5, Table 5.6 and Table 5.7, for AR = 1, 1.5 and 2, respectively. This is to provide easier comparison with dynamic analyses.

Table 5.3: Analytical and numerical solutions for reaction factors at vertical edge midpoint under static loading



5.4.2 Dynamic Analysis

The distribution pattern and the magnitude of the reaction forces are usually changing at each time increment in dynamic loading. As an example, Fig. 5.8 shows the distribution of reaction forces along the edges of SSSS square plate at two different time steps, 56.1 and 69.5 ms.

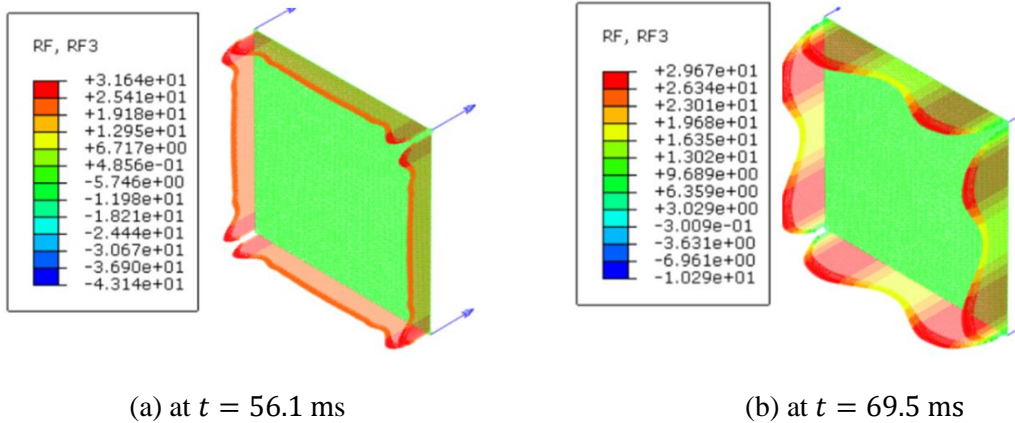


Fig. 5.8 Distribution of reaction forces (in N/mm) along the edges at two different time steps, SSSS case, $AR=1$, surface blast of TNT ($M = 100\text{kg}$, $R = 30\text{m}$)

However, it is important to mention that there is single time step that provides peak reactions at all edge points (t_p). This time step is usually few milliseconds after the arrival of the shock wave (t_a). Fig. 5.9 below shows reaction force-time history at vertical edge mid-point and a corner point for (SSSS, $AR=1$) case. It clarifies how the shock wave travelled 30 m and first hit the plate at $t_a = 56$ ms. Then, the reaction forces start to increase until reaching peak values at $t_p = 62$ ms.

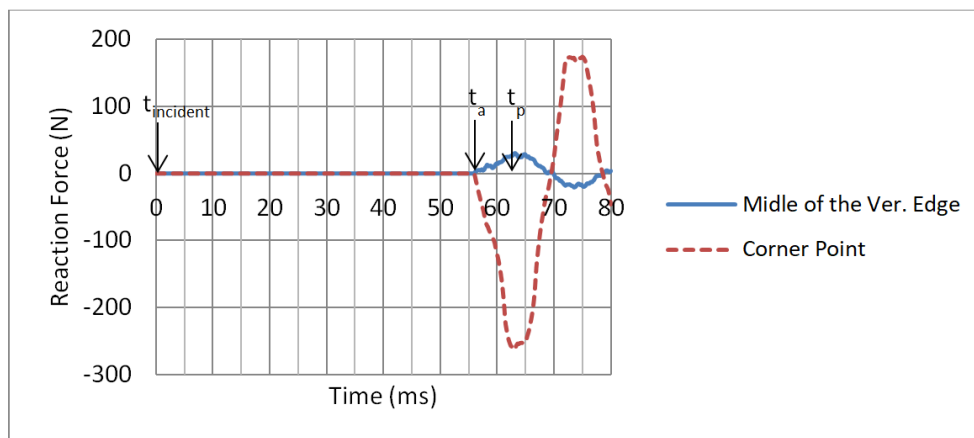


Fig. 5.9 Reaction force-time history at vertical edge mid-point and a corner point (SSSS, $AR=1$, surface blast of TNT $M = 100\text{kg}$, $R = 30\text{m}$)

It was found that t_p was different from a case to another based on boundary conditions. Table 5.4 lists $t_{incident}$, t_a , t_p and the time required to reach peak reaction forces for every BCs (ordered from the shortest to the longest).

Table 5.4: Time required to reach peak reaction forces for all BCs (ordered from the shortest to the longest), subjected to surface blast of TNT, $M = 100\text{kg}$, $R = 30\text{m}$

BC	$t_{incident}$	t_a	t_p	time to peak response ($t_p - t_a$), in <i>ms</i>
CCCC	0	56	61	5
SSSS	0	56	62	6
CFCF	0	56	64	8
SFSF	0	56	73	17

Maximum HMH stresses (in all cases) were checked for this dynamic loading and showed to be less than the yield stress of the steel material used. In other words, the cases were within the elastic range.

For this dynamic loading (which is equivalent to the static pressure discussed in Section 5.2.4), the reaction forces along the edges of the plates are shown in the second columns of Table 5.5, Table 5.6 and Table 5.7, for AR = 1, 1.5 and 2 respectively. The tables summarize static (Abaqus/Standard) and dynamic (Abaqus/Explicit) simulations for all 12 cases under investigation. In these tables, it is important to highlight that the moment and shear distribution curves for the horizontal edges were drawn for only SSSS and CCCC cases as other cases (SFSF and CFCF) have free horizontal edges.

Based on the results shown in Tables 5.5 to 5.7, the following points can be underlined:

- Each BC (SSSS, SFSF, CFCF, CCCC), has a specific ‘distribution pattern’ of reaction which stayed the same regardless to loading condition (static, dynamic), AR (1, 1.5, 2) or edge (horizontal, vertical). However, the magnitudes or values of these reaction forces were changing.
- Simply-supported cases, SSSS and SFSF, show a flat curve of almost uniformly distributed reaction forces along supporting edges, with high concentrated nodal forces at the corners.

- CFCF case has usually uniformly-distributed force and moment along vertical edge. Then, slight rise can be noticed before the corners followed by sharp negative drop at the corners.
- Reaction forces and moments in CCCC case revealed the opposite by having least values at the corners and maximum values at the edges' mid points.

The distributed reaction forces, on the edges of the plates due to dynamic loading, had different values than the static one. The justification is related to the inertia forces that changes the response depending on the boundary conditions BC and aspect ratios AR. To compare the values given in Tables 5.5 to 5.7, the dynamic/static ratio (D/S) was calculated for each point along the edges. Then the mean value was governed. This value represents the average increase or decrease in the reaction for a single edge of a case. Fig. 5.10 shows the average dynamic/static ratio (D/S)_{avg.} for all cases under investigation. Values over one mean that reaction forces due to dynamic loading are higher than the corresponding static reaction forces. Values less than one, represent the opposite. Based on the results in Fig. 5.10, the following points can be highlighted:

- For CFCF and SFSF cases, changing AR has no effect on values of (D/S)_{avg.} as the horizontal edges are already not supported. For SSSS and CCCC cases, changing AR has slight effect.
- The highest value is around 2 for CCCC case and drops as low as 0.8 for the SFSF. It is evident here that the more constrains the BCs have, the more shear and moment would be compared to static simulations. The reason to that behavior may be linked to direct transfer of the inertia energy to the supports causing higher shear and moment values. Oppositely, the SFSF case, showed 20% less dynamic response compared to the static. These results are matching the order of BC cases listed in Table 5.3, where the CCCC was at the top and the SFSF at the bottom of the hierarchy.

Table 5.5 Comparison between reaction forces along the edges of steel plates, with $AR=1$ and different BCs, using dynamic (Abaqus/Explicit) and the Static (Abaqus/Standard) analyses, under surface blast as a dynamic loading (TNT, $M = 100\text{kg}$, $R = 30\text{m}$) and its equivalent static uniform pressure (0.06 MPa)

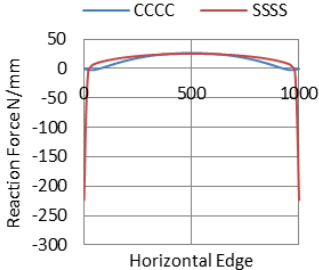
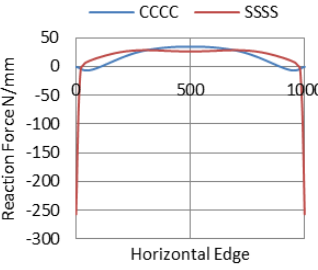
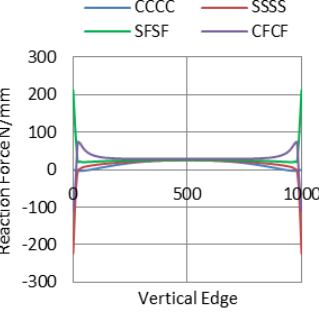
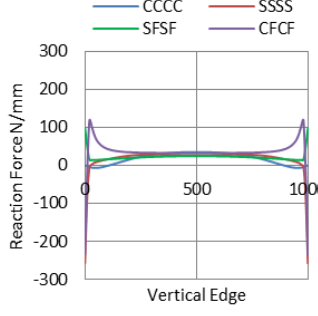
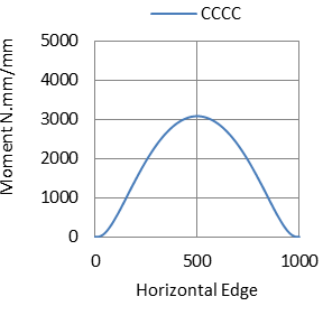
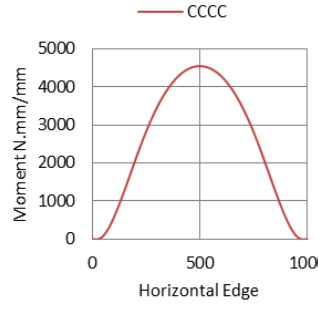
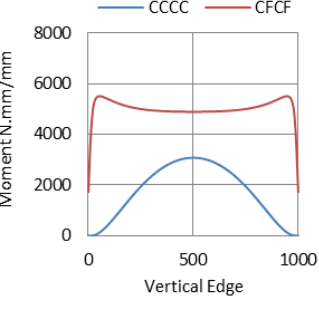
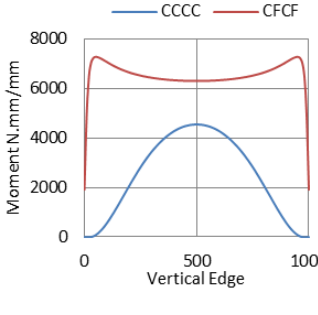
		Static (Abaqus/Standard)	Dynamic (Abaqus/Explicit)
Reaction Force	Hor. Edge		
	Ver. Edge		
Reaction Moment	Hor. Edge		
	Ver. Edge		

Table 5.6 Comparison between reaction forces along the edges of steel plates, with $AR=1.5$ and different BCs, using dynamic (Abaqus/Explicit) and the Static (Abaqus/Standard) analyses, under surface blast as a dynamic loading (TNT, $M = 100\text{kg}$, $R = 30\text{m}$) and its equivalent static uniform pressure (0.06 MPa)

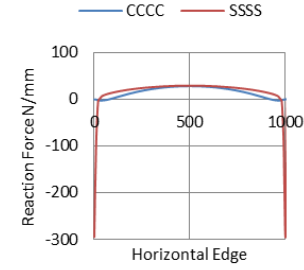
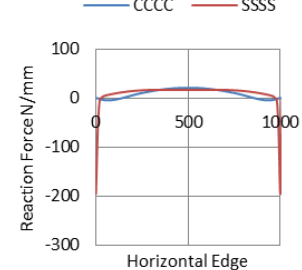
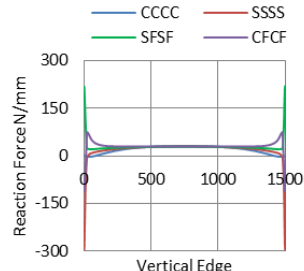
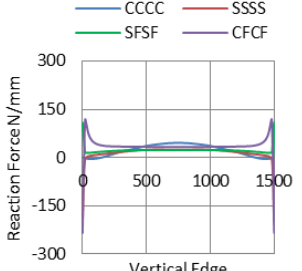
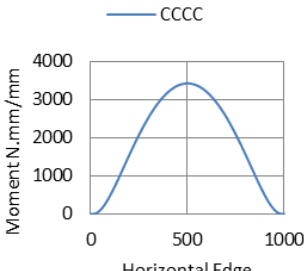
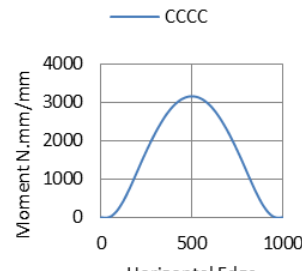
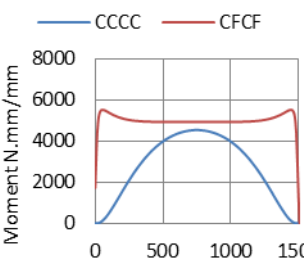
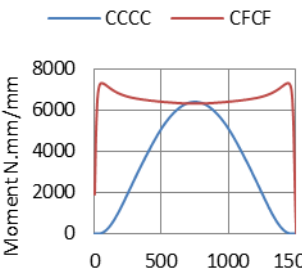
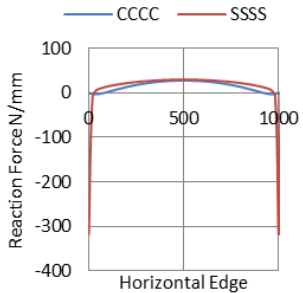
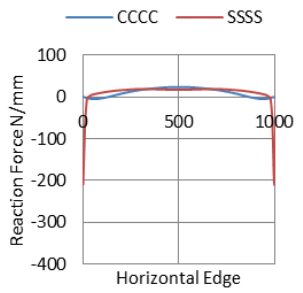
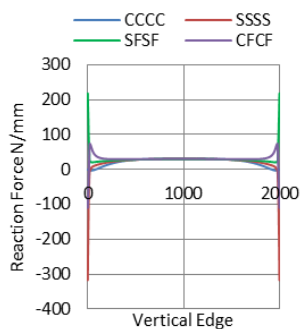
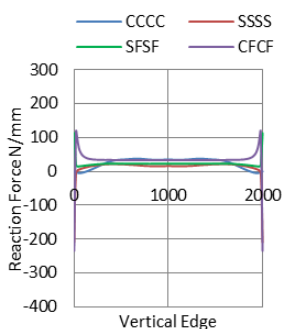
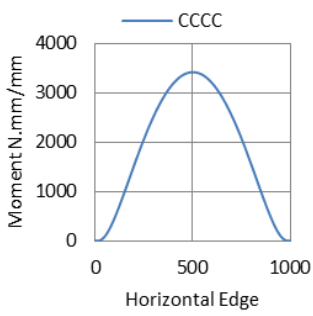
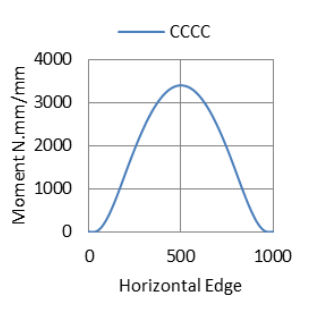
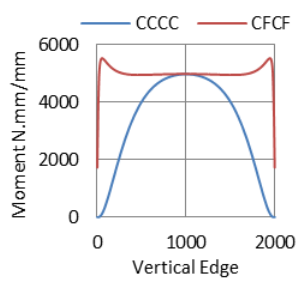
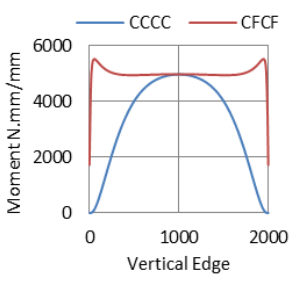
		Static (Abaqus/Standard)	Dynamic (Abaqus/Explicit)
Reaction Force	Hor. Edge		
	Ver. Edge		
Reaction Moment	Hor. Edge		
	Ver. Edge		

Table 5.7 Comparison between reaction forces along the edges of steel plates, with $AR=2$ and different BCs, using dynamic (Abaqus/Explicit) and the Static (Abaqus/Standard) analyses, under surface blast as a dynamic loading (TNT, $M = 100\text{kg}$, $R = 30\text{m}$) and its equivalent static uniform pressure (0.06 MPa)

		Static (Abaqus/Standard)	Dynamic (Abaqus/Explicit)
Reaction Force	Hor. Edge		
	Ver. Edge		
Reaction Moment	Hor. Edge		
	Ver. Edge		

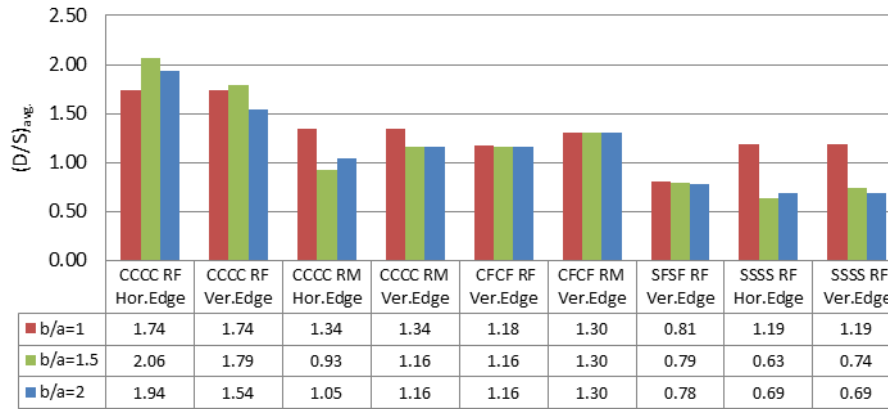


Fig. 5.10 Values of $(D/S)_{avg}$ for the horizontal and vertical edges of all cases

Based on the conclusions made earlier, it is totally the designer decision to what BC should be selected for the design of a blast resistant gate. Less constrained BC cases, such as SSSS and SFSF, revealed lower $(D/S)_{avg}$ than more constrained cases, CCCC and CFCF. In other words, simply supported cases showed better blast mitigation effects since the motion of the plates are greater than that of the clamped cases. These findings can be related to previous research on fluid-structure interaction effects on blast-loaded plates. Kambouchev, et al. [158] state that “*the motion of the structure relieves the pressure acting on it, thus reducing the transmitted impulse and, as a consequence, the effects of the blast*”. In contrast, for fixed boundary plates, the blast impulse transferred to the plate is maximum [159].

Another important point to mention is that the low “mass per unit area” of the plates analysed in this study also decreases the transmitted impulse to the plate. Lighter plates acquire velocity quickly thus relieving the pressure acting on the plate [158-161].

In short, SFSF or SSSS cases are more favoured upon CCCC and CFCF cases due to their potential blast mitigation. Moreover, the distribution of reaction forces allows efficient implementation of shock absorbers at the supports (especially at the corners where most of reaction appear as nodal forces). A closer look at SSSS and SFSF reaction forces is provided in Fig. 5.11 for further discussion.

Among the simply supported cases, this study suggests the SFSF case as the optimum option for possible future implementation of passive damping systems in blast resistant gates. This selection was based on the following reasons:

- SFSF case has corner nodal forces less in value than those for the SSSS case. In addition, the time to peak response is 0.017s higher than that for the SSSS case, 0.006s (Table 5.4). This combined together lead to lower force rate (change of force per time) and hence lower shock or impact on SFSF supporting frame.
- The reaction force is in the positive range along the length of the vertical edge, i.e. all reactions in one direction opposite to the direction of blast pressure. This is in contrast to the SSSS case where corner nodal forces are in the negative range. This in return leads to easier future application of passive damping systems as they will all behave in the same direction.

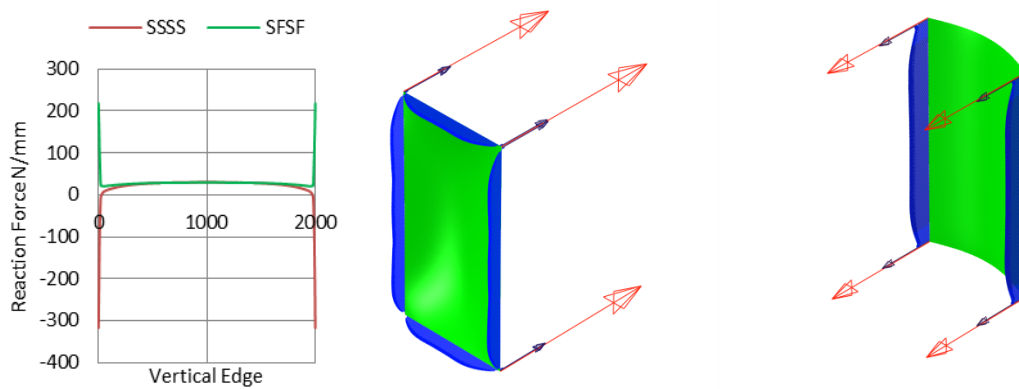


Fig. 5.11 Comparison between the distribution pattern of peak reaction forces in SSSS and SFSF cases, subjected to surface blast of TNT, $M = 100\text{kg}$, $R = 30\text{m}$

5.4.3 Effects of variation in explosive mass and position

While this study suggests SFSF case as the optimum boundary condition, mass of the explosive material and its position were modified to further examine the effect of such a variation on the reaction forces of SFSF. As mentioned in Section 5.2.4, the value of M was increased gradually with keeping R fixed at 30m. Five steps were taken at 200 kg, 400 kg, 600 kg, 800 kg and 1000 kg. Results revealed that the percentage of increase in reaction forces was linear to some extent when increasing the TNT mass (M), as shown in Fig. 5.12. Doubling the value of M led to 50% increase in reaction forces, moreover, 97 % change was observed with 4 times rise in the initial mass (200 to 800 kg). These outcomes are consistent with the study of Curry and Langdon [51], which concludes that permanent deformation also raised ‘linearly’ with increasing the explosive mass.

Results of increasing stand-off distance (R), from 5m to 30m, with keeping the TNT mass at 100 kg, are shown in Fig. 5.13. Sharp drop of 81% in the reaction force can be observed with the increase in the stand-off distance from 5 to 15m. Then, more flat curve can be noticed. It might be also important to mention that the behaviour of the steel plate was within the plastic range, with no damage initiation, throughout the TNT mass range (200 to 1000kg) and the stand-off distance (5 to 25m). Elastic behaviour was at $M = 100\text{kg}$ and $R = 30\text{m}$, as mentioned in Section 5.4.2.

When changing the position of the centroid of the explosive material in a plane parallel to the plate under consideration, it was found that this sort of change has negligible effect on reaction forces. This is due to the uniform pressure achieved from far-field explosions as confirmed by Feldgun, et al. [49]. These results were compatible with the conclusions of Jacob, et al. [50]. In addition, Yuen, et al. [46] states that “*when the stand-off distance exceeds the largest plate dimension, loading could be considered to be uniform*”.

It is crucial to re-highlight that all the combinations of TNT mass and stand-off distances considered in this study led to far-field uniform loading pattern. Table 5.8 summarize the studied combinations and their scaled distances Z (with minimum value of $1.1 \text{ m/kg}^{1/3}$). In fact, the validity of using empirical (or ConWep) method becomes questionable when predicting the loading of close-range detonations at scaled distances

less than approximately $0.4 \text{ m/kg}^{1/3}$, as the target may be located inside the fireball resulting in an interaction between the expanding detonation products (i.e., the fireball) and the blast overpressure [162, 163].

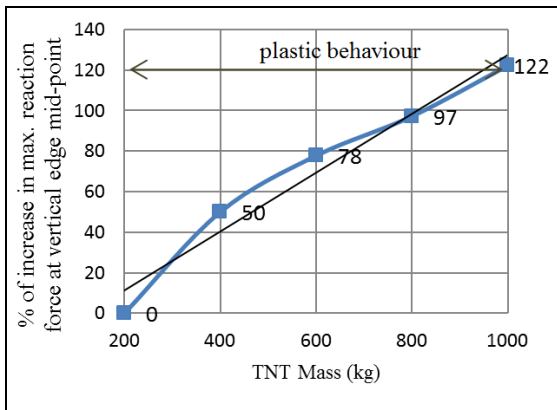


Fig. 5.12 Percentage of increase in max. reaction force at vertical edge mid-point of the SFSF, AR=1 steel plate, due to the change in TNT mass, at fixed $R = 30\text{m}$

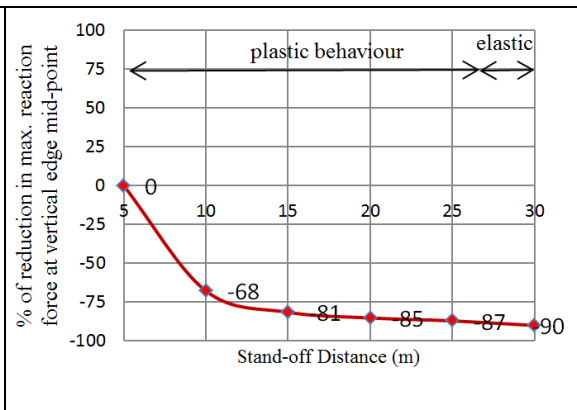


Fig. 5.13 Percentage of reduction in max. reaction force at vertical edge mid-point of the SFSF, AR=1 steel plate, due to the change in stand-off distance, for TNT mass $M = 100 \text{ kg}$

Table 5.8: TNT mass and stand-off distance combinations considered in this study and their scaled distances

		M (mass of TNT in kg)	R (stand-off distances in m)	Z (Scaled distance), $Z = M/\sqrt[3]{R}$
Section 5.4.2		100	30	6.5
Section 5.4.3	Changing M	200	30	5.1
		400	30	4.1
		600	30	3.6
		800	30	3.2
		1000	30	3.0
	Changing R	100	25	5.4
		100	20	4.3
		100	15	3.2
		100	10	2.2
		100	5	1.1

5.5 Conclusions

In this Chapter, reaction forces and their influence by boundary conditions, aspect ratios, explosive charge and stand-off distance, were investigated. The analyses cover 12 cases of four different boundary conditions and three aspect ratios. The following conclusions summarize the results:

- Static analyses revealed that the numerical results were of high similarity to the analytical outcomes. In addition, shear and moment factors for the SF/SF and C/C/F cases were less affected by the aspect ratio (AR) as the other edges are already not supported. The moment factor of C/C/C/C case has increased significantly with the increase of AR ratio unlike the S/S/S/S case which had slight increase in shear factors due to AR change.
- For dynamic loading, distributed reaction forces on the edges of the plates had different values than the static one. The average increase or decrease in the reaction for each supporting edge of a case was examined. For C/C/F and SF/SF cases, changing AR had no effect on values of dynamic/static ratio (D/S)_{avg.} as the horizontal edges are already not supported. For S/S/S/S and C/C/C/C cases, changing AR had slight influence. The second point is that less constrained BC cases, such as S/S/S/S and SF/SF, revealed lower (D/S)_{avg.} than more constrained cases, C/C/C/C and C/C/F. In other words, simply supported cases showed better blast mitigation effects since the motion of the plates are greater than that of the clamped cases, thus reducing the transmitted impulse and, as a consequence, the effects of the blast. Therefore, SF/SF or S/S/S/S cases are more favoured upon C/C/C/C and C/C/F cases due to their potential blast mitigation. Moreover, the distribution of reaction forces in simply supported cases allows efficient implementation of shock absorbers at the supports. This study selects SF/SF case as the optimum option and hence, used for Chapter 6 and 7 of this thesis.
- The effect of changing the explosive mass or position on reaction forces was then examined. Results revealed that the percentage of increase in reaction forces due to mass change was approximately linear. On the other hand, the increase in stand-off distance from 5 m to 15 m led to a sharp drop of up to 80% in the reaction forces. Then, more flat curve was observed. Changing the position of the centroid of the

explosive material in a plane parallel to the plate under consideration had negligible effect on reaction forces. This was true for far-field explosion scenarios, when the stand-off distance was more than the longest plate side. The results were compared with literature and showed high similarity.

The conclusions made in this chapter have been used for the design of a '*blast absorbing supporting frame*' in chapters 6 and 7 of this thesis, which will increase the absorbing properties of the gate. This in return, may lead to lighter and more operational blast resistant gates.

Virtual Design of the Gate

In this Chapter, the structural response of a steel gate is numerically assessed for a defined site and threat possibilities. The gate performance presented here is based on the gate itself, without any supplementary damping systems. The results are then compared with the performance of the gate equipped with the new proposed passive damper, together with supporting concrete structure (in Chapter 7).

6.1 Site plan and assumptions

The gate is assumed to secure the main entrance of a critical structure; such as embassy, ministry, or hospital; that needs highest level of protection (Grade IV in Table 2.2). In other words, no evacuation is needed and only superficial damage is expected. The building is surrounded by a reinforced concrete perimeter wall of height 4m. The gate is supported by that wall and works as the main access to the premises. Fig. 6.1 shows the explosion source, stand-off distance, gate under consideration, R.C perimeter wall and the building.

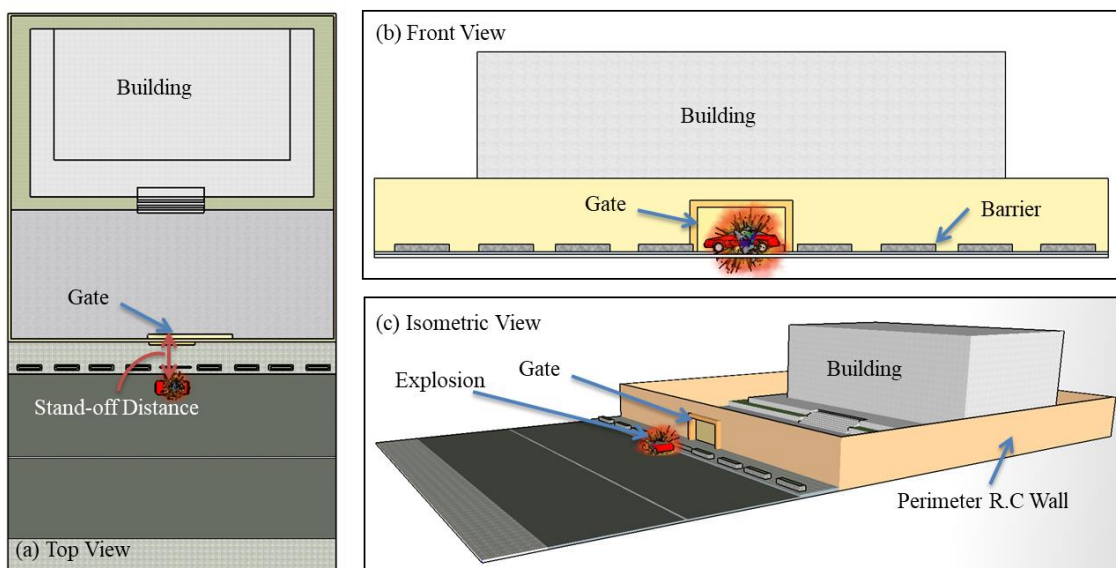


Fig. 6.1: Top (a), front (b) and isometric (c) views of the blast scene

In terms of the gate itself, the blast performance of gate assembly supposed to be in Category II of ASTM F2247-03 (Table 2.3 in this thesis); where the gate stays operable with small permanent deformation. According to UFC, an ‘operable’ door after a blast event can be achieved when door edge rotations do not exceed 2° .

In addition, the following assumptions were made in this study:

- The gate is outside the explosion fireball. In other words, the interaction with the produced gases can be neglected and that there is no afterburning effect. Afterburning (combustion of the detonation products following an explosion) can increase the duration of the positive phase and thus the impulse on near field structure,
- Any initial non-uniformity of the blast wave is ignored and the shock wave assumed to have spherical shape,
- As blast wave propagates in the air, atmospheric pressure is an important factor which varies with the altitude of the location. Therefore, it is assumed here that the blast occurs at sea level,
- The charge was uncased with no additional loading from fragmentation (for more information about fragmentation, refer to Szymczyk, et al. [152] and corresponding patent, P.418079-2017, Ekran przeciwybuchowy/Explosion-proof screen).

6.2 Geometrical and material properties of the gate

The entrance, where the blast resistant gate supposed to be attached, is required to have 2600mm clear height and 4100mm clear width. These dimensions are appropriate for the entry of small to medium-size vehicles in addition to a pedestrian lane on one side. The total dimensions of the sliding steel gate are 3000mm high and 4500mm wide (providing 200mm of bearing surface on the supports and satisfying the clear opening requirement mentioned previously). Based on the results of Chapter 5, SFSF case was selected as the best boundary condition. Hence, the gate was assumed here to be sliding between two gutters, i.e. the longest horizontal sides are simply supported and the shortest vertical sides are free.

The structure of the gate consists of a steel frame welded to front and back steel plates. The frame consists of 10 vertical and 4 horizontal rectangular steel hollow sections of 180x100 mm with c/c spacing of 500mm and 1000mm, respectively. Front, top, side and 3D views of the gate are shown in Fig. 6.2. The rectangular hollow sections assumed to have the same thickness t as the front and back plates. The gate dimensions are

constants while the thickness t is variable. Four different values of t were considered; which are 2.5, 5, 7.5 and 10 mm, giving 4 different gates, abbreviated here as, G2.5, G5, G7.5 and G10, respectively. The performance of the 4 gates is assessed in sections 6.5 and 6.6 of this Chapter.

Weldox 460E steel material has been used for both the plates and the hollow sections due to its high strength and ductility. Material model for Weldox 460E Steel is the same as used in Chapter 5, where Table 5.1 provides material parameters.

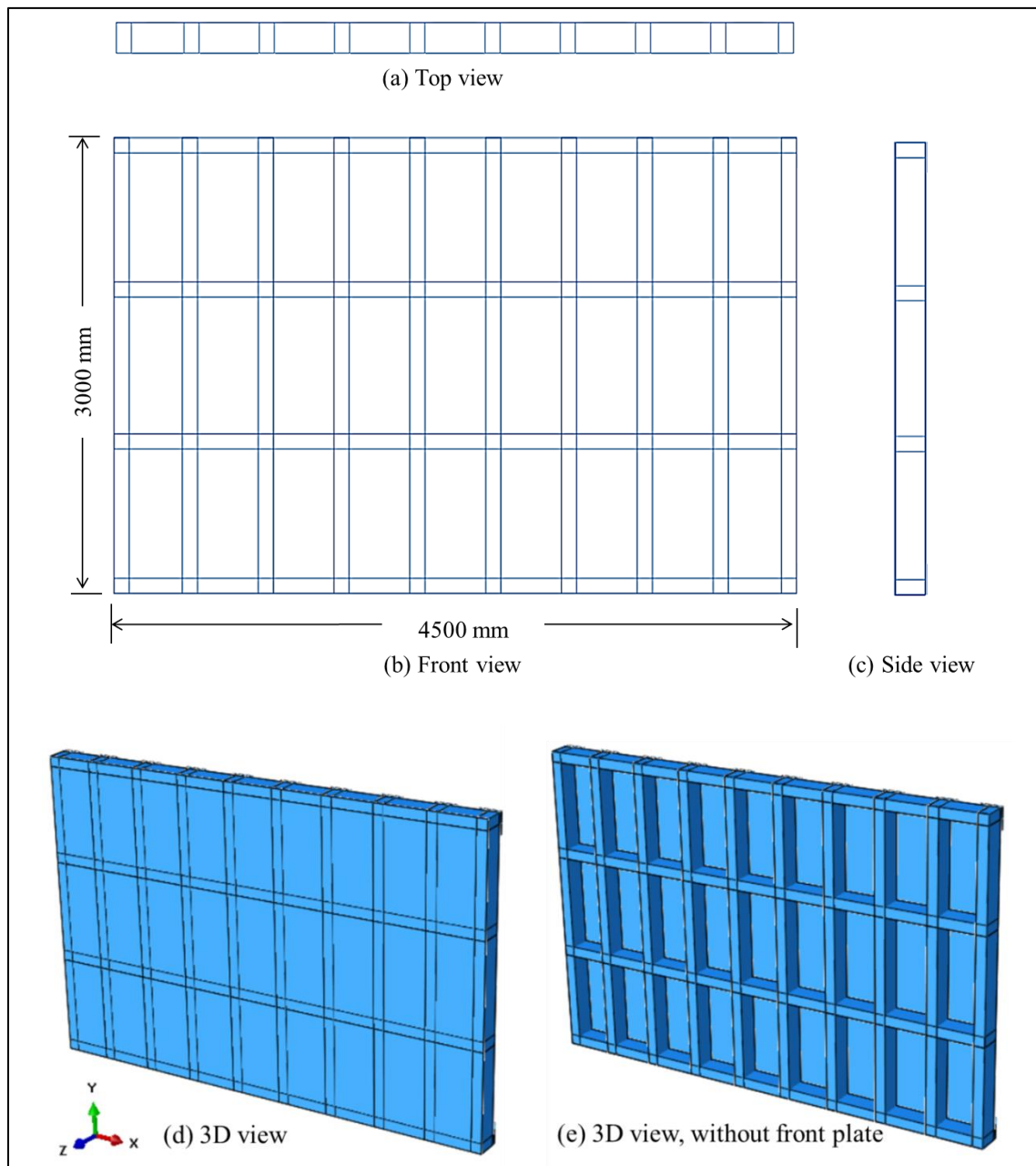


Fig.6.2: Top (a), front (b), side (c) and 3D (d) views of the Steel gate. A 3D view without frontal plate (e) shows the stiffening frame

6.3 Threat assessment and blast loading

Terrorist attacks are made by transporting explosive materials near the target point. As mentioned earlier, the mass of the explosives and stand-off distance are the main two factors to assess. The US Department of Homeland Security, in their FEMA report [164], provide a range for the mass, in TNT equivalency. The range is based on the method of transport, which might be through a luggage, automobile, vans or even truck. The maximum possible carried mass is defined as 100 lb. (45 kg) for a luggage; 450 lb. (204 kg) for a normal sedan car; 4000 lb. (1814 kg) for a van; and 100000 lb. (45359 kg) for a truck. As the sensitive building; described in Section 6.1; is situated in an urban area, trucks should be excluded and prevented from approaching the area. The remaining possibilities are either luggage (45 kg), car (~200 kg) or van (~2000 kg).

As discussed in Chapter 5 (Section 5.4.3), a stand-off distance greater than the target longest dimension, prevents near-field effect. In the current case, the longest side of the gate is 4500mm, is the minimum stand-off distance that can satisfy assumptions made in Section 6.1. The more stand-off distance, the less peak reflected pressure would be on the gate, for a specific TNT mass. Barriers are the usual used mechanisms to achieve a certain stand-off distance. According to literature survey of current blast resistant doors in Section 3.2, it was concluded that the design of a relatively light-weight, 3000x4500mm gate that could sustain 6.6 MPa of pressure is a challenging target in this thesis. Therefore, the 6.6 MPa is set as the criteria required to be met rather than a specific mass or stand-off distance. However, to represent the 6.6 MPa target, a combination of 100kg of TNT at 5m was chosen here as ConWep input parameters. This blast pressure can also be achieved from other M-R combinations, such as 45kg luggage at 3.8m, 200 kg car at 6.2m or 2000kg van at 13.5m. It is important to mention that all the M-R combinations above have the same scaled distance of $Z = 1.07 \text{ m/kg}^{1/3}$, which is more than the minimum scaled distance $0.4 \text{ m/kg}^{1/3}$ required to avoid close-range detonations (as discussed in 5.4.3).

The gates, G2.5, G5, G7.5 and G10, are assessed against 4 levels of blast pressures, 1.65 MPa, 3.3 MPa, 4.95 MPa and the maximum 6.6 MPa, achieved from 25kg, 50kg, 75kg and 100kg of TNT at R=5m, respectively. The levels are useful to evaluate the corresponding variation in reaction forces (Section 6.5.2) and the design of damping

system (Chapter 7) for each specific level. The pressure-time history of the 4 levels is shown in Fig. 6.3, based on ConWep loading on the gate frontal plate.

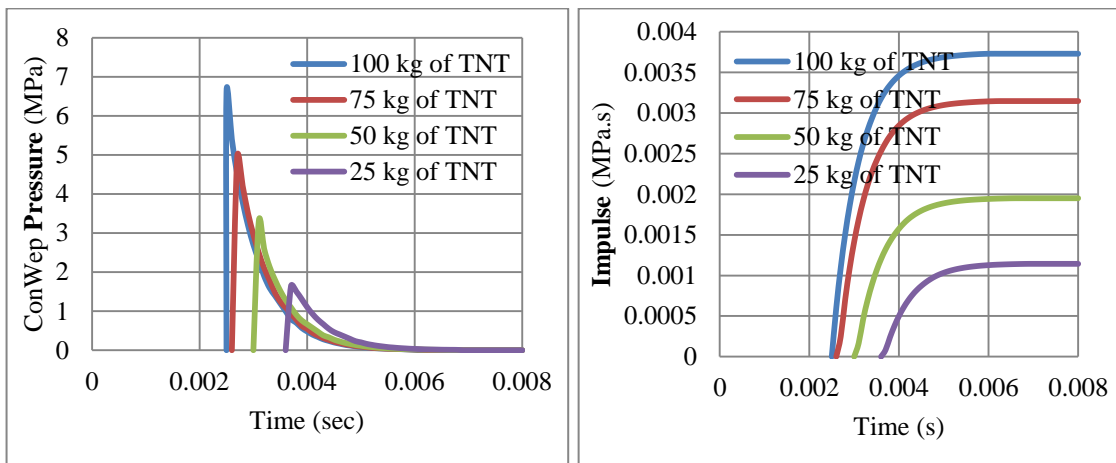


Fig. 6.3: Pressure and Impulse history of the 4 blast levels (25kg, 50kg, 75kg and 100kg, R=5m)

While the stand-off distance was set as 5m, the centroid location of the explosive mass may be located anywhere on a plane parallel and 5m apart from the gate. However, as known, peak reflected blast pressure occurs when the angle of incident is 90° . In other words, points located outside the gate projection have less effect, and hence excluded. In addition, while the gate (and its supports) is symmetric, possible positions can be taken on quarter of the gate and their effect on nearest supports can then be evaluated. Fig. 6.4 below shows 5 highlighted supports S1-S5, and 7 different positions of explosive centroid, denoted as A to G. The effect of those explosive possible locations on reaction forces is covered in Section 6.5.

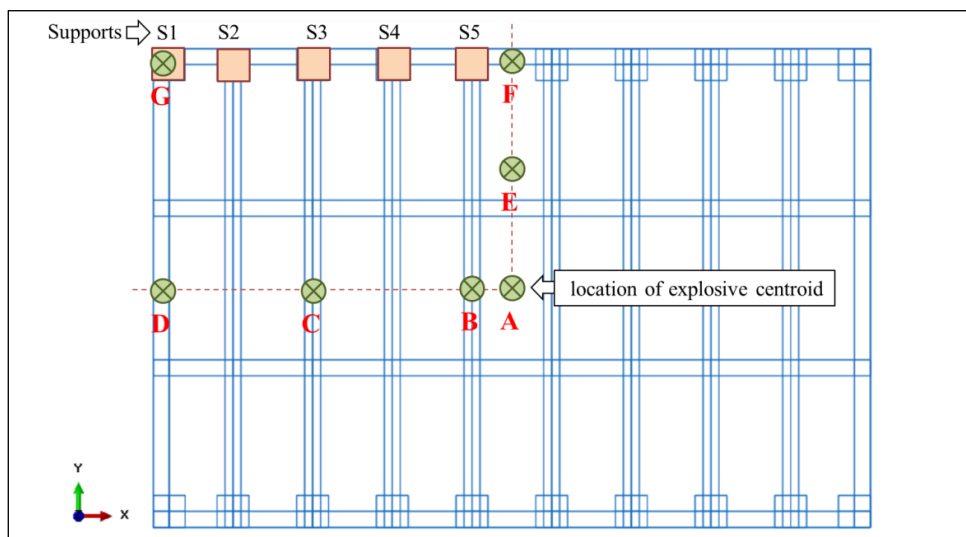


Fig. 6.4: Schematic of explosive centroid effective locations, denoted as A to G, situated on the a gate projection, with M=100kg TNT, R= 5m

6.4 Numerical modelling

The problem under investigation was numerically modelled using Abaqus/CAE and analysed using Abaqus/Explicit solver. The gate (frame and plates) were modelled using 3D deformable shell parts with 5 points of integration along the thickness t . A homogenous isotropic steel section was defined. Material behaviour was modelled as elasto-plastic with J-C strain hardening and damage initiation, Table 5.1, which can occur due to different blast pressure intensities. The 14 rectangular sections of the frame and the 2 plates were assembled so that the length of the gate is parallel to x -axis, the height to y -axis while blast pressure and corresponding deflections follow z -axis, Fig. 6.2 (d). A non-linear dynamic explicit step was used with total time of 0.02s. The “Adiabatic heating effects” was also added to include the effect of heat generated from plastic strains, setting the inelastic heat fraction $\chi = 0.9$.

To represent the welding, the 16 parts were connected using “Tie” constraint. An explicit “general contact” was also defined for the whole model, with tangential and normal behaviour contact property options. For the tangential behaviour, a “penalty” friction formulation was selected with coefficient of friction= 0.3. For the normal behaviour, “hard” contact was chosen. As mentioned earlier in this thesis, to model the blast loading, ConWep was used. As a blast targeting the gate is expected to be near the ground; “surface blast” was chosen rather than the “air blast” option. This is basically to account for reflections from the ground surface; which in return; would produce more pressure on the gate than the “air blast” option.

In terms of boundary conditions (BC), and to replicate the behaviour of the gate in reality, three BC were defined (Fig. 6.5). At time of positive blast pressure, 20 separated square steel plates of 200x200x10mm were placed behind the gate, on top and bottom sides, to hold the gate. The plates are 10mm apart from the gate and coincident with the centre line of frame sections. The 1st boundary condition, BC1 is specified at the centre of those plates as “Pin” constraining only translational DOF, as shown in Fig. 6.5 (a) and (d). BC1 will provide nodal reaction forces that would be easier to interpret and compare. In addition, they will be used as an input for the passive damper parametric study, in Chapter 7. The gate is assumed to be sliding on rollers that would allow it to move in the x - z plane with limited movement in y direction. This is presented by BC2, which limits the movement of the gate in y -axis at initial step. BC2 is applied at bottom

edges of the gate itself. At time of negative blast pressure, the gate is held from re-bounce action by 2 long rigid steel plates (200x4500x10mm), one at the top and one at the bottom, with 10mm gap from the gate, as shown in Fig. 6.5 (b) and (c). BC3 is applied at the centroid of those plates to restrict translational and rotational degrees of freedom.

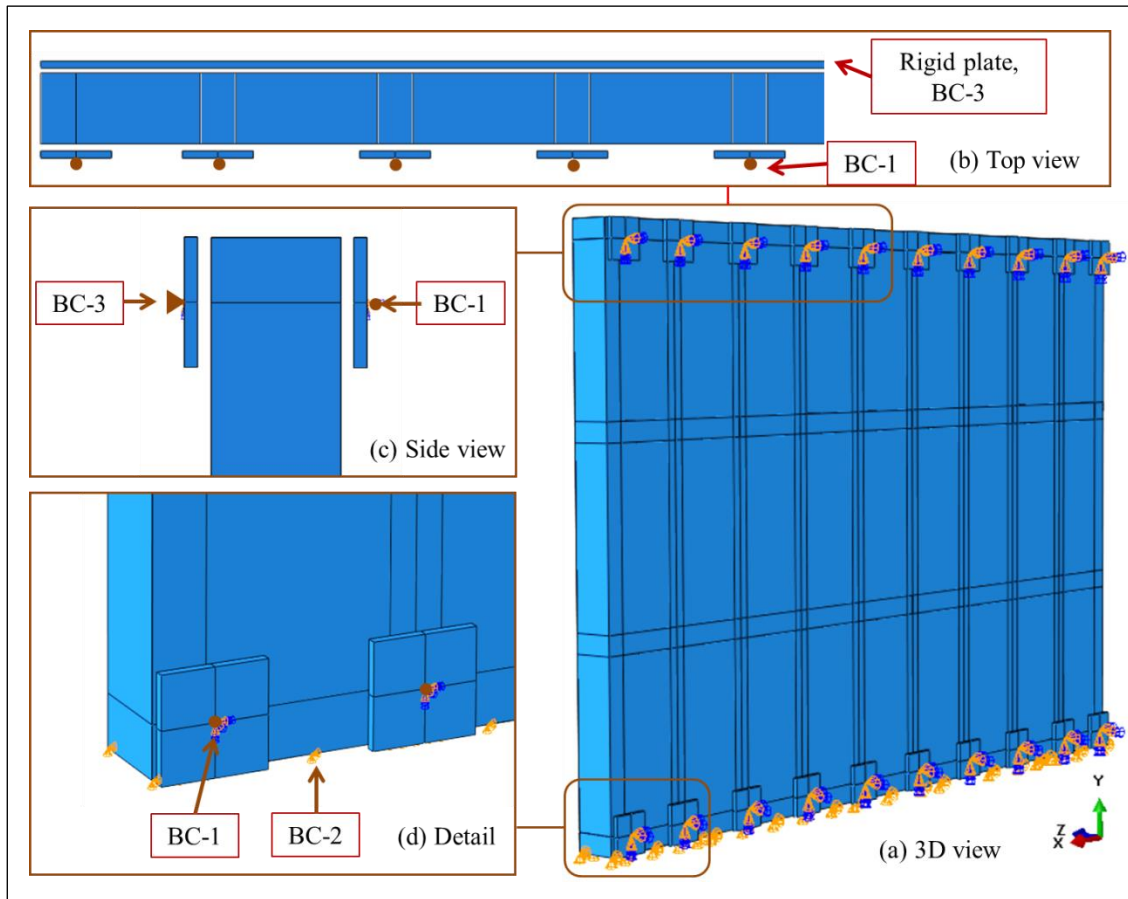


Fig. 6.5: Applied boundary conditions (a) 3D view, (b) top view, (c) side view and (d) detail

The mesh consists of linear S4R element, which is a 4-node doubly curved shell with reduced integration. As known, computational cost is a key factor in numerical simulations and the “less expensive - more accurate” model should be selected at early stages [165, 166]. Therefore, a detailed analysis of mesh size was conducted to validate the numerical model based on plastic dissipation energy of the gate and peak reaction force at middle supports. Mesh size (or finite element size) of the gate parts with ($t=5\text{mm}$) were varied from 5mm, 10mm, 20mm and 50mm. Results revealed that plastic dissipation energy and reaction force for mesh size 5mm and 10mm are nearly coincident with each other, as shown in Fig. 6.6 and Fig. 6.7. However, results for mesh size 20mm is slightly deviated with more error perceived in the 50mm option. So,

the 10mm mesh size was selected for future simulations of the gate, as it is the less expensive and more accurate model.

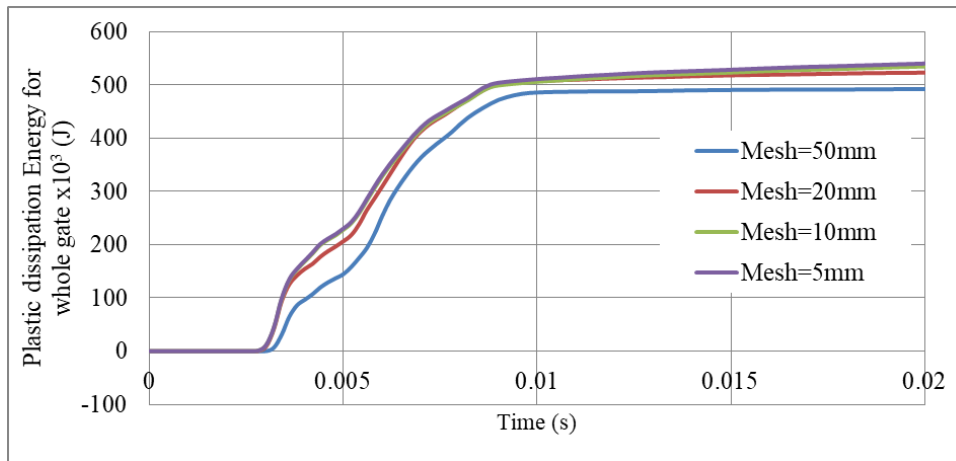


Fig. 6.6: Variation of plastic dissipation energy with mesh size, for Gate G5, M=100kg, R= 5m

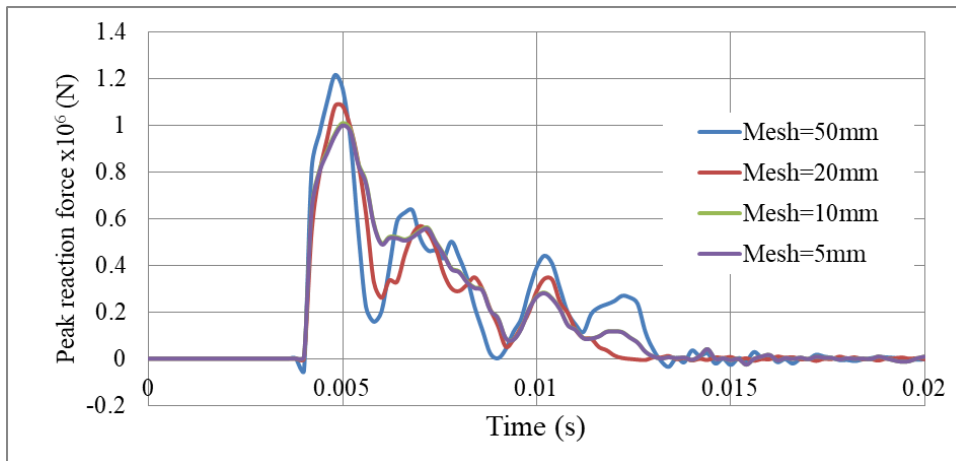


Fig. 6.7: Reaction force variation with mesh size, for Gate G5, support S5, M=100kg, R= 5m

6.5 Peak nodal reaction forces

In this section, the nodal reaction forces at supports S1-S5 (Fig. 6.4) were quantified and the effect of changing the explosive location, blast pressure level and gate mass were studied. As known, the pin support provides 3 components of reaction forces, RF_x , RF_y and RF_z . However, simulations showed that RF_x and RF_y are very small compared to RF_z (Fig. 6.8). Therefore, RF_z is the considered component in this thesis; hereafter denoted as RF ; as it is the prominent one.

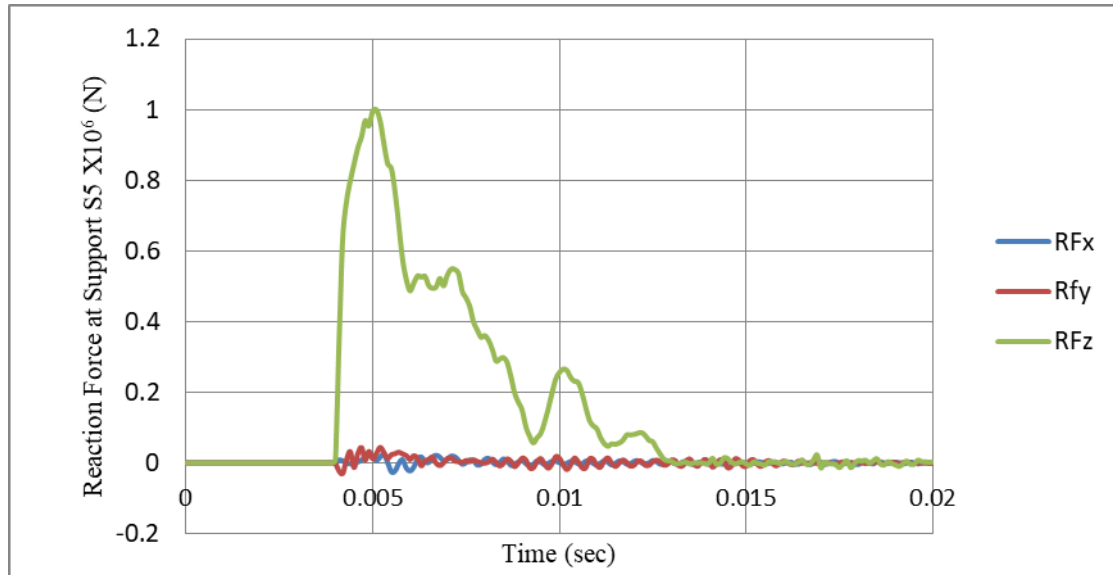


Fig. 6.8: Comparison between Rfx, Rfy and RFz at Support S5, for 100kg of TNT, R=5m, explosive location (A)

6.5.1 Effect of explosive location

The effect of the 7 different positions of explosive centroid; denoted as A to G in Fig. 6.4; on reaction forces, is shown in Fig. 6.9. Location A takes into account the probability when the explosive centroid is exactly coincident with the centre of the gate. Location B, is 250mm deviated horizontally from A, and falls exactly on the frame. Locations D and F are on the middle of the vertical and horizontal sides of the gate, respectively. Locations C and E reflect other possibilities while location G is located on the gate corner. Results in Fig. 6.9 revealed that locations A, B, E and F, had relatively similar reaction forces to each other with peak RF of 1×10^6 N. The reason might be linked to their position around the middle of the gate length, where gate frontal plate is more exposed to the spherical blast shock. On the other hand, peak RF at locations C and D were 5% less, with maximum RF of approximately 0.95×10^6 N. Location G, at the extreme corner, showed to have 10% less values.

It is important to highlight that the values of RF at supports S1-S5 for one possible explosive location, are different with each other. For example, when the explosive location was at location A, B, E or F, peak RF at S5 was 1×10^6 N, while only 0.6×10^6 N can be noticed at S1. In other words, the difference is up to 40%, more than the 10% variation due to explosive location.

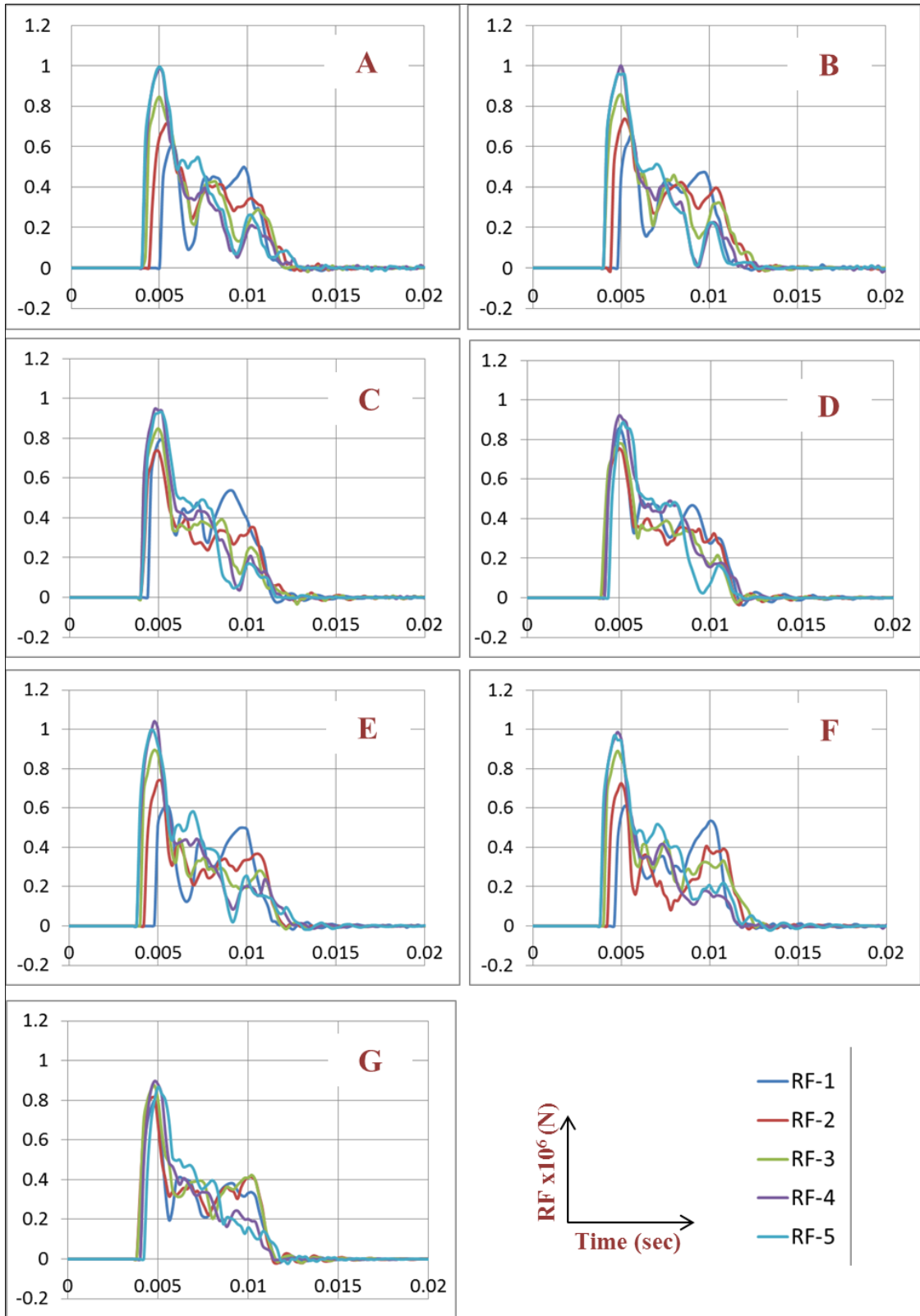
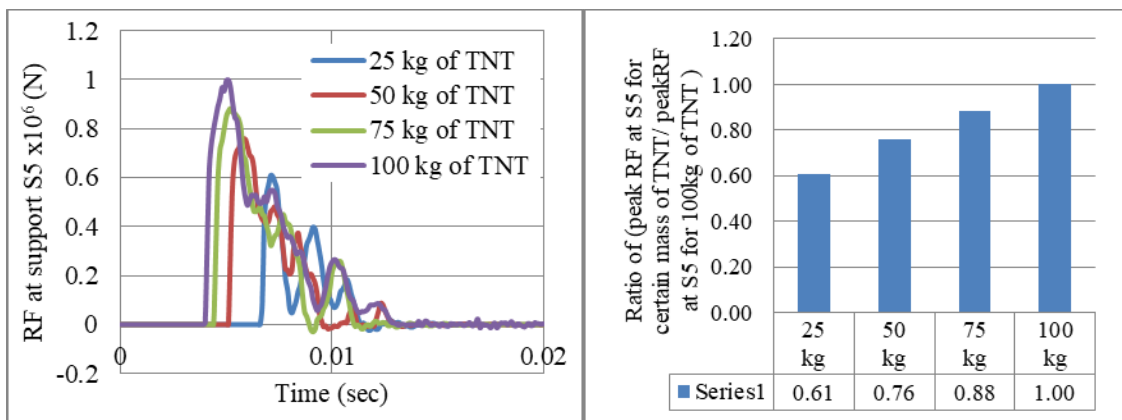


Fig. 6.9: The effect of the position of explosive centroid; denoted as A to G in Fig. 6.4; on reaction forces at supports S1-S5, Gate G5, M=100kg TNT, R=5m.

To sum up, taking different possibilities of explosive location in the analysis of the gate can be omitted, as it had minor effect on RFs. Therefore, location A was selected as the default option in this thesis. In addition, the noticeable difference in the peak RFs (up to 40%) between supports S1-S5 should be taken into consideration in the design of dampers, as will be shown in Chapter 7.

6.5.2 Effect of blast pressure level

As mentioned in Section 6.3, the gate is assessed against 4 levels of blast pressures, 1.65 MPa, 3.3 MPa, 4.95 MPa and the maximum 6.6 MPa, achieved from 25kg, 50kg, 75kg and 100kg of TNT at R=5m, respectively. It's obvious that a passive damper designed for 100kg of TNT would be too stiff if a blast of 50kg of TNT occurs. Hence, the passive damper in Chapter 7 should be designed to absorb reaction forces resulting from different blast levels (TNT mass). Fig. 6.10 (a) shows the reaction force-time history at support S5 for different masses of TNT. The ratio of peak RF for certain mass of TNT by peak RF for 100kg of TNT (RF_m/RF_{100}) is presented in Fig. 6.10 (b). Results show that the quarterly-decreasing mass of TNT did not reduce peak RF in the same pattern. For instance, a reduction from 100kg to 50kg in the mass of TNT led to only 24% fall in the peak RF at the same support ($RF_m/RF_{100} = 76\%$). In other words, the blast level – reaction force relation is not proportional, hence, the design of passive dampers should be conducted for each blast level separately.



(a) RF-time history

(b) RF_m/RF_{100}

Fig. 6.10: Effect of blast pressure level (mass of TNT) on peak RFs

6.5.3 Effect of gate mass

As mentioned in Section 6.2, four different values of t were considered; which were 2.5, 5, 7.5 and 10 mm, giving 4 different gates, abbreviated here as, G2.5, G5, G7.5 and G10, respectively. The performance of the 4 gates with and without passive dampers will be assessed later to find the “lightest” and hence more economical blast resistant gate which would stay operable after a blast event. However, the effect of the mass of the gate on RFs should be first evaluated. The mass of the 4 gates are shown in Table 6.1 ranging from 1.1 ton for the G2.5 to 4.38 tons for G10. Results (Fig. 6.11) showed that when mass was increasing, corresponding reaction forces were slightly increasing except the initial sharp rise of 23% in peak RF between G2.5 and G5. For instance, doubling the mass from 2 to 4 tons (gates G5 to G10) led to slight increase in peak RFs of only 7%. Broadly, the selection from G5, G7.5 or G10, would have slight effect on RFs and hence, the same designed dampers may work for all of them.

Table 6.1: Mass of the 4 gates G2.5, G5, G7.5 and G10

Gate	G2.5	G5	G7.5	G10
Total Mass (ton)	1.10	2.19	3.29	4.38
Mass/Area (kg/m ²)	81.12	162.23	243.35	324.47

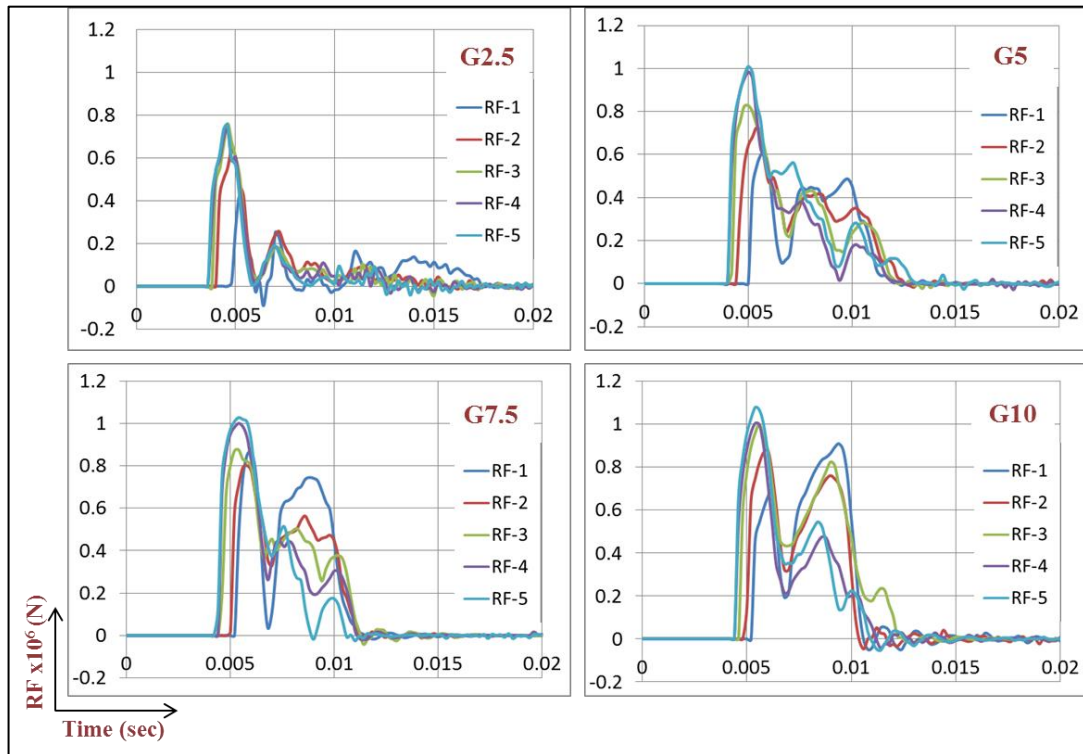


Fig. 6.11: Reaction forces for the 4 gates G2.5, G5, G7.5 and G10, under a blast of 100kg of TNT, R=5m, explosive location A

6.6 Gate performance

The performance of the 4 gates, G2.5, G5, G7.5 and G10, were assessed based on maximum plastic strain, permanent deformation and corresponding operability. The behaviour was addressed for the maximum blast pressure 6.6 MPa (from 100kg of TNT at R=5m). As mentioned in Section 6.1, according to UFC, an ‘operable’ door after a blast event can be achieved when door edge rotations do not exceed 2° . The primary supporting elements in the gate are the vertical rectangular hollow sections. Their deformation affects operability after a blast event. As shown in Fig. 6.13, a 2° rotation of an unsupported length of 750mm leads to a deformation limit $D_{\text{limit}} = 750 \sin 2^\circ = 26.2$ mm. If permanent deformation exceeds that limit, then the gate can be considered as inoperable. As an example, Fig. 6.13 shows the catastrophic failure of gate G2.5.

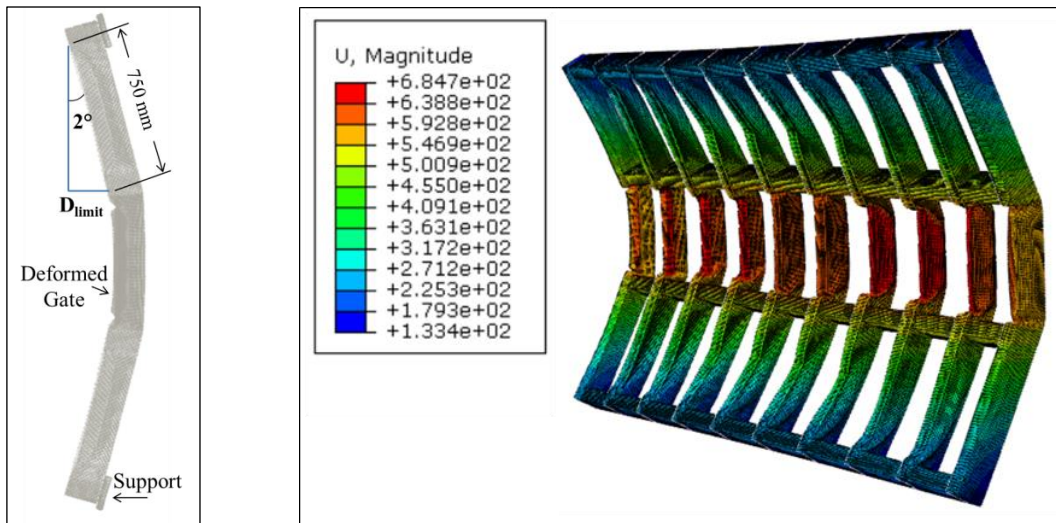


Fig. 6.12: Deformation limit Fig. 6.13: Displacement of G2.5 after 6.6 MPa blast pressure

The detailed results for peak plastic strain (PEEQ) and permanent deformation (d) are listed in Table 6.2, for the frame, front plate and back plate. The term “plastic strain” means the “maximum equivalent plastic strain through plate thickness integration points” while the “peak” considers taking the extreme value in gate component (e.g. frame). Results show that PEEQ and d values were decreasing dramatically with increasing the thickness t . In addition, d values for G2.5, G5 and G10 were more than 26.2 mm (D_{limit}). In other words, G10 was the only gate that can be considered as operable after the blast event, with peak $d_{\text{frame}} = 4.4\text{mm}$. The addition of passive dampers in Chapter 7, may reduce d values for G5 or G7.5 to D_{limit} , i.e. lighter and hence more economical gate may be used (which is one of the objective of this thesis).

- Plastic dissipation energy and strain energy are the main components of internal energy in the gate.
- The plastic dissipation energy found to be decreasing with increasing the thickness t . This is linked to the plastic deformations that are normally less for higher values of t . The plastic dissipation energy was as high as 1200×10^3 J for G2.5, and as low as 90×10^3 J for G10. In other words, light gates provide better energy absorption on the cost of more permanent deformation.
- Strain energy found to be increasing with increasing the thickness t .
- Damage dissipation energy were zero as damage criteria was not met.
- Viscous and creep dissipation energies were also zero.
- Artificial strain energy was very small (up to 2% of the total internal energy) which reflects the accuracy of the numerical model.

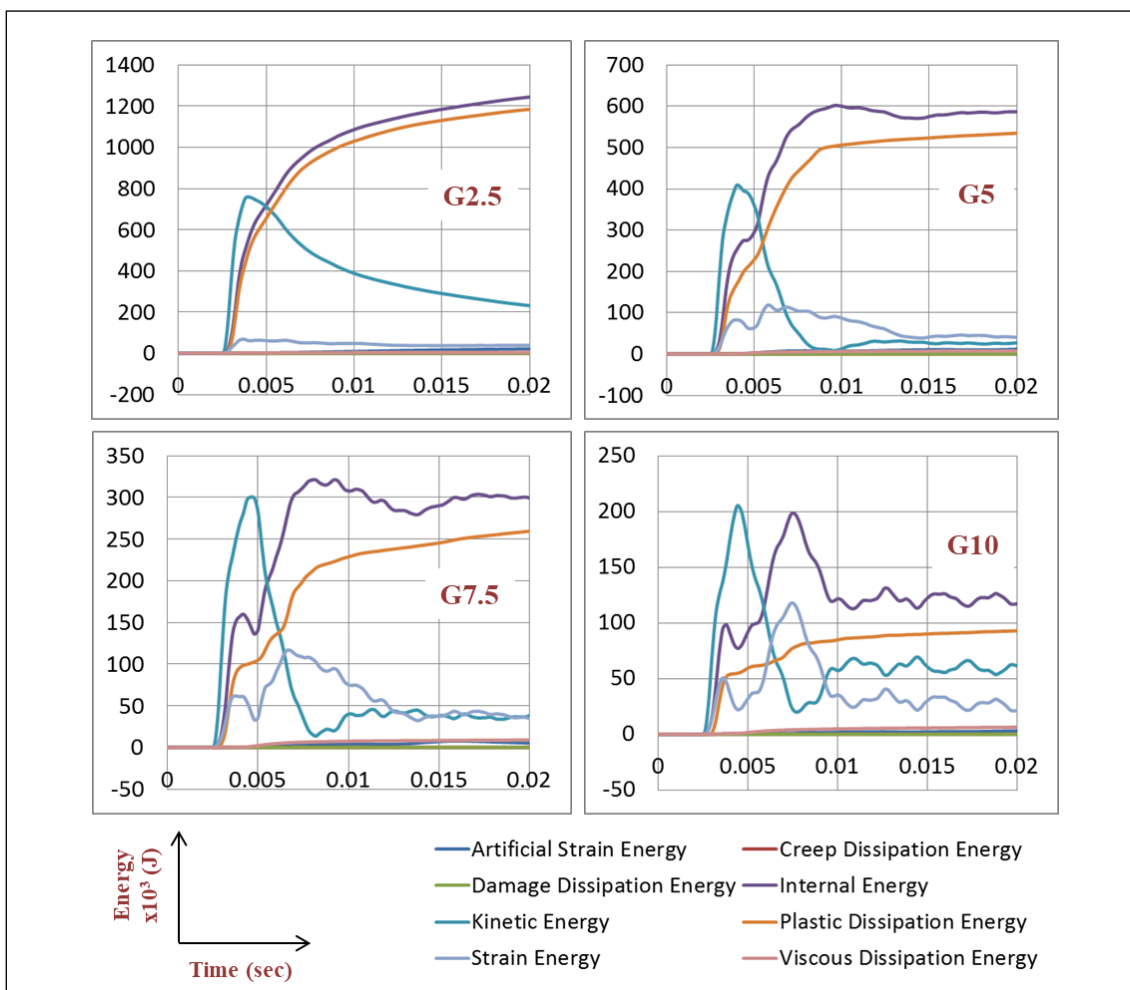


Fig. 6.15: Energy components for the 4 gates G2.5, G5, G7.5 and G10, under a blast of 6.6 MPa (from 100kg of TNT, R=5m, explosive location A)

6.7 Conclusions

The structural response of 4 gates, G2.5, G5, G7.5 and G10, were numerically assessed. Site and threat possibilities were described in addition to geometrical and material properties of the structure. Then, the numerical model was validated based on detailed mesh analysis. The analysis looked at five fields, namely, reaction forces, maximum plastic strain, permanent deformation, operability and energy components. The following points outline main conclusions of this chapter:

- Reaction forces in x and y directions are very small compared to the out-of-plane z -axis (direction of blast). Therefore, RF_z is the considered component in this thesis as it is the prominent one.
- Taking different possibilities of explosive positions located on a gate projection with 5m stand-off distance; had minor effect on RFs of up to 10%. Hence, the possibilities were omitted and the centre of the gate was selected as the default location. This agrees with the results achieved in Chapter 5 (Section 5.4.3).
- The noticeable difference in peak RFs (up to 40%), between supports S1-S5, should be taken into consideration in the design of dampers
- The blast level–reaction force relation is not proportional, hence, the design of passive dampers should be conducted for each blast level separately.
- The dampers that will be designed in Chapter 7 may work for G5, G7.5 or G10 in the same efficiency, as the mass shown to have slight effect on RFs.
- G10 was the only gate that satisfied operability condition after the blast event, with peak $d_{frame} = 4.4mm$. The addition of passive dampers in Chapter 7, may reduce d values for G5 or G7.5 to D_{limit} , i.e. lighter and hence more economical gate may be used (which is one of the objective of this thesis).
- The plastic dissipation energy found to be decreasing with increasing the thickness t . In addition, artificial strain energy was only 2% of the total internal energy which reflects the accuracy of the numerical model.

Results from this chapter were used as comparison benchmarks for Chapter 7, where the response of the gate is assessed with the new proposed damper.

Parametric Design and Application of Uniaxial Graded Auxetic Damper

The aim of this chapter is the design and assessment of a new uniaxial graded auxetic damper (UGAD). First, the geometry, material and numerical model are introduced. Then, a thorough parametric study is conducted to achieve the most efficient graded auxetic system. Moreover, the designed auxetic damper is tested and its static and dynamic constitutive relations are derived and validated analytically. Finally, the performance of the blast resistant gate with the new proposed auxetic damper is covered and comparisons with Chapter 6 are drawn.

7.1 Auxetic damper properties

7.1.1 Geometry and location

The Uniaxial Graded Auxetic Damper (UGAD) proposed in this thesis consists of 4 main components, which are the bearing plate, piston, damper body and the graded auxetic core. The bearing plate is the same as each of the 20 square steel plates which were placed as supports behind the gate in Chapter 6. It has 200x200x10mm dimensions and is the first damper component that receives the impact load of the gate. The bearing plate is pinned to the piston rod that transfers the load to the piston head. The piston is sliding inside the damper body compressing the auxetic core. The core is supposed to be a relatively cheap sacrificial auxetic structure that can be easily changed after a blast event rather than changing the whole gate. The auxetic core main task is absorbing the impact energy and reducing reaction forces on whole system supports. Damper reaction force will be denoted here as (RF_d) to be distinguished from gate reaction forces RF on rigid supports (Chapter 6).

The overall length of the damper is 900mm (uncompressed) and 590mm (fully compressed). The damper body internal chamber has clear dimensions of 210x210x

430mm, where the auxetic core is situated. It is important to mention that the focus in this thesis is on the parametric design of the auxetic core, rather than other components (damper body, piston or bearing plates). Fig. 7.1 shows the geometry of UGAD with dimensions of all its components.

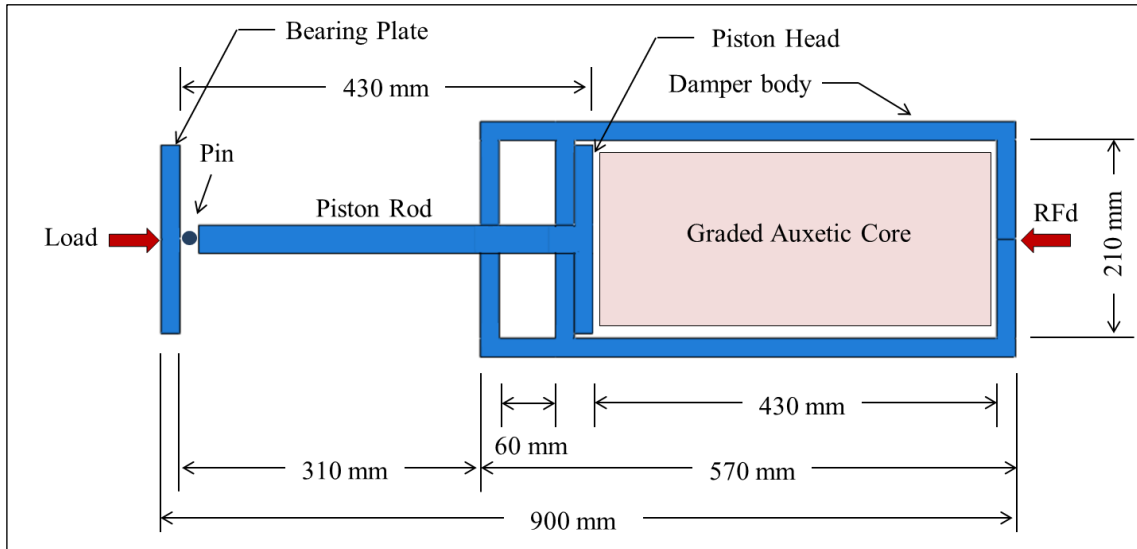


Fig. 7.1: Geometry and components of the Uniaxial Graded Auxetic Damper (UGAD) proposed in this thesis

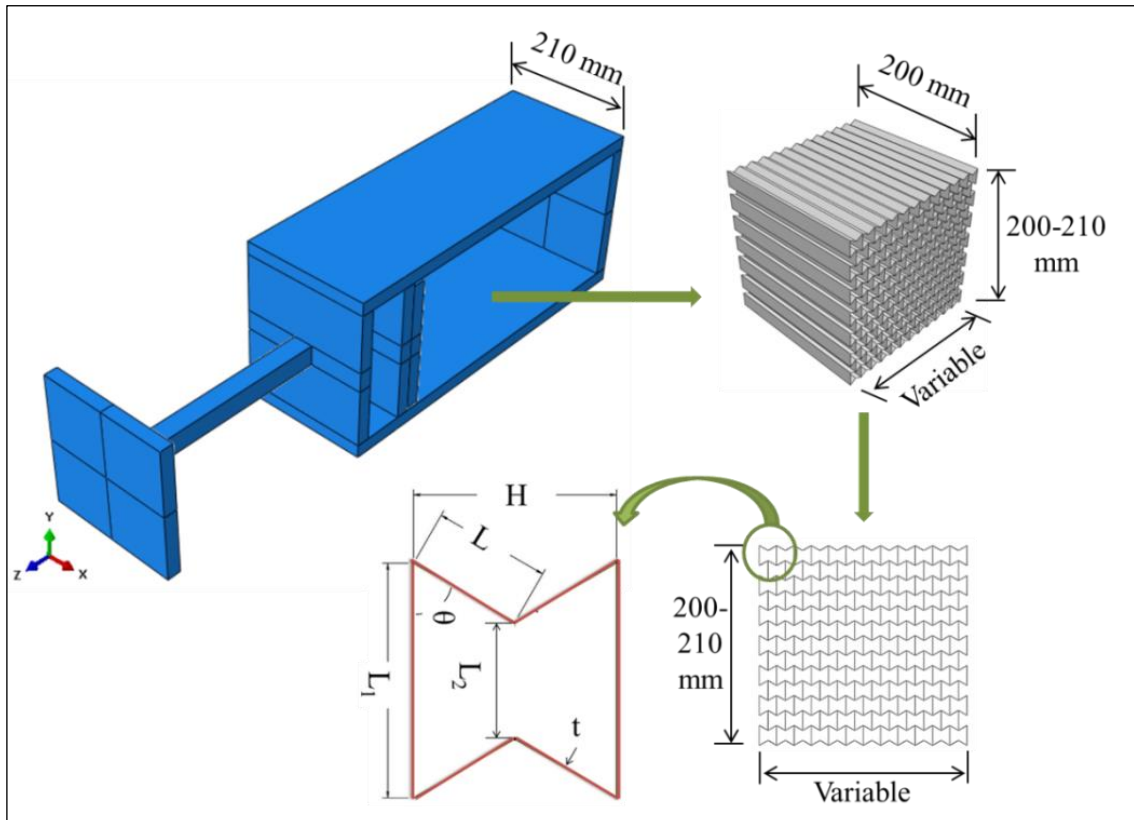


Fig. 7.2: 3D view of UGAD body, auxetic core with its dimensions

Table 7.1: Fixed and variable geometrical parameters of the UGAD auxetic core

Fixed parameters	Variable parameters
UGAD chamber internal space dimensions: 210x210x430mm	Cell dimensions L_1, L_2, L and H while $L_1=2 L$
Auxetic core extrusion depth = 200mm	cell wall thickness t
Auxetic core height = 200-210 mm	cell angle
Cell wall aspect ratio = $t/L = 0.10, 0.15, 0.20$	number of layers

In terms of the auxetic core, Table 7.1 lists fixed and variable geometrical parameters of auxetic core. The extrusion depth and height of the core are specified while the length is variable. Based on the parametric study conducted in Section 7.2, optimum cell dimensions, cell angle, number of layers and material were selected. The final selection of auxetic core thickness t , in Section 7.3, were based on each blast level. Fig. 7.2 shows 3D view of damper components and auxetic core with its parameters.

The front, rear and side views of the gate system are illustrated in Fig. 7.3. The steel gate, 20 UGADs, shear walls and a movable cover plate are the main components of the system. When the gate is closed (Fig. 7.3 A and C), the high strength steel cover plate is lifted at 45 angle allowing the gate to slide into the gutter and protects the gate from unexpected vehicles' crash. When the gate is opened (Fig. 7.3 B and D), the plate works as a bridge covering the compressible length of the UGADs. The side views (Fig. 7.3 E and F), shows the attachments of the 20 UGADs and the supporting RC shear walls.

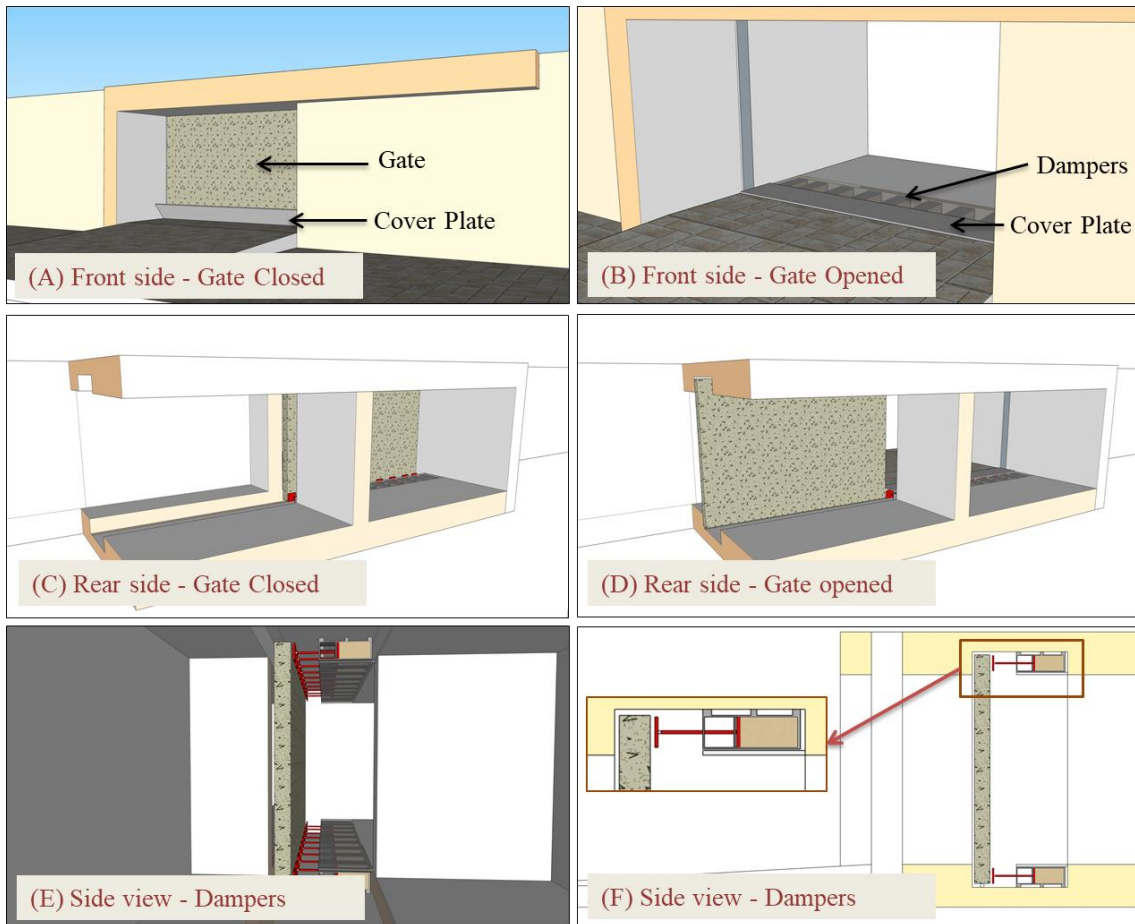


Fig. 7.3: Front, rear and side views the gate system, showing the gate, the placement of 20 UGADs, shear walls and movable cover plate.

7.1.2 Material of the auxetic core

To account for the material grade effect on the behaviour of the auxetic core under high strain rates, three different aluminium grades were selected (Table 7.2). The first one was the high strength grade AL7075-T6 (denoted here as AL1). It has a yield point of 546 MPa and used in aerospace and defence applications. The second one was the 324 MPa medium strength AL6061-T6 grade (denoted here as AL2), which is used for general structural applications. The third and the last one was the low strength grade AL6063-T4 (denoted here as AL3). This type is relatively cheaper and more available than other grades. It is widely used in manufacturing doors, windows and furniture.

Table 7.2: The three aluminium grades used for the auxetic core and their applications

Symbol	AL Grade	Strength	Yield Point (MPa)	Applications
AL 1	7075-T6	High	546	Aerospace and defence
AL 2	6061-T6	Medium	324	General Structural Applications
AL 3	6063-T4	Low	90	Door, windows, furniture

Johnson-Cook model (described in Chapter 5, Section 5.2.3) was used as the material model for the auxetic cores. The material parameters are listed in Table 7.3 for each aluminium grade. Based on Hook's Law for elastic range, Eq. (5.1) for plastic range and Eq. (5.4) for damage initiation point, the stress-strain curves of the 3 grades were drawn, for different strain rates (Fig. 7.4). In addition, assuming $\hat{T} = 0$ ($T < T_0$), $\frac{p}{q} = \frac{1}{3}$ for 1D bar strain, and substituting different values of strain rate $\dot{\epsilon}$ and plastic strain ϵ , the corresponding stress and strain at failure were achieved.

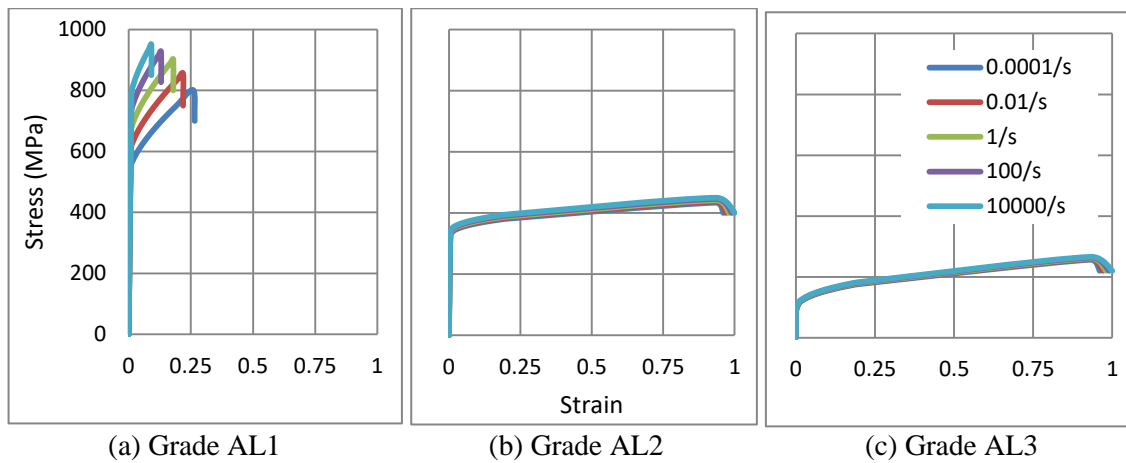


Fig. 7.4: Stress-Strain relationship for the 3 aluminium grades, at different strain rates

According to the Stress-Strain relationship for the 3 aluminium grades (Fig. 7.4), AL1 can be considered as a high strength-low ductility grade that is more rate sensitive. In contrast, the other two grades show lower strength, high ductility and less rate dependency. The parametric study in Section 7.2.3 was dedicated for the grade used and its influence on energy absorption and reaction forces.

Table 7.3: Material parameters of the 3 aluminium grades used in UGAD auxetic core

Constant	Description	Unit	AL7075-T6 [167]	AL6061-T6 [152]	AL6063-T4 [168]
E	Modulus of Elasticity	MPa	$71.7 \cdot 10^3$	$69 \cdot 10^3$	$68.9 \cdot 10^3$
ν	Poisson's ratio	-	0.33	0.33	0.33
ρ	Mass density	t/mm ³	$2.81 \cdot 10^{-9}$	$2.703 \cdot 10^{-9}$	$2.703 \cdot 10^{-9}$
A	Yield Strength	MPa	546	324	89.6
B	Ultimate Strength	MPa	678	113	172
n	work-hardening exponent	-	0.71	0.42	0.42
$\dot{\epsilon}_0$	Reference Strain rate	S ⁻¹	$1 \cdot 10^{-4}$	$1 \cdot 10^{-4}$	$1 \cdot 10^{-4}$
C	strain rate factor	-	0.024	0.002	0.002
D_c	Critical Damage	-	0.3	0.3	0.3
p_d	Damage threshold	-	0	0	0
C_p	Specific heat	mm ² .K /S ²	$960 \cdot 10^6$	$910 \cdot 10^6$	$910 \cdot 10^6$
χ	Taylor Quinney empirical constant/inelastic heat fraction	-	0.9	0.9	0.9
T_m	Melting Temperature	K	750	925	616
T_0	Room Temperature	K	293	293.2	293.2
m	thermal-softening exponent	-	1.56	1.34	1.34
d_1	-	-	-0.068	-0.77	-0.77
d_2	-	-	0.451	1.45	1.45
d_3	-	-	-0.952	0.47	0.47
d_4	-	-	-0.036	0.00314	0.00314
d_5	-	-	0.697	1.6	1.6

7.1.3 Numerical Model

As mentioned in Section 7.1.1, optimizing the bearing plate, piston and damper body are out of the scope of this thesis. Therefore, they were modelled as 3D parts with rigid body constraints applied to each one of them separately. Boundary conditions and loading were applied to their reference points (RP) as shown in Fig. 7.5. They were meshed using linear C3D8R element type (an 8 node linear brick, reduced integration) with mesh size of 10mm.

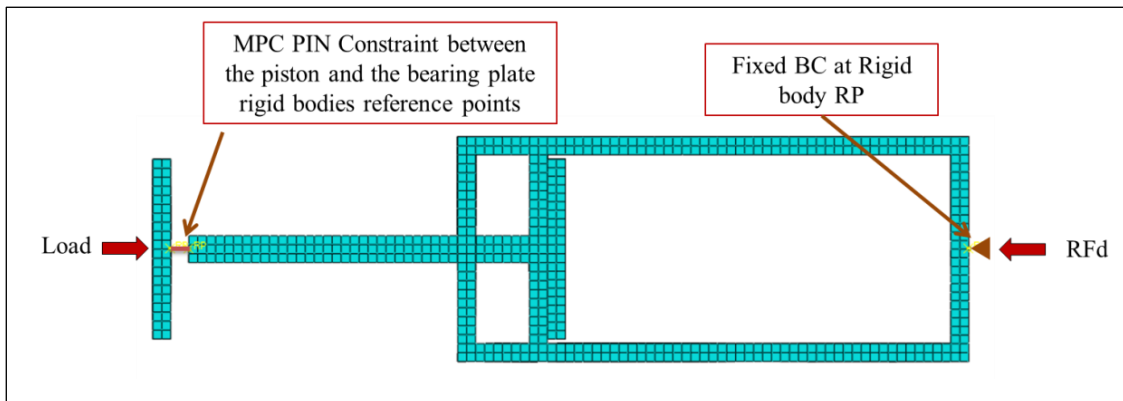


Fig. 7.5: BCs and constraints of the bearing plate, piston and damper body

In terms of the auxetic core, mesh element type was linear S4R, which is a 4-node doubly curved shell with reduced integration. A detailed mesh analysis was conducted to find the more accurate-less expensive element size. The analysis was for certain auxetic core parameters and loading condition with changing the size of the mesh (denoted here as SM). Results are presented in Fig. 7.6 based on SM/L ratios (cf. Fig. 7.2).

It was found that the more accurate-less expensive element size was when $SM/L = 0.25$ (i.e. when the mesh size is quarter the cell wall length L). Additional analysis for the mesh size in the extrusion direction found to have no effect on results, as the auxetic core is uniform in the extrusion direction. Hence it was set equal to the value of L.

As geometry, material, loading and boundary conditions of the gate system are symmetric, quarter the system was modelled. This reduces the number of UGADs analysed from 20 to 5, and hence the computational cost. Fig. 7.7 shows quarter of the gate, the 5 corresponding UGADs and affected degrees of freedom due to symmetry. The numerical model of the gate itself was discussed and checked in Chapter 6.

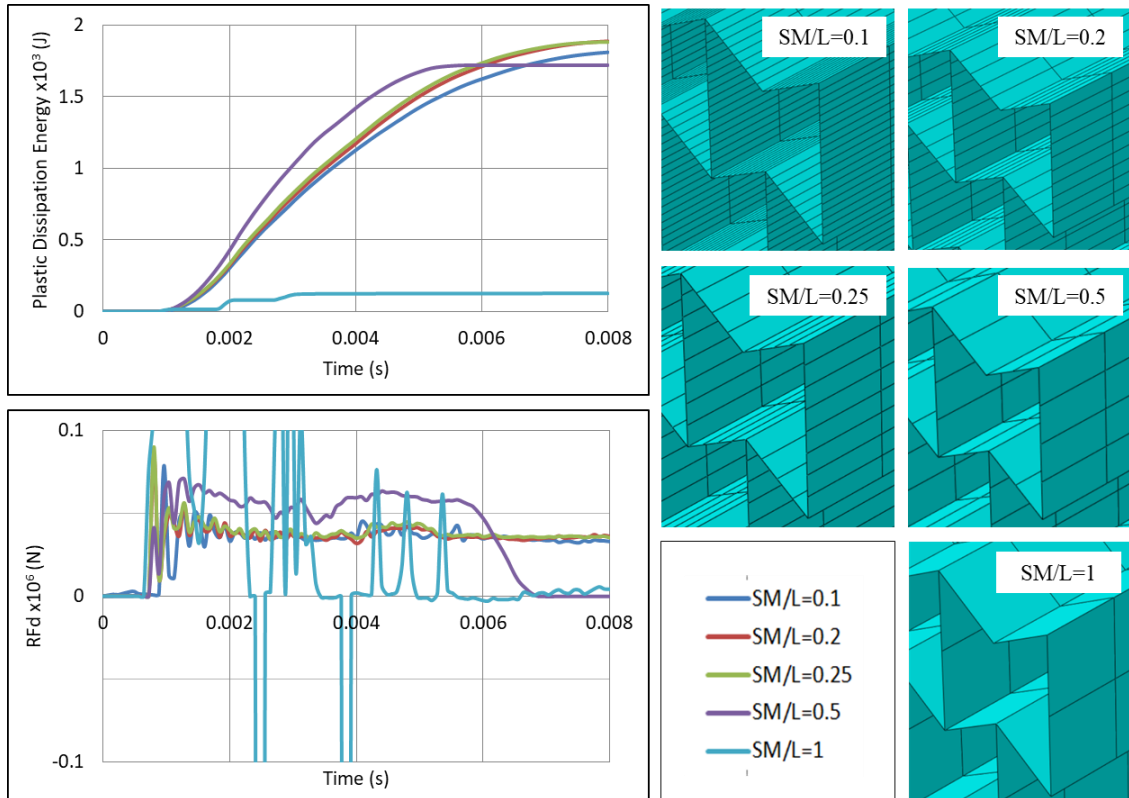


Fig. 7.6: Finding the most accurate-less expensive auxetic core model (different SM/L ratios), based on comparing plastic dissipation energy (PDE) and reaction force (RFd), for an auxetic core of $L=10\text{mm}$, $t=1\text{mm}$, S4R elements, AL3 aluminium, pulse load of $0.5 \times 10^6 \text{ N}$ in 0.002s

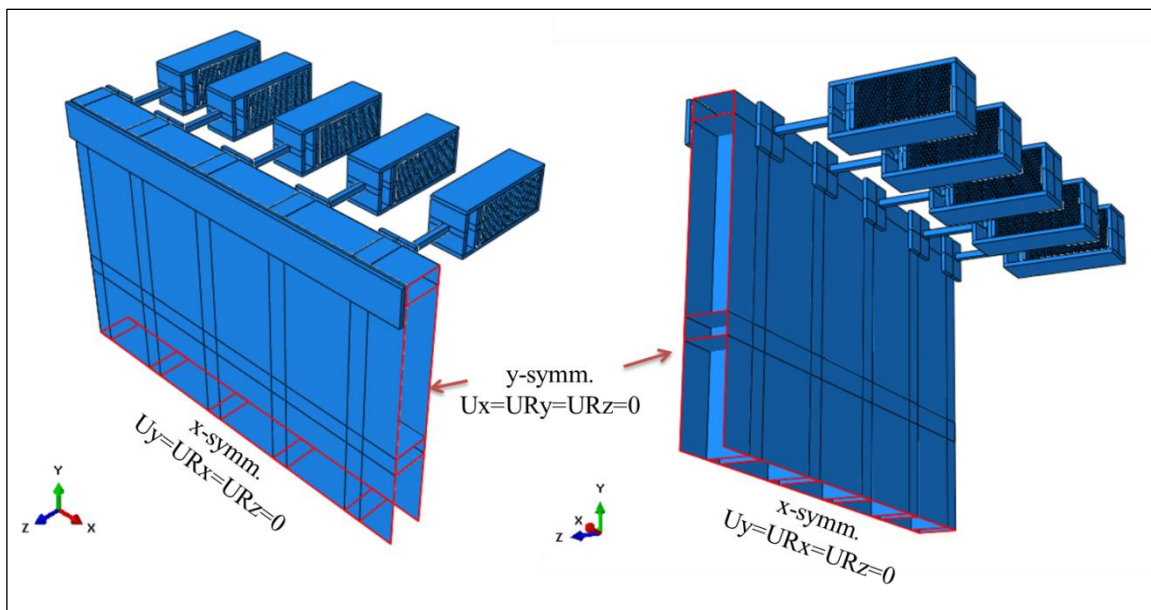


Fig. 7.7: Numerical model of quarter of the system showing the symmetry about x and y

7.2 Parametric study of the auxetic core

In this section, a thorough parametric study is conducted to achieve an efficient auxetic core for the gate system under investigation. The study first takes into account the loading direction on the auxetic core. Then, optimum cell dimensions, material grades and cell angles, are checked. Moreover, a comparison with non-auxetic honeycomb topology is made. Lastly, the effect of changing number of layers of the auxetic core is also covered. The study is based on changing one variable (from the mentioned above) at a time, and keeping other parameters fixed, as conducted by Imbalzano, et al. [94] and Liu, et al. [117].

As this section is related to geometrical/material parametric study, loading had to be kept the same to validate the comparisons. A pulse 'P' of 0.5×10^6 N at 0.002s was applied on the UGAD. The loading rate was selected based on the RF perceived in Chapter 6 that had the same loading rate. The controlled parameters were the ratio of reaction force to applied load (RFd/P) and plastic dissipation energy (PDE). As known, solid bodies transmit applied loads directly to supports, leading to reaction forces equal to the applied load. However, auxetic structures supposed to absorb the shock, leading to less reaction forces at the back. Therefore, the ratio RFd/P, monitored in this section, highlights the reduction in reaction force which auxetic core may do. Results are validated and compared with the reviewed literature in Section 3.3.

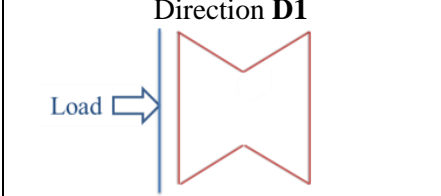
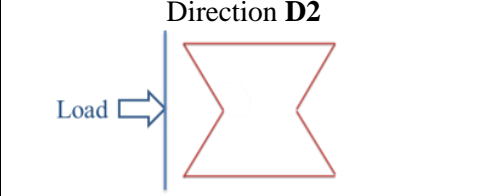
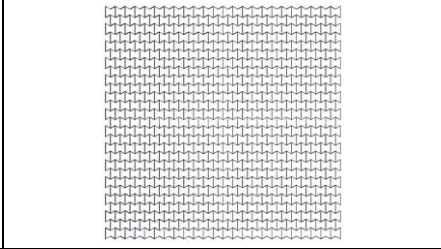
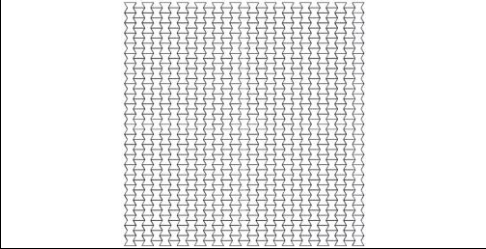
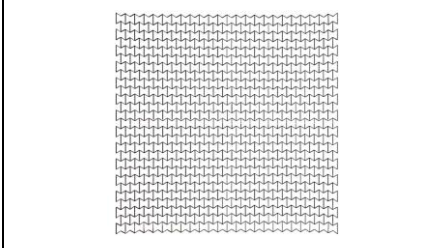
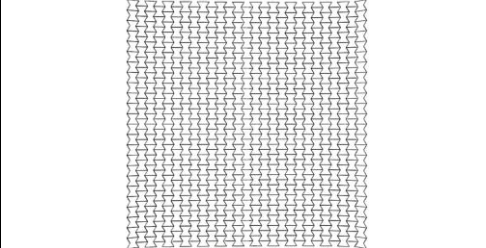
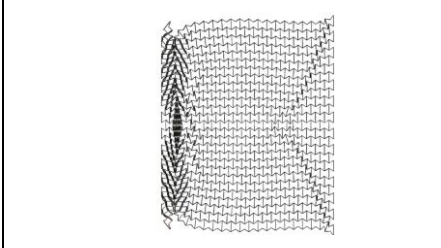
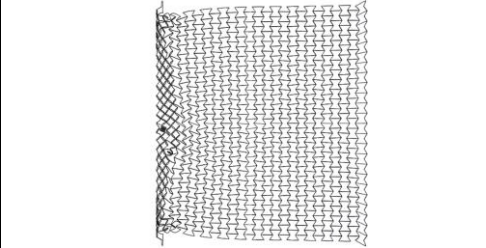
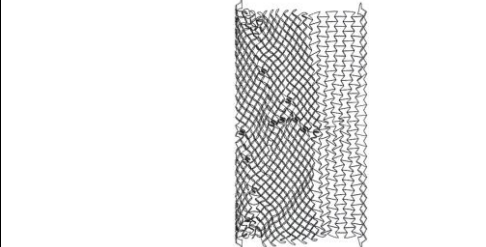
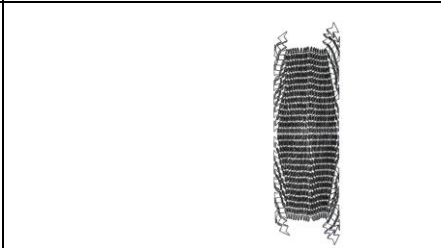
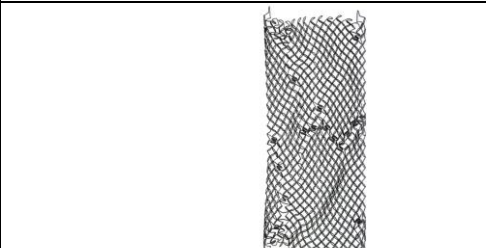
7.2.1 Loading direction

As re-entrant auxetics have anisotropic properties, its important at first to check the direction at which the auxetic core should be loaded to achieve more PDE and less RFd. Two auxetic cores with ($t=0.75\text{mm}$, $L=5\text{mm}$, $t/L=0.15$, $\theta=60^\circ$, AL2 grade) were loaded in two different directions, namely here, D1 and D2. Table 7.4 shows the collapse and deformation modes from time 0-0.004 s for the two loading configurations.

In terms of loading direction D1 (Table 7.4), initial localization bands occurs at the proximal (loaded) and distal (supported) ends that spreads quickly over the whole section. In addition, cells near the horizontal symmetry axis are compressed while those near the free boundaries are in tension state. This leads to transverse shrink or auxetic

behaviour. At final time step, 0.004s, the core is fully collapsed with compressed length to total length ratio of 75% (Fig. 7.8).

Table 7.4: Loading directions D1 and D2 and their effect on the collapse mode and deformation of an auxetic core ($t=0.75\text{mm}$, $L=5\text{mm}$, $t/L=0.15$, $\theta=60^\circ$, AL2 grade)

Time (s)	Direction D1 	Direction D2 
0		
0.001		
0.002		
0.003		
0.004		

In contrast, loading direction D2 shows a local deformation at proximal (loaded) end of the core, which propagates forward layer by layer to the distal (supported) end. Negligible necking or transverse shrink can be observed. The non-auxetic behaviour of D2 for this high loading rate agrees with the findings of Zhang, et al. [105]. At final time step, 0.004s, the core is not fully collapsed with compressed length to total length ratio of 60% (Fig. 7.8).

It is evident from Fig. 7.9 that the plastic dissipation energy PDE with respect to time of direction D1 is higher than that of D2. This can be justified to the auxetic effect that leads to more energy absorption [9]. In terms of reaction force (Fig. 7.10), D1 showed better performance with less RFd/P ratio, except for the final collapse reaction. The full collapse in D1 should be avoided through optimizing the geometrical parameters of the auxetic core (as will be shown in next sections). In short, the auxetic core would be situated in the UGAD and loaded as in direction D1 due to its better performance.

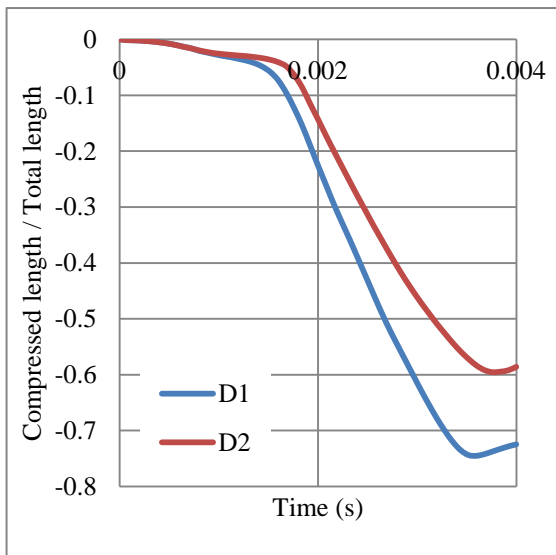


Fig. 7.8: Ratio of compressed length to total length per time, for an auxetic core loaded in two different directions D1 and D2 ($t=0.75\text{mm}$, $L=5\text{mm}$, $t/L=0.15$, $\theta=60^\circ$, AL2 grade)

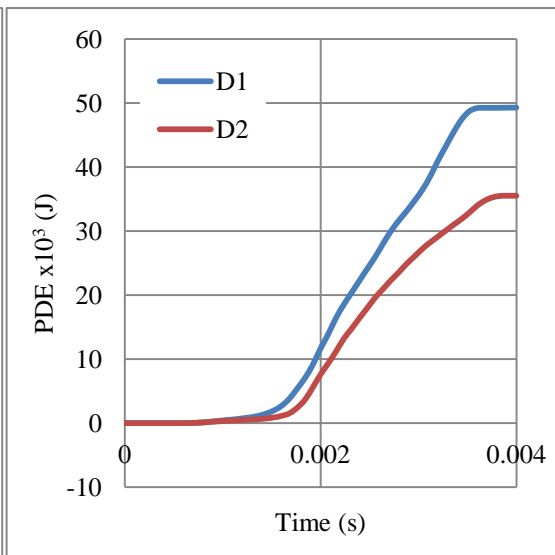


Fig. 7.9: Plastic dissipation energy PDE with respect to time, for an auxetic core loaded in two different directions D1 and D2 ($t=0.75\text{mm}$, $L=5\text{mm}$, $t/L=0.15$, $\theta=60^\circ$, AL2 grade)

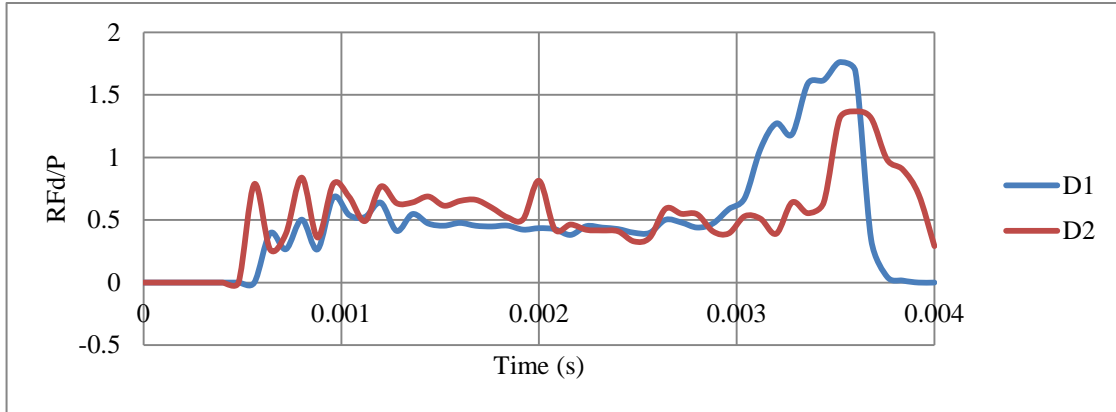
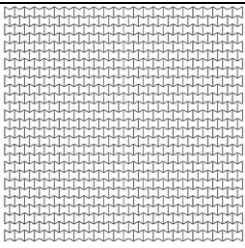
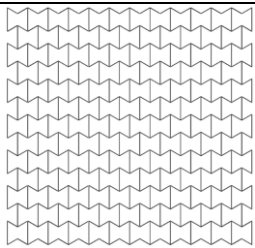
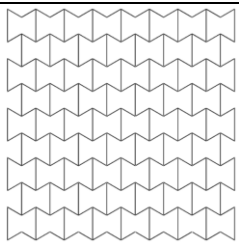


Fig. 7.10: Ratio of RFd/P with respect to time, for an auxetic core loaded in two different directions D1 and D2, ($t=0.75\text{mm}$, $L=5\text{mm}$, $t/L=0.15$, $\theta=60^\circ$, AL2 grade)

7.2.2 Cell dimension

Manufacturing an auxetic core with small cells is more difficult and requires precise technology compared to a core with larger cell dimensions. However, smaller cells may lead to more plastic hinges and hence more PDE. Therefore, three different auxetic cores with 3 different cell dimensions were tested. According to Fig. 7.2, that shows the auxetic cell with its parameters, it is evident that L and θ are the controlling factors of cell dimension (as $L_1=2L$, and L_2 relates to θ). The cell dimensions were varied here based on changing the value of L while keeping θ constant at 60° . Table 7.5 shows the 3 auxetic cores (denoted here as A, B and C) with 3 different cell dimensions and their properties. It was crucial to also change wall thickness t to achieve the same t/L ratio, here fixed at 0.2.

Table 7.5: Auxetic cores with 3 different cell dimensions and their properties

	A	B	C
Shape			
L	5	10	15
t	1	2	3
Total Length	208	208	208
Total height	205	200	210
No. of layers	24x27	12x13	8x9
Mass (kg)	7.212	7.158	7.639
Fixed factors	$\theta = 60^\circ$, $t/L=0.2$, Extrusion depth=200mm, pulse load 500000N in 0.002s		

As the mass of the 3 auxetic cores were different, the PDE was divided by the mass to normalise the results. Fig. 7.11 shows ratio of PDE/Mass with respect to time, for the 3 different cell dimensions A, B and C. It is clear that auxetic core B (with $L=10\text{mm}$) has the best PDE among others.

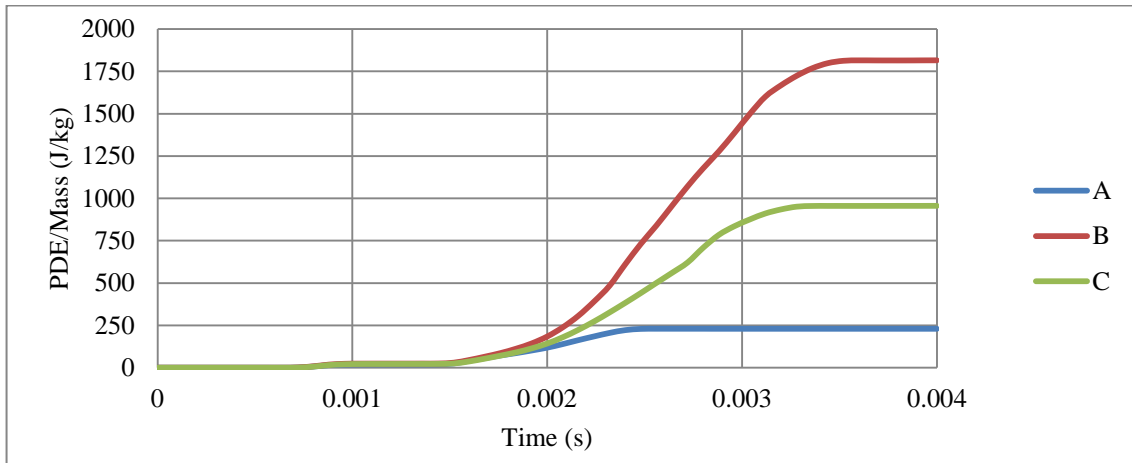


Fig. 7.11: Ratio of PDE/Mass with respect to time, for 3 different cell dimensions A, B and C with $\theta = 60^\circ$, $t/L=0.2$, subjected to same loading conditions.

In terms of reaction force, Fig. 7.12 shows RFd/P–time history for 3 different cell dimensions A, B and C, while Fig. 7.13 highlights the peak values of RFd/P. It can be noticed that cell dimension B had the least RFd/P, leading to less reaction force, and hence stress, on the back of the damper. So cell size B, with $L=10\text{mm}$, was the selected dimension for following sections.

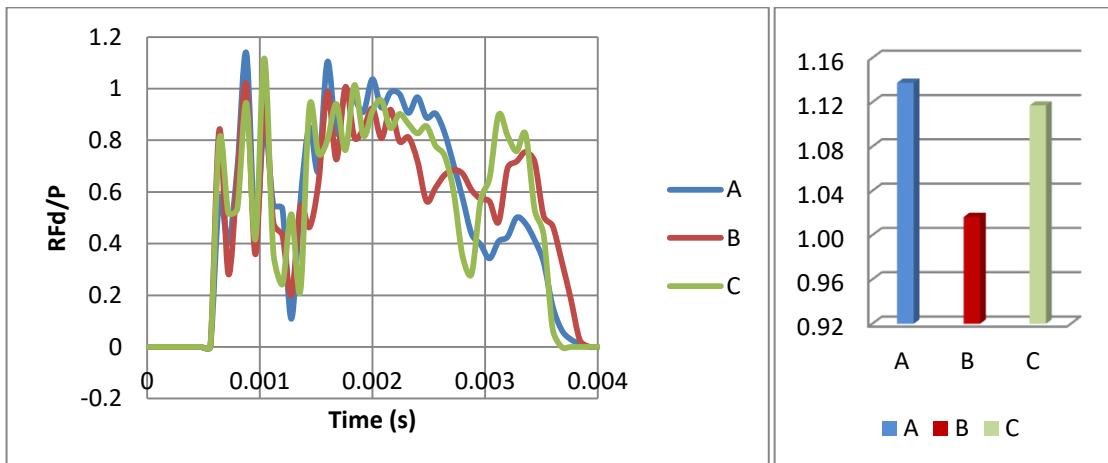


Fig. 7.12: RFd/P–time history, for 3 different cell dimensions A, B and C with $\theta = 60^\circ$, $t/L=0.2$, subjected to same loading conditions

Fig. 7.13: Peak value of RFd/P, for the 3 cell dimensions A, B and C

7.2.3 Aluminium grade

The parametric study in this section is dedicated for finding the influence of the used aluminium grade on energy absorption and reaction forces. Three aluminium grades (AL1, AL2 and AL3) were selected and described in Section 7.1.2 of this Chapter. Three auxetic cores were tested having three different grades and same geometrical parameters ($L=10\text{mm}$, $t=2\text{mm}$, $t/L=0.2$, $\theta=60^\circ$) and loading condition. As the grades have different densities, and hence different mass of auxetic sections, the PDE were also normalized based the mass. This was to validate the comparison based on the energy dissipated per each kg of material.

Results (Fig. 7.14 and Fig. 7.15) show that the weaker and more ductile the aluminium grade, the better is the performance, in terms of PDE and RFd/P. For example, the energy dissipated by an auxetic core made by AL3 is 9 times higher than AL2. Moreover, no energy dissipation noticed for AL1 as the latest is high strength aluminium. The use of relatively weak grade, such as AL3 with yield point of 90 MPa, allows more deformation in the core and greater energy absorption. In return, RFd/P for AL3 was also less than that for AL1. Therefore, aluminium grade AL3 (6063-T4) was selected for the UGAD due to its overall performance, low cost and high availability.

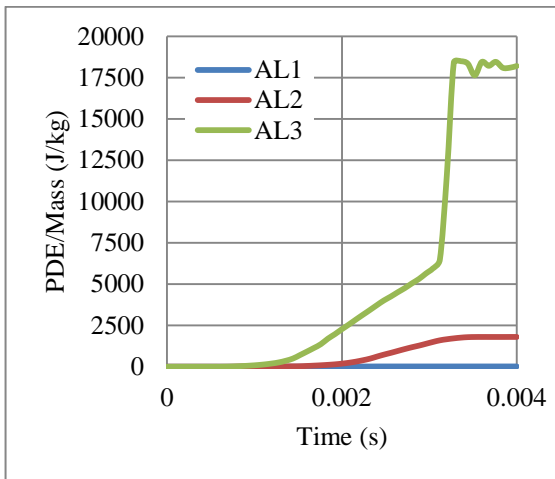


Fig. 7.14: Ratio of PDE/Mass with respect to time, for 3 different Aluminium grades AL1, AL2 and AL3, of an auxetic core with $L=10\text{mm}$, $t=2\text{mm}$, $t/L=0.2$

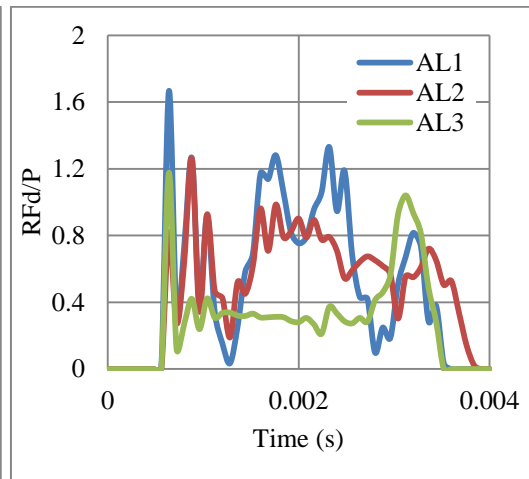
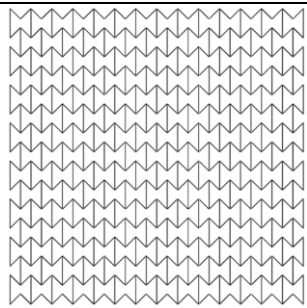
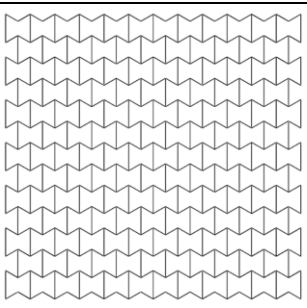
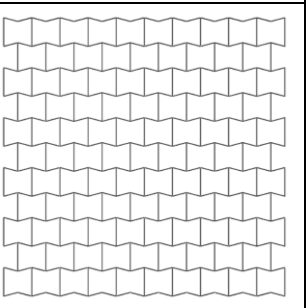


Fig. 7.15: RFd/P time history, for 3 different Aluminium grades AL1, AL2 and AL3, of an auxetic core with $L=10\text{mm}$, $t=2\text{mm}$, $t/L=0.2$

7.2.4 Cell angle

As mentioned earlier, cell angle θ plays an important role in the performance of re-entrant auxetic structures, as it changes the Poisson's ratio, auxetic behaviour and, consequently, PDE and RFD. In this section, three cell angles were considered, $\theta=45^\circ$, 60° and 75° . Cell angles less than 45° were not taken, as interior cell surfaces may contact each other. The size of the auxetic core block was kept approximately as $200 \times 200 \times 200 \text{mm}$. The exact total length, height, number of layers, and mass, of the 3 auxetic cores with 3 different cell angles are shown in Table 7.6. Other factors were kept constant such as loading direction D1, cell dimension B ($L=10 \text{mm}$), Grade AL3, $t=2.6 \text{mm}$, $t/L=0.26$, extrusion depth= 200mm , pulse load 500000N in 0.002s .

Table 7.6: Auxetic cores with 3 different cell angles and their properties

	Angle= 45°	Angle= 60°	Angle= 75°
Shape			
Total Length	198	208	193
Total height	201	200	194
No. of layers	14x15	12x13	10x11
Mass (kg)	12.4	9.3	6.6
Fixed Parameters	Loading direction D1, Cell dimension B ($L=10 \text{mm}$), Grade AL3, $t=2.6 \text{mm}$, $t/L=0.26$, Extrusion depth= 200mm , pulse load 500000N in 0.002s		

Visibly, as the angle increases, the number of layers decreases, reducing PDE and the overall mass of the core. For instance, the mass of an auxetic core with $\theta=45^\circ$ is double that of $\theta=75^\circ$, as illustrated in Fig. 7.17. On the other hand, according to Imbalzano, et al. [94]; reviewed in Table 3.2; the bigger is the angle θ , the more energy dissipation is

perceived. The contradiction in this physical behaviour is illustrated by the normalized PDE in Fig. 7.16. Therefore, angle 60° showed to have the best PDE of 3700 (J/kg), as it had average angle, number of layers and mass compared to other angles.

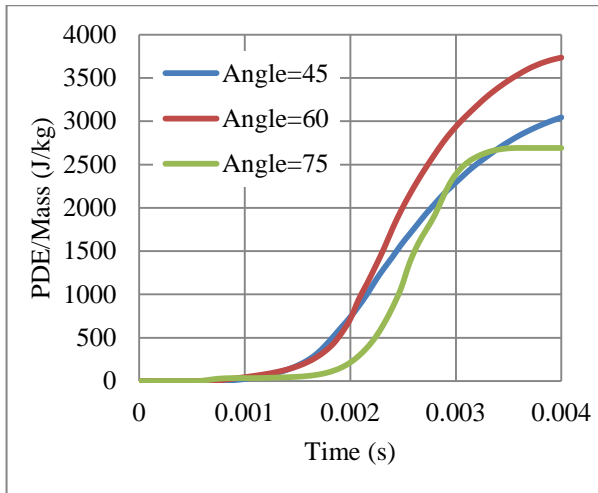


Fig. 7.16: PDE/Mass with respect to time, for 3 different cell angles, of an auxetic core with $L=10\text{mm}$, $t=2.6\text{mm}$, $t/L=0.26$

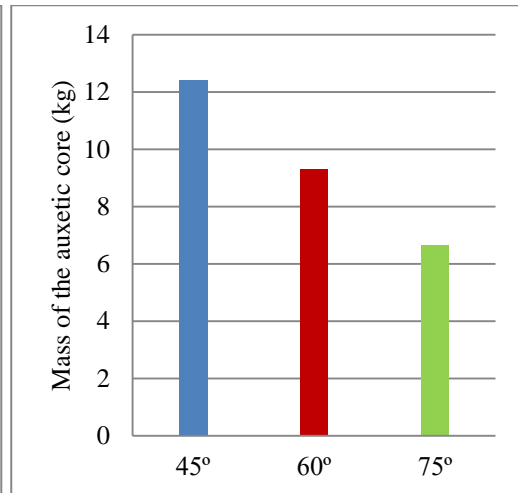


Fig. 7.17: Mass of auxetic cores with 3 different cell angles, and $L=10\text{mm}$, $t=2.6\text{mm}$, $t/L=0.26$

Results for reaction forces (Fig. 7.18) showed that the smaller is the angle, the lower is the reaction force. Peak values of RFd/P (Fig. 7.19) for $\theta=45^\circ$, 60° and 75° were 0.58, 0.62 and 0.88, respectively. The outcomes are consistent with other researchers' conclusions [94]. However, as peak RFd/P for $\theta=45^\circ$ and 60° are close to each other, $\theta=60^\circ$ had been selected for the UGAD as it had clear higher PDE potential.

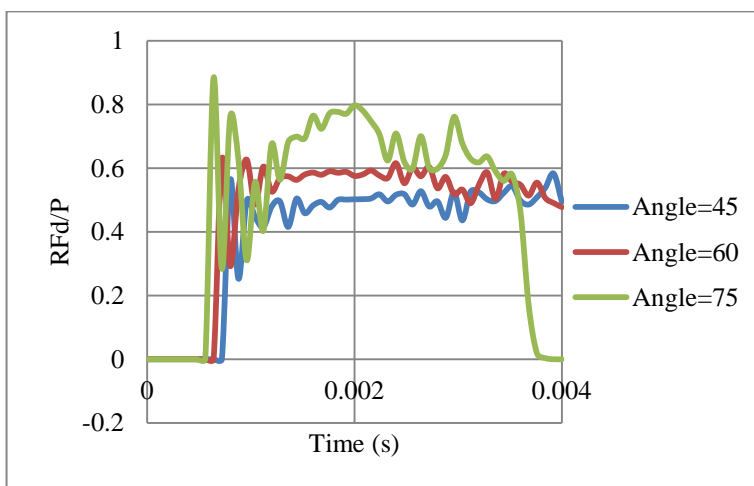


Fig. 7.18: RFd/P with respect to time, for 3 different cell angles, of an auxetic core with $L=10\text{mm}$, $t=2.6\text{mm}$, $t/L=0.26$

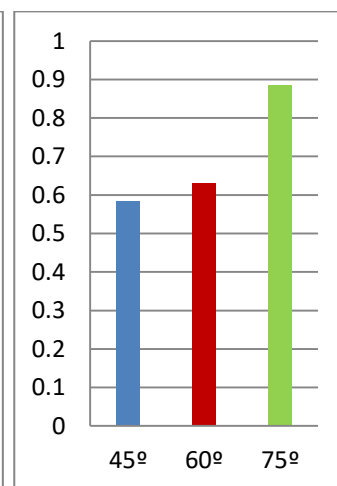


Fig. 7.19: Max. value of RFd/P for 3 different cell angles

7.2.5 Re-entrant auxetics vs. non-auxetic Honeycombs

In this section, a comparison was performed between re-entrant auxetic and non-auxetic honeycomb cores of the same geometrical properties and loading conditions. Based on conclusions of previous sections, loading direction D1, Grade AL3, Cell dimension B ($L=10\text{mm}$), $t=2.6\text{mm}$, $t/L=0.26$, $\theta_{Aux}=60^\circ$, $\theta_{Hex}=120^\circ$ were selected. As known and approved by researchers in this field (Chapter 3, Section 3.4), auxetic structures performs better against impulsive loadings in terms of higher energy dissipation and lower RFd/P than conventional hexagonal structures, due to densification in the shape of lateral necking. These results clearly presented in Fig. 7.20 and Fig. 7.21 below.

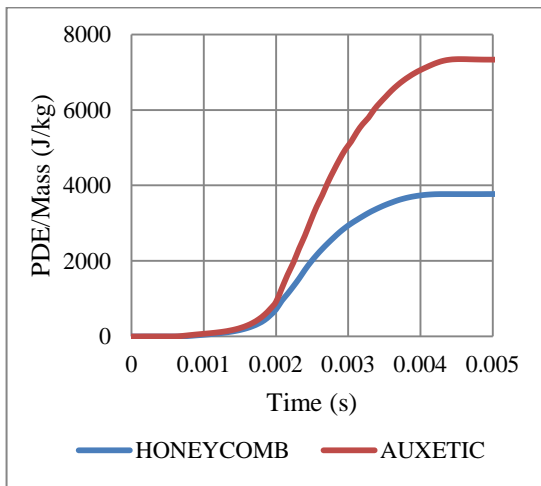


Fig.7.20: PDE/Mass with respect to time, for auxetic and honeycomb cores of the same geometrical properties and loading conditions, loading direction D1, Grade AL3, Cell dimension B ($L=10\text{mm}$), $t=2.6\text{mm}$, $t/L=0.26$, $\theta_{Aux}=60^\circ$, $\theta_{Hex}=120^\circ$.

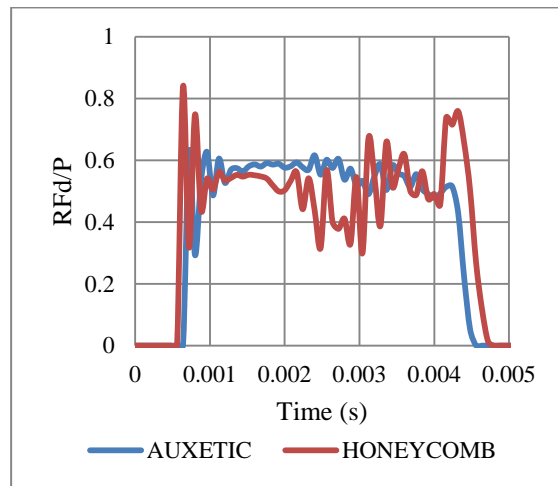
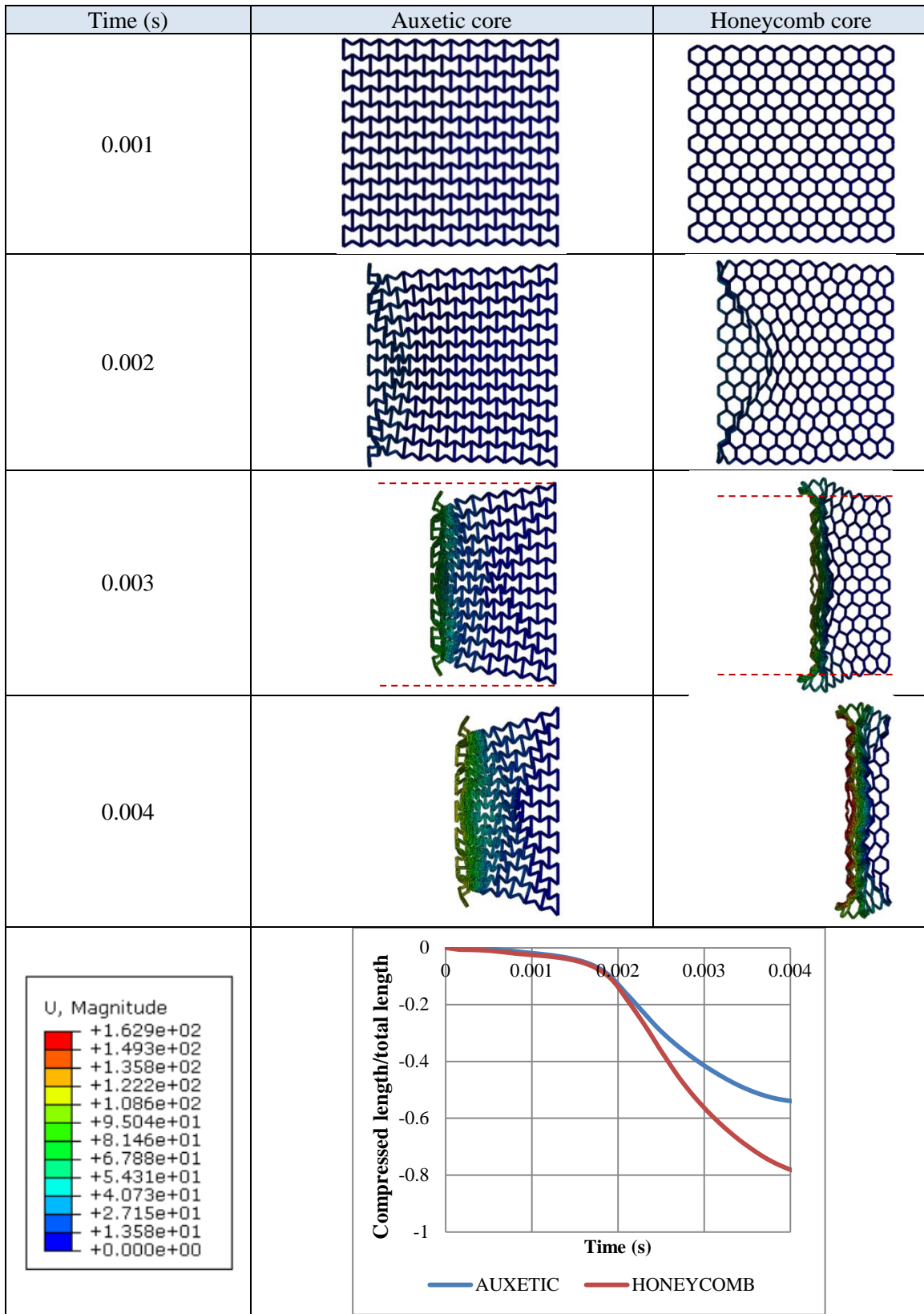


Fig.7.21: RFd/P with respect to time, for auxetic and honeycomb cores of the same geometrical properties and loading conditions, loading direction D1, Grade AL3, Cell dimension B ($L=10\text{mm}$), $t=2.6\text{mm}$, $t/L=0.26$, $\theta_{Aux}=60^\circ$, $\theta_{Hex}=120^\circ$.

The detailed deformation patterns of auxetic and honeycomb cores are shown in Table 7.7. The crushing pattern of the auxetic reveals densification in the shape of transverse shrink and diamond-like core leading to negative Poisson's ratio. The negative Poisson's ratio and transverse shrink make it easier to change the crashed auxetic core in the UGAD after a blast event. The final compressed length is only 55% of the undeformed total length. In contrast, the hexagonal core bulges in the transverse direction showing a positive Poisson's ratio (like any other non-auxetic material). The final compressed length is 80% of the undeformed total length. In other words, under the same impact load, auxetic cores needs smaller crushing strain and time to stop the impact plate [117].

Table 7.7: Deformation patterns of auxetic and honeycomb cores of the same geometrical properties and loading conditions, loading direction D1, Grade AL3, Cell dimension B (L=10mm), t=2.6mm, $t/L=0.26$, $\theta_{Aux}=60^\circ$, $\theta_{Hex}=120^\circ$.



7.2.6 Number of layers

In addition to the previous parametric studies, the number of layers an auxetic core would need to absorb effectively an impact load also had to be checked. Here, 3 auxetic cores with 3 different number of layers were tested, which were 4, 8 and 12 layers. They have the same geometrical properties and loading conditions, loading direction D1, Grade AL3, Cell dimension B ($L=10\text{mm}$), $t=2.6\text{mm}$, $t/L=0.26$, $\theta_{Aux}=60^\circ$.

Under the same impact load of 500000N in 0.002s, the 3 auxetic cores responded differently, as shown in Fig. 7.22. The 4 layers core was fully collapsed, while the 8 and 12 layers were able to stop the impact before full densification is reached.

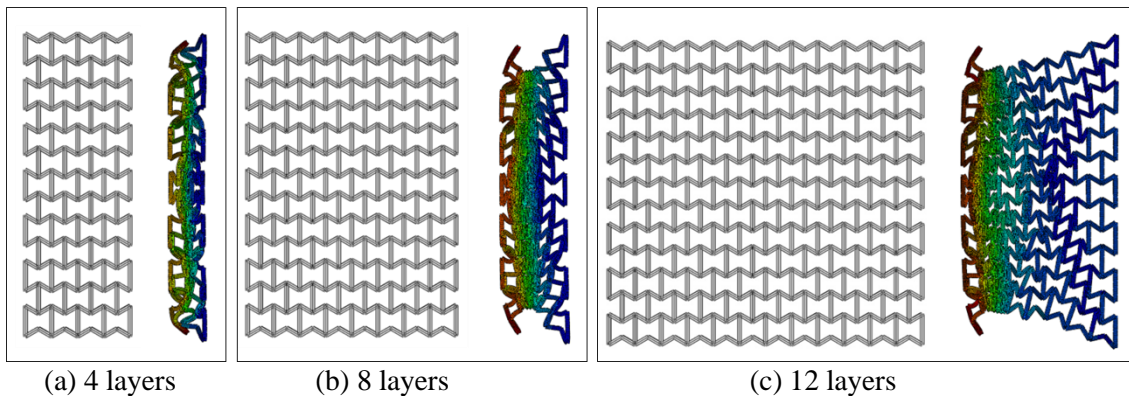


Fig. 7.22: Deformation patterns of 3 auxetic cores with different number of layers of the same geometrical properties and loading conditions, having the same loading direction D1, Grade AL3, Cell dimension B ($L=10\text{mm}$), $t=2.6\text{mm}$, $t/L=0.26$, $\theta_{Aux}=60^\circ$.

In terms of PDE (Fig. 7.23), it can be seen that the more is the number of layers, the more PDE is perceived due to the availability of more plastic hinges. These numerical findings match the results of Imbalzano, et al. [94]. In addition, the change from 4 to 8 layers raised the PDE dramatically by 74% (from 19000 J to 33000 J). In contrast, the PDE of 12 layers was only 6% higher than that of 8 layers (from 33000 J to 35000 J).

In the parametric study of optimum number of layers, normalizing the PDE by mass should not be considered as it misleads the physical interpretation. Fig. 7.24 shows how PDE/Mass reversed the hierarchy (i.e. the 4 layers core seems to have the highest value of PDE because it was divided by the smallest mass).

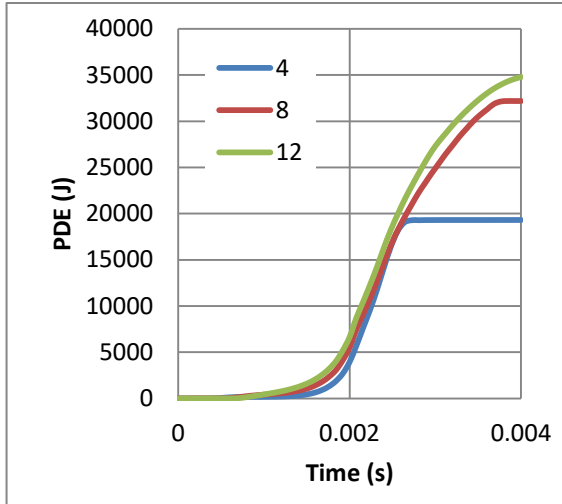


Fig. 7.23: PDE with respect to time, for auxetic cores of different no. of layers, having the same geometrical properties and loading conditions, $L=10\text{mm}$, $t=2.6\text{mm}$, $t/L=0.26$, cell angle= 60° , AL3

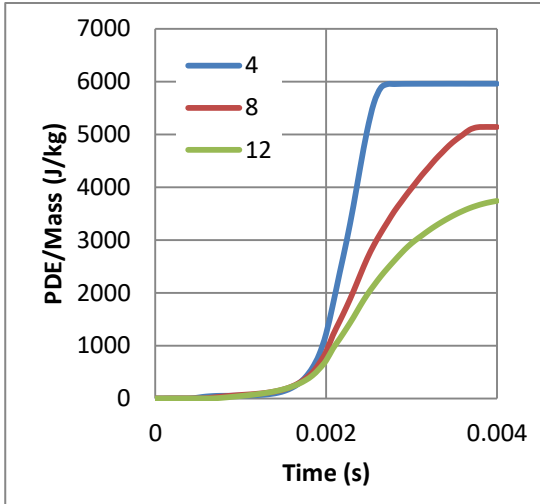


Fig. 7.24: PDE/Mass with respect to time, for auxetic cores of different no. of layers, having the same geometrical properties and loading conditions, $L=10\text{mm}$, $t=2.6\text{mm}$, $t/L=0.26$, cell angle= 60° , AL3

In terms of reaction forces (Fig. 7.25 and Fig. 7.26), the full collapse of the 4 layers led to reaction on the support with 77% magnification of the applied load P ($RF_d/P=1.77$). On the other hand, the 8 and 12 layers absorbed the impact transferring 79% and 64% of the applied load P , respectively. Zhang, et al. [105], state that when the number of layers is greater than 10, the dynamic response of auxetic structures tends towards stability, i.e., less change in RF_d/P and PDE should be expected (as seen in Fig. 7.23 and Fig. 7.25).

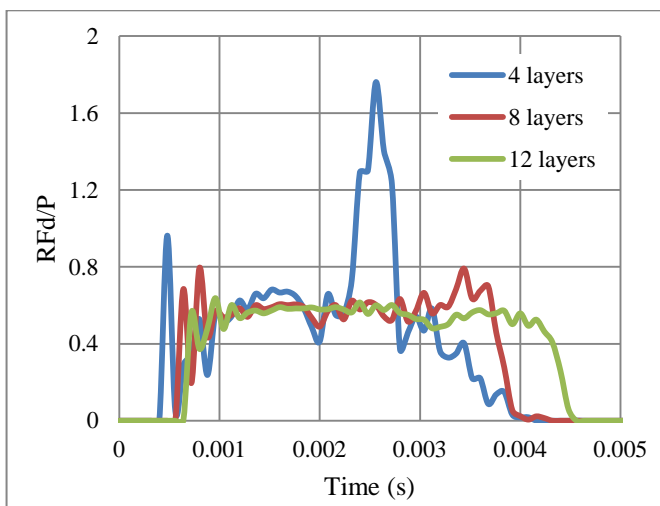


Fig.7.25: RF_d/P with respect to time, of 3 auxetic cores with different number of layers of the same geometrical properties and loading conditions, having the same loading direction $D1$, Grade AL3, Cell dimension B ($L=10\text{mm}$), $t=2.6\text{mm}$, $t/L=0.26$, $\theta_{Aux}=60^\circ$

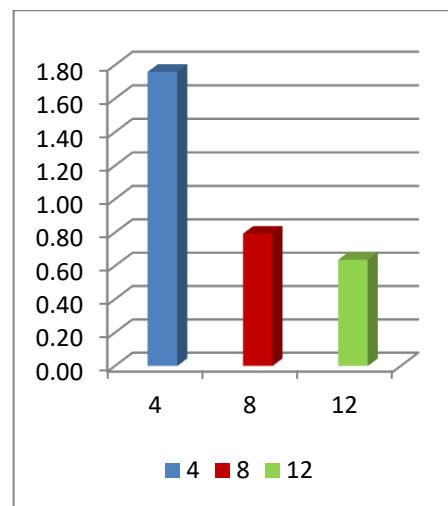


Fig.7.26: Peak value of RF_d/P of 3 auxetic cores with different number of layers; having the same geometrical properties and loading conditions

7.3 Cell wall thickness t

The parametric study, presented in Section 7.2, focused on 6 parameters that had to be optimized for better performance of the Uniaxial Graded Auxetic Damper (UGAD). The selected parameters were loading direction D1, cell dimension B ($L=10\text{mm}$), aluminium grade AL3 (6063-T4), cell angle $\theta=60^\circ$, auxetic rather than honeycomb, and lastly; 8-12 layers was the range for effective number of layers.

In this section, the cell wall thickness t is selected. It is the only remaining parameter and it has to be optimized based on real loading from a gate subjected to blast pressure. As mentioned in Section 6.3, the design of the gate and its dampers would be based on 4 levels of blast pressures, 1.65 MPa, 3.3 MPa, 4.95 MPa and the maximum 6.6 MPa, achieved from 25kg, 50kg, 75kg and 100kg of TNT at $R=5\text{m}$, respectively. As the gate was supposed to withstand the 1st low blast level (1.65 MPa), the UGADs were responsible for the remaining 3 levels. Therefore, 3 auxetic cores with 3 different values of t would be placed in the damper body as a “*graded auxetic system*” with graded properties described using step functions. The first is Aux.1 that should be optimised to absorb the 3.3 MPa blast pressure from 50kg TNT at $R=5\text{m}$ (Section 7.3.1). The second is Aux.2 that supposed to absorb the 4.95 MPa blast pressure from 75kg TNT at $R=5\text{m}$ (Section 7.3.2). The last one is Aux.3 that would absorb the 6.6 MPa blast pressure from 100kg TNT at $R=5\text{m}$ (Section 7.3.3). Each auxetic core has 8 layers leading to a total 24 layers that can fit into the damper body (430mm), as shown in Fig. 7.27.

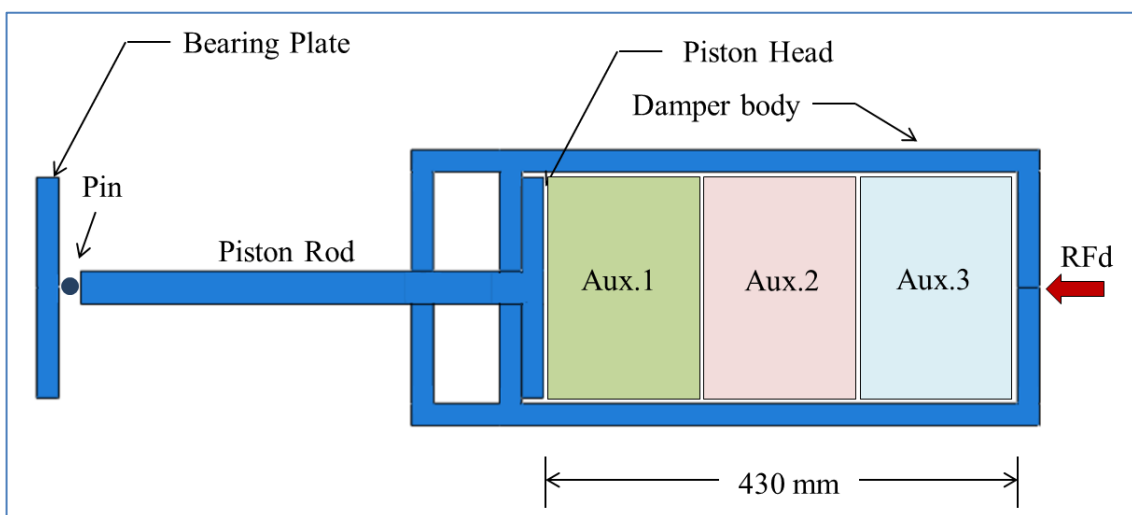


Fig. 7.27: Uniaxial Graded Auxetic Damper (UGAD) cross-section with 3 auxetic cores for 3 different blast levels

As one blast level was possible to simulate at a time, a temporary supporting wall was placed in the damper body to hold the auxetic core under investigation in place. Fig. 7.28 shows temporary supporting wall and the numerical model to find optimum t for an auxetic core. The best value of t was the one provides highest PDE and lowest RFd.

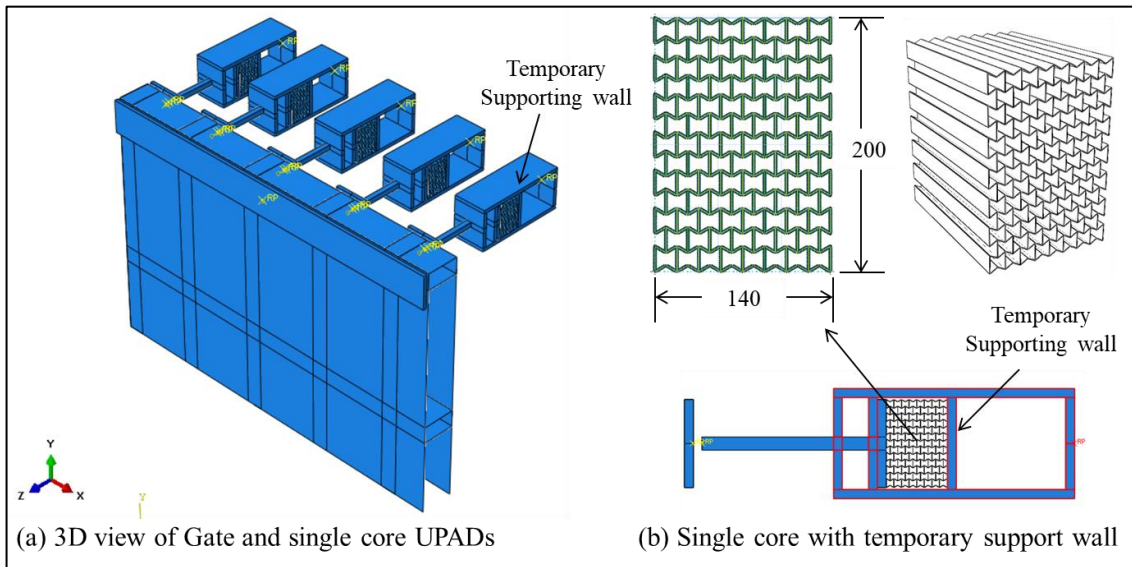


Fig. 7.28: Parametric design of cell wall thickness t for a single auxetic core subjected to certain blast level, loading direction D1, $L=10\text{mm}$, aluminium grade AL3, cell angle $\theta=60^\circ$.

7.3.1 Optimum value of t for 3.3 MPa blast level (50kg TNT, R=5m)

The first auxetic core is Aux.1 that should be optimised to absorb gate reaction forces resulting from 3.3 MPa blast pressure from 50kg TNT at R=5m. The reaction forces (RFd) at the back of UGADs at supports S1-S5, are presented in Fig. 7.29, for $t = 1, 1.4$ and 1.8mm. It can be noticed that $t=1.4$ mm had the lowest values of reaction forces with peak RFd of 160 000 N. It is important to recall that under the same blast level, the peak RF on rigid supports (without UGADs) was 760 000 N (Chapter 6, Fig. 6.10a). In other words, 79% of the reaction forces were absorbed by the auxetic core. The results can be justified to the high PDE that the 1.4mm core had, as presented in Fig. 7.30.

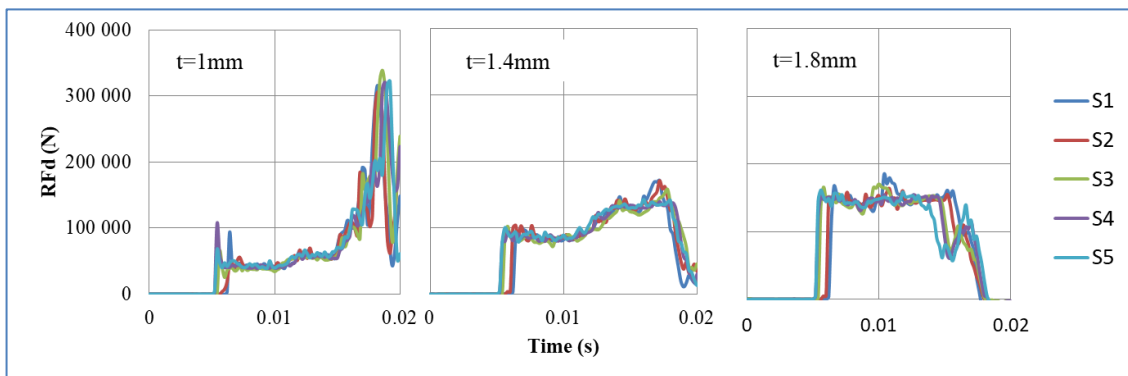


Fig. 7.29: Parametric design of the first auxetic core (Aux.1) to absorb gate reaction forces resulting from 3.3 MPa blast pressure from 50kg TNT at R=5m. Curves present the values of RFd at supports S1-S5, for $t = 1, 1.4$ and 1.8mm.

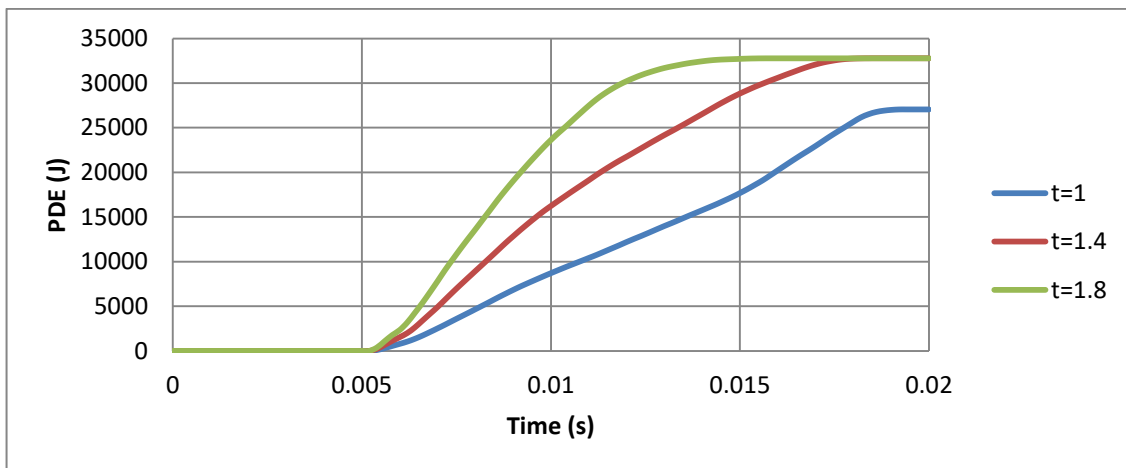


Fig. 7.30: Parametric design of the first auxetic core (Aux.1) to absorb gate energy resulting from 3.3 MPa blast pressure from 50kg TNT at R=5m. Curves present PDE, for $t = 1, 1.4$ and 1.8mm.

7.3.2 Optimum value of t for 4.95 MPa blast level (75kg TNT, R=5m)

The second auxetic core is Aux.2 that should be optimised to absorb gate reaction forces resulting from 4.95 MPa blast pressure from 75kg TNT at R=5m. The reaction forces (RFd) at the back of UGADs at supports S1-S5, are presented in Fig. 7.31, for $t = 1.4$, 1.8 and 2.2mm. The graphs reveals that $t=1.8$ mm had the lowest values of reaction forces with peak RFd of 315 000 N. Under the same blast level, the peak RF on rigid supports (without UGADs) was 880 000 N (Chapter 6, Fig. 6.10a). In other word, 65% of the reaction forces were absorbed by the auxetic core. The results can be justified to the high PDE that the 1.8mm core had, as presented in Fig. 7.32.

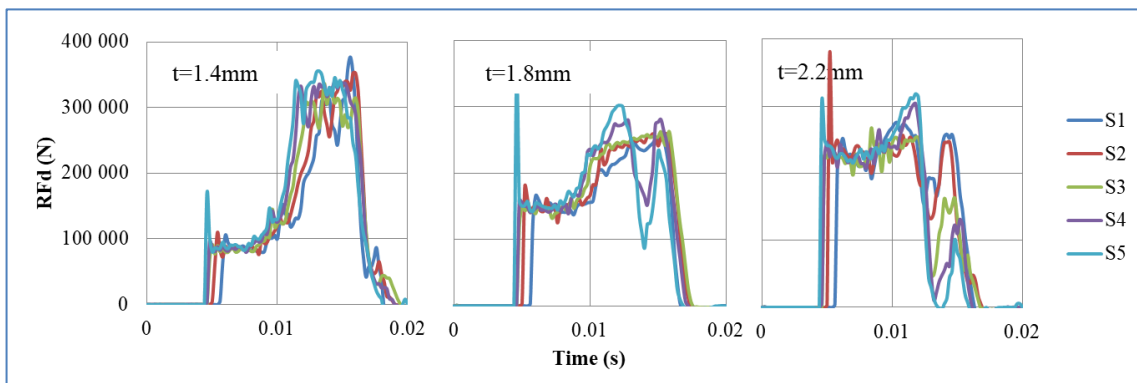


Fig. 7.31: Parametric design of the second auxetic core (Aux.2) to absorb gate reaction forces resulting from 4.95 MPa blast pressure from 75kg TNT at R=5m. Curves present the values of RFd at supports S1-S5, for $t = 1.4$, 1.8 and 2.2mm.

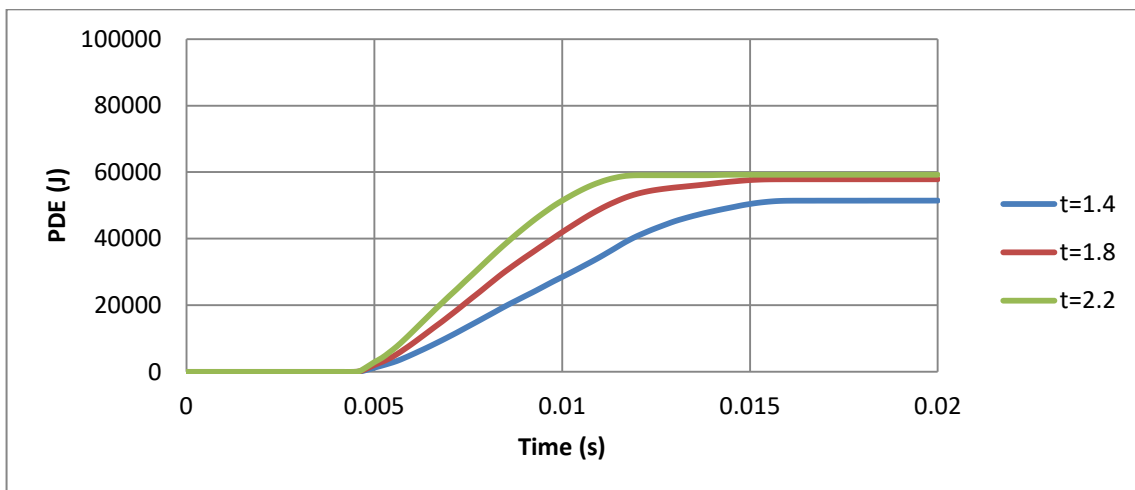


Fig. 7.32: Parametric design of the second auxetic core (Aux.2) to absorb gate energy resulting from 4.95 MPa blast pressure from 75kg TNT at R=5m. Curves present PDE, for $t = 1.4$, 1.8 and 2.2mm.

7.3.3 Optimum value of t for 6.6 MPa blast level (100kg TNT, R=5m)

The third auxetic core is Aux.3 that should be optimised to absorb gate reaction forces resulting from 6.6 MPa blast pressure from 100kg TNT at R=5m. The reaction forces (RFd) at the back of UGADs at supports S1-S5, are presented in Fig. 7.33, for $t = 1.8, 2.2$ and 2.6 mm. It can be noticed that $t=2.2$ mm had the lowest values of reaction forces with peak RFd of 510 000 N. Under the same blast level, the peak RF on rigid supports (without UGADs) was around 1000000 N (Chapter 6, Fig. 6.10a). In other word, 49% of the reaction forces were absorbed by the auxetic core. The results can be justified to the high PDE that the 2.2mm core had, as presented in Fig. 7.34.

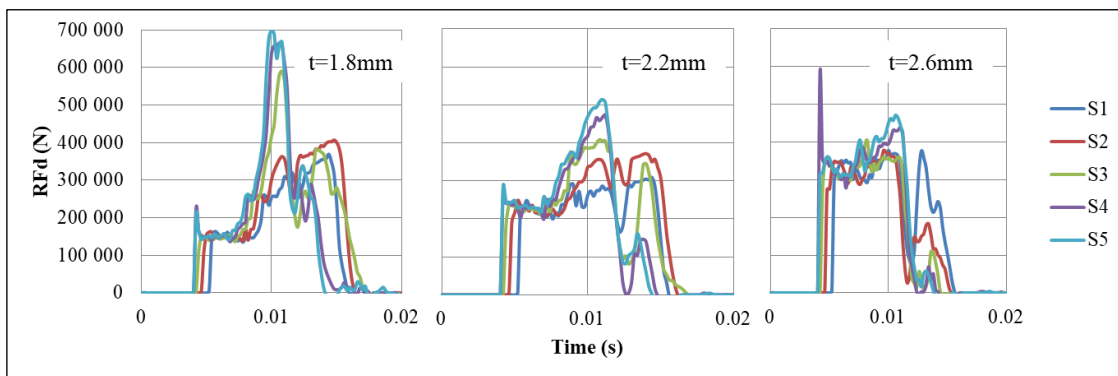


Fig. 7.33: Parametric design of the third auxetic core (Aux.3) to absorb gate reaction forces resulting from 6.6 MPa blast pressure from 100kg TNT at R=5m. Curves present the values of RFd at supports S1-S5, for $t = 1.8, 2.2$ and 2.6 mm.

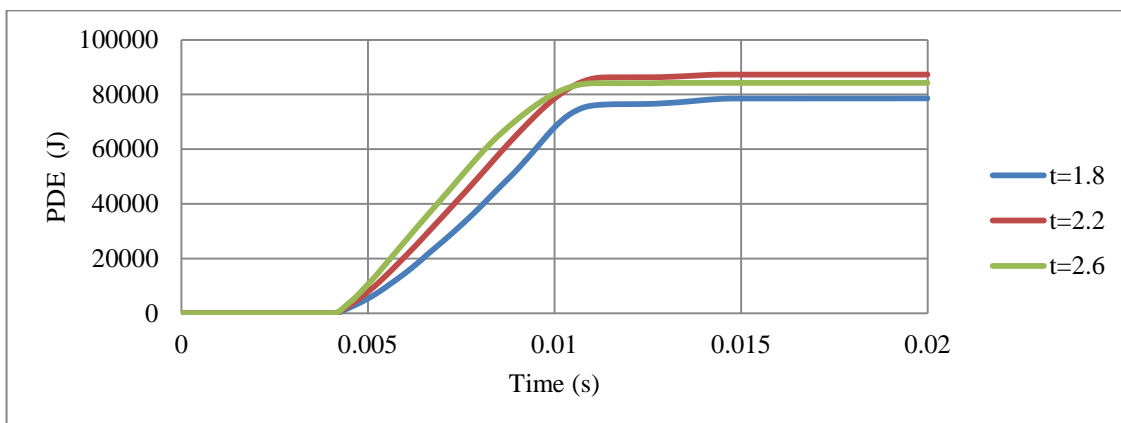


Fig. 7.34: Parametric design of the third auxetic core (Aux.3) to absorb gate energy resulting from 6.6 MPa blast pressure from 100kg TNT at R=5m. Curves present PDE, for $t = 1.8, 2.2$ and 2.6 mm.

In conclusion, the lightest-most effective 3 auxetic cores that would be fitted in the UGAD; namely Aux.1, Aux.2 and Aux.3, should have a cell wall thickness t of 1.4, 1.8 and 2.2mm, respectively.

7.4 Final properties of the UGAD

Based on the parametric studies conducted in Sections 7.2 and 7.3, the final geometrical and mechanical properties of the three auxetic cores are described here in this section. Table 7.8 shows the auxetic cores and lists their properties. They have the same L , θ , material grade, size and hence, overall volume. The cell-wall thickness t is the variable parameter; which in return; leads to distinct mass, density and relative density. The density of each auxetic core (ρ) was achieved from dividing the mass of each core by the undeformed volume V ($V=140 \times 200 \times 200 \text{ mm} = 5.6 \times 10^6 \text{ mm}^3$). The relative density ρ^* is the ratio of the auxetic core density (ρ) to the density of the material used (ρ_s):

$$\rho^* = \rho / \rho_s \quad (7.5)$$

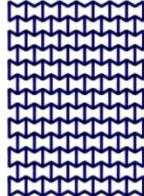
The relative density ρ^* can also be calculated analytically using [84]:

$$\rho^* = \frac{\rho}{\rho_s} = \frac{1}{2} \frac{t}{L} \frac{(\frac{L_1}{L} + 2)}{\cos \theta (\frac{L_1}{L} + \sin \theta)} \quad (7.6)$$

The relative density is an important parameter as it shows also the void ratio in cellular metals. The void ratio can be calculated as:

$$\frac{V_v}{V} = (1 - \rho^*) \times 100. \quad (7.7)$$

Table 7.8: The three auxetic cores with their geometric and mechanical properties

	Aux.1	Aux.2	Aux.3
Shape			
Shared parameters	L=10mm, cell angle $\theta=60^\circ$, Grade AL3 ($\rho_s=2.703 \times 10^{-9} \text{ t/mm}^3$), Size= 140x200x200mm, volume of one core $V= 5.6 \times 10^6 \text{ mm}^3$		
t (mm)	1.4	1.8	2.2
t/L	0.14	0.18	0.22
Mass (ton)	0.00338	0.00434	0.00530
Mass (kg)	3.38	4.34	5.30
Density ρ (t/mm^3)	6.036×10^{-10}	7.75×10^{-10}	9.46×10^{-10}
Relative Density $\rho^* = \rho / \rho_s$	0.223	0.287	0.35
Void ratio %	77.7	71.3	65

It can be perceived from Table 7.8 that the relative density increased with increasing t . In addition, Aux.1 had the highest void ratio of 77.7% compared to Aux.3 that had 65%.

Crushing an auxetic structure pass through 4 states. The 1st is the linear elastic state (cell wall bending). The 2nd is the stress undulation (cell wall collapse). The 3rd is the plateau region where plastic bending occurs. The last is the densification state, when the cell walls touch each other [9]. It is the plateau region that is important in characterizing the dynamic crushing of auxetic structures for energy absorbing applications [105]. The plateau stress can be defined as “the average nominal stress between the first stress peak and the compressive stress corresponding to the densification strain” [105]. Fig. 7.35 shows the stress-strain curve of Aux.1 under 20m/s constant impact velocity, highlighting the 4 stages of crushing a re-entrant auxetic structure mentioned above. The crushing strength was calculated based on RFD divided by impact area (200x200mm).

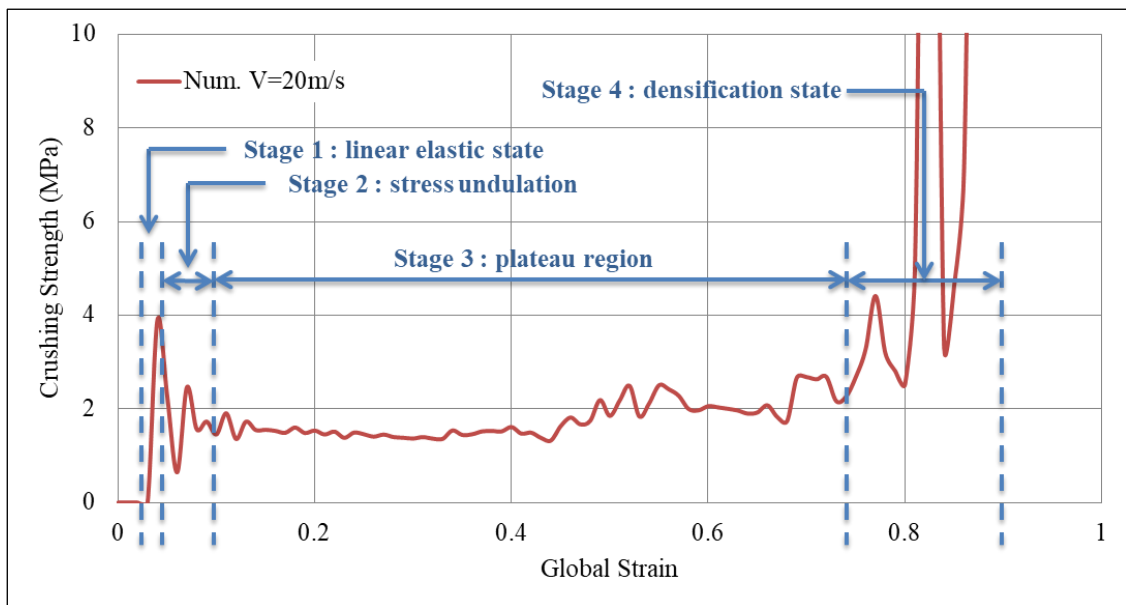


Fig. 7.35: Stress-strain curve of Aux.1 under 20m/s impact velocity, showing the 4 stages of crushing a re-entrant auxetic structure.

Based on the rigid, perfectly plastic, locking material simplified model (r-p-p-l model), the theoretical expression for dynamic plateau stress (dynamic crushing strength) of re-entrant auxetics is [9, 169]:

$$\sigma_d = \sigma_0 + \frac{\rho}{\varepsilon_d} v^2, \quad (7.8)$$

where, v is the impact velocity, ε_d is the locking strain, which can be found from the stress-strain curve under quasi-static uniaxial compression, σ_0 is the static plateau stress calculated following Gibson and Ashby [84] as:

$$\sigma_0 = \frac{2 \sigma_{ys} \left(\frac{t}{L}\right)^2}{3}. \quad (7.9)$$

Implementing the periodic collapse mechanism of re-entrant auxetics, Hou, et al. [9] derived the analytical expression of “dynamic crushing strength” as a function of cell-wall aspect ratio t/L and the impact velocity v :

$$\sigma_d = \left[\frac{2 \sigma_{ys} \left(\frac{t}{L}\right)^2}{3} \right] + \left[\frac{16 \rho_s \left(\frac{t}{L}\right)}{7 \sqrt{3} - 28 \left(\frac{t}{L}\right)} \right] v^2 \quad (7.10)$$

where the first part is the static plateau stress (Eq. (7.9)) and the second part is the additional hardening (based on impact velocity). By substituting the values of t , L , σ_{ys} and ρ_s in Eq. (7.10); for each auxetic core (Aux.1, Aux.2 or Aux.3); the dynamic crushing strength can be found analytically for any impact velocity v . It is important to highlight that the second part of Eq. (7.10) approaches to zero when the impact velocity is less than or equal to 1m/s (i.e. equal to static plateau stress). Therefore, three velocities were selected to compare analytical and numerical dynamic crushing strength, namely, 1m/s, 20m/s and 40m/s. The analytical solution of Eq. (7.10) for Aux.1, for example, gives plateau stress of 1.17, 1.47 and 2.35 MPa for the 3 velocities, respectively. Fig. 7.36 shows numerical stress-strain curve of Aux.1 under different impact velocities, compared to analytical “dynamic crushing strength”. A very good agreement can be seen in the plateau region for all impact velocities. The comparison of analytical and numerical outcomes presented here can be considered as a validation of the auxetic core numerical model.

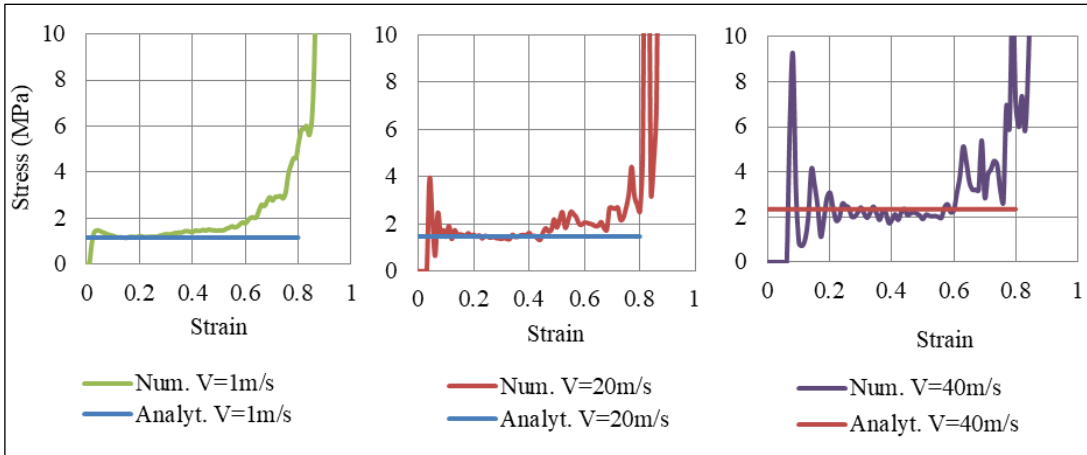


Fig. 7.36: Numerical stress-strain curve of Aux.1 under different impact velocities, compared to analytical “dynamic crushing strength”

The stress-strain curve of the 3 auxetic cores together in the UGAD under different impact velocities; 1m/s, 20m/s and 40m/s; are shown in Fig. 7.37. The progressive collapse is evident, through compressing Aux.1, then Aux.2 and Aux.3, in sequence. The performance of the 3 auxetic cores together have led to wide plateau region (80% of total crushing strain) and variant strength range (1-10 MPa), which in return, can justify the superior performance of the UGAD under different blast levels.

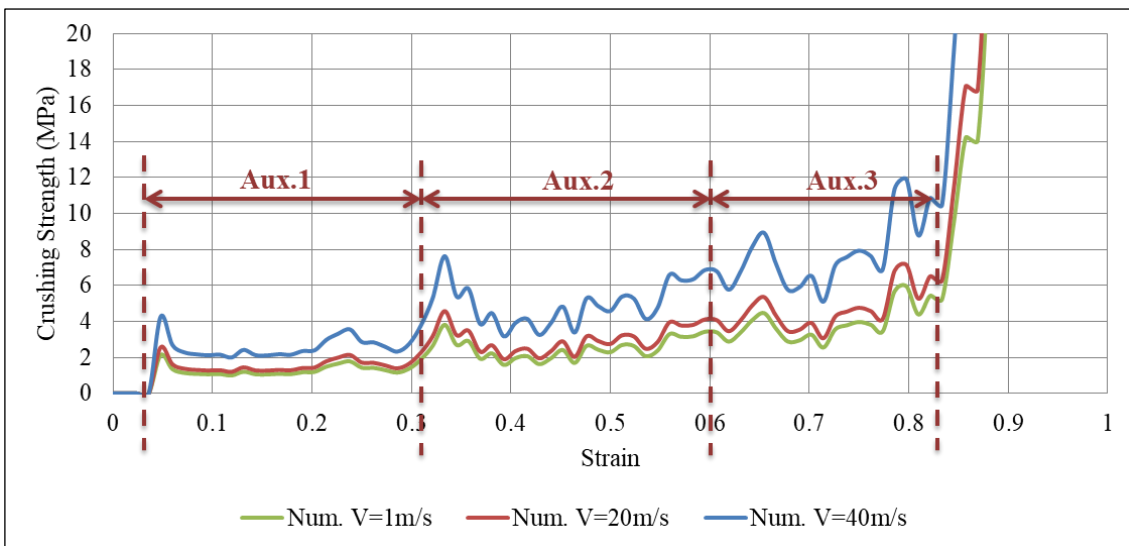


Fig. 7.37: Stress-strain curve of the 3 auxetic cores together in the UGAD under different impact velocities, 1m/s, 20m/s and 40m/s.

7.5 Gate behaviour with the proposed auxetic damper

The achievement of lighter, and hence more economical, gate is one of the objective of this thesis. In Chapter 6 (Section 6.6), the performance of the 4 gates G2.5, G5, G7.5 and G10 (on rigid supports) were assessed, based on maximum plastic strain, permanent deformation and corresponding operability. The behaviour was addressed for the maximum blast pressure of 6.6 MPa (from 100kg of TNT at R=5m). Gate G10 was the only gate that can be considered as operable after the blast event, with peak $d_{frame} = 4.4mm$, less than D_{limit} (26.2mm).

In this section, the behaviour of the remaining 3 gates; G2.5, G5 and G7.5; were assessed with the application of the proposed uniaxial graded auxetic damper (UGAD) designed earlier. Table 7.9 shows plastic strain, permanent deformation and operability of the gates with the proposed auxetic damper, subjected to 6.6 MPa blast pressure from 100kgTNT at R=5m. Both G7.5 and G5 were passed the operability requirement with $d_{frame} < D_{limit}$ (26.2mm). The frame permanent deformation of G7.5 dropped from 28.4 to 4mm with the addition of the UGADs. Furthermore, the frame permanent deformation of G5 decreased from 40.5 to 22mm with the addition of the UGADs, making G5 as the lightest-operable option that can withstand the blast pressure target of 6.6 MPa.

Table 7.9: Plastic strain, permanent deformation and operability of the gates with the proposed auxetic damper, subjected to 6.6 MPa blast pressure from 100kgTNT at R=5m.

		Peak Plastic Strain			Permanent Deformation d (mm)			Operable
Gate	t (mm)	Frame	Front Plate	Back Plate	Frame	Front Plate	Back Plate	(Yes/No)
G2.5	2.5	0.93	0.89	0.19	676	613	609	No
G5	5	0.1	0.17	0.156	22	51	24	Yes
G7.5	7.5	0.03	0.16	0.1	4	19	8	Yes

Permanent deformation of Gate G5 and the UGAD (at support S5, Fig. 6.4) are shown in Figures 7.38-7.41, for different blast pressures. It is explicit that up to 3.3 MPa blast pressure (Fig. 7.38 and Fig. 7.39), the 1st auxetic core (Aux.1) was the only deformed one with maximum deformation of 92mm. In other words, only Aux.1 has to be changed after such a blast event. Nonetheless, blast pressures between 3.3 and 6.6 MPa (Fig. 7.40 and Fig. 7.41), induces a plastic deformation in both Aux.1 and Aux.2 cores, i.e. both of them should be replaced after such a high blast event. Although Aux.3 was designed in

Section 7.3.3 to absorb the 6.6 MPa blast pressure, the first two cores were able to absorb the impact up to their capacity without deforming the third core (Aux.3). This is an extremely important advantage, hence Aux.3 hereafter will work as a factor of safety for unexpected higher blast loads or multiple explosions in a short period of time.

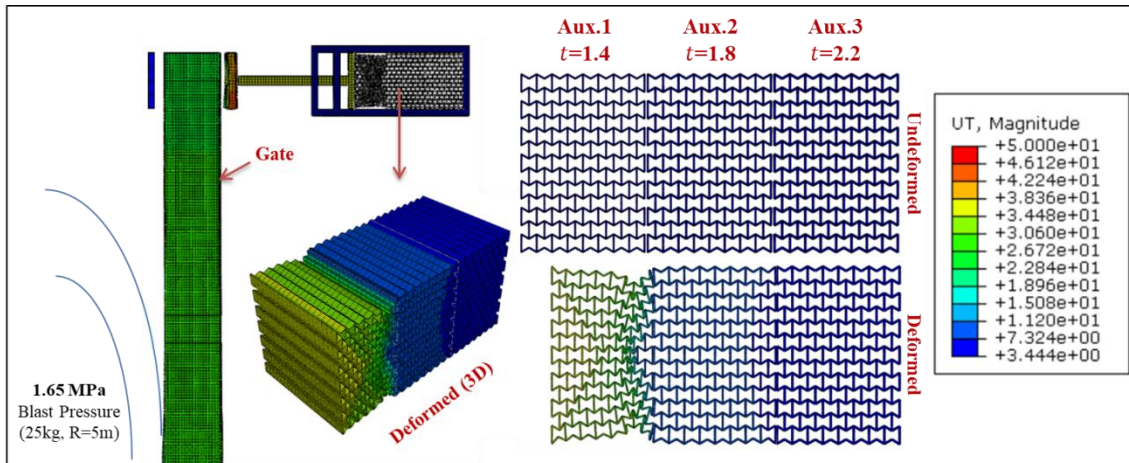


Fig. 7.38: Displacement of Gate G5 and the Auxetic damper after a blast pressure of 1.65 MPa from 25kg TNT at R=5m

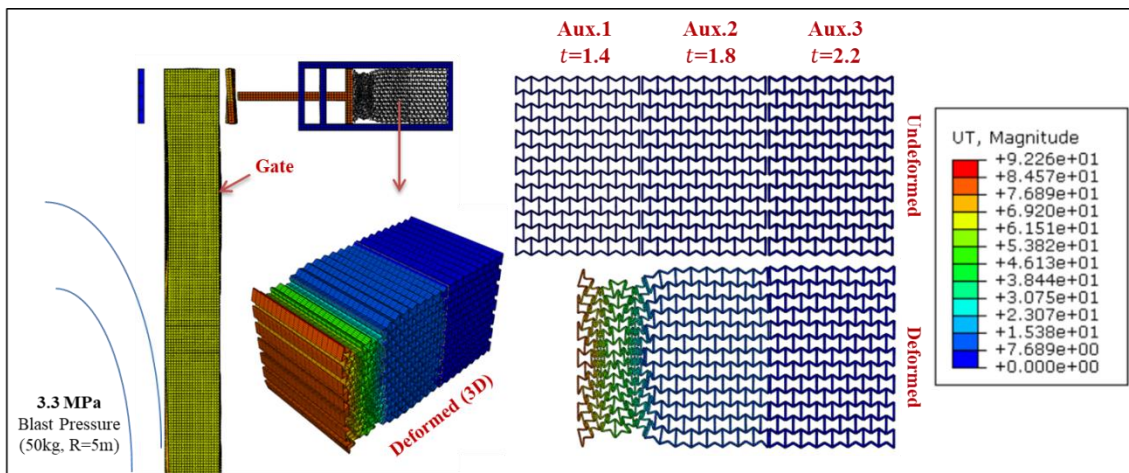


Fig. 7.39: Displacement of Gate G5 and the Auxetic damper after a blast pressure of 3.3 MPa from 50kg TNT at R=5m

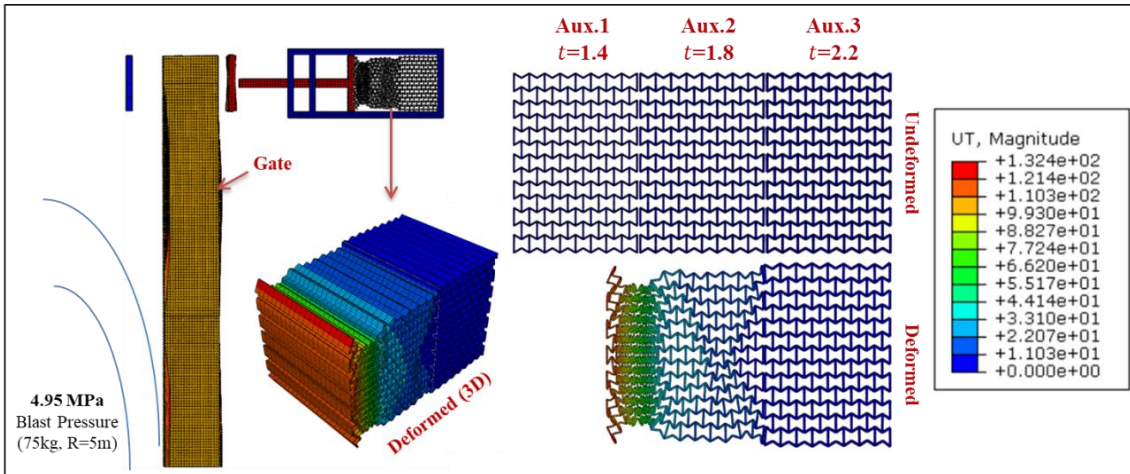


Fig. 7.40: Displacement of Gate G5 and the Auxetic damper after a blast pressure of 4.95 MPa from 75kg TNT at R=5m

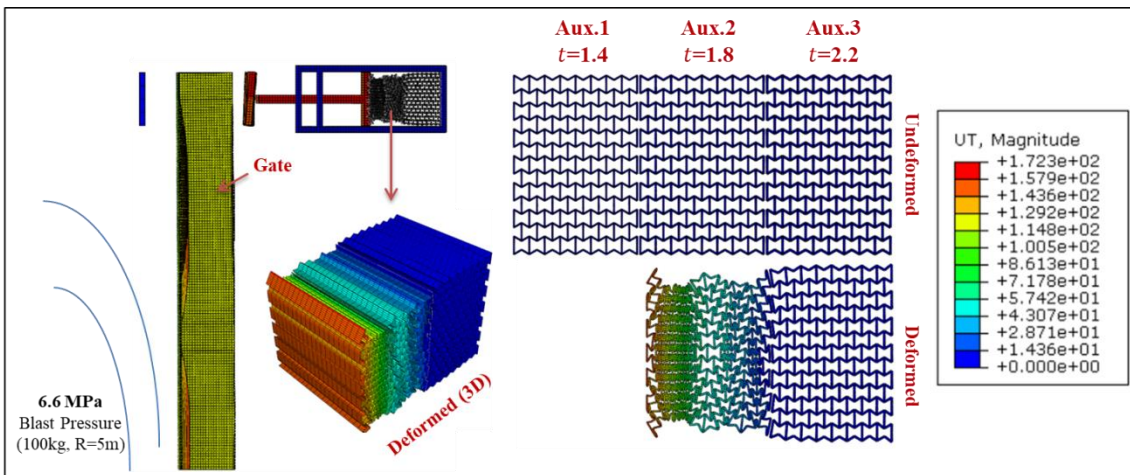


Fig. 7.41: Displacement of Gate G5 and the Auxetic damper after a blast pressure of 6.6 MPa from 100kg TNT at R=5m

The displacements of pistons' head (i.e. compressed length of auxetic cores) at supports S1-S5 (Fig. 7.42), shows the integrity of the gate and the movement as one large body. The maximum was 167mm at S5, while the lowest was 161 at S1. So, the difference was only 6mm. The results can also be presented in terms of pistons' head velocity (i.e. velocity of compressing auxetic cores). Fig. 7.43 shows that the velocities of compressing auxetic cores in all UGADs were coincident, with peak velocity of about 20m/s.

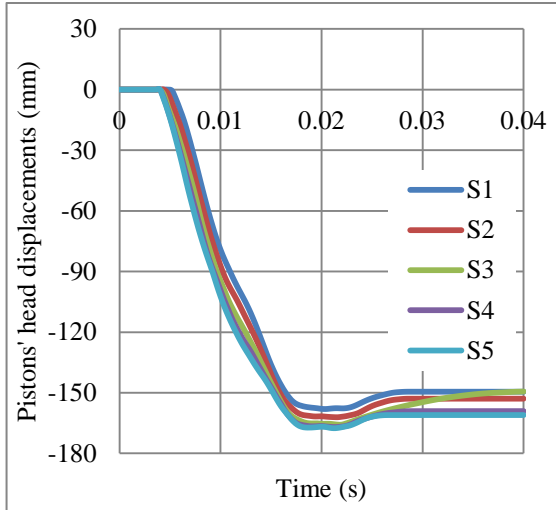


Fig. 7.42: Displacements of Pistons' heads (i.e. compressed length of auxetic cores) at supports S1-S5, after a blast pressure of 6.6 MPa from 100kg TNT at R=5m, Gate G5.

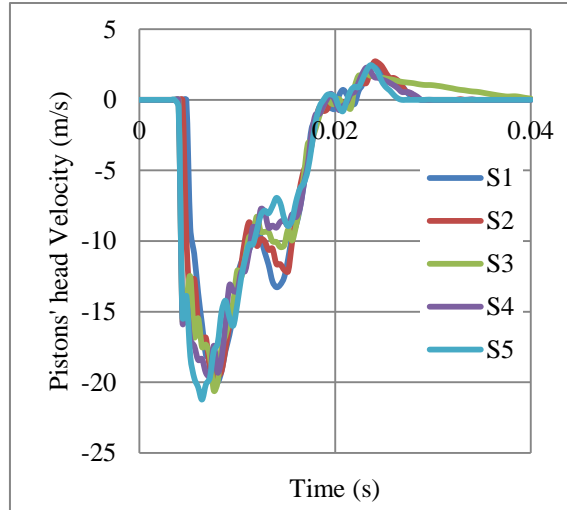


Fig. 7.43: Velocity of Pistons' heads (i.e. velocity of compressing auxetic cores) at supports S1-S5, after a blast pressure of 6.6 MPa from 100kg TNT at R=5m, Gate G5.

The reduction of gate reaction forces was one of the objectives of this thesis, which would in return; reduce the required cross section and strength of the whole system supports. Fig. 7.44 and Fig. 7.45 compare the reaction forces at supports S1-S5, without and with the proposed auxetic dampers, respectively. It is clearly shown that peak reaction force (which is at support S5) was dropped from 1×10^6 to 0.51×10^6 N (49% of reduction).

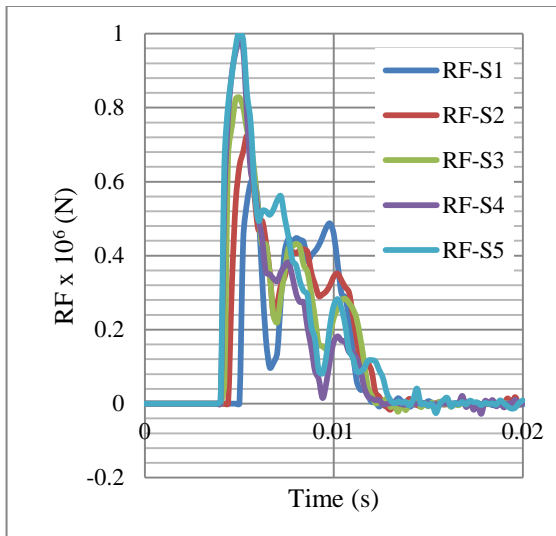


Fig. 7.44: Reaction forces RF at supports S1-S5 without external dampers, after a blast pressure of 6.6 MPa from 100kg TNT at R=5m, Gate G5.

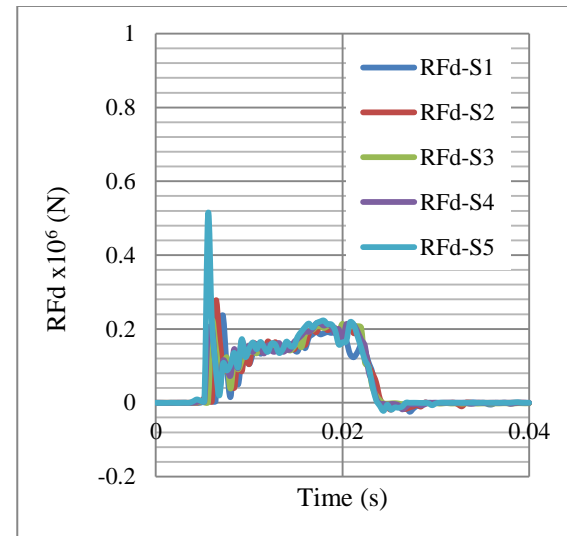


Fig. 7.45: Reaction forces RFd at supports S1-S5 with the auxetic dampers, after a blast pressure of 6.6 MPa from 100kg TNT at R=5m, Gate G5.

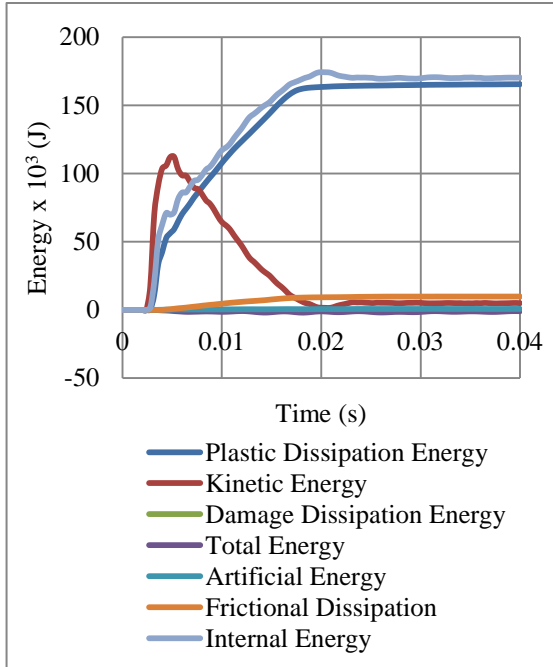


Fig. 7.46: Energy components of the model (shown in Fig. 7.7), after a blast pressure of 6.6 MPa from 100kg TNT at R=5m, Gate G5.

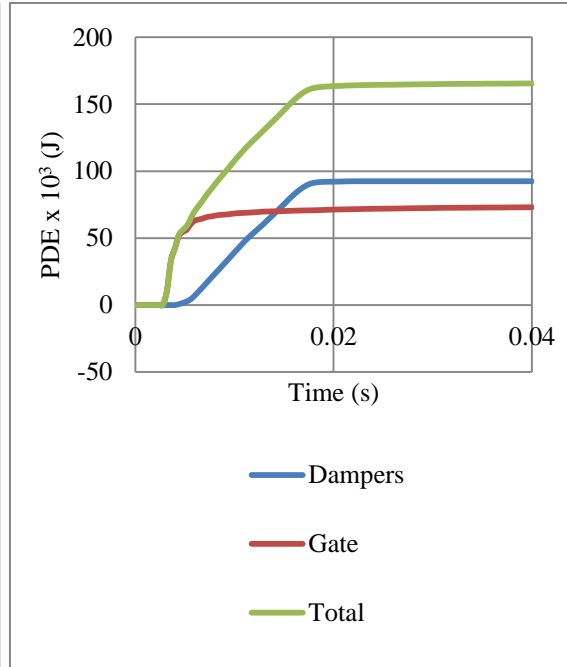


Fig. 7.47: PDE by the dampers, gate and the total PDE in the model (shown in Fig. 7.7), after a blast pressure of 6.6 MPa from 100kg TNT at R=5m, Gate G5.

Fig. 7.46 presents the energy components of the Gate G5 model (shown in Fig. 7.7), after a blast pressure of 6.6 MPa. It shows that internal energy in the whole model ($174 \times 10^3 \text{J}$) constitute of major plastic dissipation ($164 \times 10^3 \text{J}$) and minor frictional dissipation ($10 \times 10^3 \text{J}$), with no dissipation due to damage. Based on that successful damping, the kinetic energy is mitigated. It is also important to highlight that the value of artificial energy is near zero, which reflects that the numerical model of the system was accurate to high extent.

In addition, Fig. 7.47 shows that 56% of the total PDE in the system was achieved from the UGADs, while 44% from the gate. The additional PDE gained from those light weight auxetic cores justifies the significant reduction in permanent deformations and reaction forces.

Despite the fact that the maximum considerable blast pressure taken in this thesis as target was 6.6 MPa (from 100kg TNT at R=5m), it is worth checking the behaviour of the system beyond that limit. Fig. 7.48 shows the displacement of Gate G5 and the Auxetic damper after a blast pressure of 9.9 MPa (from 150kg TNT at R=5m), i.e. 1.5

times more than the target. The third auxetic core (Aux.3) was surprisingly able to absorb the additional pressure without a full crash of the gate on to the supports. In addition, the gate maintained its integrity preventing access to the premises. However, the gate exceeded the operability limit with large permanent deformations and aesthetic defects. If such an extreme blast level is expected on site, then it is recommended to use Gate G7.5 instead.

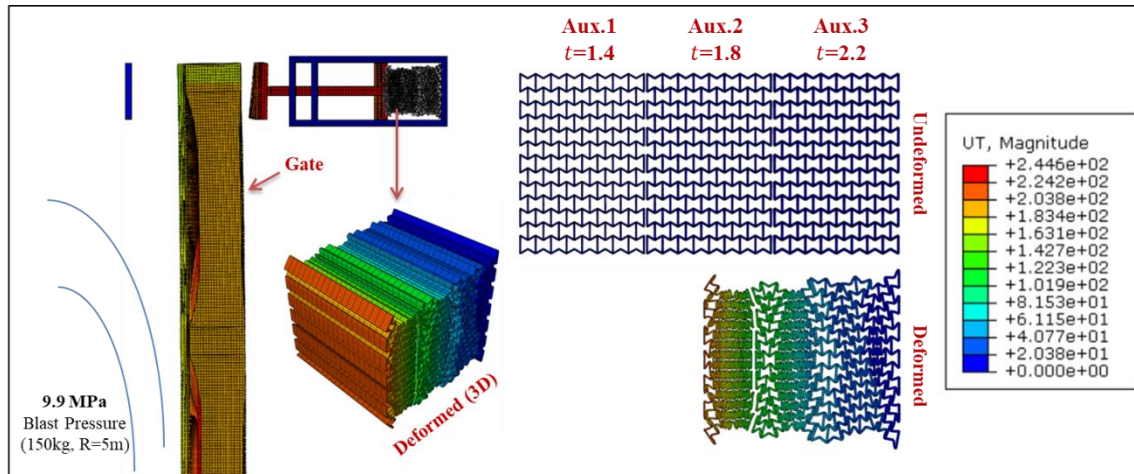


Fig. 7.48: Displacement of Gate G5 and the Auxetic damper after a blast pressure of 9.9 MPa from 150kg TNT at R=5m

Although the design of the damper body was out of the scope of this thesis (as mentioned in Section 7.1.1), one may suspect that the piston rod (shown in Fig. 7.1) would withstand peak RFD of 500 000 N (Fig. 7.45). Therefore, the strength and lateral buckling are checked here. If the cross-sectional dimensions are 35x35mm, the peak stress in the rod would be 408 MPa, less than the yield point of the steel material used. In terms of buckling, according to Euler's formula $P_{cr} = \pi^2 EI / (KL)^2$, the critical load P_{cr} can be calculated, beyond which a column would buckle. The modulus of elasticity E is given as 200×10^3 MPa. Moment of inertia $I = \frac{bh^3}{12} = \frac{35^4}{12} = 125052 \text{ mm}^4$. The effective length factor K is 2 for free-end column, and the unsupported length of the column is 310mm (shown in Fig. 7.1). Then, critical load P_{cr} is 642 150 N, greater than the applied axial load. In other words, the piston rod would stay in elastic range with no lateral buckling, when subjected to peak reaction forces generated from 100kg TNT at 5m.

7.6 Designing a reinforced concrete supporting structure

The final stage was to propose a reinforced concrete frame that would support the gate and the UGADs. This concrete frame supposed to stay in elastic range within the 6.6 MPa blast level under consideration. It is subjected to a direct blast from the explosion in addition to loads from the UGADs (distributed on small surfaces).

The reinforced concrete structure consists of a slab, beams, columns, and a base. The total size of the structure has a length of 6100mm (in x -axis), height of 4000mm (in y -axis) and depth of 3000mm (in z -axis). Fig. 7.49 provides the dimensions, where the front (a), side (b), top (c) and 3D view (d) are shown. In addition, Fig. 7.49, (e) and (f), show the side and 3D view of the concrete frame, when the gate and UGADs are in place.

In terms of reinforcement, Fig. 7.50 shows their distribution in the concrete frame. The main reinforcement of the beams and columns were $\emptyset 25\text{mm}$ distributed evenly @150mm c/c while the stirrups were $\emptyset 12\text{mm}@150\text{mm } c/c$. Each of the slab and the base had two grids of $\emptyset 12\text{mm}@150\text{mm } c/c$ in both directions. B490 was the chosen grade for steel reinforcement with yield strength of 490 MPa. Reinforcement material parameters were the same provided in Table 5.1 leading to a comprehensive material model that covers elastic, plastic, strain hardening and damage stages. Generally, reinforcing steel grades, with ~ 500 MPa characteristic strength, has replaced Grade 250 and Grade 460 throughout Europe, as they satisfy the three recommended ductility classes in BS 1992-1-1:2004 (Eurocode 2). The steel bars were modelled using 2-node linear beam element (B31) with mesh size of 100mm. The interaction between the steel bars and the concrete were added using the ‘embedded elements’ feature provided by Abaqus, as recommended in literature.

In terms of boundary conditions, the concrete frame is assumed to be fixed at bottom surface of its base, in addition to fixing the end nodes of the main columns’ steel bars (as shown in Fig. 7.50 (a) and (b)). The simulation of the substructure (foundation and soil) were out of the scope of this study as they required proper geotechnical modelling with soil-structure interaction.

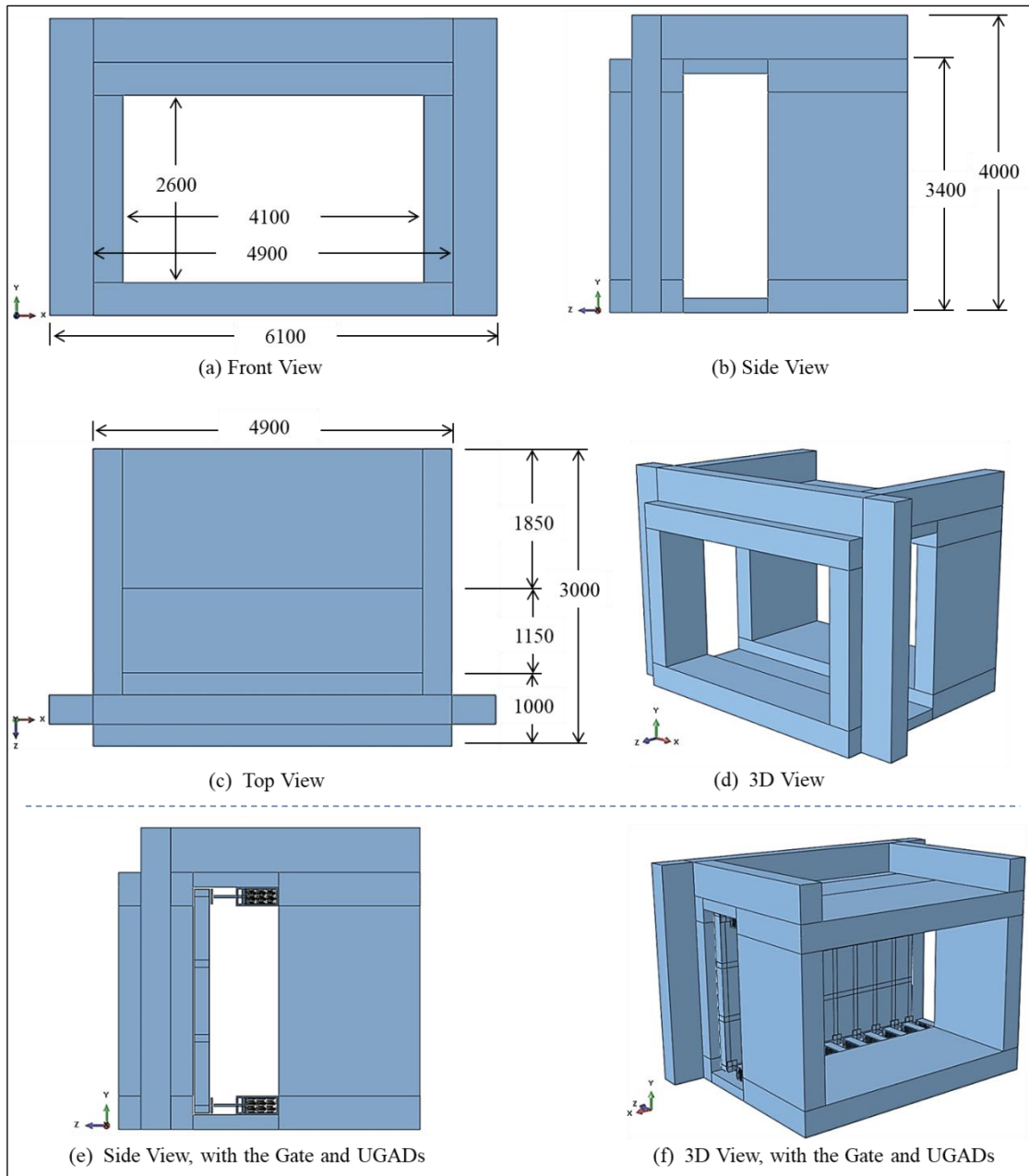


Fig. 7.49: Front, side, top and 3D view of the proposed concrete frame with its dimensions

The concrete was modelled using explicit 8-node linear brick element (C3D8R) with reduced integration and hourglass control. Mesh size was 50mm, which proved to be accurate for the scale of the problem under investigation. The Ultra High Performance Fiber Reinforced concrete (UHP-FRC) was used due to its superior mechanical properties, of quasi-static compression and tension of up to 200 MPa and 15 MPa, respectively [170, 171].

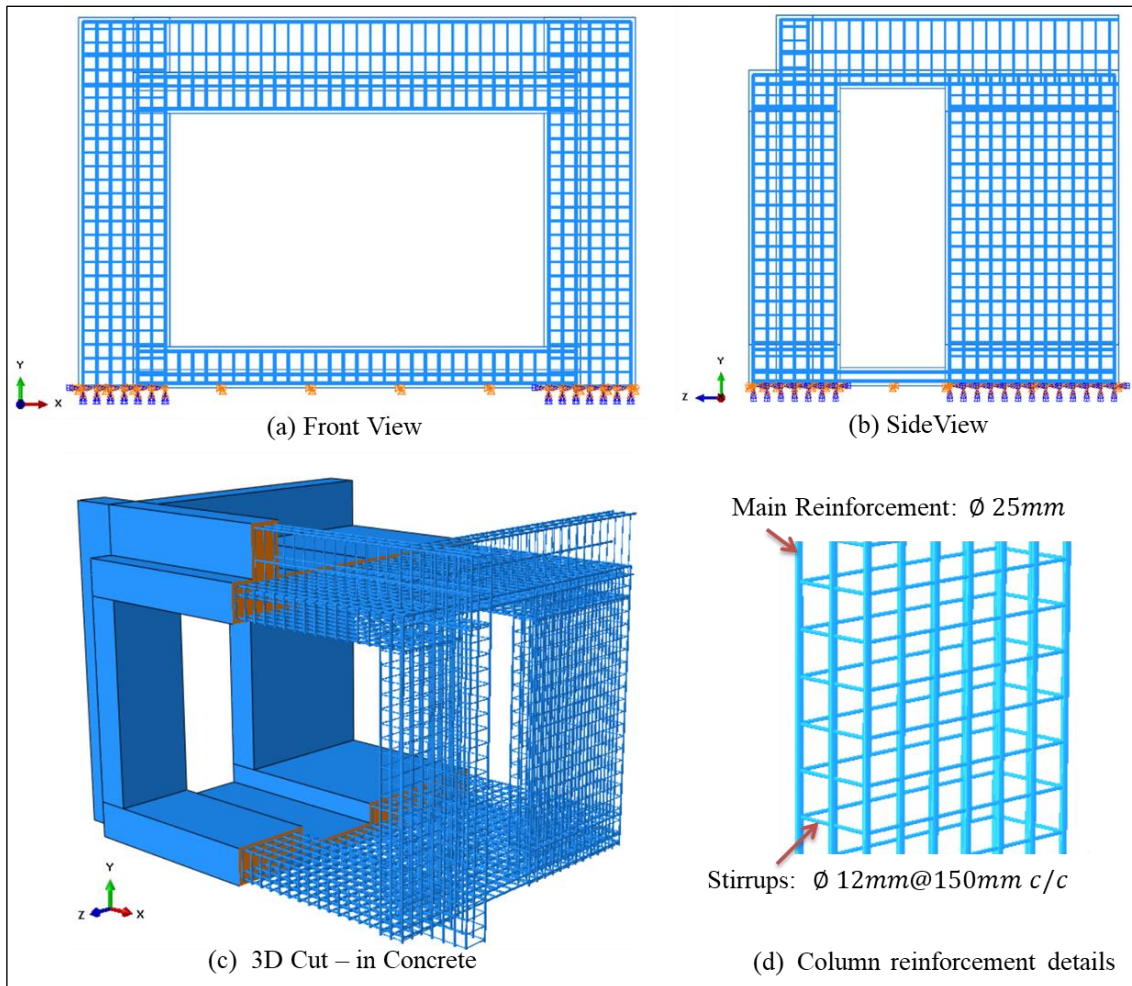


Fig. 7.50: Reinforcement and boundary conditions of the concrete frame

The material behaviour of concrete has been specified using the Concrete Damage Plasticity (CDP) model. CDP model provides a general capability of modelling concrete or any quasi-brittle materials under static, dynamic or cyclic loading. The model was first introduced by Lubliner, et al. [172] for monotonic loading, and later was extended, by Lee and Fenves [173], for dynamic and cyclic loading. The CDP is selected here as it allows the definition of plastic range together with strain rate hardening and damage, both in tension and compression, using a set of adjustable parameters measured experimentally for any type of concrete [174].

The typical uniaxial compression and tensile stress-strain curves, specified by CDP model, are shown in Fig. 7.51. The compression response starts with an elastic phase till reaching initial yield (σ_{c0}). Then, it is followed by plastic hardening phase up to an ultimate stress (σ_{cu}). The final phase is the stress-softening response, as illustrated by Fig. 7.51 (a). In uniaxial tension, the response follows a linear elastic phase up to a

failure stress (σ_{t0}), beyond which, the formation of micro-cracks is presented by a softening/cracking phase, inducing strain localization in the concrete [39].

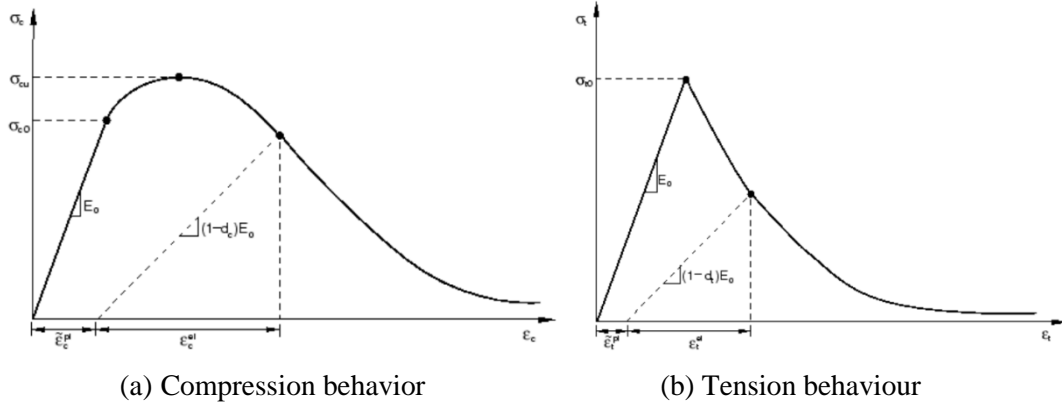


Fig. 7.51: The typical uniaxial compression and tensile stress-strain constitutive relations in the CDP model [39].

In ABAQUS built-in CDP model, the non-linear response of concrete is defined as tabular input of stress-inelastic strain. From experimental stress-strain curves, the inelastic/cracking strain can be calculated as,

$$\begin{aligned}\varepsilon_c^{in} &= \varepsilon_c - \frac{\sigma_c}{E_0}, \\ \varepsilon_t^{in} &= \varepsilon_t - \frac{\sigma_t}{E_0},\end{aligned}\tag{7.11}$$

where, the subscripts c and t refer to the compression and tension, respectively; ε_c^{in} and ε_t^{in} are the inelastic strains; ε_c and ε_t are the total strains; σ_c and σ_t are the stresses; and E_0 is the initial (undamaged) elastic modulus.

The stiffness degradation is considered by defining two scalar variables; compressive damage parameter (d_c), and tensile damage parameter (d_t). They are assumed to be functions of plastic strains and can take values from zero (representing the undamaged material), to one (representing the complete damage) [39]. Damage parameters can be calculated as follow,

$$d_c = 1 - \frac{\sigma_c E_0^{-1}}{\sigma_c E_0^{-1} + \varepsilon_c^{in} (1-b_c)},\tag{7.12}$$

$$d_t = 1 - \frac{\sigma_t E_0^{-1}}{\sigma_t E_0^{-1} + \varepsilon_t^{in} (1-b_t)},$$

where the proportional factors, b_c and b_t , range between 0-1 and can be determined experimentally based on curve-fitting of cyclic uniaxial compressive and tension tests. The inelastic strains (ε_c^{in} and ε_t^{in}) and damage parameters (d_c and d_t) are automatically converted by ABAQUS to plastic strains (ε_c^{pl} and ε_t^{pl}) using,

$$\begin{aligned} \varepsilon_c^{pl} &= \varepsilon_c^{in} - \frac{d_c}{(1-d_c)} \frac{\sigma_c}{E_0}, \\ \varepsilon_t^{pl} &= \varepsilon_t^{in} - \frac{d_t}{(1-d_t)} \frac{\sigma_t}{E_0}. \end{aligned} \tag{7.13}$$

Stiffness recovery factors for compression (ω_c) and tension (ω_t) can be specified for reverse loading. The compressive stiffness can be assumed as recoverable after crack closure, when the load changes from tension to compression, i.e., $\omega_c=1$. However, tensile stiffness is not recoverable, as crushing micro-cracks have already developed at that stage, i.e., $\omega_t = 0$ [39, 174]. The later values are the default stiffness recovery factors defined in ABAQUS, which give the load cycle presented in Fig. 7.52.

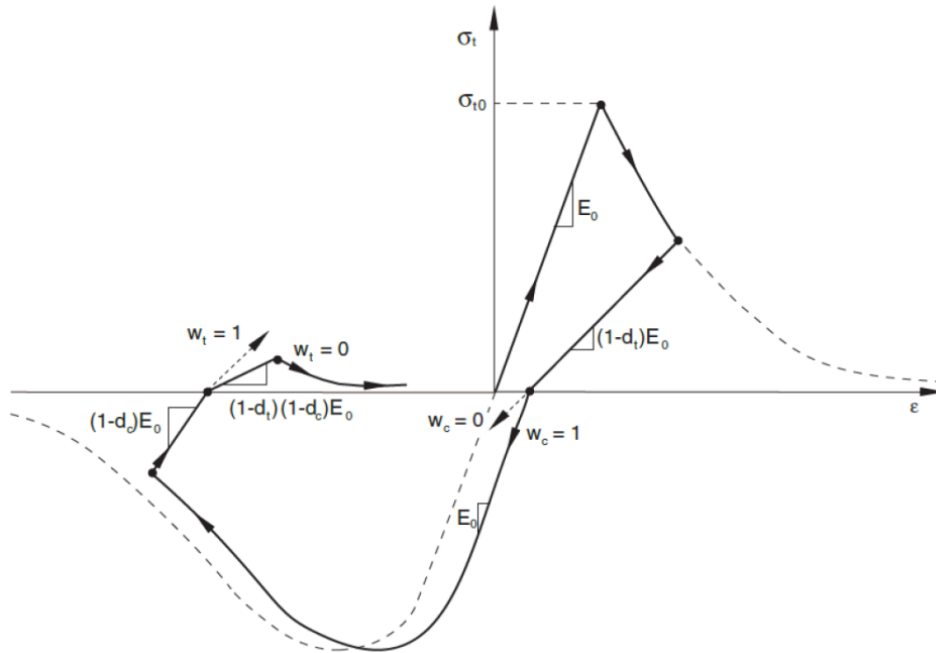


Fig. 7.52: The uniaxial load cycle of CDP model with default stiffness recovery factors [39]

From the point of view of herein study, it is critical to model the increase of concrete strength at high strain rates, for both compression and tensile behaviour. The Dynamic Increase Factor (DIF) for normal strength of concrete is well-documented in the literature [175-177]. Fig. 7.53 shows the strain rate-DIF relationship based on different studies [178]. Millard, et al. [179], state that those DIF can be used in a conservative design of UHP-FRC structures. Based on Fig. 7.53, Table 7.10 was prepared, for the range of strain rates expected in the model.

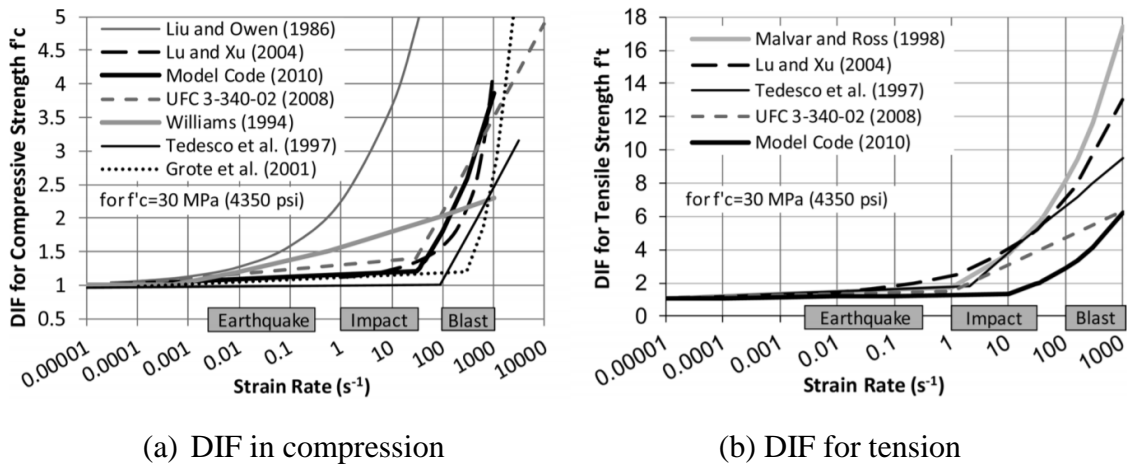


Fig. 7.53: Strain rate-DIF relationship for compression and tension, adopted from [178]

Table 7.10: Dynamic Increase Factors (DIF) implemented in the concrete material model

Strain rate	Dynamic Increase Factors (DIF)	
	Compression	Tension
0.01	1	1
1	1.2	2
100	1.8	4

As an input values for the ABAQUS Concrete Damage Plasticity (CDP) model, the material parameters of the UHP-FRC, are adopted from [171], and listed in Table 7.11.

Table 7.11: UHP-FRC material parameters (adopted from [171])

Description	Value	Description	Value
Modulus of Elasticity	43970 MPa	Eccentricity	0.1
Poisson's ratio	0.2	K_c	0.666
Mass density	$2.565 \cdot 10^{-9} \text{ t/mm}^3$	σ_{b0}/σ_{c0}	1.16
Dilation angle	39°	Viscosity parameter	0.0001

The quasi-static tension and compression stress-strain relationships for the UHP-FRC applied in the modelling, are based on the experimental tests, presented by Yang, et al. [180]. Then, they were increased, for different strain rates, based on the dynamic increase factor listed earlier in Table 7.10. Using Eq. (7.13), and damage parameters (presented in Fig. 7.54), the plastic strains were computed and then plotted versus compressive and tensile stresses (as shown in Fig. 7.55). It is clear that peak quasi-static compressive strength is 196.7 MPa while the tension strength is 13 MPa (for strain rate $\sim 0.01 \text{ s}^{-1}$), which reflects the high strength and ductility of this type of concrete.

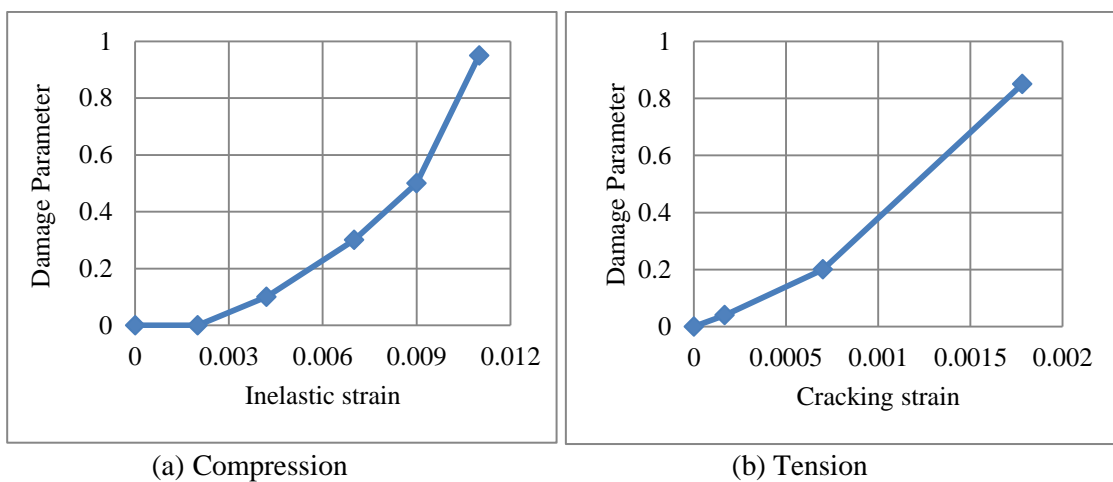


Fig. 7.54: Damage parameters, adopted in the CDP material model of the UHP-FRC, with respect to the inelastic and cracking strains of uniaxial compression and tension, respectively.

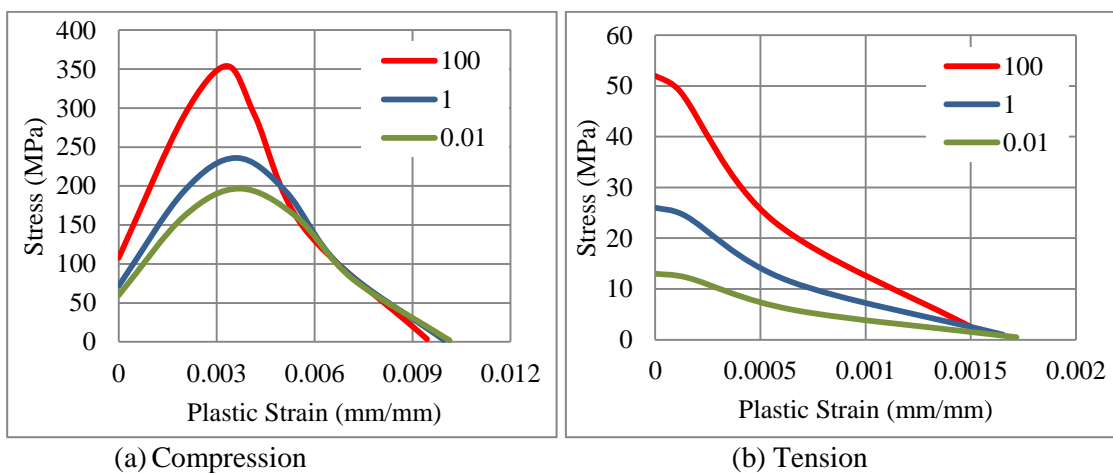


Fig. 7.55: Plastic strain with respect to compressive and tensile stresses, for different strain rates, adopted in the CDP material model of the UHP-FRC, presented in this study.

The discussed constitutive parameters for concrete were then applied to check supporting structure validity for the $M=100\text{kg}$, $R=5\text{m}$ explosion. It is important to mention that the standoff distance $R=5\text{m}$ is counted from the centroid of the explosive mass to the steel gate. While the concrete frame was 1m closer to the detonation source (Fig. 7.49), therefore, the blast peak overpressure on concrete frame was 8 MPa ; more than the 6.6 MPa limit specified in this thesis. Under the recently mentioned intense blast pressure, the reinforcement was successful in keeping the integrity of the concrete frame, gate and UGADs in place. However, although UHP-FRC with sufficient reinforcement was used, the concrete frame experienced tension damage in the form of multiple cracks. This can be linked to the fact that the concrete frame (with longest exposed dimension= $6100\text{mm} > R=4\text{m}$) is within the ‘close-range’ concentrated blast pressure. To prevent such tension cracks in the concrete for $M=100\text{kg}$, the standoff distance have to be increased through vehicle barriers/bullroads. Therefore, in the next stage of this study, the closest allowable stand-off distance was investigated. It was found that the standoff distance should be doubled to $R=10\text{m}$ ($R=9\text{m}$ to the concrete frontal face).

Thus, for the $M=100\text{kg}$ at $R=10\text{m}$, results revealed that the reinforcement stays in the elastic range (as shown in Fig. 7.56). In terms of the concrete, no damage in compression was observed with very limited tension cracks that can be neglected. Fig. 7.57 shows the tension and compression damage in the concrete material.

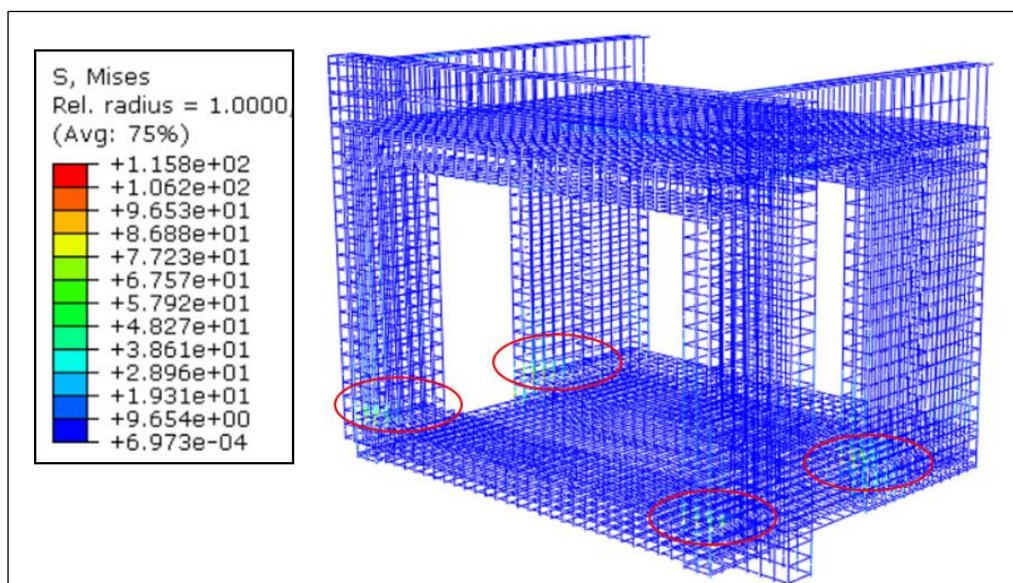


Fig. 7.56: Distribution of peak HMH stresses in the steel reinforcement, for $M=100\text{kg}$ TNT, $R=10\text{m}$.

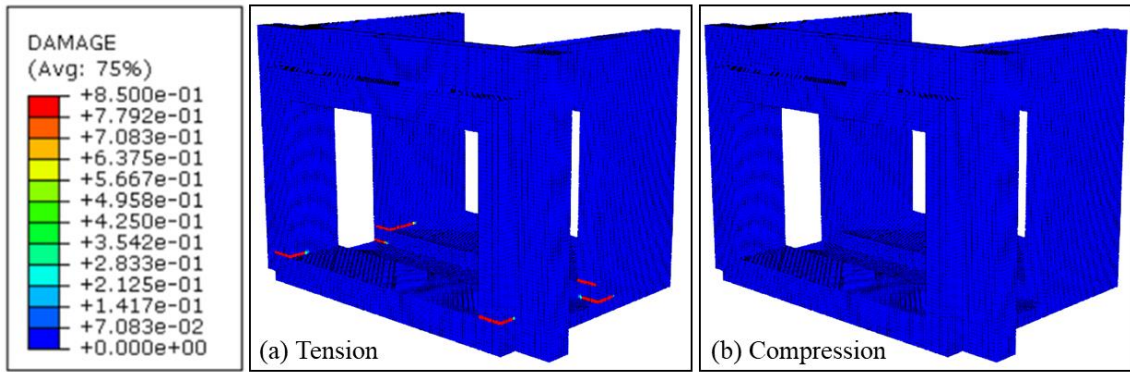


Fig. 7.57: Tension and compression damage in the concrete material, for M=100kg TNT, R=10m.

The deformations of the concrete frame was also checked, as excessive elastic deflections may indirectly influence the performance of the UGADs, and hence the operability of the gate. Fig. 7.58 shows peak elastic deflections in the concrete frame and its reinforcement, for M=100kg TNT, R=10m. The deflections are increasing gradually from 0 (near the base) to only 1mm (in the area supporting upper UGADs). The influence of such a drift of $(1/3000)=0.03\%$ is very small and can be neglected. The maximum deflections can be seen at upper inverted beams with peak value of only 1.38mm.

In short, the concrete structure proposed in this section showed to be effective in supporting the gate and the UGADs. It was demonstrated that, for M=100kg and R=10m, the performance of the steel reinforcement was in the elastic range, with minimal damage in UHP-FRC that can be accepted. Further re-designing of the concrete frame, for M=100kg and R=5m, is the author’s interest as a future task.

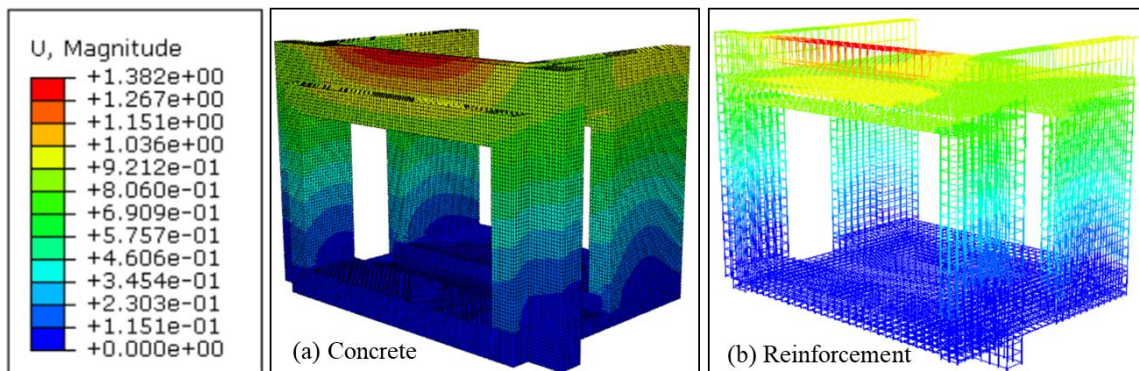


Fig. 7.58: Peak deflections (mm) in the concrete fame and reinforcement, for M=100kg TNT, R=10m.

The final numerical model (Gate, UGADs and the reinforced concrete support) consists of 2976364 elements, from which 387776 are linear hexahedral elements of type C3D8R, 2560560 are linear quadrilateral elements of type S4R and 28028 are linear line elements of type B31. The computational time of running the model with the explicit solver, on 8 cores processor, was approximately 25 hrs.

The final step was to look at the energy components, to check the accuracy of the whole numerical model (Gate, UGADs and the reinforced concrete support). According to Fig. 7.59, the internal energy was mainly composed of plastic and frictional energy dissipations. About 93% of the kinetic energy was dropped sharply in only 0.01s, showing the superior influence of the UGADs to eliminate the movement of the gate. Finally, the artificial strain energy was so small, fluctuating near zero, which reflects the accuracy of the whole numerical model.

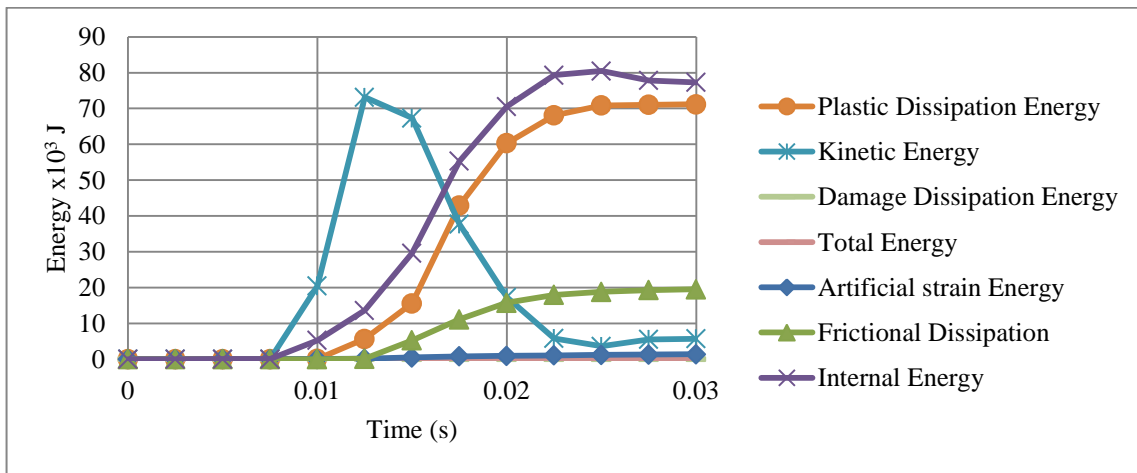


Fig. 7.59: Energy components in the whole numerical model (Gate, UGADs and the reinforced concrete support), subjected to a blast pressure from 100kg of TNT, R=10m

CONCLUSIONS

The aim of this thesis was the design of a new passive damping system, of auxetic nature, for the supporting frame of a relatively light weight-operable blast resistant steel gate that can resist multiple high intensity blast pressure, of up to 6.6 MPa. The objectives of this research, mentioned in (Chapter 1, Section 1.2), are answered briefly here in the same order:

1. The reviewed literature in Chapter 3 shows first that steel gate failure mechanism depends mainly on boundary conditions, loading pattern and corresponding reaction forces. Moreover, design of a relatively light-weight gate that could sustain 6.6 MPa of pressure was a challenging target in this thesis. In addition, the unique behavior of negative poisson's ratio in auxetics provides superior energy absorption. Lastly, use of passive dampers in general and auxetics in particular, in the supporting frame of blast resistant gates has been unnoticed. Therefore, this thesis, "*Application of passive damping systems in blast resistant gates*", tries to fill this original gap.
2. Reaction forces and their influence by boundary conditions, aspect ratios, explosive charge and stand-off distance were investigated (Chapter 5). Static analyses revealed that the numerical results were of high similarity to the analytical outcomes. For dynamic loading, distributed reaction forces on the edges of the plates had different values than the static one. The average increase or decrease in the reaction for each supporting edge of a case was examined through a dynamic/static ratio $(D/S)_{avg}$. Less constrained BC cases, such as SSSS and SFSF, revealed lower $(D/S)_{avg}$ than more constrained cases, CCCC and CFCF, since the motion of the plates are greater than that of the clamped cases, thus reducing the transmitted impulse and, as a consequence, the effects of the blast. In addition, simply supported cases were less sensitive to aspect ratio change, as the other two edges were already unsupported. Therefore, the distribution of reaction forces in simply supported cases expected to allow efficient implementation of shock absorbers at the supports. The study selects SFSF case as the optimum option. The effect of changing the explosive mass or position on reaction forces was then examined. Results revealed that the percentage

of increase in reaction forces due to mass change was approximately linear. On the other hand, the increase in stand-off distance led to a sharp drop in reaction forces. Finally, changing the position of the centroid of the explosive material in a plane parallel to the plate under consideration had negligible effect on reaction forces.

3. The case study and threat possibilities were described in addition to geometrical and material properties of the gate (Chapter 6). In addition, the numerical model was validated based on detailed mesh analysis. The design of the gate was based on 4 levels of blast pressures, 1.65 MPa, 3.3 MPa, 4.95 MPa and the maximum 6.6 MPa, achieved from 25kg, 50kg, 75kg and 100kg of TNT at R=5m, respectively. The analysis looked at five fields, namely, reaction forces, maximum plastic strain, permanent deformation, operability and energy components. The structural response of 4 gates, G2.5, G5, G7.5 and G10, were numerically assessed. Reaction forces in x and y directions are very small compared to the out-of-plane z - axis (direction of blast). Therefore, RF_z was the considered component in this thesis as it is the prominent one. The passive dampers that would be attached later on may work for G5, G7.5 or G10 in the same efficiency, as the mass shown to have slight effect on RFs. Gate G10 was the only gate that satisfied operability condition (without dampers) after the blast event, with peak $d_{frame} = 4.4mm$. The plastic dissipation energy found to be decreasing with increasing the thickness t . In addition, artificial strain energy was only 2% of the total internal energy which reflects the accuracy of the numerical model.
4. A thorough parametric study was conducted in Chapter 7 to design a new uniaxial graded auxetic damper (UGAD). Then, its static and dynamic constitutive relations were derived and validated analytically. The proposed UGAD consists of 4 main components, which are the bearing plate, piston, damper body and 3 auxetic cores, for 3 different blast levels. The parametric study, presented in Section 7.2, focused on 6 parameters that had to be optimized for better performance of the UGAD. The selected parameters were loading direction D1, cell dimension B (L=10mm), aluminum grade AL3 (6063-T4), cell angle $\theta=60^\circ$, auxetic rather than honeycomb, and lastly; 8-12 layers was the range for effective number of layers. In terms of cell wall thickness t of the auxetic cores, the lightest-most effective 3 auxetic cores that was fitted in the UGAD; namely Aux.1, Aux.2 and Aux.3, had cell wall thickness t of 1.4, 1.8 and 2.2mm, respectively. The selection of optimum parameters were based on the ratio of reaction force to applied load (RF_d/P) and plastic dissipation

energy (PDE). A very good agreement was noticed between the numerical and analytical plateau region for all impact velocities, which can be considered as a validation of the auxetic core numerical model. The performance of the 3 auxetic cores together have led to wide plateau region (80% of total crushing strain) and variant strength range (1-10 MPa), which in return, can justify the superior performance of the UGAD under different blast levels. The auxetic nature (negative Poisson's ratio) and transverse shrink make it easier to change the compressed auxetic core in the UGAD after a blast event.

5. The behavior of the remaining 3 gates; G2.5, G5 and G7.5; were assessed with the application of the proposed UGAD. Both G7.5 and G5 passed the operability requirement. With the addition of the UGADs, the frame permanent deformation of G5 decreased from 40.5 to 22mm, making G5 as the lightest-operable option that can withstand the blast pressure target of 6.6 MPa. In addition, 49% reduction in peak reaction forces was recorded which can reduce the required cross section and strength of the concrete supports. Results also showed that internal energy in the whole model composed mainly of plastic dissipation, small frictional dissipation, and no dissipation due to damage. 56% of the total plastic dissipation energy in the system was achieved from the UGADs, while 44% from the gate. Based on that successful energy dissipation, the kinetic energy was mitigated. The additional plastic dissipation energy gained from those sacrificial light-weight auxetic cores justifies the significant reduction in permanent deformations and reaction forces. Finally, a proper reinforced concrete supporting frame was designed, and showed to stay in the elastic range.

The novel uniaxial graded auxetic damper (UGAD) proposed in this thesis can be designed to withstand other blast pressures, based on changing the cell-wall thickness of its auxetic cores. In addition, the UGAD idea may be used in different scales for other structural applications, such as; blast-resistant façade for retrofitting sensitive buildings; Elevator (absorbing unexpected crash of elevators or cable failure in multi-story buildings); Crash energy absorbing systems in motor vehicles' front bumpers; and many other possible applications. For future research, the author recommends testing the same UGAD for other applications, trying different auxetic topologies or materials. Herein the additive manufacturing techniques are of main importance.

Bibliography

- [1] T. Ngo, P. Mendis, A. Gupta, and J. Ramsay, "Blast loading and blast effects on structures—an overview," *Electronic Journal of Structural Engineering*, vol. 7, pp. 76-91, 2007.
- [2] M. Anderson and D. Dover, "Lightweight, blast-resistant doors for retrofit protection against the terrorist threat," in *2nd International Conference on Innovation in Architecture, Engineering and Construction (AEC)*, Loughborough University, UK, 2003.
- [3] W. Chen and H. Hao, "Experimental investigations and numerical simulations of multi-arch double-layered panels under uniform impulsive loadings," *International Journal of Impact Engineering*, vol. 63, pp. 140-157, 2014.
- [4] W. Chen, "Experimental and Numerical Studies of Novel Protective Panels Against Blast and Impact Loadings," Doctoral Dissertation, University of Western Australia, 2013.
- [5] W. Chen and H. Hao, "Numerical study of a new multi-arch double-layered blast-resistance door panel," *International Journal of Impact Engineering*, vol. 43, pp. 16-28, 2012.
- [6] N. Yun, D. Shin, S. Ji, and C. Shim, "Experiments on blast protective systems using aluminum foam panels," *KSCE Journal of Civil Engineering*, vol. 18, pp. 2153-2161, 2014.
- [7] Q. Fang, L. Chen, and M. Du, "Theoretical and numerical investigations in effects of end-supported springs and dampers on increasing resistance of blast doors," *Engineering Mechanics*, vol. 3, p. 035, 2008.
- [8] G. Imbalzano, P. Tran, T. D. Ngo, and P. V. Lee, "A numerical study of auxetic composite panels under blast loadings," *Composite Structures*, vol. 135, pp. 339-352, 2016.
- [9] X. Hou, Z. Deng, and K. Zhang, "Dynamic Crushing Strength Analysis of Auxetic Honeycombs," *Acta Mechanica Solida Sinica*, vol. 29, pp. 490-501, 2016.
- [10] S. Mannan, *Lees' Process Safety Essentials: Hazard Identification, Assessment and Control*: Butterworth-Heinemann, 2013.
- [11] FEMA (Federal Emergency Management Agency), "Primer for Design of Commercial Buildings to Mitigate Terrorist Attacks," ed. USA: FEMA, 2003.

- [12] H. Draganić and V. Sigmund, "Blast loading on structures," *Tehnicki vjesnik / Technical Gazette*, vol. 19, p. p643, 2012.
- [13] D. Dusenberry, *Handbook for blast resistant design of buildings*: John Wiley & Sons, 2010.
- [14] A. Brara and J. Klepaczko, "Experimental characterization of concrete in dynamic tension," *Mechanics of materials*, vol. 38, pp. 253-267, 2006.
- [15] J. M. Biggs and B. Testa, *Introduction to structural dynamics*. New York: McGraw Hill, 1964.
- [16] EN 1991-1-7, "Eurocode 1-Actions Of Structures-Part 1-7: General Actions: Accidental Actions," *Brussels, European Committee for Standardization*, 2006.
- [17] US DoD (US Department of Defence), *United Facilities Criteria UFC 3-340-02, Structures to resist the effects of accidental explosions*. Washington DC, USA: US Government Printing Office, 2008.
- [18] W. Wang, D. Zhang, F. Lu, and R. Liu, "A new SDOF method of one-way reinforced concrete slab under non-uniform blast loading," *Structural Engineering and Mechanics*, vol. 46, pp. 595-613, 2013.
- [19] S. A. Mazek, "Performance of sandwich structure strengthened by pyramid cover under blast effect," *Structural Engineering and Mechanics*, vol. 50, pp. 471-486, 2014.
- [20] K. Lee, T. Kim, and J. Kim, "Local response of W-shaped steel columns under blast loading," *Structural engineering and mechanics*, vol. 31, pp. 25-38, 2009.
- [21] S. Gong, Y. Lu, Z. Tu, and W. Jin, "Validation study on numerical simulation of RC response to close-in blast with a fully coupled model," *Structural Engineering and Mechanics*, vol. 32, pp. 283-300, 2009.
- [22] P. W. Sielicki, "Masonry Failure under Unusual Impulse Loading," PhD Thesis, Publishing House of Poznan University of Technology, Poznan, Poland, 2013.
- [23] C. Amadio and C. Bedon, "FE assessment of dissipative devices for the blast mitigation of glazing façades supported by prestressed cables," *Structural Engineering and Mechanics*, vol. 51, pp. 141-162, 2014.
- [24] P. Sielicki, T. Łodygowski, H. Al-Rifaie, and W. Sumelka, "Designing of Blast Resistant Lightweight Elevation System-Numerical Study," *Procedia Engineering*, vol. 172, pp. 991-998, 2017.
- [25] R. Andreotti, M. Colombo, A. Guardone, P. Martinelli, G. Riganti, and M. di Prisco, "Performance of a shock tube facility for impact response of structures," *International Journal of Non-Linear Mechanics*, vol. 72, pp. 53-66, 2015.

- [26] E. Courtney, A. Courtney, and M. Courtney, "Shock tube design for high intensity blast waves for laboratory testing of armor and combat materiel," *Defence Technology*, vol. 10, pp. 245-250, 2014.
- [27] A. Freidenberg, A. Aviram, L. K. Stewart, D. Whisler, H. Kim, and G. A. Hegemier, "Demonstration of tailored impact to achieve blast-like loading," *International Journal of Impact Engineering*, vol. 71, pp. 97-105, 2014.
- [28] T. Rodriguez-Nikl, G. Hegemier, and F. Seible, "Blast simulator testing of structures: methodology and validation," *Shock and vibration*, vol. 18, pp. 579-592, 2011.
- [29] P. Huson, R. J. Asaro, L. Stewart, and G. A. Hegemier, "Non-explosive methods for simulating blast loading of structures with complex geometries," *International Journal of Impact Engineering*, vol. 38, pp. 546-557, 2011.
- [30] Dassault Systems. *Abaqus Unified FEA, Complete Solutions For Realistic Simulation*.
- [31] Dassault Systèmes, "ABAQUS documentation collection," 2013.
- [32] X. Luo, X. Qian, H. Zhao, and P. Huang, "Simulation analysis on structure safety of refuge chamber door under explosion load," *Procedia Engineering*, vol. 45, pp. 923-929, 2012.
- [33] X. Lu and J. Jiang, "Dynamic FEA and Simulation for A Series of Blast-Resist-door," *Proceedings of ISSST*, pp. 839-843, 2002.
- [34] V. Salomoni, G. Mazzucco, G. Xotta, R. Fincato, C. Majorana, and M. Schiavon, "Nonlinear Modelling, Design, and Test of Steel Blast-Resistant Doors," *Advances in Mechanical Engineering*, vol. 5, p. 908373, 2013.
- [35] L. Chen, Q. Fang, Y. Zhang, and Y. Zhang, "Rate-sensitive numerical analysis of dynamic responses of arched blast doors subjected to blast loading," *Transactions of Tianjin University*, vol. 14, pp. 348-352, 2008.
- [36] Dassault Systèmes, *Abaqus Theory Manual*, 2009.
- [37] N. Rebelo, J. Nagtegaal, L. Taylor, and R. Passman, "Comparison of implicit and explicit finite element methods in the simulation of metal forming processes," in *ABAQUS Users Conf., Newport, RI*, 1992.
- [38] T. Devarco, S. Shaw, and D. Thomas, *MSC Nastran Explicit Nonlinear User Guide* vol. SOL 700. USA: MSC. Software Corporation, 2012.
- [39] Dassault Systèmes, *Abaqus documentation*. USA: Dassault Systemes Simulia Corporation, 2016.
- [40] D. Hyde, "Conventional weapons program (ConWep) US Army Waterways Experimental Station," *Vicksburg, MS, USA*, 1991.

- [41] C. Kingery and G. Bulmash, "Technical Report ARBRL-TR-02555: Air Blast Parameters from TNT Spherical Air Burst and Hemispherical Burst," *AD-B082*, vol. 713, 1984.
- [42] P. Mamrak, "Pressure evolution inside complex corridor system induced by blast action," Master of Science, Faculty of Civil and Environmental Engineering, Poznan University of Technology, Poland, 2011.
- [43] C. Mougeotte, P. Carlucci, S. Recchia, and H. Ji, "Novel approach to conducting blast load analyses using Abaqus/Explicit-CEL," in *2010 SIMULIA Customer Conference*, 2010.
- [44] D. Bonorchis and G. Nurick, "The effect of welded boundaries on the response of rectangular hot-rolled mild steel plates subjected to localised blast loading," *International journal of impact engineering*, vol. 34, pp. 1729-1738, 2007.
- [45] G. Nurick and G. Shave, "The deformation and tearing of thin square plates subjected to impulsive loads-an experimental study," *International Journal of Impact Engineering*, vol. 18, pp. 99-116, 1996.
- [46] S. C. K. Yuen, G. Nurick, G. Langdon, and Y. Iyer, "Deformation of thin plates subjected to impulsive load: Part III—an update 25 years on," *International Journal of Impact Engineering*, 2016.
- [47] N. Rudrapatna, R. Vaziri, and M. Olson, "Deformation and failure of blast-loaded square plates," *International Journal of Impact Engineering*, vol. 22, pp. 449-467, 1999.
- [48] E. Borenstein and H. Benaroya, "Loading and structural response models of circular plates subjected to near field explosions," *Journal of Sound and Vibration*, vol. 332, pp. 1725-1753, 2013.
- [49] V. Feldgun, D. Yankelevsky, and Y. Karinski, "A nonlinear SDOF model for blast response simulation of elastic thin rectangular plates," *International Journal of Impact Engineering*, vol. 88, pp. 172-188, 2016.
- [50] N. Jacob, G. Nurick, and G. Langdon, "The effect of stand-off distance on the failure of fully clamped circular mild steel plates subjected to blast loads," *Engineering Structures*, vol. 29, pp. 2723-2736, 2007.
- [51] R. Curry and G. Langdon, "Transient response of steel plates subjected to close proximity explosive detonations in air," *International Journal of Impact Engineering*, 2016.
- [52] V. Aune, G. Valsamos, F. Casadei, M. Larcher, M. Langseth, and T. Børvik, "Numerical study on the structural response of blast-loaded thin aluminium and steel plates," *International Journal of Impact Engineering*, vol. 99, pp. 131-144, 2017.

- [53] C. Koh, K. Ang, and P. Chan, "Dynamic analysis of shell structures with application to blast resistant doors," *Shock and Vibration*, vol. 10, pp. 269-279, 2003.
- [54] J. Shen, G. Lu, Z. Wang, and L. Zhao, "Experiments on curved sandwich panels under blast loading," *International Journal of Impact Engineering*, vol. 37, pp. 960-970, 2010.
- [55] J. Shen, G. Lu, L. Zhao, and Z. Qu, "Response of curved sandwich panels subjected to blast loading," *Journal of Performance of Constructed Facilities*, vol. 25, pp. 382-393, 2011.
- [56] L. Chen, F. Qin, Z. Ya-Dong, Z. Yi, and F. Jun-Yu, "Numerical and Experimental Investigations on the blast-resistant properties of arched RC blast doors," *International Journal of Protective Structures*, vol. 1, pp. 425-441, 2010.
- [57] M. Hsieh, J. Hung, and D. Chen, "Investigation on the blast resistance of a stiffened door structure," *Journal of Marine Science and Technology*, vol. 16, pp. 149-157, 2008.
- [58] A. Mohammed, K. Rao, and H. Abdulkader, "Analysis of Plates Subjected to Blast Loads," 2013.
- [59] M. D. Goel, V. A. Matsagar, and A. K. Gupta, "Dynamic response of stiffened plates under air blast," *International Journal of Protective Structures*, vol. 2, pp. 139-155, 2011.
- [60] L. S. B. Veeredhi and N. R. Rao, "Studies on the Impact of Explosion on Blast Resistant Stiffened Door Structures," *Journal of The Institution of Engineers (India): Series A*, vol. 96, pp. 11-20, 2015.
- [61] TM5-1300, "Structures to Resist the Effects of Accidental Explosions," ed. USA: US Departments of Army, US Navy, Air Force, 1990.
- [62] T. W. Morgan, "Lightweight armored panels and doors," ed: Google Patents, 2003.
- [63] M. C. Mandall, "Ablative blast resistant security door panel," ed: Google Patents, 2006.
- [64] C. W. De Silva, *Vibration damping, control, and design*: CRC Press, 2007.
- [65] S. Adhikari, *Structural dynamic analysis with generalized damping models: analysis*: John Wiley & Sons, 2013.
- [66] R. Lewandowski and Z. Pawlak, "Dynamic analysis of frames with viscoelastic dampers modelled by rheological models with fractional derivatives," *Journal of sound and Vibration*, vol. 330, pp. 923-936, 2011.
- [67] H. Al-Rifaie and S. Wilkinson, "Improving the Seismic Performance of Buildings by Increasing Structural Damping," in *Proceedings of the Fifteenth*

- International Conference on Civil, Structural and Environmental Engineering Computing*, J. Kruis, Y. Tsompanakis, and B. H. V. Topping, Eds., ed Stirlingshire, UK: Civil-Comp Press, 2015.
- [68] H. Al-Rifaie, A. Glema, and M. Malendowski, "Vertical Seismic Load Effects on the Response of Structures with Toggle Brace Dampers," in *Proceedings of the Fifteenth International Conference on Civil, Structural and Environmental Engineering Computing*, J. Kruis, Y. Tsompanakis, and B. H. V. Topping, Eds., ed Stirlingshire, UK: Civil-Comp Press, 2015.
- [69] C. W. De Silva, *Vibration: fundamentals and practice*: CRC press, 2006.
- [70] M. Yang and P. Qiao, "High energy absorbing materials for blast resistant design," *Blast Protection of Civil Infrastructures and Vehicles Using Composites*, p. 88, 2010.
- [71] H. S. Monir, "Flexible blast resistant steel structures by using unidirectional passive dampers," *Journal of Constructional Steel Research*, vol. 90, pp. 98-107, 2013.
- [72] W. Chen and H. Hao, "Numerical study of blast-resistant sandwich panels with rotational friction dampers," *International Journal of Structural Stability and Dynamics*, vol. 13, p. 1350014, 2013.
- [73] C. Bedon and C. Amadio, "Passive control systems for the blast enhancement of glazing curtain walls under explosive loads," *The Open Civil Engineering Journal*, vol. 11, 2017.
- [74] F. Zhu, G. Lu, D. Ruan, and Z. Wang, "Plastic deformation, failure and energy absorption of sandwich structures with metallic cellular cores," *International Journal of Protective Structures*, vol. 1, pp. 507-541, 2010.
- [75] W. Lee, "'Cellular solids, structure and properties'," *Materials Science and Technology*, vol. 16, p. 233, 2000.
- [76] R. B. Pecherski, M. Nowak, and Z. Nowak, "Virtual metallic foams. Application for dynamic crushing analysis," *International Journal for Multiscale Computational Engineering*, vol. 15, 2017.
- [77] Z. Nowak, M. Nowak, R. Pecherski, M. Potoczek, and R. Sliwa, "Numerical simulations of mechanical properties of alumina foams based on computed tomography," *Coupled Field Problems and Multiphase Materials*, p. 107, 2017.
- [78] E. Andrews, W. Sanders, and L. J. Gibson, "Compressive and tensile behaviour of aluminum foams," *Materials Science and Engineering: A*, vol. 270, pp. 113-124, 1999.
- [79] M. F. Ashby, T. Evans, N. A. Fleck, J. Hutchinson, H. Wadley, and L. Gibson, *Metal foams: a design guide*: Elsevier, 2000.

- [80] E. Koza, M. Leonowicz, S. Wojciechowski, and F. Simancik, "Compressive strength of aluminium foams," *Materials Letters*, vol. 58, pp. 132-135, 2004.
- [81] D. Papadopoulos, I. C. Konstantinidis, N. Papanastasiou, S. Skolianos, H. Lefakis, and D. Tsipas, "Mechanical properties of Al metal foams," *Materials letters*, vol. 58, pp. 2574-2578, 2004.
- [82] L. Peroni, M. Avalle, and M. Peroni, "The mechanical behaviour of aluminium foam structures in different loading conditions," *International Journal of Impact Engineering*, vol. 35, pp. 644-658, 2008.
- [83] H. N. Wadley, K. P. Dharmasena, M. He, R. M. McMeeking, A. G. Evans, T. Bui-Thanh, *et al.*, "An active concept for limiting injuries caused by air blasts," *International Journal of Impact Engineering*, vol. 37, pp. 317-323, 2010.
- [84] L. J. Gibson and M. F. Ashby, *Cellular solids: structure and properties*: Cambridge university press, 1999.
- [85] K. P. Dharmasena, H. N. Wadley, Z. Xue, and J. W. Hutchinson, "Mechanical response of metallic honeycomb sandwich panel structures to high-intensity dynamic loading," *International Journal of Impact Engineering*, vol. 35, pp. 1063-1074, 2008.
- [86] X. Li, P. Zhang, Z. Wang, G. Wu, and L. Zhao, "Dynamic behavior of aluminum honeycomb sandwich panels under air blast: Experiment and numerical analysis," *Composite Structures*, vol. 108, pp. 1001-1008, 2014.
- [87] H. Rathbun, D. Radford, Z. Xue, M. He, J. Yang, V. Deshpande, *et al.*, "Performance of metallic honeycomb-core sandwich beams under shock loading," *International journal of solids and structures*, vol. 43, pp. 1746-1763, 2006.
- [88] L. Hu and T. Yu, "Dynamic crushing strength of hexagonal honeycombs," *International Journal of Impact Engineering*, vol. 37, pp. 467-474, 2010.
- [89] D. Okumura, N. Ohno, and H. Noguchi, "Post-buckling analysis of elastic honeycombs subject to in-plane biaxial compression," *International Journal of Solids and Structures*, vol. 39, pp. 3487-3503, 2002.
- [90] Z. Zou, S. Reid, P. Tan, S. Li, and J. Harrigan, "Dynamic crushing of honeycombs and features of shock fronts," *International Journal of Impact Engineering*, vol. 36, pp. 165-176, 2009.
- [91] D. Ruan, G. Lu, B. Wang, and T. X. Yu, "In-plane dynamic crushing of honeycombs—a finite element study," *International Journal of Impact Engineering*, vol. 28, pp. 161-182, 2003.
- [92] S. Xu, J. H. Beynon, D. Ruan, and G. Lu, "Experimental study of the out-of-plane dynamic compression of hexagonal honeycombs," *Composite Structures*, vol. 94, pp. 2326-2336, 2012.

- [93] A. A. Nia and M. Sadeghi, "The effects of foam filling on compressive response of hexagonal cell aluminum honeycombs under axial loading-experimental study," *Materials & Design*, vol. 31, pp. 1216-1230, 2010.
- [94] G. Imbalzano, S. Linforth, T. D. Ngo, P. V. S. Lee, and P. Tran, "Blast resistance of auxetic and honeycomb sandwich panels: Comparisons and parametric designs," *Composite Structures*, 2017.
- [95] T. Lim, *Auxetic materials and structures*: Springer, 2014.
- [96] R. Lakes, "Foam structures with a negative Poisson's ratio," *Science*, vol. 235, pp. 1038-1041, 1987.
- [97] R. Lakes, "Advances in negative Poisson's ratio materials," *Advanced Materials*, vol. 5, pp. 293-296, 1993.
- [98] A. Alderson, "A triumph of lateral thought," *Chemistry & Industry*, vol. 17, pp. 384-391, 1999.
- [99] W. Yang, Z.-M. Li, W. Shi, B.-H. Xie, and M.-B. Yang, "Review on auxetic materials," *Journal of materials science*, vol. 39, pp. 3269-3279, 2004.
- [100] A. Alderson and K. Alderson, "Auxetic materials," *Proceedings of the Institution of Mechanical Engineers, Part G: Journal of Aerospace Engineering*, vol. 221, pp. 565-575, 2007.
- [101] Y. Liu and H. Hu, "A review on auxetic structures and polymeric materials," *Scientific Research and Essays*, vol. 5, pp. 1052-1063, 2010.
- [102] G. N. Greaves, "Poisson's ratio over two centuries: challenging hypotheses," *Notes Rec. R. Soc.*, vol. 67, pp. 37-58, 2013.
- [103] Y. Prawoto, "Seeing auxetic materials from the mechanics point of view: a structural review on the negative Poisson's ratio," *Computational Materials Science*, vol. 58, pp. 140-153, 2012.
- [104] A. Yeganeh-Haeri, D. J. Weidner, and J. B. Parise, "Elasticity of or-cristobalitez A silicon dioxide with a negative Poisson's ratio," *Science*, vol. 257, p. 31, 1992.
- [105] X. Zhang, H. Ding, L. An, and X. Wang, "Numerical Investigation on Dynamic Crushing Behavior of Auxetic Honeycombs with Various Cell-Wall Angles," *Advances in Mechanical Engineering*, vol. 7, p. 679678, 2015.
- [106] F. Scarpa, P. Pastorino, A. Garelli, S. Patsias, and M. Ruzzene, "Auxetic compliant flexible PU foams: static and dynamic properties," *physica status solidi (b)*, vol. 242, pp. 681-694, 2005.
- [107] F. Scarpa, J. Yates, L. Ciffo, and S. Patsias, "Dynamic crushing of auxetic open-cell polyurethane foam," *Proceedings of the Institution of Mechanical Engineers, Part C: Journal of Mechanical Engineering Science*, vol. 216, pp. 1153-1156, 2002.

- [108] T. Allen, J. Shepherd, T. Hewage, T. Senior, L. Foster, and A. Alderson, "Low-kinetic energy impact response of auxetic and conventional open-cell polyurethane foams," *physica status solidi (b)*, vol. 252, pp. 1631-1639, 2015.
- [109] T. Lim, A. Alderson, and K. Alderson, "Experimental studies on the impact properties of auxetic materials," *physica status solidi (b)*, vol. 251, pp. 307-313, 2014.
- [110] E. C. Yang, T. D. Ngo, D. Ruan, and P. Tran, "Impact resistance and failure analysis of plain woven curtains," *International Journal of Protective Structures*, vol. 6, pp. 113-136, 2015.
- [111] Y. Hou, R. Neville, F. Scarpa, C. Remillat, B. Gu, and M. Ruzzene, "Graded conventional-auxetic Kirigami sandwich structures: Flatwise compression and edgewise loading," *Composites Part B: Engineering*, vol. 59, pp. 33-42, 2014.
- [112] M. Schenk, S. D. Guest, and G. J. McShane, "Novel stacked folded cores for blast-resistant sandwich beams," *International Journal of Solids and Structures*, vol. 51, pp. 4196-4214, 2014.
- [113] C. Lira, P. Innocenti, and F. Scarpa, "Transverse elastic shear of auxetic multi re-entrant honeycombs," *Composite Structures*, vol. 90, pp. 314-322, 2009.
- [114] K. E. Evans and A. Alderson, "Auxetic materials: functional materials and structures from lateral thinking!," *Advanced materials*, vol. 12, pp. 617-628, 2000.
- [115] F. Scarpa, S. Blain, T. Lew, D. Perrott, M. Ruzzene, and J. Yates, "Elastic buckling of hexagonal chiral cell honeycombs," *Composites Part A: Applied Science and Manufacturing*, vol. 38, pp. 280-289, 2007.
- [116] W. Miller, C. Smith, and K. Evans, "Honeycomb cores with enhanced buckling strength," *Composite Structures*, vol. 93, pp. 1072-1077, 2011.
- [117] W. Liu, N. Wang, T. Luo, and Z. Lin, "In-plane dynamic crushing of re-entrant auxetic cellular structure," *Materials & Design*, vol. 100, pp. 84-91, 2016.
- [118] F. Scarpa, L. Ciffo, and J. Yates, "Dynamic properties of high structural integrity auxetic open cell foam," *Smart Materials and Structures*, vol. 13, p. 49, 2003.
- [119] M. Grujicic, R. Galgalikar, J. Snipes, R. Yavari, and S. Ramaswami, "Multi-physics modeling of the fabrication and dynamic performance of all-metal auxetic-hexagonal sandwich-structures," *Materials & Design*, vol. 51, pp. 113-130, 2013.
- [120] P. V. Pikhitsa, M. Choi, H. J. Kim, and S. H. Ahn, "Auxetic lattice of multipods," *physica status solidi (b)*, vol. 246, pp. 2098-2101, 2009.

- [121] T. Hughes, A. Marmier, and K. Evans, "Auxetic frameworks inspired by cubic crystals," *International Journal of Solids and Structures*, vol. 47, pp. 1469-1476, 2010.
- [122] T. Bückmann, N. Stenger, M. Kadic, J. Kaschke, A. Frölich, T. Kennerknecht, *et al.*, "Tailored 3D mechanical metamaterials made by dip-in direct-laser-writing optical lithography," *Advanced Materials*, vol. 24, pp. 2710-2714, 2012.
- [123] J. H. Lee, J. P. Singer, and E. L. Thomas, "Micro-/nanostructured mechanical metamaterials," *Advanced materials*, vol. 24, pp. 4782-4810, 2012.
- [124] F. Cote, V. Deshpande, N. Fleck, and A. Evans, "The out-of-plane compressive behavior of metallic honeycombs," *Materials Science and Engineering: A*, vol. 380, pp. 272-280, 2004.
- [125] K. Wang, Y.-H. Chang, Y. Chen, C. Zhang, and B. Wang, "Designable dual-material auxetic metamaterials using three-dimensional printing," *Materials & Design*, vol. 67, pp. 159-164, 2015.
- [126] J. Shen, S. Zhou, X. Huang, and Y. M. Xie, "Simple cubic three-dimensional auxetic metamaterials," *physica status solidi (b)*, vol. 251, pp. 1515-1522, 2014.
- [127] R. Critchley, I. Corni, J. A. Wharton, F. C. Walsh, R. J. Wood, and K. R. Stokes, "The Preparation of Auxetic Foams by Three-Dimensional Printing and Their Characteristics," *Advanced Engineering Materials*, vol. 15, pp. 980-985, 2013.
- [128] A. Ajdari, H. Nayeb-Hashemi, and A. Vaziri, "Dynamic crushing and energy absorption of regular, irregular and functionally graded cellular structures," *International Journal of Solids and Structures*, vol. 48, pp. 506-516, 2011.
- [129] Z. Zheng, J. Yu, and J. Li, "Dynamic crushing of 2D cellular structures: a finite element study," *International Journal of Impact Engineering*, vol. 32, pp. 650-664, 2005.
- [130] I. Liu, *Continuum mechanics*: Springer Science & Business Media, 2013.
- [131] J. Bonet and R. D. Wood, *Nonlinear continuum mechanics for finite element analysis*: Cambridge university press, 1997.
- [132] G. A. Holzapfel, *Nonlinear solid mechanics* vol. 24: Wiley Chichester, 2000.
- [133] R. Richards Jr, *Principles of solid mechanics*: CRC Press, 2000.
- [134] G. T. Mase, R. E. Smelser, and G. E. Mase, *Continuum mechanics for engineers*: CRC press, 2009.
- [135] R. Abeyaratne, *Lecture Notes on The Mechanics of Elastic Solids Volume II: Continuum Mechanics*. Cambridge, USA: Massachusetts Institute of Technology, 2012.
- [136] D. Brands, "Geometrical Modeling and Numerical Simulation of Heterogeneous Materials," Universität Duisburg-Essen, 2012.

- [137] Y. Liu. (2003). *Introduction to the finite element method*.
- [138] J. Fish and T. Belytschko, *A first course in finite elements* vol. 517: Wiley New York, 2007.
- [139] P. Seshu, *Textbook of finite element analysis*: PHI Learning Pvt. Ltd., 2003.
- [140] J. Sun, K. Lee, and H. Lee, "Comparison of implicit and explicit finite element methods for dynamic problems," *Journal of Materials Processing Technology*, vol. 105, pp. 110-118, 2000.
- [141] H. M. Hilber and T. J. Hughes, "Collocation, dissipation and [overshoot] for time integration schemes in structural dynamics," *Earthquake Engineering & Structural Dynamics*, vol. 6, pp. 99-117, 1978.
- [142] H. Al-Rifaie and W. Sumelka, "Numerical analysis of reaction forces in blast resistant gates," *STRUCTURAL ENGINEERING AND MECHANICS*, vol. 63, pp. 347-359, 2017.
- [143] C. W. Lim, S. Cui, and W. Yao, "On new symplectic elasticity approach for exact bending solutions of rectangular thin plates with two opposite sides simply supported," *International journal of solids and structures*, vol. 44, pp. 5396-5411, 2007.
- [144] S. Chakraverty, *Vibration of plates*. USA: CRC press, 2008.
- [145] G. R. Johnson and W. H. Cook, "A constitutive model and data for metals subjected to large strains, high strain rates and high temperatures," in *Proceedings of the 7th International Symposium on Ballistics*, 1983, pp. 541-547.
- [146] G. R. Johnson and W. H. Cook, "Fracture characteristics of three metals subjected to various strains, strain rates, temperatures and pressures," *Engineering fracture mechanics*, vol. 21, pp. 31-48, 1985.
- [147] M. GRAŻKA and J. JANISZEWSKI, "Identification of Johnson-Cook Equation Constants using Finite Element Method," *Engineering Transactions*, vol. 60, pp. 215–223, 2012.
- [148] A. Shrot and M. Bäker, "Determination of Johnson–Cook parameters from machining simulations," *Computational Materials Science*, vol. 52, pp. 298-304, 2012.
- [149] T. Børvik, O. Hopperstad, T. Berstad, and M. Langseth, "A computational model of viscoplasticity and ductile damage for impact and penetration," *European Journal of Mechanics-A/Solids*, vol. 20, pp. 685-712, 2001.
- [150] W. Sumelka and T. Łodygowski, "The influence of the initial microdamage anisotropy on macrodamage mode during extremely fast thermomechanical processes," *Archive of Applied Mechanics*, vol. 81, pp. 1973-1992, 2011.

- [151] T. Łodygowski, A. Rusinek, T. Jankowiak, and W. Sumelka, "Selected topics of high speed machining analysis," *Eng. Trans*, vol. 60, pp. 69-96, 2012.
- [152] M. Szymczyk, W. Sumelka, and T. Łodygowski, "Numerical investigation on ballistic resistance of aluminium multi-layered panels impacted by improvised projectiles," *Archive of Applied Mechanics*, pp. 1-13, 2017.
- [153] A. Love, *A Treatise on the Mathematical Theory of Elasticity* vol. 1: Cambridge University Press, 2013.
- [154] S. P. Timoshenko and S. Woinowsky-Krieger, *Theory of plates and shells*: McGraw-hill, 1959.
- [155] V. Meleshko, "Bending of an elastic rectangular clamped plate: Exact versus 'engineering' solutions," *Journal of Elasticity*, vol. 48, pp. 1-50, 1997.
- [156] P. Sielicki and M. Stachowski, "Implementation of Sapper-Blast-Module, a Rapid Prediction Software for Blast Wave Properties," *Central European Journal of Energetic Materials*, vol. 12, pp. 473--486, 2015.
- [157] C. Lim, W. Yao, and S. Cui, "Benchmark symplectic solutions for bending of corner-supported rectangular thin plates," *IES Journal Part A: Civil and Structural Engineering*, vol. 1, pp. 106-115, 2008.
- [158] N. Kambouchev, L. Noels, and R. Radovitzky, "Nonlinear compressibility effects in fluid-structure interaction and their implications on the air-blast loading of structures," *Journal of Applied Physics*, vol. 100, p. 063519, 2006.
- [159] G. Taylor, "The pressure and impulse of submarine explosion waves on plates," *The scientific papers of GI Taylor*, vol. 3, pp. 287-303, 1963.
- [160] N. Kambouchev, R. Radovitzky, and L. Noels, "Fluid-structure interaction effects in the dynamic response of free-standing plates to uniform shock loading," *Journal of Applied Mechanics*, vol. 74, pp. 1042-1045, 2007.
- [161] A. Vaziri and J. W. Hutchinson, "Metal sandwich plates subject to intense air shocks," *International Journal of Solids and Structures*, vol. 44, pp. 2021-2035, 2007.
- [162] S. E. Rigby, A. Tyas, S. D. Clarke, S. D. Fay, J. J. Reay, J. A. Warren, *et al.*, "Observations from preliminary experiments on spatial and temporal pressure measurements from near-field free air explosions," *International Journal of Protective Structures*, vol. 6, pp. 175-190, 2015.
- [163] J. Shin, A. S. Whittaker, and D. Cormie, "TNT Equivalency for Overpressure and Impulse for Detonations of Spherical Charges of High Explosives," *International Journal of Protective Structures*, vol. 6, pp. 567-579, 2015.
- [164] M. Chipley, W. Lyon, R. Smilowitz, P. Williams, C. Arnold, W. Blewett, *et al.*, "Primer to Design Safe School Projects in Case of Terrorist Attacks and School

- Shootings. Buildings and Infrastructure Protection Series. FEMA-428/BIPS-07/January 2012. Edition 2," *US Department of Homeland Security*, 2012.
- [165] K. Wisniewski and E. Turska, "Improved nine-node shell element MITC9i with reduced distortion sensitivity," *Computational Mechanics*, pp. 1-25, 2017.
- [166] K. Wisniewski, P. Kowalczyk, and E. Turska, "Analytical DSA for explicit dynamics of elastic-plastic shells," *Computational Mechanics*, vol. 39, pp. 761-785, 2007.
- [167] N. Brar, V. Joshi, and B. Harris, "Constitutive Model Constants for Al7075-t651 and Al7075-t6," in *Aip conference proceedings*, 2009, pp. 945-948.
- [168] ASM Specification Aerospace Metals. Aluminum 6063-T4 [Online]. Available: <http://asm.matweb.com>
- [169] S. Reid and C. Peng, "Dynamic uniaxial crushing of wood," *International Journal of Impact Engineering*, vol. 19, pp. 531-570, 1997.
- [170] A. Hassan, S. Jones, and G. Mahmud, "Experimental test methods to determine the uniaxial tensile and compressive behaviour of ultra high performance fibre reinforced concrete (UHPFRC)," *Construction and building materials*, vol. 37, pp. 874-882, 2012.
- [171] R. Solhmirzaei and V. Kodur, "Modeling the response of ultra high performance fiber reinforced concrete beams," *Procedia Engineering*, vol. 210, pp. 211-219, 2017.
- [172] J. Lubliner, J. Oliver, S. Oller, and E. Onate, "A plastic-damage model for concrete," *International Journal of solids and structures*, vol. 25, pp. 299-326, 1989.
- [173] J. Lee and G. L. Fenves, "Plastic-damage model for cyclic loading of concrete structures," *Journal of engineering mechanics*, vol. 124, pp. 892-900, 1998.
- [174] H. Othman, "Performance of ultra-high performance fibre reinforced concrete plates under impact loads," Ph.D, Civil Engineering, Ryerson University, Toronto, Canada, 2016.
- [175] L. J. Malvar and J. E. Crawford, "Dynamic increase factors for concrete," Naval Facilities Engineering Service Center Port hueneme CA1998.
- [176] L. J. Malvar and C. A. Ross, "Review of strain rate effects for concrete in tension," *Materials Journal*, vol. 95, pp. 735-739, 1998.
- [177] Q. Li and H. Meng, "About the dynamic strength enhancement of concrete-like materials in a split Hopkinson pressure bar test," *International Journal of solids and structures*, vol. 40, pp. 343-360, 2003.
- [178] S. Guner and F. J. Vecchio, "Simplified method for nonlinear dynamic analysis of shear-critical frames," *ACI Structural Journal*, vol. 109, p. 727, 2012.

- [179] S. Millard, T. Molyneaux, S. Barnett, and X. Gao, "Dynamic enhancement of blast-resistant ultra high performance fibre-reinforced concrete under flexural and shear loading," *International Journal of Impact Engineering*, vol. 37, pp. 405-413, 2010.
- [180] I. Yang, C. Joh, and B. Kim, "Flexural response predictions for ultra-high-performance fibre-reinforced concrete beams," *Magazine of Concrete Research*, vol. 64, pp. 113-127, 2012.